Order Number 9417099

Interpretation of ice sheet stratigraphy: A radio-echo sounding study of the Dyer Plateau, Antarctica

Weertman, Bruce Randall, Ph.D.

University of Washington, 1993

U·M·I
300 N. Zeeb Rd.
Ann Arbor, MI 48106

Interpretation of Ice Sheet Stratigraphy: A Radio-Echo Sounding Study of the Dyer Plateau, Antarctica

by

Bruce Randall Weertman

A dissertation submitted in partial fulfillment
of the requirements for the degree of

Doctor of Philosophy

University of Washington

1993

Approved by Charles F. Raymond
(Chairperson of Supervisory Committee)

Program Authorized
to Offer Degree **Geophysics Program**

Date **December 15, 1993**

In presenting this dissertation in partial fulfillment of the requirements for the Doctoral degree at the University of Washington, I agree that the Library shall make its copies freely available for inspection. I further agree that extensive copying of this dissertation is allowable only for scholarly purposes, consistent with "fair use" as prescribed in the U.S. Copyright Law. Requests for copying or reproduction of this dissertation may be referred to University Microfilms, 1490 Eisenhower Place, P.O. Box 975, Ann Arbor, MI 48106, to whom the author has granted "the right to reproduce and sell (a) copies of the manuscript in microform and/or (b) printed copies of the manuscript made from microfilm."

Signature 

Date **December 14, 1993**

University of Washington

Abstract

Interpretation of Ice Sheet Stratigraphy: A Radio-Echo Sounding Study of the Dyer Plateau, Antarctica

by Bruce Randall Weertman

Chairperson of the Supervisory Committee: Professor Charles F. Raymond
Graduate Program in Geophysics

Determining the flow history of ice sheets is an issue central to glaciology. Stratigraphic ice horizons provide the only known natural markers for inferring velocity at depth. Stratigraphy can be detected by radio-echo sounding (RES, also called radar) and dated by coring, which together determine the age field in the ice. In this thesis it is shown for the first time how ice flow can be deduced from stratigraphy. As a first step a method is given for the deduction of the spatial pattern of accumulation from shallow dated stratigraphy. The effects of densification and horizontal divergence are determined. It is then shown how, and when, internal motion can be deduced from dated stratigraphy. A theory is developed to deduce streamlines assuming steady-state flow and mass conservation. The theory does not require rheological assumptions or a spatial accumulation rate pattern. The theory can be used to determine internal deformation rates, accumulation rate history and whether or not observed stratigraphy is consistent with steady-state flow.

As part of a collaborative program involving the British Antarctic Survey, the Byrd Polar Research Center, the Polar Ice Coring Office and the University of Washington, the author has used a newly devised RES system to measure the geometry of internal stratigraphy and ice thickness on the Dyer Plateau Ice Sheet, Antarctic Peninsula. RES-determined stratigraphy was dated by comparison to ice core stratigraphy. A prominent shallow RES horizon probably associated with the eruption of Tambora (1815) was used for estimating the spatial accumulation rate pattern. The estimated pattern is consistent with the pattern measured from burial markers indicating that the new method is accurate and that the recent accumulation rate pattern is not different from the 175 year average. An analysis of ice core stratigraphy indicates that over the past 500 years the accumulation rate has varied and over the past 50 years has had an increasing trend. However, dated RES stratigraphy (top half of ice column) appears to be consistent with steady-state flow suggesting that climate variations over the past 500 years have not been sufficient to alter ice flow.

Contents

List of Figures

Acknowledgments

I would like to thank Professor Charlie Raymond for the making this dissertation possible. He has spent many hours guiding me through my research and helping me with my manuscript. At the same time he has given me freedom to pursue my own ideas. I have had the pleasure of spending two field seasons with him on the Dyer Plateau. During the long hours spent shivering around a theodolite and sharing meals in a warm tent, I have gained an appreciation for his knowledge of glaciology and his genuine love of nature.

Professors Edwin Waddington and Robert Crosson gave me many constructive comments while I prepared my text. Many of the ideas presented here stem from conversations I had with my office mates Al Rasmussen, David Morse, Tony Gades, Kurt Cuffey, John Firestone, Bob Benedict, Jim Cunningham, Howard Conway and Torquil Smith. The highly efficient office staff of the Geophysics Program have come to my rescue countless times. I would like to thank Professor John Booker for the support he gave me during my first three years in graduate school.

My field work would not have been possible without the British Antarctic Survey. I feel lucky to have worked with them. I would especially like to thank the BAS scientists David Peel, Rob Mulvaney and John Moore for their cooperation. Field work was made much easier with the cheerful help of the BAS general assistants Rodger Bays, Bill Dark and Nick Lewis. Much of the field work preparation was done by BAS personal at Rothera station. I would also like to thank Professor Lonnie Thompson (Byrd Polar Research Center, Ohio State University) for making his ice core data available. Ice core drilling at the primary drill site was preformed by Bruce Koci (Polar Ice Coring Office, Fairbanks, Alaska). Bruce Koci also assisted us in making vertical strain measurements.

The success of the radio-echo sounding instrumentation would not have been possible without the ingenuity of John Chin. His expertise in high-voltage electronics was invaluable in designing the impulse transmitter. Much of the instrumentation construction was skillfully executed by Jeff Mclean.

Finally I would like to thank my family. Throughout my childhood my parents gave me an environment that encouraged scientific curiosity. My wife Leslie has been a constant source of support. Although our son Johannes has not exactly quickened my work, he has brought much joy into my life. The importance of Leslie's mother, Susan, cannot be overlooked. She has spent many hours caring for Johannes and her cheerful presence has made our lives much more enjoyable.

Funding for this work was provided by the University of Washington Geophysics Program (John Booker, chairman) and by the National Science Foundation under grant DPP 8716243 - *Geophysical Surveys and Ice Flow Modelling to Support Ice Coring for Paleoclimate in the Antarctic Peninsula.*

To my son Johannes and my wife Leslie

It is fun to have fun
But you have to know how.
Dr. Seuss

Chapter 1

Introduction

No other commonly occurring non-vaporous geophysical material rivals glacial ice's transparency to radio waves. This transparency makes it possible to sound even the thickest ice sheets. Strong dielectric contrasts universally exist at the bottoms of glaciers, ice sheets and ice shelves and give rise to strong reflections. Internal dielectric contrasts also exist within ice bodies and these appear as internal reflection horizons. Although not yet completely conclusive, there is evidence (e.g. Millar, 1981) that some, if not most, strong internal reflection horizons are caused by acid fallout from volcanic eruptions. These kinds of reflection horizons represent former ice sheet surfaces and reveal internal stratigraphy. Because internal reflection horizons appear to be tied to chronographic events, they can serve a useful indicators of ice motion.

In this thesis I will assume that radio-echo sounding[1] (RES) internal reflection horizons are depostionally related and hence reveal isochrone shapes. With this assumption I will work towards understanding the flow of an ice sheet based on the shapes of RES internal reflection horizons. My approach will be fundamentally different than previous attempts to correlate internal layering and flow (e.g. Whillans, 1976). In previous work isochrone shapes predicted by ice flow modelling have been compared with observed RES internal reflection horizons; here we shall follow a somewhat opposite course. The shapes of reflection horizons will be used to deduce the flow that gave them their geometeries. Working in this more direct manner will not require force balance calculations or input mass balance and will give us better insight into the relationship between time, age and flow and the geometrical characteristics of internal layer structures.

The ice sheet discussed in this thesis is located in the middle of the Antarctic Peninsula in a region known as the Dyer Plateau (figure 1.1). This site was visited three times during the austral summers of 1988-89, 1989-90 and 1991-92 as part of an ice core drilling

1. Throughout this dissertation the words 'radio-echo sounding' and 'radar' are used interchangeably.

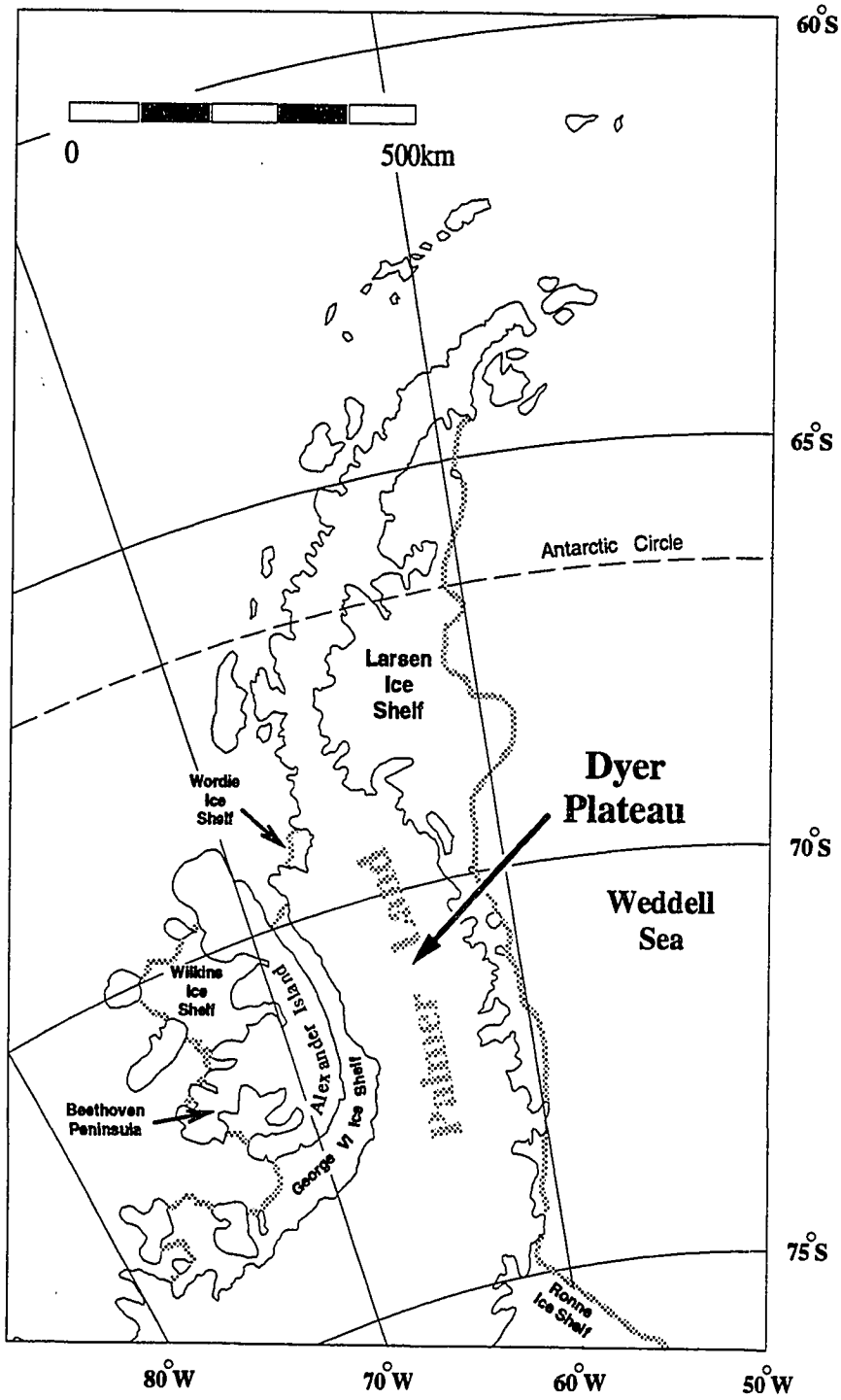

Figure 1.1: Map of the Antarctic Peninsula showing the location of the Dyer Plateau where field work was done.

project involving the British Antarctic Survey (BAS), Byrd Polar Research Center at Ohio State University (BPRC), the Polar Ice Coring Office (PICO) and the University of Washington (UW).

During the 1988-89 season the author and Rodger Bays[2] deployed and partially surveyed a surface marker network approximately 20 km long and 8 km wide straddling the divide of the Antarctic Peninsula (figure 1.2). During that same field season two 100 meter ice cores[3] were extracted from a site located 6 km west of the divide crest. In the next field season (1989-90) the author along with Charlie Raymond[4] and Bill Dark[2] resurveyed and expanded the marker network and collected RES data throughout the expanded network. At that same time, two 235 meter ice cores were extracted from the divide crest and two 50 meter ice cores were extracted from 4 km east of the divide crest[5]. Vertical markers were placed within one of the 200 meter boreholes and their relative positions measured. During the 1990-91 field season Con Curtis[2] and Bruce Crawford[2] extended all of the survey poles to prevent them from being buried. Finally, during the 1991-92 field season the author, Charlie Raymond, Nick Lewis[2] and Rob Mulvaney[6] resurveyed the marker array, performed additional RES and remeasured the vertical markers within the borehole.

This thesis is primarily about the analyses of RES data collected from the Dyer Plateau. Towards this end we shall bring into play measurements of surface motion, borehole vertical marker motion and ice core density and age. A central objective is to determine whether or not the Dyer Plateau Ice Sheet has experienced any significant past changes of flow. Although this thesis is specifically oriented towards analyzing measurements from one region, the methods and theory developed here are general and should be applicable to other regions.

---

2. General assistant, BAS.
3. Members involved with ice core extraction and analysis included Lonnie Thompson (BPRC), Rob Mulvaney, Guy Coulson, Keith Makinson and Phil Poole (BAS).
4. Professor, UW.
5. Members involved with ice core extraction and analysis included Lonnie Thompson (BPRC), Keith Najmulski (BPRC), Bruce Koci (PICO), Andy Reid (BAS) and David Peel (BAS)
6. Scientist, BAS.

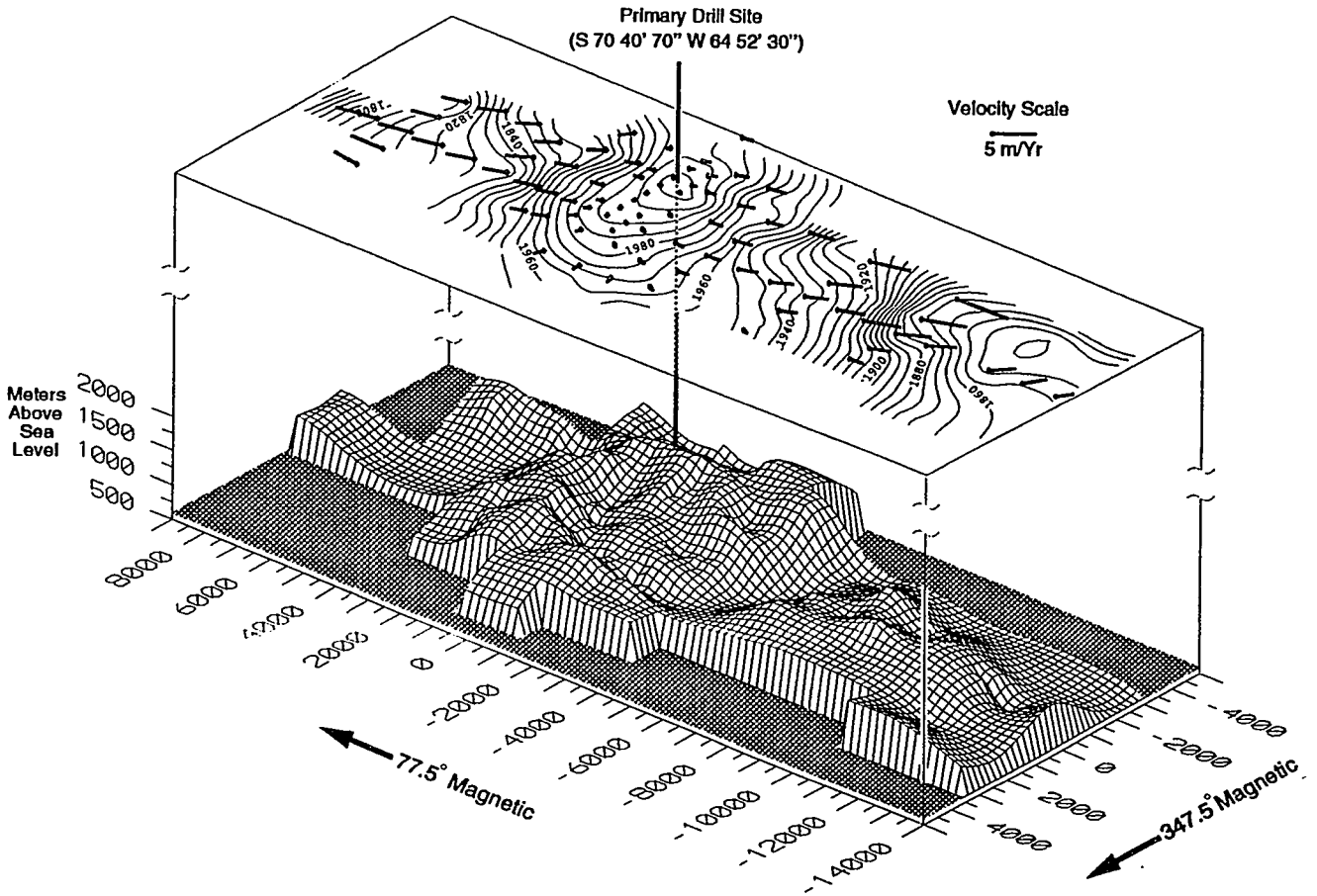

Figure 1.2: A perspective view of the surface and bed topographies in the region of the Dyer Plateau studied. The distances are in meters and the surface contour interval is 5 meters. Small dots represent pole locations and short lines represent measured pole velocities. 347.5° mag. is 8.3° east of geographic north.

Determining the flow history of large ice bodies is an issue central to glaciology for several important reasons. Changes in ice flow can complicate the interpretation of ice core records. For example, if the location of an ice divide were to migrate, folds might be introduced into the layering structure; an ice core taken through such a fold would sample ice of the same age more than once. Changes of ice flow can be caused by changes in climate. For example, an increase of ice velocity and surface altitude and slope could result from an increase of mass balance. Perhaps most intriguing, changes of ice flow may have dramatic effects on the climate. It has long been realized that continental and marine ice sheets are potentially unstable (Weertman, 1961; 1974). Recently, Bond *et al.* (1993) have documented an apparent link between ocean-atmosphere temperature changes and Laurentide ice sheet dynamics in the North Atlantic region during the previous 20 to 80 kyr. Ice sheet modelling by MacAyeal (Lehman, 1993) indicates that changing bed conditions caused by geothermal heat flux may have caused the Laurentide ice sheet to "purge" into the North Atlantic every ~7,000 years[7]. Additionally, there has been speculation that the West Antarctic ice sheet is unstable (e.g. Hughes, 1973). If it were to collapse, it would raise the world sea level by ~5 meters and would alter the climate of the remainder of Antarctica. In the past decade there has been a focused effort to understand the dynamics of the ice streams that drain the West Antarctic ice sheet because it is believed that the ice streams control the fate of the ice sheet (Alley and Whillans, 1991). Recent RES observations by Jacobel et al. (1991) have revealed complex internal layering in ice stream C. This ice stream has simple surface and bed topographies; if the observed horizons represent isochrones, it is difficult to understand how steady-state flow could cause them to be shaped the way that they are.

In the second chapter I begin by giving background discussions about the geographical and climatological setting of the Dyer Plateau and the physics of RES. This is done to show the motivations for studying the Dyer Plateau and the physical principals which govern RES.

---

7. According to MacAyeal's model, at the beginning of a purge cycle the bed was frozen. As the ice sheet thickened its insulating action also increased and geothermal heat eventually caused the bed to rise above the melting point resulting in a purge.

Earlier RES researchers have experienced difficulty detecting internal reflection horizons as well as bed echoes. In the third chapter I discuss the lightweight RES instrumentation developed for and used on the Dyer Plateau. The instrumentation successfully recorded continuous internal reflection horizons and bed echoes. The chapter includes a detailed description of a high powered transmitter which was partially responsible for the success of the field work.

In the fourth chapter I describe the steps taken to bring the collected RES data into a scientifically useful form. This includes descriptions of how the RES data was collected, displayed, organized and converted from radio wave travel times to ice depths.

Chapters three and four provide the basic information needed to enable the newly developed radar methods to be easily used in the future.

At this point I am ready to investigate what flow information can be extracted from the RES data. In the fifth chapter I show how the spatial pattern of the depth of a shallow internal reflector (dating from 1815 and probably associated with the eruption of Tambora) can be used to determine the spatial pattern of snow accumulation. By using such a horizon it is possible to infer the pattern of accumulation rate over a large area quickly and without the need to revisit.

In the sixth chapter I develop a mathematical relation between time, age and flow and show under what circumstances a velocity field can be determined from an age field. I then show a simple method for determining streamlines from a steady-state age field. This method is applied to RES and ice core data. The deduced streamlines are interpreted and are also compared with streamlines determined from surface motion measurements. The primary goal of the analysis is to determine if non-steady-state flow is required to explain ice sheet stratigraphy and, if so, what type of non-steady-state flow.

Finally, in chapter 7 I briefly summarize the results of this thesis and discuss the implications of this thesis on future RES research.

Chapter 2

Background

In this chapter two very separate subjects are presented as background material to this thesis: the geographic and climatological setting of the Dyer Plateau and the physics of internal reflection horizons observed in radio echo sounding (RES). The discussion of the setting of the Dyer Plateau is presented to show why the Dyer Plateau ice sheet is glaciologically interesting and to demonstrate the type of information that might be gained by studying it. The discussion of internal reflections is presented to give an understanding of the physics involved in the creation of internal reflections and what is presently understood about them.

2.1 - Geographic and Climatological Setting of the Dyer Plateau

2.1.1 - Geographic Influences

The Antarctic Peninsula extends 1500 kilometers northward from its base, Ellsworth Land (S 75°), to its tip, the Trinity Peninsula (S 68°). The Dyer Plateau (S 71°, W 64°) is situated on the crest of the Antarctic peninsula just south of its middle in a region known as Palmer Land (figure 1.1). Because of its altitude (1500-2000 m asl) the Dyer Plateau is cold (10 meter temperature of -21°C) and does not in general experience summer surface melting as do the surrounding costal regions. This makes the Dyer Plateau a desirable region for ice core drilling.

Atmospheric circulation in Antarctica is typified by permanent high pressure situated over East Antarctica and 2-5 cyclones orbiting it at the approximate latitude of S 60° (Zwally et al.; 1983). The backbone of the Antarctic Peninsula is an S-shaped mountain range of sufficient altitude (~2000 meters) to influence weather on the continental scale. The Antarctic Peninsula tends to anchor cyclones on its east and west sides. On average this results in a relatively cold northerly flow on the Antarctic Peninsula's eastern side and relatively warm southerly flow on it's western side thus giving the Antarctic Peninsula an east-west average temperature contrast of approximately 7°C (Drewry and Morris, 1992).

This east-west gradient contrasts with the general meridional temperature gradient of most of the antarctic.

Because the Dyer Plateau is located at the spine of the Antarctic Peninsula, its local weather is primarily influenced by systems originating from both the south-western Weddell and north-eastern Bellingshausen Seas. Any long term east-west shift in the geostrophic flow pattern should therefore have a pronounced effect on the Dyer Plateau's weather. For example, if the flow pattern were to advance 500 km eastward it is likely that the Dyer Plateau would mainly experience weather systems originating in the Bellingshausen Sea. If any such shift has taken place in the last few thousand years it should be detectable in the ice of the Dyer Plateau.

The difference in temperature between the east and west coasts is evident in the latitudinal extent of ice shelves along the two coasts (figure 1.1). On the relatively cold east coast the Larsen Ice Shelf extends nearly to the tip of the Antarctic Peninsula while on the relatively warm west coast the most northerly ice shelf, the Wordie, is 600 km further south.

Due to the circular shape of the antarctic continent and the general circular circulation pattern around it, most of Antarctica does not experience a significant maritime weather influence; the Antarctic Peninsula is an exception. Because precipitation on the Antarctic Peninsula is mainly derived from air masses arriving directly from the ocean areas surrounding it, the precipitation there is likely to contain more oceanic impurities than precipitation arriving in the high continental regions of Antarctica. The impurity content will be related to such factors as nearby oceanic biological activity, sea surface roughness and sea ice extent. Precipitation on the Antarctic Peninsula also samples global atmospheric conditions differently than the rest of Antarctica due to its lower latitude. As air masses move southward, away from the Southern Ocean, they loose moisture and the isotopes, chemicals and dust which they carry are fractionated. By comparing ice core records taken from the Antarctic Peninsula and the interior of Antarctica, it maybe possible to better understand the fractionation process, and the significance and meaning of archived climatic signals in all of Antarctica.

2.1.2 - Sea Ice

In contrast to the Arctic Ocean, the Southern Ocean experiences a large seasonal variation in sea ice extent. The minimum and maximum sea ice coverages occur in February and September respectively and range from $4\times10^6 km^2$ to $20\times10^6 km^2$. This range in variability roughly equals the surface area of South America and is greater than the surface area of the permanent antarctic ice cover.

Sea ice plays an important role in modifying the weather in the antarctic by acting as an effective barrier to the exchange of heat and mass between the atmosphere and ocean and by greatly increasing the ocean surface albedo (Zwally et al., 1983). Sea ice's effectiveness in modifying the weather is in part determined by the amount of open water leads within it. Leads can be caused by differential flow and wave action. Because of this the coupling between sea ice and weather is complex. In general the sea ice extent is greater during cold periods, such as the *little ice age*[1] (Zwally et al., 1983), and in general sea ice should amplify cold periods and help to decrease precipitation during them.

The topographic barrier of the Antarctic Peninsula coupled with the embayment associated with the Ronne and Filchner Ice Shelves and the general oceanic and atmospheric currents result in a well formed cyclonic gyre in the Weddell Sea. Associated with the gyre are relatively cold ocean water temperatures and high sea ice concentrations (Zwally et al., 1983). The relatively cold water temperatures along with a generally cold northerly flow of air on the western side of the Weddell Sea results in year round sea ice coverage on the western Weddell Sea. By blocking the ocean-atmosphere exchange of heat this permanent ice pack insures that northerly moving air masses which reach the east coast of the Antarctic Peninsula remain cold.

2.1.3 - Glacial Change

In the last one and a half decades the Wordie Ice Shelf has rapidly disintegrated and is now nearly completely gone (Doake and Vaugan, 1991). The northern end of the Larsen Ice Shelf has retreated 40 km since the 1940's, the Spartan Glacier on the center of the east coast of Alexander Island is thinning at the rate of 0.27 m a^{-1} and ice rises on the east coast

1. This is known to be true of the arctic and conjectured as true in antarctic.

of the Antarctic Peninsula appear to be thinning at a rate of approximately 0.5 m a^{-1} (Doake 1982). Taken together this information seems to indicate a general pattern of negative mass balance. However, annual snow fall observations from Halley and Faraday stations and inferred accumulation rates from Dolleman and James Ross Islands indicate that there has been an increase in accumulation rates starting around the turn of the century (Morris, 1991). Thus it is likely that the recent ice thinning and retreat of ice fronts has been due to temperature increases. Historic temperature records date back to around 1945. They appear to show a general warming trend. However a rigorous statistical analysis by Sansom (1989) shows that the trend could be simply due to meteorological noise.

Although the Antarctic Peninsula accounts for only 6.8% of the surface area of the continent it gathers 25% of Antarctica's precipitation (Drewry and Morris, 1992). Because the peninsula experiences such large precipitation rates it is likely that it can have a significant influence on sea level change.

The Dyer Plateau receives approximately half a meter of ice equivalent precipitation per year. This is much larger than the precipitation received in most of Antarctica. High mass balance rates decrease the residency time of ice in ice sheets. Because of this the Dyer Plateau is a disadvantageous location for the recovery of ice from ancient times such as the last ice age which ended approximately 10,000 years ago. However, because annual layers are thicker there, it is a good location for the recovery of ice containing a detailed record of the precipitation during recent climatic events such as the Little Ice Age which occurred during A.D. 1450 - 1850 (Imbrie and Imbrie, 1979).

The response of the total Antarctic Peninsula ice mass to climatic warming will be more complex than the response of the rest of Antarctica because the Antarctic Peninsula spans so many climate regimes. Although warming will increase mass balance in high cold areas by raising atmospheric humidity levels and hence precipitation, it will simultaneously decrease mass balance in low lying regions by increasing ablation. In the long run this may cause the net ice mass in the Antarctic Peninsula to increase but in the short run it may cause it to decrease (Drewry and Morris, 1992).

Because the ice sheets covering the Antarctic Peninsula are much smaller and expe-

rience much higher accumulation rates than those covering the rest of Antarctica, the Antarctic Peninsula will have a significantly shorter response time to climatic change (e.g. Jóhannesson and others, 1989); if CO_2 green house warming scenarios become a reality the Antarctic Peninsula should be the first part of Antarctica to show significant signs of impact (Drewry and Morris, 1992).

2.2 - Radio Echo Sounding - Physics of Internal Reflections

The study of the physics of internal reflections is a field which is by no means mature and has its share *maybe's* and *probably's*. At the simplest level internal reflections can be explained as a result of spatial variations of the complex electrical permittivity. Beyond this level there are several likely explanations but proving which one's are correct or dominant is often difficult.

In RES experiments radio waves of the frequency band 1MHz to 1GHz are directed into an ice body and the energy which is scattered from within and off the bottom of the ice body is recorded. Because the magnetic permeability, μ, of water and ice is not significantly different from that of free space all scattering must be due to variations of the complex permittivity ε^* (see page 139). Variations of ε^* can be further broken down into variations of: (1) the high and low frequency permittivities, (2) the dielectric relaxation process of the ice and (3) the bulk electrical conductivity of the ice. (1) has been found to depend mainly on temperature and density while (2) and (3) have been found to depend on present and past temperature, density and chemistry.

2.2.1 - Wave Attenuation

In appendix A.1 I derive the wave equation for an electromagnetic wave travelling in a lossy dielectric. For materials which are weakly attenuating its solution is well approximated by the complex frequency domain equation

$$\vec{E} \equiv \vec{E}_0 e^{-\left(\frac{\sigma}{2}\sqrt{\frac{\mu}{\varepsilon}} + i\omega\sqrt{\mu\varepsilon}\left(1+\frac{1}{8}\left(\frac{\sigma}{\omega\varepsilon}\right)^2\right)\right)z}, \qquad (2.3)$$

where $i \equiv \sqrt{-1}$ and ω is angular frequency. The quantity

$$z_c = \frac{2}{\sigma}\sqrt{\frac{\varepsilon}{\mu}}$$

is the characteristic distance of attenuation. σ and ε are frequency dependant and in polar ice sheets they yield $z_c \approx 1000m$ at RES frequencies. Because the thicknesses of the great polar ice sheets are of this same scale it is possible to sound their depths. In contrast, the solid earth has characteristic distances of attenuation (at RES frequencies) ranging from 10 centimeters (limestone) to 100 meters (granite).

For polar ice at RES frequencies

$$\frac{1}{8}\left(\frac{\sigma}{\omega\varepsilon}\right)^2 \ll 1.$$

Consequently, wavelength in polar ice depends on the permittivity and not the effective conductivity.

2.3.1 - Reflection from a Dielectric Interface

The simplest type of dielectric interface is the boundary between two half-spaces of different dielectric permittivities.

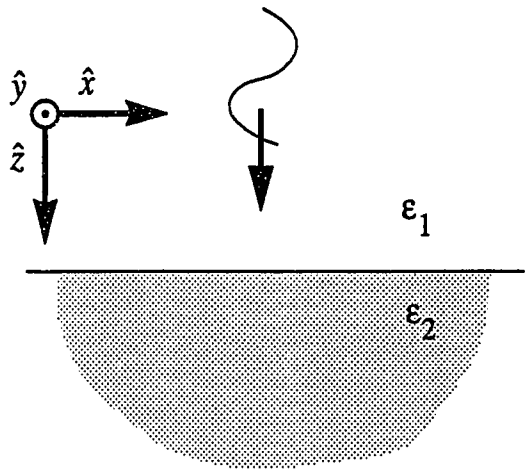

Figure 2.1: Electromagnetic wave hitting a dielectric interface.

In appendix A.2 I show a derivation of the reflection coefficient, r, for such an interface for the two principal polarizations. For the polarization of the electric field in the plane of incidence the reflection coefficient is found to be

$$r = \frac{\sqrt{1 - \frac{\varepsilon_1}{\varepsilon_2}\sin^2\Theta} - \sqrt{\frac{\varepsilon_2}{\varepsilon_1}}\cos\Theta}{\sqrt{1 - \frac{\varepsilon_1}{\varepsilon_2}\sin^2\Theta} + \sqrt{\frac{\varepsilon_2}{\varepsilon_1}}\cos\Theta},$$

where Θ is the angle of incidence. For the polarization of the electric field normal to the plane of incidence, r is found to be

$$r = \frac{(1 - (\varepsilon_1/\varepsilon_2)^2\sin^2\Theta)^{-1/2} - \sqrt{\varepsilon_2/\varepsilon_1}\sec\Theta}{(1 - (\varepsilon_1/\varepsilon_2)^2\sin^2\Theta)^{-1/2} + \sqrt{\varepsilon_2/\varepsilon_1}\sec\Theta}.$$

These two equations are well known as Fresnel's laws of reflection.

The power reflection coefficient, $R \equiv |r|^2$, of the first polarization decreases with increasing angle of incidence whereas the power reflection coefficient of the second polarization shows the opposite behavior. This is illustrated in figure A.2. For low dielectric contrast ratios, as one would expect to find in most ice bodies, the power reflection coefficient of the first polarization drops to zero at an angle of incidence close to 45°; this is called the Brewster angle. At angles of incidence beyond the Brewster angle the power reflection coefficient increases and at the grazing angle (90°) is unity.

2.3.2 - Reflection from a Thin Layer

In appendix A.3 I show a derivation of the reflection coefficient of a reflecting layer which is thin compared to the wavelength, λ. The power reflection coefficient is shown to be approximately

$$R \approx \frac{\Theta^2}{4}\left|\frac{\Delta\varepsilon}{\varepsilon}\right|^2 \qquad \Theta \ll 2\pi$$

where $\Delta\varepsilon$ is the difference in permittivity between the layer and the host material and $\Theta \equiv 2\pi l/\lambda$ (l = layer thickness). In the appendix I consider three types of thin layers: (1) a thin layer of a different conductivity, (2) a thin layer with a different density, and (3) a thin layer of water. In the appendix I have evaluated the first two types of layers for realistic values of conductivity and density contrasts for a 10 centimeter thick layer and the

third type of layer for a 1 millimeter thick film of water. At the frequency evaluated (10 MHz) the first two layers are shown to have approximately identical power reflection coefficients[2] ($-72dB$ and $-74dB$) but the water film is shown to have a reflection coefficient which is four orders of magnitude larger ($-32dB$).

The first type of layer (layer of different conductivity) is shown to have the interesting property that its reflection coefficient is frequency invariant. Since the second type of layer has a power reflection coefficient which is proportional to squared frequency it may be possible to discriminate reflectors due to density and conductivity contrasts by examining their frequency dependance.

If the layer is not thin compared to the wavelength, the reflection coefficient has a more complex behavior. It can be shown that a layer which is a quarter of a wavelength thick will have a reflection coefficient very close to zero. For example consider a 100 MHz radio wave traveling through ice which has a velocity of propagation of $167 \text{meters}/\mu\text{S}$. At this frequency the wavelength will be 1.67 meters and a quarter wavelength will be 42 centimeters. However, a 10 MHz radio wave will have a quarter wavelength of 4.2 meters. Thus a high frequency 100 MHz radar would not be able to detect layers of close to half a meter thickness whereas a low frequency 10 MHz radar could.

2.3.3 - Causes of Dielectric Variability

I now wish to address what causes dielectric variations. To do this it is necessary to examine in detail the dielectric behavior of ice. For the frequency range of zero to 1 GHz ice has been found to closely follow the electrical circuit analog shown in figure 2.2

2. The decibel, dB, is defined as 10log (power reflected/power incident).

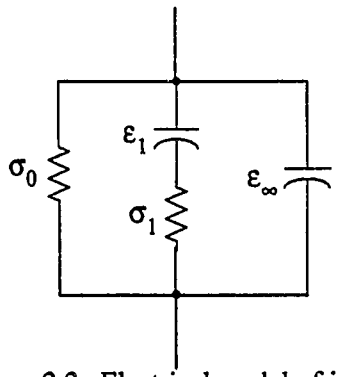

Figure 2.2: Electrical model of ice valid for the RES frequency band.

In this model σ_0 represents the low frequency conductivity, ε_∞ represents the high frequency permittivity, $\sigma_0 + \sigma_1$ represents the high frequency conductivity and $\varepsilon_\infty + \varepsilon_1$ represents the low frequency permittivity. Variations in any one of these parameters will cause the complex permittivity to vary which in turn can result in observed internal reflections.

The four parameters shown in the electrical model can be interpreted as physical processes occurring within the ice.

Interpretation of Model Parameters:

σ_0 - Bulk conductivity of the ice resulting from, amongst other things, the motion of Bjerrum and ion defects.

ε_∞ - High frequency permittivity resulting from electron cloud distortion

ε_1 - Portion of low frequency permittivity due to water molecule reorientation.

σ_1 - Loss factor associated with water molecule reorientation.

$\tau = \varepsilon_1/\sigma_1$ is the time constant associated with water molecule reorientation in response to an applied electric field. Experimentally ε_∞ has be found to be primarily a function of ice density while ε_1 is dependent on density and temperature. On the other hand σ_0 and σ_1 seem to be dependent on temperature, structure, chemistry and density. ε_∞ and ε_1 are also weakly related to air bubble shape and orientation. I have analyzed the effect of air bubble shape on ε_∞ and ε_1 based on a model presented by Ackley and Kelehir

(1979) and have found that it is strongest for low density ice (firn) but causes only a 1% difference.

The effects of temperature, chemistry and structure on σ_0 and σ_1 are complex and not completely understood. In general there are large differences between polar ice (mean temperature below -10° C) and temperate ice. Temperate ice exhibits a σ_0 approximately 3 orders of magnitude lower than that of polar ice. In Glen and Paren (1975) in situ measurements of σ_0 made by using the four electrode technique show a conductivity of 0.008μS/m for temperate ice and 10μS/m for polar ice despite the polar ice being much colder.

The high frequency conductivities of temperate and polar ices are not systematically different which suggest that a different mechanism is at work for the relaxation process than for the bulk conduction process. There is reason to believe that acid concentrates at grain edges (Mulvaney & others 1988) in a liquid state, providing a means of conduction. In temperate ice, melt water flow may flush out these acid conduits and thus reduce bulk conductivity. Moore & others (1990) show that ice from Dolleman island, Antarctica has a high frequency conductivity which is linearly dependent on acid and salt content. If the acid also effects the low frequency conductivity, it can be seen how the high frequency conductivity is dependent on both impurities since the higher frequency conductivity is the sum of σ_0 and σ_1. In the same paper the relaxation frequency is also shown to be linearly dependent on acid and salt content. Since the relaxation frequency is thought to depend principally on σ_1 and not on ε_1 it is difficult to explain why it should depend on acid content unless some of the acid does not reside on the grain edges and the relaxation mechanism involves the acid.

σ_∞ also appears to be dependent on the thermal history of the ice, at least in firn. The high frequency conductivity of a piece of firn collected from Byrd, Antarctica was found to increase by half an order of magnitude after it had been warmed to –7°c for two days and then cooled back down to –45°c (Reynolds, 1985).

In order to test the significance of density variations Millar (1981) plotted observed internal reflection strengths from Dome C, Antarctica along with expected reflection

strength based on known density fluctuations with depth. He found that for the upper 1.5 kilometers the internal reflection strengths could be accounted for by the density fluctuations, but below that depth some other mechanism was necessary.

Work needs to be done to determine what physical parameters are dominant causes of electrical variations and resulting internal reflections. It will be necessary to combine chemical and electrical measurements of ice cores with RES reflection patterns. It is possible that most significant reflectors are associated with sulfuric acid rich volcanic horizons. If this is found to be true then it should possible to date the ice column over large surface areas by detailed examination of RES profiles. In chapters five and six I show how dated reflection horizons can be used to deduce spatial accumulation rate patterns and internal ice sheet velocities.

Chapter 3

Instrumentation

In principal most ice radar systems are relatively simple. They are similar to sonar systems found on ships but the signal used is electromagnetic instead of acoustic. A basic ice radar system consists of a high powered radio frequency transmitter, a transmitter antenna, a receiver antenna, an amplifier and a signal recorder. The transmitter delivers a pulse of electrical energy to the transmitter antenna. The transmitter antenna radiates a portion of the energy into space. Some fraction of the radiated energy finds its way into the ice and some of that energy is reflected back upwards to the ice surface from interfaces within and at the bottom of the ice. Some of the returned energy is captured by the receiver antenna and is then passed to the receiver preamplifier. The amplified signal is then sent to the signal recorder. The signal recorder is typically an oscilloscope coupled with either a camera, a computer or simply the human eye. Radars that use pulse packets which are short relative to the center frequency period of oscillation are called impulse radars and radars that use pulse packets which are long relative to the center frequency period of oscillation are called pulsed radars (see § 3.3).

3.1 - Recording Systems Used on the Dyer Plateau

In this section I give an overview of two impulse RES profiling systems which I have assembled and used on the Dyer Plateau. The two systems differed primarily in the oscilloscopes and computers which they used.

Figure 3.1 shows how the recording systems were configured for RES profiling. A snowmobile was used for towing the radar systems. It was tied to a Nansen sledge carrying the transmitter equipment which was in turn tied to a second Nansen sledge carrying the receiver equipment. The distances separating the snowmobile and sledges are indicated in the figure.

The recording systems primarily used a pair of 20 meter resistively loaded dipole antennas with center frequencies near 5 MHz. The forward halves of the antenna dipoles

were attached to the tow ropes while the trailing halves were simply dragged on the snow (see figure 3.1).

The forward transmitter sledge carried the transmitter and a battery power supply while the rear receiver sledge carried a generator (or box of batteries), a preamplifier and a thermally insulated box containing an oscilloscope, a computer and some other circuitry. A thermally insulated box was used in order to keep the recording circuitry warm enough to operate. Attached to the rear of the receiver sledge was a bicycle wheel odometer. While profiling on the Dyer Plateau one person, usually Charlie Raymond, drove the snowmobile while another person, usually myself, manned the receiver equipment. .

Figures 3.2 and 3.3 show the two recording systems in greater detail. The system shown in figure 3.2 (2432 system) was operated during the 1989-90 field season while the system shown in figure 3.3 (222 system) was operated during the 1991-92 field season. I gathered most of the Dyer Plateau data using the 2432 system.

The 2432 system utilizes a Tektronix 2432 oscilloscope coupled with a PC-compatible Tektronix 2402 computer. The 2432 is a full featured digital oscilloscope which requires line voltage to operate. This was suppled by a small gas powered generator. The 2432 oscilloscope communicates with the computer via an IEEE-488 interface. Because the IEEE-488 is a parallel interface, it is possible to transfer waveform information quickly from the oscilloscope to the computer.

The 2402 computer contains a digital/analog interface board. The board is connected to a circuit that monitors a pressure transducer and another circuit that monitors the rotations of the trailing bicycle wheel.

The 222 system utilizes a Tektronix 222 digital oscilloscope coupled with a laptop PC-compatible computer. The 222 oscilloscope does not have as many features as the 2432 oscilloscope, but it is extremely compact and can be powered from a car battery. It communicates with the computer via an RS-232 serial port. This interface is considerably slower than the IEEE-488 interface. I have used the parallel port of the laptop computer to communicate with a counter circuit tied to the bicycle wheel. The 222 system did not include a pressure transducer circuit.

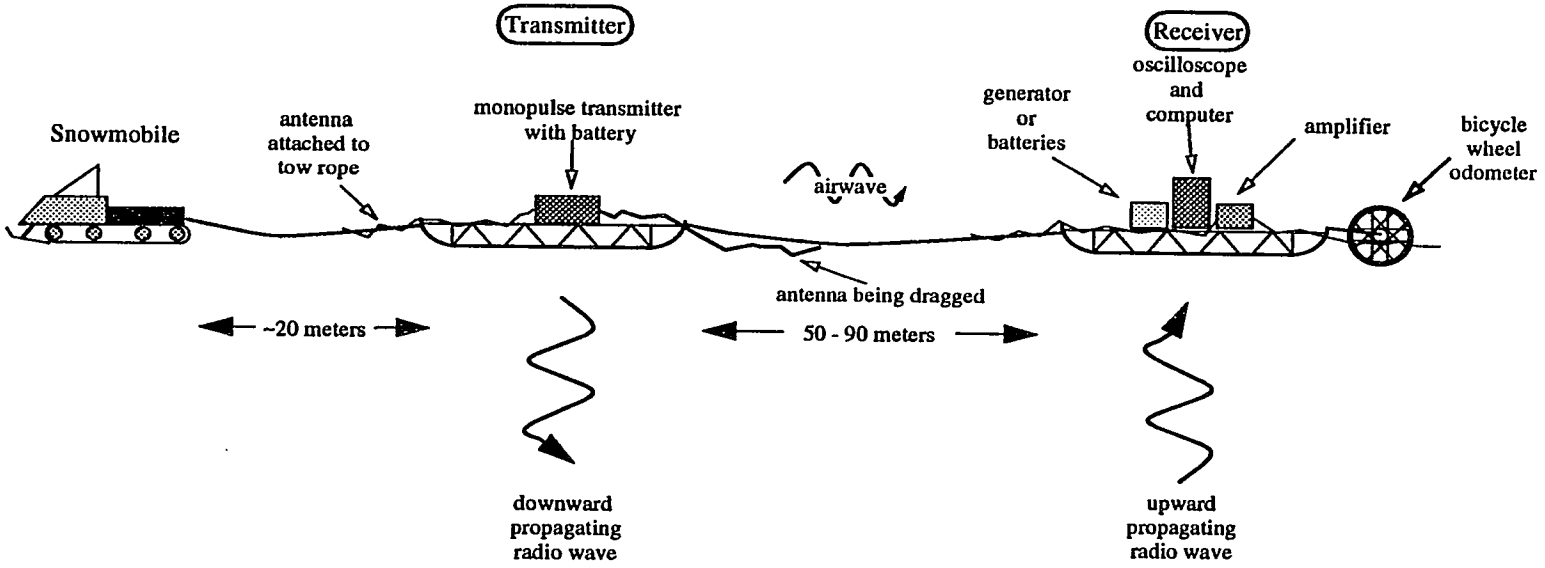

Figure 3.1: Configuration of monopulse RES systems used on the Dyer Plateau.

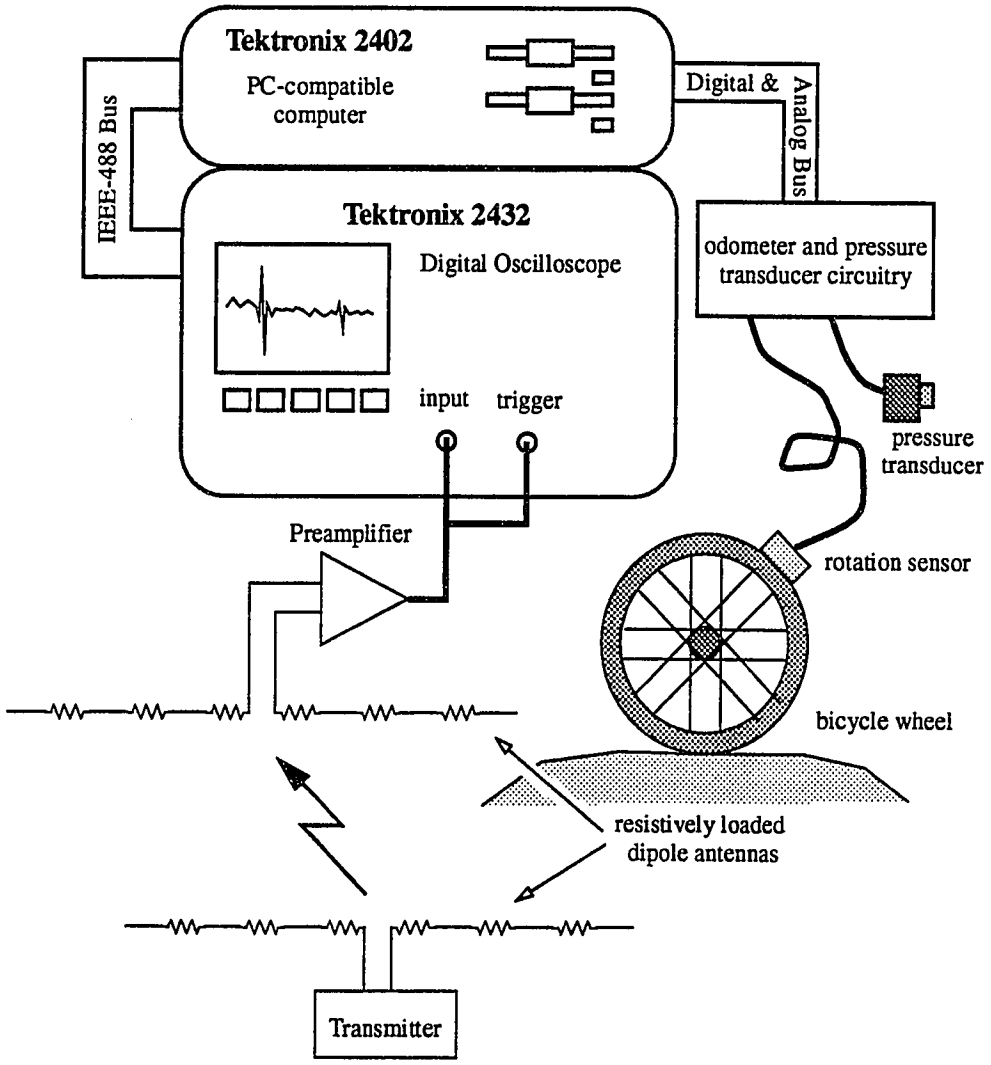

Figure 3.2: Schematic diagram of the 2432 recording system. The receiver circuitry was powered by a small gas powered generator. The transmitter was powered by a 12 volt battery.

The 222 recording system was originally used on the Agassiz Ice Cap, Ellesmere Island by Ed Waddington in May 1991. This recording system generally yields inferior results to those of the 2432 system but its lightweight nature and low power requirements makes it more practical in situations where weight is a premium.

3.2 - Recording Methods

Earlier radar systems displayed their received signals on oscilloscope screens which

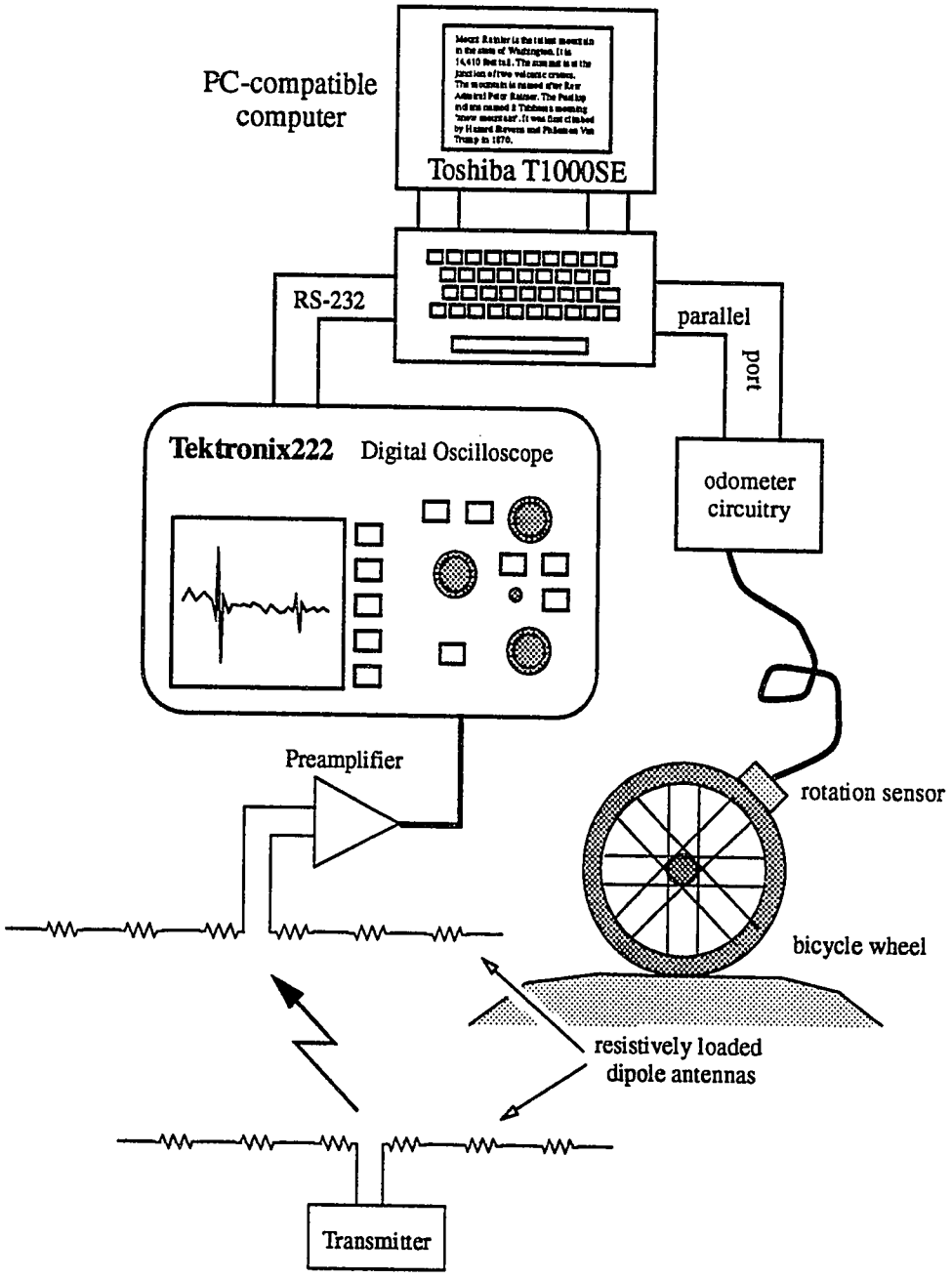

Figure 3.3: Schematic diagram of the 222 recording system. The receiver and transmitter circuitry was powered by 12 volt batteries.

were then photographed. The photographs were taken from oscilloscopes displaying either in the *a-display* mode or in the *z-display* mode. In the a-display mode the horizontal axis

of an oscilloscope screen is used to represent time while the vertical axis of the oscilloscope screen is used represent signal amplitude; this is the way in which an oscilloscope is normally operated in an engineering laboratory. In the z-display mode the horizontal axis of the oscilloscope screen is also used to represent time but the visual intensity along the trace shown on the oscilloscope screen is used to represent the strength of the signal being recorded. With the a-display mode, photographs of an oscilloscope screen are taken at regular intervals along a traverse with each sounding requiring its own photographic frame. With the z-display mode photographic film is continuously run past the oscilloscope screen and an image is built up in a similar fashion to how an image is created on a television screen.

The two display methods are complementary. The a-display method allows a detailed examination of signal strengths and shapes while the z-display mode allows trends in signal shapes to be easily seen. Ideally an experimenter would record using both methods simultaneously.

With analog recordings it is typically very difficult to extract information not immediately apparent at the time a recording was made. Digital recordings have the advantage of allowing the data to be displayed in either of the two modes after it has been recorded. On play back of the recorded data, display parameters can be adjusted to enhance aspects of the data which may have otherwise been missed. For example, contrast levels can be adjusted in a z-display to emphasize weak reflections coming from internal layers in an ice sheet. Because of this capability it is often possible to find reflections which were not observed at the time a recording was made.

3.3 - Frequency Range of Ice Radars

In the four decade wide frequency band of 100 kHz to 1 GHz ice is relatively transparent to radio-waves. This broad range of frequencies allows two different transmission schemes to be used: monopulse and pulsed. Monopulsed systems radiate single cycles of electromagnetic waves and usually are capable of recording both amplitudes and phases of the received reflected signals. They generally operate from the low end of the transparency band (100 kHz) up to roughly 20 MHz. Pulsed systems cover the high end of the

transparency band ranging from 20 MHz up to 1 GHz. Pulsed systems radiate electromagnetic wave packets which are tens to several hundred cycles long. Except for the most modern high speed digital recording systems, pulsed radars do not record phase information because the frequency of the radiated signal is so high. Instead the signal is *detected* by passing it through a diode and then a low pass filter. When this is done the phase information is lost.

In general antenna size is inversely related to antenna frequency; monopulse antennas tend to be long (~20 meters) while pulsed antennas are usually fairly short (~2meters). For this reason monopulse systems are not as well suited for airborne work, although they have been used in this way (Watts and Wright, 1981). Pulsed antennas can be fixed under airplane wings and the metal wing surfaces can be advantageously used as reflectors for increasing antenna directionality.

3.4 - Monopulse Transmitter Design

Monopulse transmitters were used for all of the work which we have done. In concept monopulse transmitters are simple. The rudimentary design of a monopulse transmitter is shown in figure 3.4.

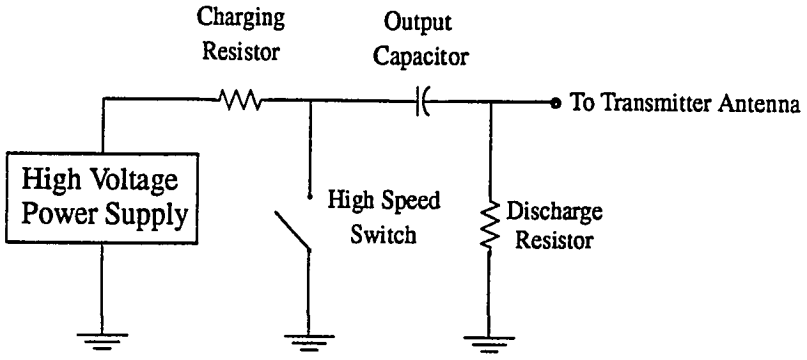

Figure 3.4: Simplified circuit diagram of a monopulse transmitter.

Initially, the high speed switch is in an open state and the output capacitor (typically $0.005\mu f$) is charged to a high voltage via the charging resistor (typically $1k\Omega$). The transmitter is *fired* when the high speed switch is closed. This causes the voltage on the antenna side of the capacitor to abruptly *swing* from a ground voltage to the negative of the voltage that was formerly on the high speed switch side of the capacitor. This abrupt swing causes

an electromagnetic wave to propagate down the length of the antenna.

After a short period of time[1] the voltage on the antenna side of the capacitor returns to ground due to charge leaking out through the discharge resistor (also typically 1kΩ). At this point the capacitor is recharged and ready to be fired again.

The maximum theoretical rate at which a monopulse transmitter can be fired will be determined by the time constants associated with the charging and discharge resistors and the capacitor. For the values stated here this rate is roughly 200kHz. This is an impracticably high repetition rate for three reasons: (1) at this rate the high voltage power supply must deliver more than 2 k Watts, (2) oscilloscopes are not capable of recording traces at this rate and (3) at this pulse rate pulses are sent into the ice faster than it takes for a pulse to make a round trip from the surface to the bottom of the ice and back if the ice is more than 500 meters deep. The oscilloscope which I have used is only capable of recording traces at a rate of 20 Hz. In order to reduce the time the oscilloscope waits between available signals, I have set my transmitter so that it operates at a rate a few times higher than 20 Hz.

Two fundamental components of the monopulse transmitter are difficult to design and build: (1) a high efficiency, high voltage supply capable of producing at least 1000 volts and (2) a switch for the output capacitor(s) that is both extremely fast and capable of withstanding high voltage.

Most high voltage supplies use a transformer to generate high voltage. A time-varying current is applied to the primary coils of the transformer and high voltage is generated at the secondary coils. If it is assumed that the resistance in the wires is negligeable and there is perfect magnetic coupling between the two coils, the ratio of the input to output voltages will be the same as the ratio of the turns of the input and the output windings. To have a transformer develop high voltage it therefore necessary to have few windings on its input side relative to its output side. If a transformer is lossless then the power which goes into it should be the same as what comes out of it. On either side of a transformer the power will be the current multiplied by the voltage. Because the voltage on the input side

1. $Time \cong R_{dischargc} \bullet C_{output} \cong 1\text{k}\Omega \bullet 0.005\mu\text{f} = 5\mu Sec.$

is small (~12 V) it is necessary to supply large currents to produce significant power. This presents a design difficulty because: (1) large currents are not easily switched, (2) large wiring must be used to handle the large currents and (3) large instantaneous currents must be demanded from the input power supply.

The high voltage switch of the output capacitors is even more difficult to design and assemble. For a typical transmitter the output switch must switch 1000 volts in 10^{-8} seconds! This requires a slew-rate of $100\text{kV}/\mu\text{S}$. Achieving such a rapid switching rate is the single most difficult engineering challenge in making a monopulse transmitter.

The speed at which the switch goes from infinite resistance to no resistance is critical in determining the highest frequency that the transmitter is capable of generating. If the switch closes quickly enough the frequency characteristics of the transmitter antenna will determine the frequency which is radiated. If the switch does not close quickly enough the transmitter will determine the frequency that is radiated. Monopulse radar antennas are simply resistively loaded dipole antennas. The resistance per unit length, r, along the length of a dipole increases with distance from the antenna feed point. The resistance per unit length along an antenna is usually given by the equation

$$r = \frac{\psi}{[L-x]}$$

where ψ determines the damping factor of the antenna and L is the half length of the antenna (Wu and King, 1965). The resistance is necessary to keep the antennas from ringing. As the wave generated by the transmitter propagates out onto the antenna, part of its energy is radiated and part of its energy is absorbed by the resistive loading. The more the antenna is loaded the less it will ring. However, the more it is loaded the less energy it will radiate. Therefore a trade-off must be made between energy radiated and ringing.

In the RES configurations that we have used for our field work in Antarctica and elsewhere the transmitter and receiver antennas are laid directly on the snow. The physics of the radiation properties of a resistively loaded antenna on a dielectric are complex (Annan, 1973). I have found that the antenna system that I have assembled yields useful results but I have not attempted to understand in detail the physics of it or how it could be

made to work better.

3.4.1 - Avalanche-Transistor Switch

The first monopulse ice radar transmitters utilized bipolar transistors in an avalanching mode to do the switching (Watts and Wright, 1981). Avalanching occurs when the electric field in the junction region of a semiconductor device becomes strong enough to ionize the semiconductor atoms and produce an avalanche of additional charge carriers (Hayt and Neudeck, 1976). The voltage at which this occurs is called the zener breakdown voltage. This value is a function of the doping levels in the p- and n-type regions of the device. When the breakdown takes place it can be destructive and destroy the device. However if a small enough amount of energy passes through the device it can survive.

Two similar designs have been used in avalanche-transistor switches. In the first design the transistors are tied in series to the output capacitor. Initially the capacitor has no charge on it. As current flows through the charging resistor the capacitor accumulates charge and its voltage increases. Eventually the voltage on the capacitor reaches a point at which one of the transistors avalanches and goes from a non-conducting to a conducting state. When this occurs the other transistors suddenly have more voltage placed across them and they also avalanche. The avalanching is extremely rapid and can occur in just a few nanoseconds.

In this design the repetition rate at which the transmitter fires is determined by the voltage of the high-voltage supply, the size of the charging resistor attached to the high-voltage supply, the size of the capacitor and the zener breakdown voltage of the weakest transistor.

In the second design one of the switches is externally fired by applying a TTL[2] level pulse to its base. When the switched transistor goes into conduction it imposes additional voltage on the other transistors and they then avalanche.

A chief difficulty in building an avalanche-transistor switch is in the selection of appropriate transistors. The zener breakdown voltage is extremely sensitive to doping levels. A large batch of transistors must be purchased and sorted through to find transistors

2. Transistor-Transistor Logic

which have the desired avalanching behavior. Out of a large batch only a few transistors may have the desired level. Another difficulty is that the breakdown voltage is often not consistent; from one avalanche to the next there can be large variations in the breakdown voltage. An avalanche-transistor switch which uses external switching can overcome this difficulty but only within limitations. When the switched transistor closes it must be able to force the other transistors into avalanching. Additionally, the other transistors must not spontaneously break down before the switched transistor is triggered.

3.4.2 - MOSFET Switch

Because of the difficulties associated with the avalanche transistor switch, John Chin, an Engineer at the University of Washington Geophysics program, developed a switch which uses MOSFETs (Metal Oxide Semiconductor Field Effect Transistor) instead of the avalanche bipolar transistors used in earlier designs. In his design the MOSFETs are not used in an avalanching mode and as a result their behavior is more easily predicted by the transistor manufacturer's specifications. The MOSFET switch is simple but innovative. Figure 3.5 shows its basic design. When a positive voltage is applied to the

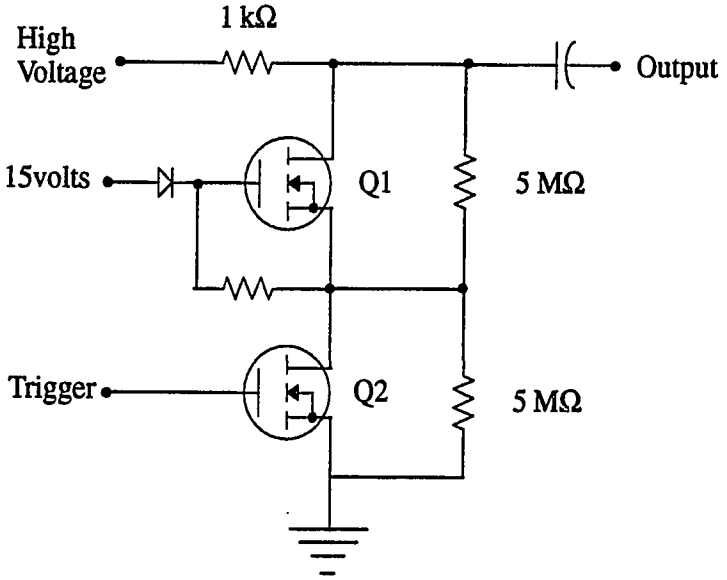

Figure 3.5: Basic design of John Chin's high speed MOSFET switch.

gate of transistor Q1 the transistor goes into conduction. This creates a positive voltage difference across the gate and source of Q2 which in turn causes it to go into conduction. In principal more than two such MOSFET's could be cascaded together in this fashion. Each of the MOSFET's used in our transmitter can *standoff*[3] 500 volts. This limits the voltage standoff of the high speed switch to 1000 volts. By *mirroring* the design to a bipolar configuration it is possible double the voltage and quadrupole the power of the single sided design.

The gates of the MOSFETs have considerable capacitance (~500pF). *Driving* this capacitance is the single greatest challenge to making a MOSFET switch quickly. To make a MOSFET switch, the voltage between the gate and the source must be increased from zero to ten volts. This is accomplished by depositing five nanocoulombs of charge on the transistor's gate. If the transistor is to be switched in ten nanoseconds then an average current of half an ampere must flow during the period of time in order to deposit this charge. Switching half an ampere of current over the extremely short period of time of ten nanoseconds is difficult. In Chin's design three stages of bipolar transistors are used to drive this current. Careful selection of the bipolar transistors and their accompanying resistors is needed in order to make the MOSFET's switch quickly and symmetrically between the positive and negative sides of the transmitter. However, once the components are selected the circuit is stable. In a recent redesign of the transmitter (not presented here), these bipolar transistors have been replaced by MOSFET's. Consequently, the switching speed and symmetry can now easily be adjusted.

3.4.3 - High Voltage Power Supply

One of the critical design challenges of the monopulse transmitter was to develop a high voltage supply that consumes little power. John Chin achieved this goal by using a pulsed transformer design. Shortly before each firing of the transmitter the a pulse of current approximately 15 microseconds long is sent into the primary side of the transformer. By using a pulsed rather than a continuously cycled transformer the high voltage power

---

3. Standoff voltage is the maximum voltage that can be placed across a circuit before it breaks down.

supply only needs to draw power when it is needed. For the work that we have done the transmitter was fired at a rate of only 50 Hz. At 50 Hz the power supply draws current less than 0.1% of the time. At this rate the high voltage power supply draws less power than the supporting logic circuitry. The transmitter can be operated at rates of up to 30 kHz. At this speed the high voltage supply operates half-time and draws over 100 watts.

Figure 3.6 shows an empirical relationship found between transmitter pulse rate and

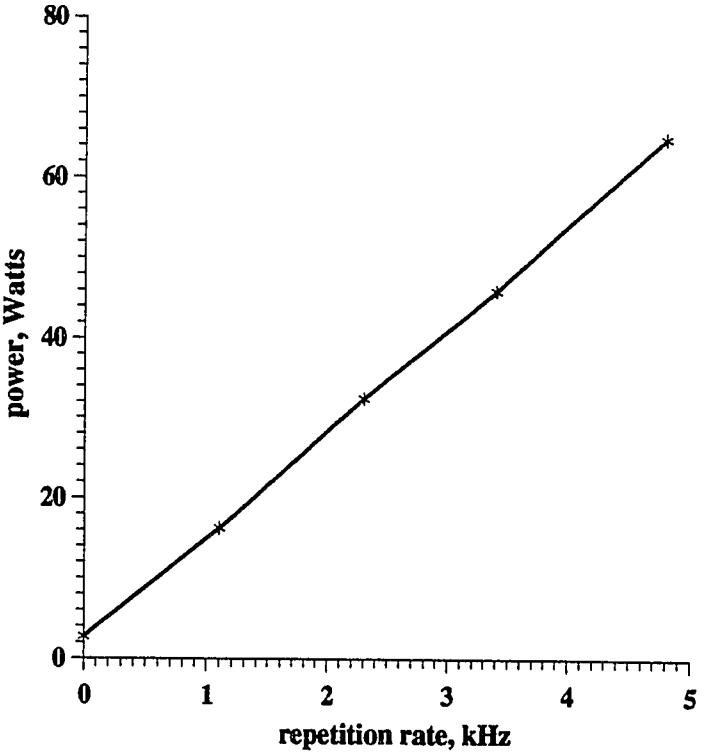

Figure 3.6: Empirical relationship between transmitter pulse rate and power consumption.

input power required by the transmitter. The quiescent power requirement is 2.5 watts. After applying linear regression to the empirical power relation the slope of the curve, which should be the same as the energy per pulse, is found to be 13.0 mJ. Given this energy and the size of the two capacitors, the charging resistors and output voltage a power supply efficiency can be calculated. The theoretical energy required to charge the capacitors is given by

$$\begin{aligned}
\text{energy} &= 2\times\text{energy}_{capacitor} + 2\times\text{energy}_{resistor} \\
&= 2\left(\frac{1}{2}CV^2\right) + 2\int_0^\infty I^2 R\,dt \qquad \left(I = \frac{V}{R}e^{-t/(RC)}\right) \\
&= CV^2 + CV^2 \\
&= 2CV^2 \\
&= 10\text{ mJ} \qquad (V = 1000\text{v}),\ (C = 5\times10^{-9}\text{f})
\end{aligned}$$

where the factors of two are required because the transmitter is bipolar[4]. This gives a power supply efficiency of 77%. Notice that the size of the charging resistors does not affect the theoretical power requirement.

When the transformer is pulsed it deposits charge on the output capacitors. The amount of charge, and hence the voltage, delivered to the capacitors depends on the input voltage to the transformer and the length of time that the transformer is pulsed. The transmitter was designed to run on standard 12 volt batteries. An empirical relation can be found between the input voltage and the pulse time required to achieve an output of ±1000 volts over a range of input voltage between 10 and 13 volts. A compensation circuit which includes a *555-timer* integrated circuit (a standard component) and an operational amplifier is used to generate a pulse of the appropriate length of time over the 10 to 13 volt range. This circuit is able to produce an output voltage which is steady to within a few percent over the supply voltage range.

The two transistors which switch the transformer on and off are able to withstand only 15 volts. This places a high end voltage limitation on the high voltage power supply circuit[5]. By selecting transistor switches capable of withstanding higher voltages the high voltage power supply could be extended to operate with higher input voltages. Below 9 volts the ±15 volt power supply to the supporting logic circuitry will not operate.

3.4.4 - Supporting *Logic* Circuitry

Because of the pulsed nature of the high voltage power supply it is necessary to have

---

4. Because the RC time constant is much less then the pulse rate the definite time integral of the power passing through the resistor, $\int_0^\infty I^2 R dt$, is taken to fall completely between two pulses.
5. This is not normally an issue because the transmitter is usually powered by a 12 volt battery.

supporting circuitry that controls the timing of the charging of the output capacitors and the firing of the output switch. It is necessary to have circuitry which:

- regulates the output voltage at ±1000 volts over the input range of 10-13 volts,
- shuts the transmitter off if the input voltage falls below 9.5 volts (this prevents intermittent behavior at low battery voltages),
- guarantees that the output capacitors will be completely charged when the output switch is closed,
- prevents the output capacitors from being charged while the switch is closed,
- prevents the output capacitors from being charged before they have finished discharging (this protects against over charging),
- prevents the transmitter from operating if a short is placed across the output.

The first point has already been discussed in § 3.4.2. The electronics with which all six points are realized are tightly coupled together and involve a blend of analog and digital design. The over all design philosophy was to create an inherently reliable and self protecting system. The reader is referred to appendix B for the exact details of the transmitter circuit design.

3.5 - Preamplifier

In the RES system which I have used, the electromagnetic signal that is captured by the receiver antenna is amplified by a pre-amplifier before it passed to the digitizing oscilloscope. This increases the signal strength so that it will be above the noise floor of the oscilloscope. However there are other reasons for using a preamplifier. For example, by using a non-linear preamplifier it is possible to increase the dynamic range[6] of the recording system and by using a bandpass filter preamplifier it is possible to increase the signal to noise ratio by rejecting unwanted high-frequency and low-frequency noise.

Figure 3.7 shows a hypothetical transfer function of a compression amplifier used to increase the dynamic range of a radar recording system. When a compression amplifier is used the resolution of the input signal will vary with signal level and will be proportional to

6. In this case dynamic range is taken to be the ratio of the largest to smallest detectable signals.

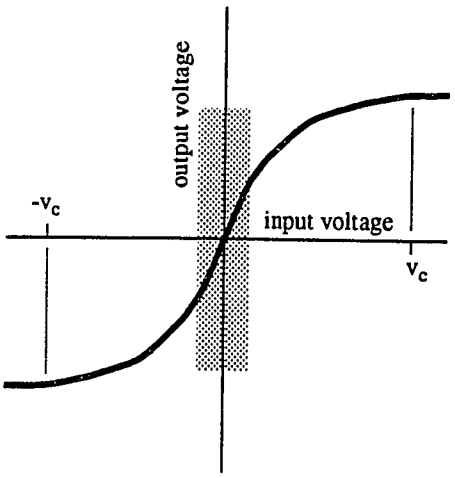

Figure 3.7: Hypothetical transfer function of a compression amplifier. The horizontal axis represents the input voltage and the vertical axis represents the output voltage. The two axis do not necessarily have the same scale. V_c is the voltage at which the amplifier clips the input signal. Stippling indicates the voltage range in which the compression amplifier acts linearly.

$$\text{Resolution} \propto \frac{dV_{out}}{dV_{in}}.$$

At large positive and negative voltages the compression amplifier will clip the received signal; beyond the clip voltage the resolution of the recording system will be zero.

In principal a compression amplifier enables the simultaneous detection of faint reflections and strong near surface reflections without losing all of the information about the strong signal's strength as would an amplifier which simply clips large signals.

Compression amplifiers have some disadvantageous aspects. Because they are non-linear they complicate the frequency response. If the *base-line* of the input signal is non-zero it will cause a non-symmetric response between the positive and negative sides of a signal. This will cause the generation of odd frequency harmonics from pure sine wave input signals. The monopulse transmitter output is composed of a very short sine wave packet and a comparatively weak step jump with an exponential decay which is several microseconds long. The step jump is caused by the step in voltage at the transmitter antenna feed point when the high speed switch is closed and the exponential decay is

caused by the transmitter output capacitors draining through the discharge resistors. This weak jump can result in such a base-line off-set. Another source of base-line offset can come from the amplifier itself if its internal d.c. off-set is not set properly or if it drifts.

A second difficulty associated with compression amplifiers is setting their transfer characteristics. Ideally the experimenter will know a priori the shape and amplitude of the received signal when designing a compression amplifier. This is usually not the case and once *out-on-the-ice* time is too precious to allow the design of an amplifier. Typically some guess must be made as to the shape of the received signal and a design chosen from that. Each ice sheet has its own unique combination of opacity and depth and hence will require its own unique compression amplifier for each radar configuration used on it.

Two designs of compression amplifiers were used on the Dyer Plateau. Each design had very similar transfer characteristics. Both designs utilized high speed operational amplifiers (op-amps) built by the Comlinear Corporation. For compression, one of the designs utilized the non-linear characteristics of diodes while the other used a monolithic multistage compression amplifier built by the Micro Electronics Corporation. Figures 3.8 and 3.9 are circuit diagrams of the two designs and figure 3.10 is the corresponding com-

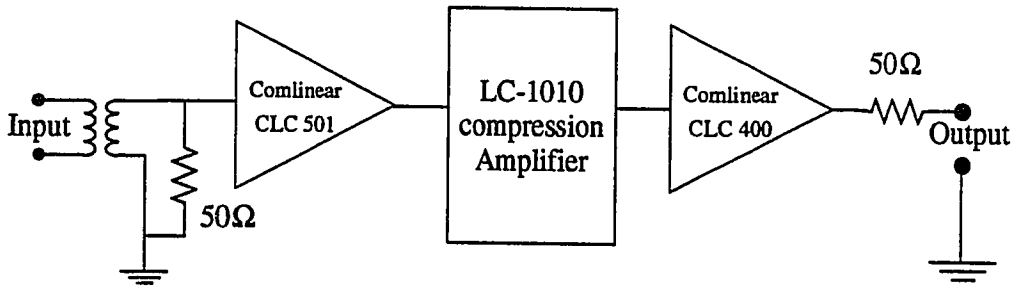

Figure 3.8: Simplified circuit diagram of the compression amplifier which utilized an LC-1010 compression amplifier built by the Micro Electronics Cooperation.

pression characteristics of the two amplifiers taken around 2 MHz.

For the work I have done on the Dyer Plateau most of the reflected signal was much smaller than I anticipated. As a result, the preamplifier was operated close to its zero

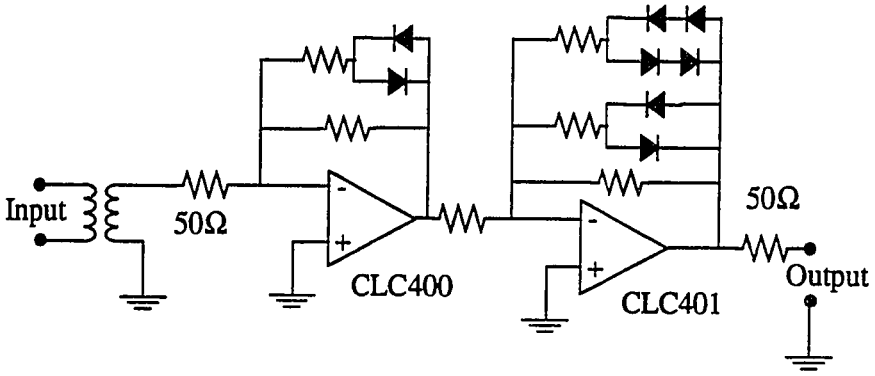

Figure 3.9: Simplified circuit diagram of the amplifier which utilized the nonlinear characteristics of diodes to achieve compression. The operational amplifier integrated circuits are products of the comlinear corporation.

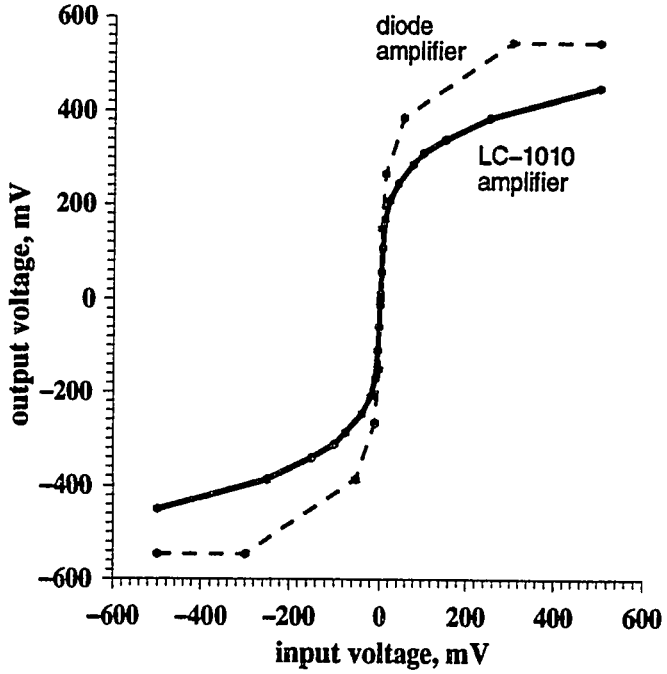

Figure 3.10: Compression characteristics of the two compression amplifiers built.

crossing and the gain of the oscilloscope had to be set to a large value. Portions of the sig-

nals which were relatively large were then clipped by the oscilloscope. For the portions of the signals which were not clipped by the oscilloscope the amplifiers worked well as linear amplifiers with amplitude gains of about 40.

Other approaches could be used to improve the dynamic range of the radar. An ideal method would be to use a computer feed-back loop which would adjust the compression amplifier to tailor it to the signal which is being received. Feed-back parameters could be chosen to determine how much of the recorded signal would be devoted to expanding low level signals relative to high level ones. A time-varying-gain amplifier could also be used to improve the dynamic range of the recording system. A computer could determine an enveloped shape of the returned signal. The enveloped shape would then be used to set time varying gain. Where the envelope's amplitude is small the amplifier's gain could be set large and where the envelope's amplitude is large the gain could be set small. Great care would have to be taken to insure that electrical noise originating in the computer would not contaminate the input signal.

A time varying gain system has been successfully used by Steve Hodge on ice-stream B in West Antarctica. The system which he employed used a preset gain sequence which went in discrete upward jumps. The time varying gain was triggered by a fiber optic cable which was attached to the transmitter. His system has one drawback; the discrete jumps in the gain leave strong horizontal visual artifacts in the recorded record. By using smooth increases in the gain this problem could be avoided.

I have also designed, built and used a bandpass preamplifier. The preamplifier has been successfully operated on the Dyer Plateau by myself and Charlie Raymond as well as on Taylor Dome near Ross Island in Antarctica by David Morse and Ed Waddington

(Waddington et al., 1991). Figure 3.11 is a schematic of the preamplifier. In addition to

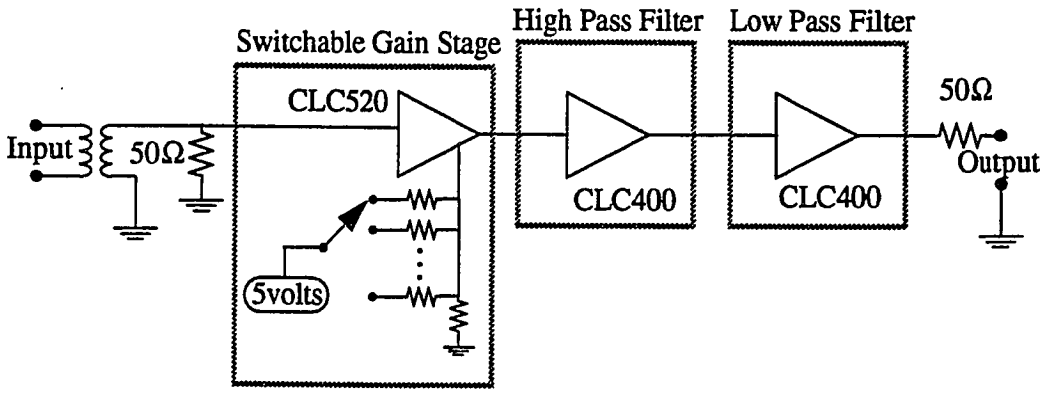

Figure 3.11: Simplified circuit diagram of the 1-10MHz band pass amplifier. At a frequency of 5MHz the gain is switchable from 3.4 to 54. All operational amplifiers are manufactured by the Comlinear Cooperation.

being a band pass filter the amplifier also has adjustable gain. The gain can be adjusted between 10 dB and 35 dB. The filter passes frequencies between 1 MHz and 10 MHz. Outside the pass band, the filter roles off at 20 dB of amplitude gain per decade of frequency.

The theoretical and measured amplitude and phase frequency response of the preamplifier is shown in figures 3.12 and 3.13. The theoretical and experimental responses match closely. This indicates that the amplifier is well understood. It is important that the amplifier be well characterized so that its effects can be accurately taken into account when the recorded time series are analyzed.

The bandpass preamplifier is beneficial in two respects: (1) it helps to eliminate spurious electrical noise present outside of the frequency band of interest and (2) it removes the low frequency signal associated with discharge of the transmitter output capacitors. On the Dyer plateau we have observed significant ionospheric and cultural noise at all times of day except between approximately 9:00 and 15:00 local time. Figure 3.14 is an example of data collected during the quiet and noisy times of day. Unfortunately much of the noise

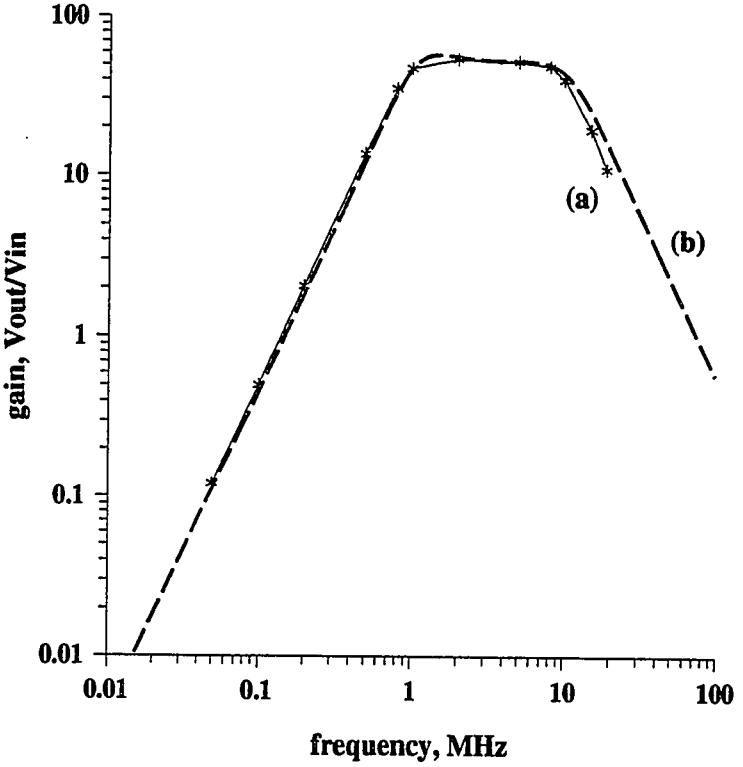

Figure 3.12: Measured (a) and calculated (b) amplitude frequency responses of the 1-10MHz band pass amplifier.

occurs in the same frequency band that the radar uses. This greatly reduces the effectiveness of the bandpass preamplifier.

The Tektronix 2432 oscilloscope has a built in low-pass filter with a cutoff frequency of 30 MHz. This is effective at preventing a large amount of high frequency noise from being recorded but is not needed if a bandpass preamplifier is used.

3.6 - Defeating Generator Noise

The 2432 system utilized a gas powered generator for its electrical power. Sparkplug ignition noise and noise generated by generator brushes was found to be significant in the frequency band used by the ice radar. Its reduction to acceptable levels posed an engineering challenge. After a great deal of experimentation outdoors but close to the engineering laboratory three steps were found that reduced this noise: (1) placing the generator in a

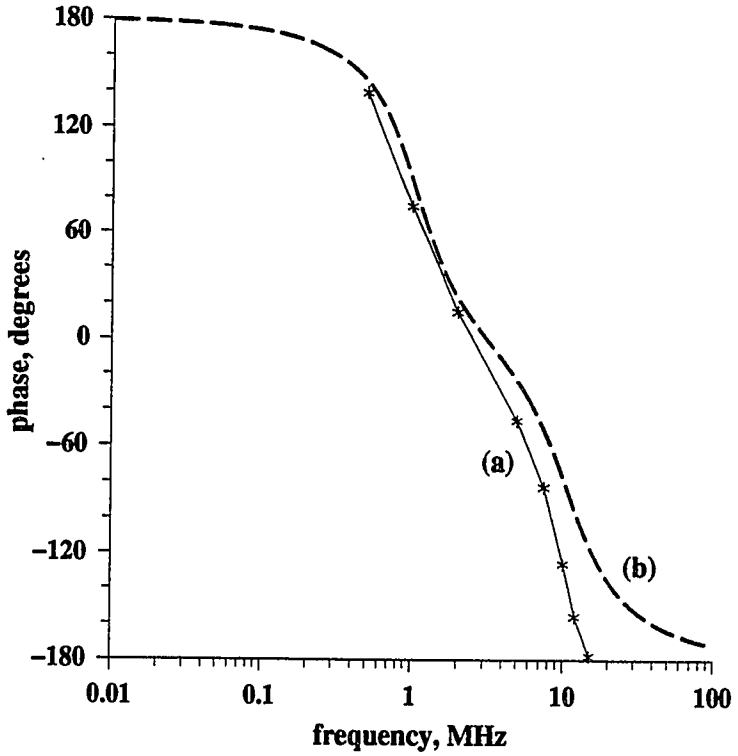

Figure 3.13: Measured (a) and calculated (b) phase frequency responses of the 1-10MHz band pass amplifier.

wire *Faraday* cage tied to the ground of the power system, (2) running the power out of the wire cage through a radio noise reduction power line filter and (3) passing the output of the receiver antenna through a radio frequency transformer.

I found that the placement of the generator within the wire cage was important; if the sparkplug of the generator was placed too close to the cage the noise level increased dramatically. I also found, somewhat surprisingly, that the wire cage did not have to completely surround the generator. In fact simply placing the generator on a large metal plate seemed to have at least half the beneficial effect of placing it completely in a metal box.

The second step had a surprisingly small effect on reducing the noise. I presume that this was because the ground was not tied to a *solid* ground plane in field operation and that noise was able to leak directly out through the ground. I tested this presumption in the laboratory by tying the power supply to a building ground and observing the elimination of

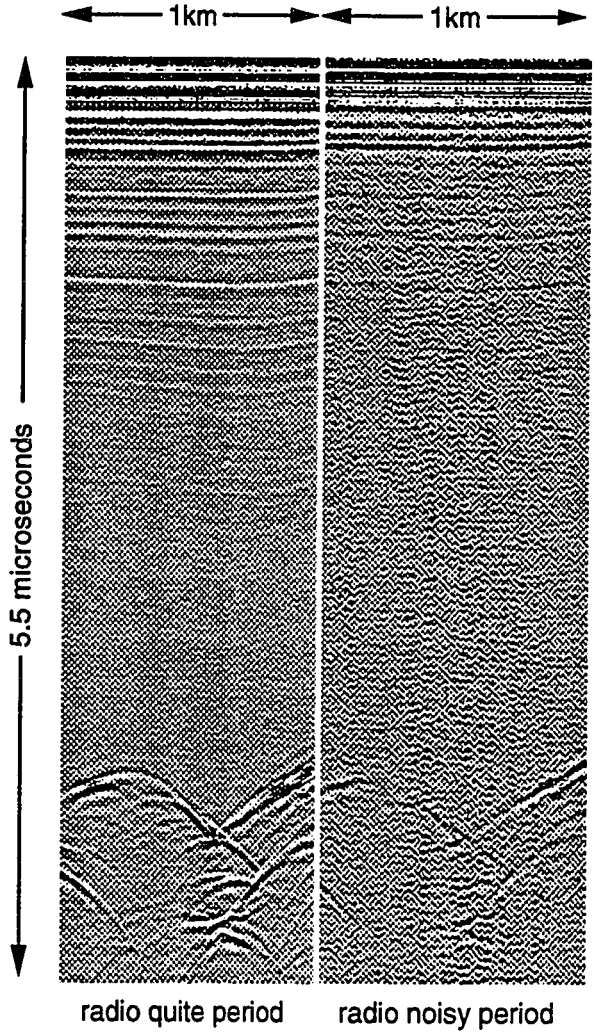

Figure 3.14: An example of an two identical radar traverses collected during a radio-quiet time of day (left) and a radio-noisy time of day (right).

most of the noise at the receiver.

Apparently the whole recording instrument, including the antennas, oscillates with electromagnetic energy when the generator produces noise. One might not expect the preamplifier to detect this noise. However, if one side of the antenna is tied to ground and other side is tied to the preamplifier input then there will be an electrical asymmetry which may produce a differential generator noise input. This leads to the third step for reducing

generator noise which is to pass the output of the receiver antennas through a radio frequency transformer before passing it to the preamplifier. Doing this uncouples the power supply ground from the antenna and results in a major reduction in noise observed at the amplifier.

The gain on the oscilloscope channel used for triggering must be set to a level where the trigger circuitry can discriminate between the generator noise and the air-wave. If the gain is set too large both the air-wave and the generator noise will be clipped. If this happens then it will not be possible to set the trigger level to a voltage where the trigger fires exclusively on the air-wave and not on the noise. For this reason it is useful to have one channel of the oscilloscope used for recording the signal and another channel used for triggering the oscilloscope; the recording channel is set to a high gain to get good signal resolution while the triggering channel is set to a lower gain for air-wave/generator noise discrimination.

The generator noise is spike-like in character and occurs on the order of 100 times per second. If the oscilloscope is triggering only on the transmitter air-wave then the probability of detecting the generator noise in any given recorded trace is roughly equal to the length of the recording window multiplied by the frequency of the noise. For most of the work done the recording window was 10^{-5} seconds long. Multiplied by a noise frequency of 100 events per second this gives a noise detection probability of 10^{-3}. The oscilloscope *stacks* roughly 100 traces for each trace that it records. This will result in approximately one in every ten recorded traces being corrupted by generator noise.

3.7 - Defeating Electronics Noise

In addition to the electrical noise produced by the generator there is also problematical noise produced by the recording electronics circuitry. Most of the electronics noise can be adequately contained by using shielded cables and by placing the preamplifier away from the computer communications hardware.

The 2432 system was originally designed so that it could communicate with the user via a monitor and a special environmentally toughened keyboard. The monitor was placed in a grounded metal box and was connected to the computer via a shielded cable. In field

use it was discovered that the monitor radiated significant amounts of electrical noise and so this configuration was abandoned.

Chapter 4

Data Organization and Preliminary Analysis

In this chapter I discuss the preliminary steps taken to bring the RES data collected from the Dyer Plateau into a useful form for scientific analysis. The subject matter presented here ranges from how the data files were collected and stored to how the recorded RES echoes were converted from travel times to ice depths. Much of the information presented here concerns the many programs necessary to bring the data into a useful form. It is likely that future RES experimenters will require similar programs and many of the programs mentioned here should be applicable to future data sets.

4.1 - Data Gathering

Figure 4.1 is a flow diagram depicting the relationship between the hardware, software and the RES data files generated by the recording systems. This flow diagram is applicable to both the 2432 and the 222 recording systems. In this section I briefly discuss the three software sections shown in the diagram.

4.1.1 - Diagnostic Software

The diagnostic software is used to verify that the bicycle wheel odometer circuitry was working properly and, in the case of the 2432 recording system, that the barometric pressure sensor circuitry was working properly. The diagnostic programs are typically run immediately after the profiling systems are assembled in the field, whenever some difficulty arrises or when the barometric pressure transducer zero offset must be adjusted.

4.1.2 - Recording Software

As the recording system is towed across the snow surface the recording program monitors the distance travelled using the bicycle wheel odometer. When the program observes that a set distance increment has been travelled, usually 10 meters, it instructs the oscilloscope to transfer a waveform to the computer where it is temporarily stored. Because the recording systems were often physically shaken as data were gathered and disk drives are sensitive to vibration while operating, data could not be directly written to

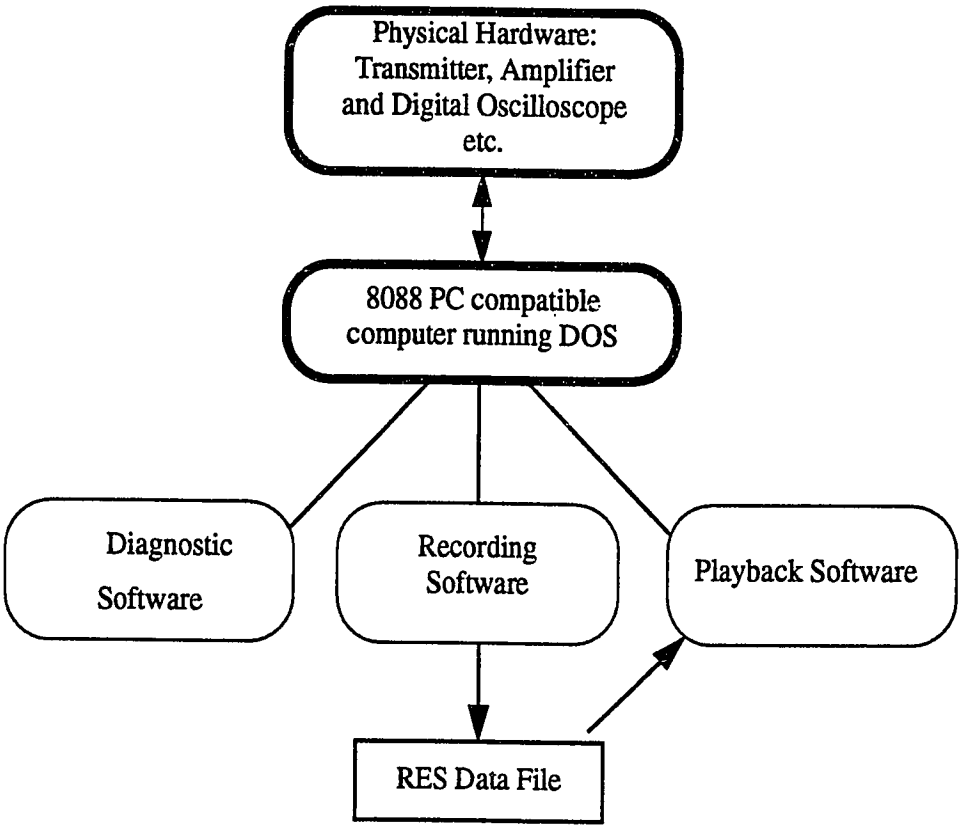

Figure 4.1: Software and hardware layout of the recording systems.

floppy disk while profiling. Instead, the data were written to a buffer RAM memory. When the buffer was close to full profiling was interrupted briefly and the data were transferred to disk.

Figure 4.2 illustrates how RES data files are organized. Each file contains one file header and many record header/trace data pairs. A file header contains information pertinent to an entire file whereas a record header contains information which is pertinent to the trace of RES data which directly follows it.

The 2432 system recording program writes file headers that completely describe the configuration of the 2432 oscilloscope. This information includes oscilloscope settings of

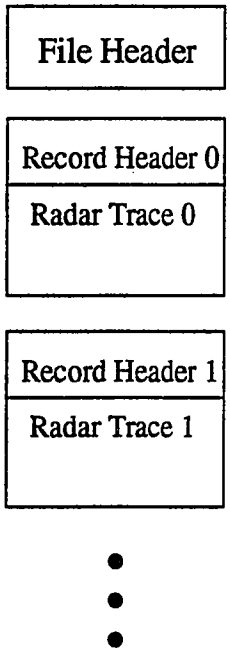

Figure 4.2: A depiction of how the RES radar data files are structured.

the sweep rate, the gain of the input channel, the gain of the trigger channel, the trigger's threshold voltage level and many more parameters. Both system recording programs allow the user to key in information to be included in the file headers.

The 222 oscilloscope has far fewer configuration parameters and it was possible to include all of them with each recorded waveform without significantly increasing the size of the data files. The bicycle wheel odometer measurement, time and, in the case of the

2432 system, pressure transducer measurements are included in the record headers.

Both of the recording system programs display odometer measurements as they run. As the recording systems are driven past fixed reference points such as survey poles the operator should note the odometer measurement and write it into a log book. The information included in the log book can then later be combined with survey measurements and the odometer measurements in the record headers to determine where each RES trace was collected. This also allows frequent calibration of the barometer to altitude (§ 4.2.2). The recording programs also keep track of and display how much memory is available in terms

of distance. This enables the operator to anticipate good stopping points for the transfer of data to disk.

Both of the oscilloscopes are able to internally stack waveforms. The 2432 and 222 oscilloscopes are able to stack up to 256 and 4 traces respectively. Stacking is beneficial because it helps to increase the signal to noise ratio of repetitive signals. Unfortunately, because the stack rates of both of the oscilloscopes are fairly low, to achieve significantly improved signal to noise ratios by stacking and at the same time collect traces every 10 meters, it has been necessary to run the profiling systems at about five kilometers per hour.

4.1.3 - In Field Playback Software

For many reasons it is important that all RES recording systems have a means of playing back their recorded data in-the-field. Playing back recorded data helps to confirm that the recording software is working properly, helps to identify intermittent problems with the recording hardware and helps to identify whether or not there is structure hidden in the data such as internal reflectors or bottom topography. Bugs in the system can also be identified. The 2432 and 222 recording systems required separate playback programs. In

both systems waveforms are displayed in 'wiggle' format (figure 4.4). The user can configure the programs to display the waveforms with different scales and different offsets between traces. As the data is played back record header information is also displayed.

4.2 - Preliminary Data Inspection

The collected data were transferred to a UNIX based computer where most of the data analysis was done. Figure 4.3 is a flow diagram outlining how the RES data were initially analyzed. Several programs for unpacking the RES data files were written and used. The data collected by the 222 and the 2432 recording systems were stored in different formats and required different programs for deciphering them.

The unpack programs make it possible to inspect the file and record headers and they also make it possible to strip out the waveform information and store it as binary raster information or to print it as a *wiggle plot.* In the raster format the RES data is stored as a matrix in which each column of the matrix corresponds to a seperate trace of RES data. In a wiggle plot indivdual RES traces are plotted side by side (see figure 4.4).

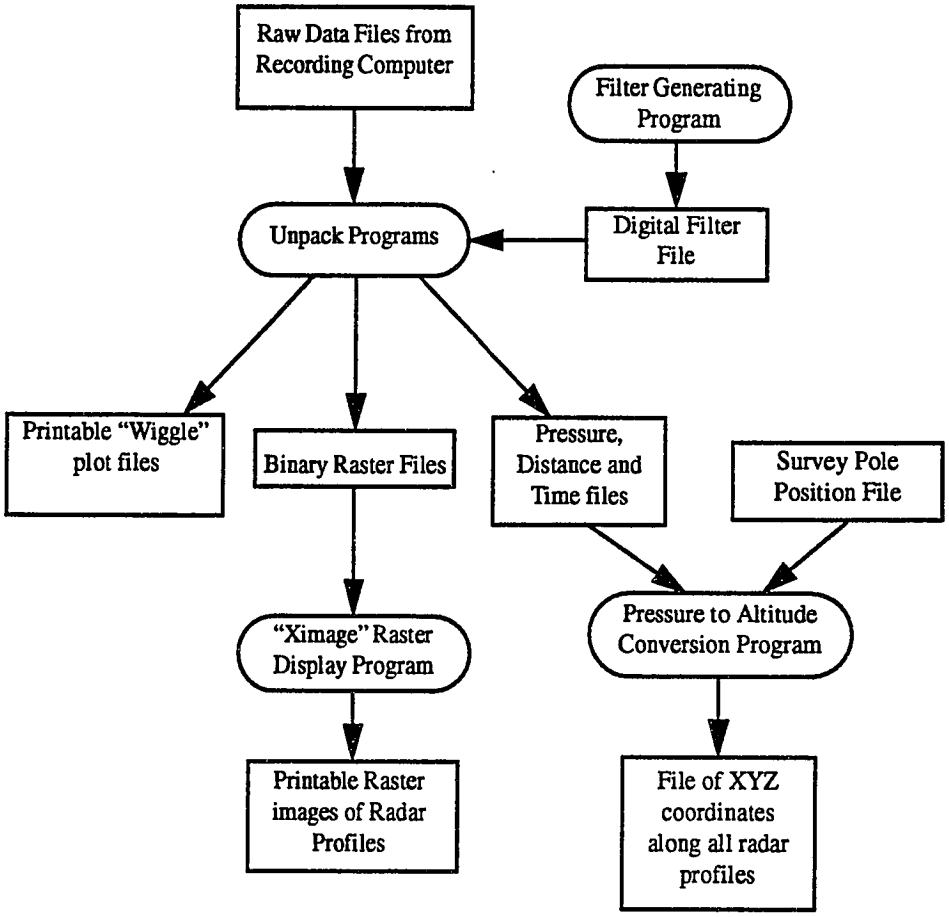

Figure 4.3: Flow diagram of preliminary data inspection.

4.2.1 - Display of Waveform Data

For my preliminary work I have made use a public domain image display program named *Ximage* for displaying waveforms stored in *raster* format. A generally useful feature of the *Ximage* program is its ability to generate color and grey scale palettes that can later be used by other display programs. A palette is a table which assigns colors to numbers. By adjusting the palette it is possible to bring out details in the RES data.

Figure 4.4 shows a comparison of a section of RES data which has been displayed in raster format with a carefully adjusted palette next to the same section which has been displayed using a series of side by side wiggle lines[1]. The raster display brings out features in the data which are difficult to identify in the wiggle display. For this reason raster display

was chosen as the primary data display method for the remaining data analysis.

A program was written for generating digital filters for use with the RES data. The digital filters are simply files consisting of strings of numbers. Filtering is accomplished by convolving the digital filters with the RES data. All of the digital filters are odd in length and are symmetrical; because the filters are symmetrical they have zero phase response. Before convolution the 8 bit integer RES data are converted to floating point. After convolution the floating point data are converted back into 8 bit integer and any data points laying outside the 8 bit range are clipped.

Digital filtering is advantageous in many respects. The zero offset of each trace has small variations within a single file of RES data and has large variations between files. These variations in offset can be distracting to the eye, making it necessary to choose separate palettes for each section or combinations of sections of RES data; a digital filter with a zero response at zero frequency can be used to remove the zero offset and hence the variations of the d.c. offset between different traces.

The transmitter emits a low frequency signal which is associated with the high speed transmitter switch closing and the discharge of the transmitter output capacitors (§ 3.5). The coupling of this low frequency signal to the receiver has large variations, presumably due to significant variations of the antennas coupling as they pass over the snow surface. A digital filter that has a small response below approximately 200 kHz can be used to eliminate this low frequency signal[2].

4.2.2 - Treatment of Barometric Data

As previously mentioned, the 2432 system included a barometer to enable continuous measurements of the ice surface altitude; every time a trace was acquired and recorded

a barometric pressure was also recorded. Unfortunately, due to the instrumentation, the barometric measurements have no absolute scale, complicating the conversion of barometric measurements to surface altitude. Additionally, the air pressure drifts as the

---

1. The wiggle and raster displays are respectively equivalent to the a-display and z-display modes discussed in § 3.2.
2. 200 kHz is the inverse of the time constant associated with the discharge of the transmitter capacitors.

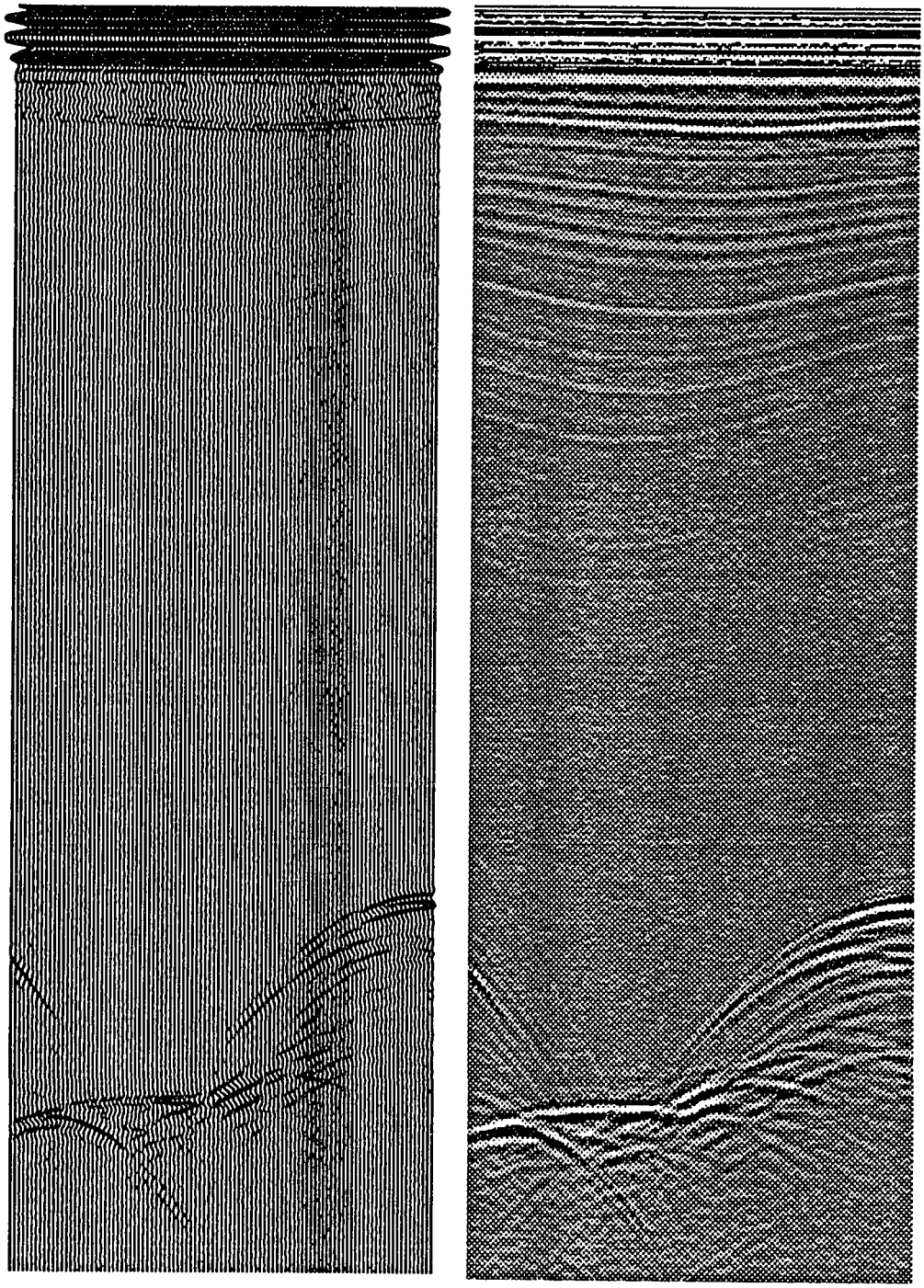

Figure 4.4: A side by side comparison of a section of radar data displayed in *wiggle* format (left) and *raster* format (right). The raster format reveals more internal structure but the wiggle format allows a better inspection of waveform shapes.The section is 1 km wide and 5.5 μ sec long.

weather changes.

I investigated the barometric data to determine its accuracy in predicting surface altitudes. Pressure measurements made at survey poles, where relative surface altitudes are known to an accuracy of ~15cm, were used to investigate the relationship between pressure and altitude. Figure 4.5 is a scatter plot of all of the pressure measurements made at

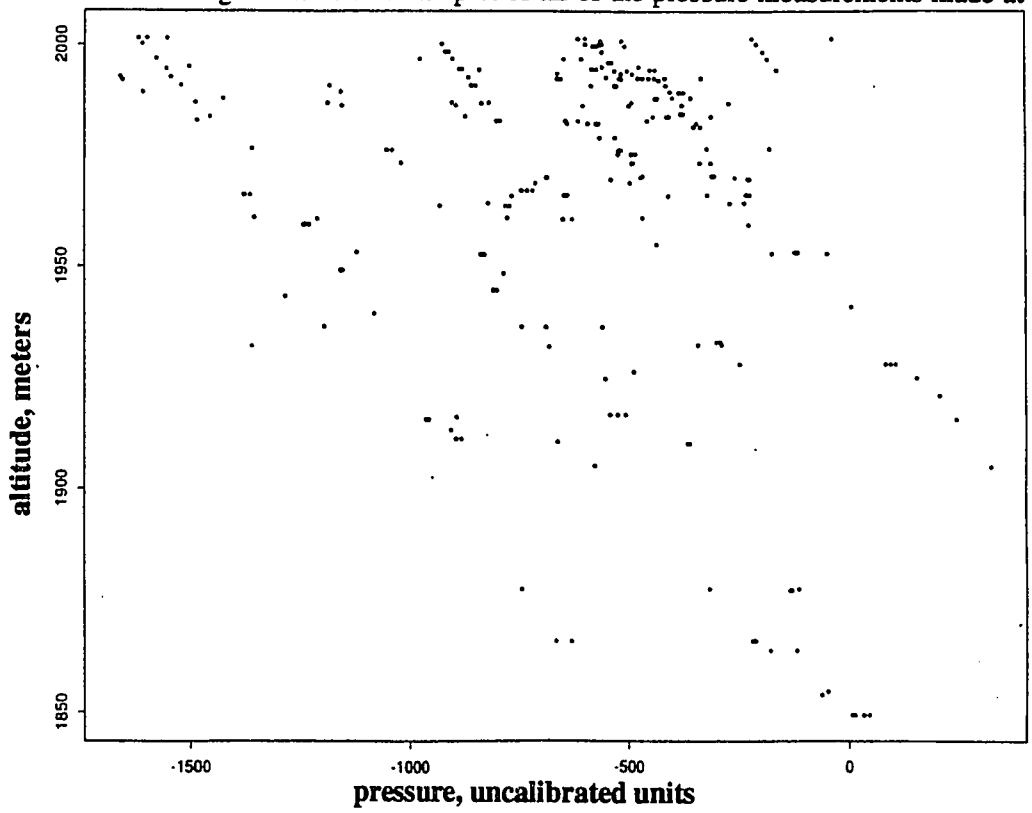

Figure 4.5: A scatter plot of barometric measurements made at known altitudes. The horizontal axis represents pressure (uncalibrated units) and the vertical axis represents altitude (meters above sealevel). The measurements tend to cluster on line segments. See text for explanation.

survey poles plotted against the altitude at those poles. The points on the plot are scattered but have a grain. If the weather did not cause the air pressure to vary with time these data points should have been clustered around a single curve. The scatter plot appears to be a

collage of data points laying on separate curves. Each seperate curve seems to represent a collection of data points collected over a time interval of stable pressure. I tested this by assuming that the measured pressures were proportional to altitude plus offsets that changed each day. This assumption yielded a system of overly determined equations for which a least squares solution could be found. Subtraction of the determined daily offsets from the pressure measurements moved the scattered data points close to a single curve. This shows that the measurements are in fact accurate indicators of surface altitude.

To achieve consistancy between altitudes from pressure and survey measurements I next assumed that between survey poles n and $n+1$, the altitude, z, was related to the pressure, P, by

$$z = z_n + k(P_n - P) + drift\,(t - t_n)\,.$$

In this equation z_n is the survey measurement at pole n, k is the constant of proportionality found by the least squares analysis, P_n is the pressure measurement at pole n, t is the time, t_n is time when pressure was measured at pole n and *drift* is a constant choosen so that the altitude predicted from the pressure measured at pole $n+1$ matches the survey measurement. A comparison of estimates made from identical profiles indicates that the altitude estimates are accurate to within 2 meters over most of the survey array.

Altitudes were estimated at every location where a sounding was recorded. These altitudes were combined and a *minimum curvature* 75×75 node surface was fit to them. This digitized surface was used in all further analysis requiring surface altitudes. The estimated surface altitudes are shown in figures 1.2 (page 4), 5.4 (page 75), 6.9 (page 112) and 6.10 (page 113).

4.3 - Automated Data Retrieval

Because of the large volume of data, it was necessary to have a means of automatically retrieving desired profiles of RES data and it was also necessary to have a means of attaching cartesian coordinates to the retrieved profiles in order to identify where they were collected. Both of these issues were addressed in a program which I wrote and named *TRAP* (TRace Assembly program). Figure 4.6 illustrates the flow of data into and out of *TRAP*. To operate *TRAP* the user selects a sequence of survey pole names between

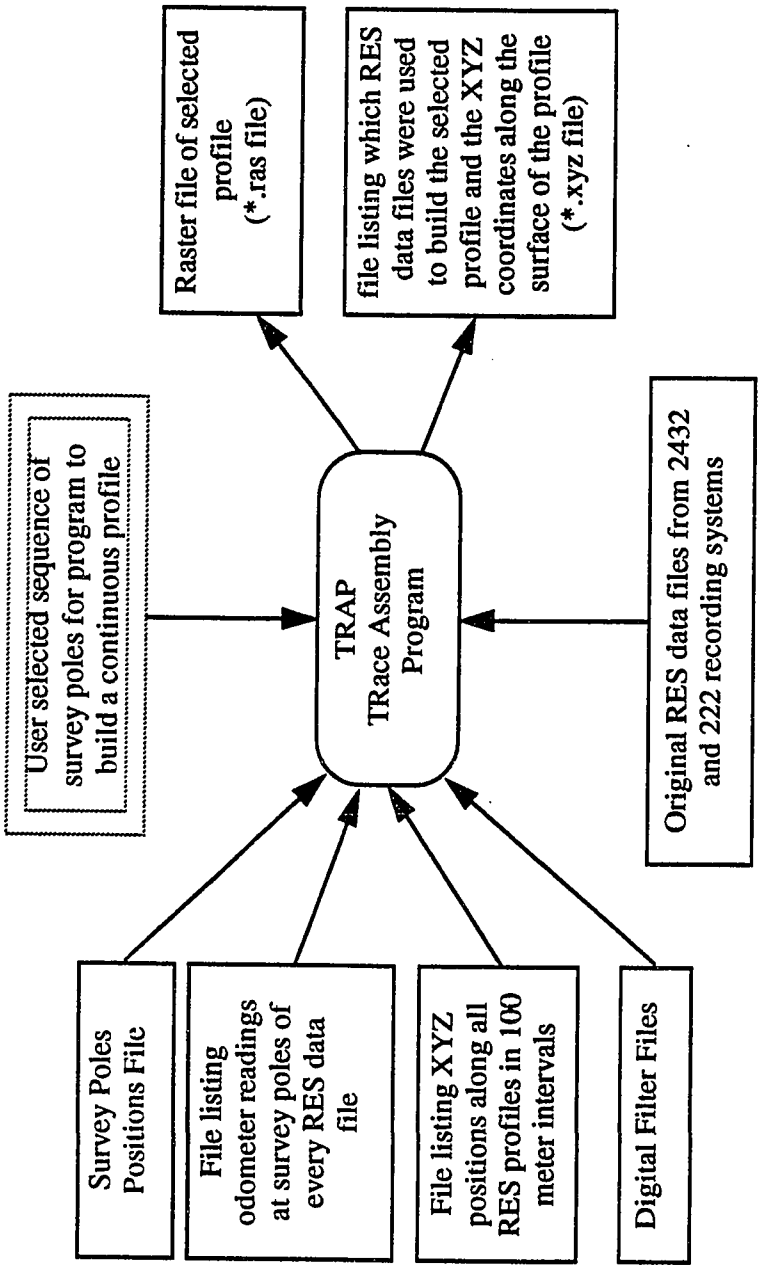

Figure 4.6: A depiction of the flow of information into and out of the program TRAP.

which RES profiles are desired. The program determines which RES data files run between the selected poles and, if there is more than one file available for any one section, the program prompts the user to select which RES data file to use for that section. The program is able to use data from both the 2432 and the 222 recording systems.

TRAP generates two files when it is run. The first file is a raster image of the assembled RES traces. The second file is a list of the cartesian coordinates of where the assembled traces were recorded. Also included in the second file is a list of the names of the RES data files from which the raster image was generated.

The 2432 and 222 digital oscilloscopes are able to record the signal which occurs shortly before a trigger event happens. This is a feature, known as pre-triggering, is common to most digital oscilloscope. Digital oscilloscopes are able to pre-trigger because they continuously record the input signal into a circular buffer. When a trigger event occurs they save the buffer data recored immediately before the trigger event. Pre-triggering is useful because it does not require that triggering parameters be set exactly the same for each RES traverse. For example, if on one RES traverse the trigger is set to activate on the negative edge of the airwave and on another traverse the trigger is set to activate on the positive edge of the airwave, the two recorded signals will have different phase shifts. By recording the signal which happens slightly before the trigger event it is possible to use a computer algorithm to find a consistent trigger point in all of the waveforms recorded; the program *TRAP* uses such an algorithm. Additionally, the algorithm used in *TRAP* detects the polarity of the recorded signal. If necessary, it changes the polarity to insure that that is is the same in all assembled traces. This makes it unnecessary to have the RES antennas plugged into the transmitter and receiver with the same polarity every time the radio echo sounder is reassembled.

4.4 - Migration of RES Data

Before proceeding with further analysis I wanted to determine how well the nadir assumption would work in interpreting observed reflections from internal stratigraphy and ice bottom topography for the data collected on the Dyer Plateau. The nadir assumption supposes that the observed reflections come from directly beneath the point half-way between the transmitter and receiver. If this assumption does not hold then interpreting the geometry of the reflecting surfaces which give rise to the observed reflections becomes much more difficult.

Bed slopes give an indication of the accuracy of the nadir assumption. For a per-

fectly horizontal bed the nadir assumption is accurate and the depth to the bed is simply the one-way travel time divided by the velocity of propagation[3]. As bed slope increases the nadir assumtion becomes less accurate. For depths much greater than the transmitter and receiver separation distance the fractional difference in depth between the actual depth and the depth found from the nadir assumption is approximately $1 - slope$. For example, when bed slopes are less than 18° the nadir estimate of depth is less than 5% different than the actual depth. All of the internal layer bed slopes observed in the Dyer Plateau data are well below 18°.

In order to further investigate the deficiencies of the nadir assumption I wrote a system of programs for migrating the RES data. Migration is the process of recovering the positions of the true reflecting surfaces from an observed reflection pattern. Seismologist working with data collected from reflection seismology experiments first developed migration techniques. There are many different techniques for migration. I choose to use a now classic method first described by Hagedoorn in 1954 which is based on the concept of maximum convexity. The book *Geophysical Signal Analysis* (Robinson and Treitel, 1980)

gives a good description of this migration method.

In describing migration it is useful to define *physical space* and *record space*. Physical space is the space in which the ice sheet exists. It has as its dimensions horizontal distance and vertical depth. Record space is the space in which the RES profile exists. It has as its dimensions horizontal distances and two way travel time. The process of creating a RES profile maps physical space into record space. The process of migration attempts to find the reflecting surfaces in physical space that were mapped into the record space.

A point reflector in physical space will result in a curve in record space. This curve will be a hyperbola if the transmitter and receiver have zero separation distance and the ice has a constant velocity depth profile. The resulting curve in the record space is referred to as a *maximum convexity curve*.

Each sampled point in physical space will act to some degree as point reflector

3. Assuming a transmitter receiver separation distance of zero and a depth independent velocity profile.

which will map into a maximum convexity curve in record space. The kernel of Hagedoorn's method is the assumption that the reflection coefficient of any point can be estimated from the average of the recorded signal over any point's corresponding maximum convexity curve. This assumption will be valid if signals present along a maximum convexity curve which are not due to the curve's corresponding reflection point cancel out when averaged.

Since the radio echo sounder uses a waveform of finite wavelength it is not necessary to use an infinitesimally thin maximum convexity curve. Also, since the transmitter is not omnidirectional and the ice attenuates signal strength, the maximum convexity curves need only be of finite length in time.

Figure 4.7 is a flow diagram of the programs that I wrote and have used for migrating data collected from the Dyer Plateau. The program *mkhyp* generates a table of maximum convexity curves which can then be used by the migration program *maxc*. The file *mig_param.h* contains information which controls the shape and size of the maximum convexity curves generated by *mkhyp*. The program *maxc* migrates the raster images generated by the program *TRAP*.

As has been shown, the nadir approximation is adequate for finding the depths of internal layer reflections. In regions where the bottom is rugged, migration yields significantly different estimates of the depth.

As previously discussed, the nadir approximation assumes the first bottom echo observed in each trace is due to a reflector present directly beneath the point where that trace was collected; this will be true only for the traces that are collected from locations at the apexes of reflection hyperbolas. This is illustrated in figure 4.8. The figure depicts a hypothetical reflection pattern caused by reflectors present on a down dipping flat surface. The first reflections observed are consistently above the actual bed. However, if the tops of the hyperbolas are used in estimating the location of the reflecting surface then the correct reflecting surface is found.

Figure 4.9 is an example of a section of RES data before and after migration. This section of data was selected because of its relatively rugged internal layering and bottom

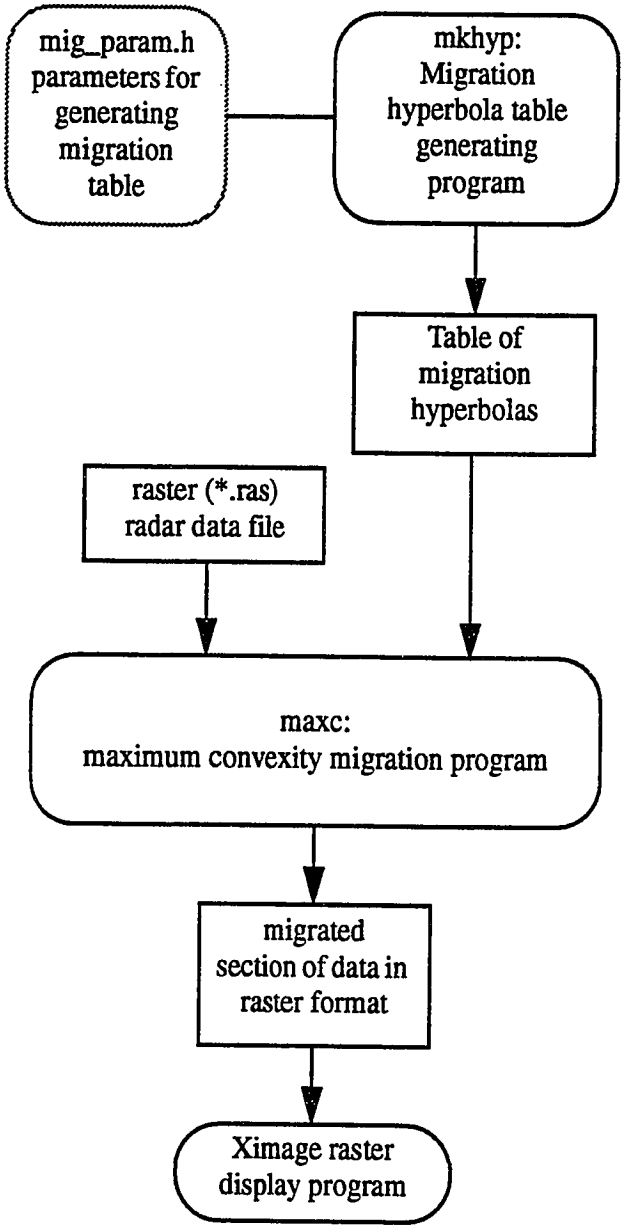

Figure 4.7: A depiction of the flow of data involved in the migration of radar data.

topography. The migrated bottom echo is seen to map into a nice smooth curve with some upward leakage into the migrated internal layer reflections which are seen to be significantly washed out after migration.

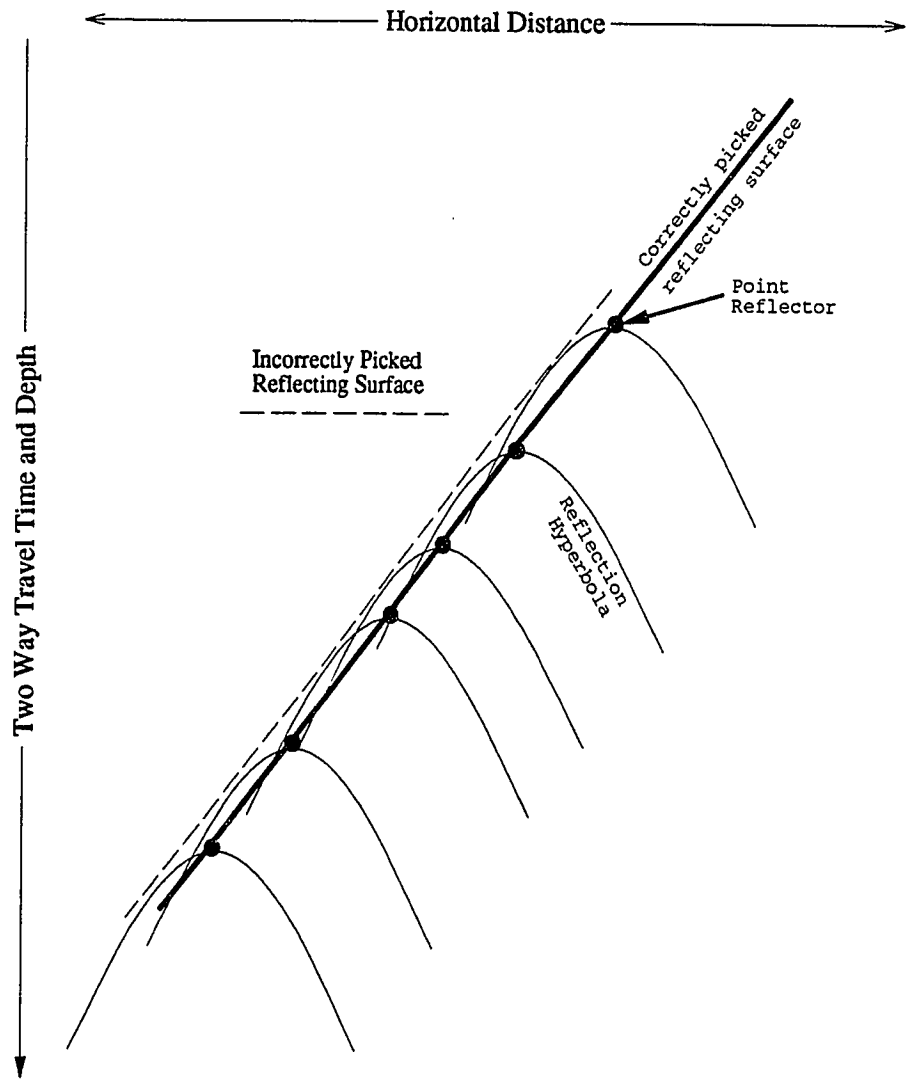

Figure 4.8: A diagram illustrating the relation between a string of point reflectors on a tilted flat surface and the recorded profile. If the reflection pattern is interpreted incorrectly, the depth to the true reflecting surface will usually be under estimated.

Figure 4.10 shows 3 picked[4] internal layers and the bottom echo from the migrated section. The reflections were picked from both the migrated (heavy lines) and un-migrated (thin lines) data. The bottom reflections picked from un-migrated data were picked only

4. See § 4.5.

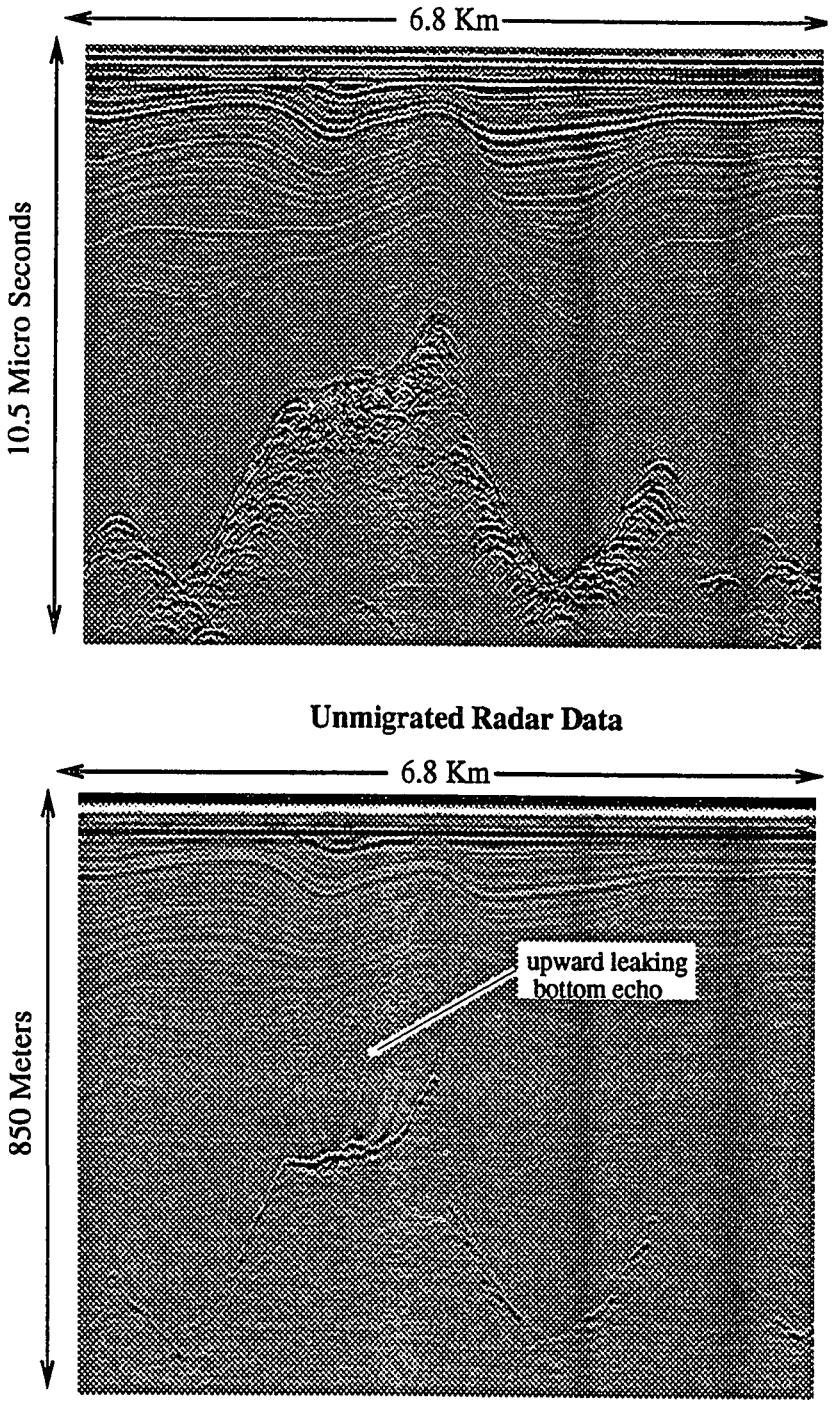

Figure 4.9: A comparison of an un-migrated (upper panel) and migrated (lower panel) section of radar data.

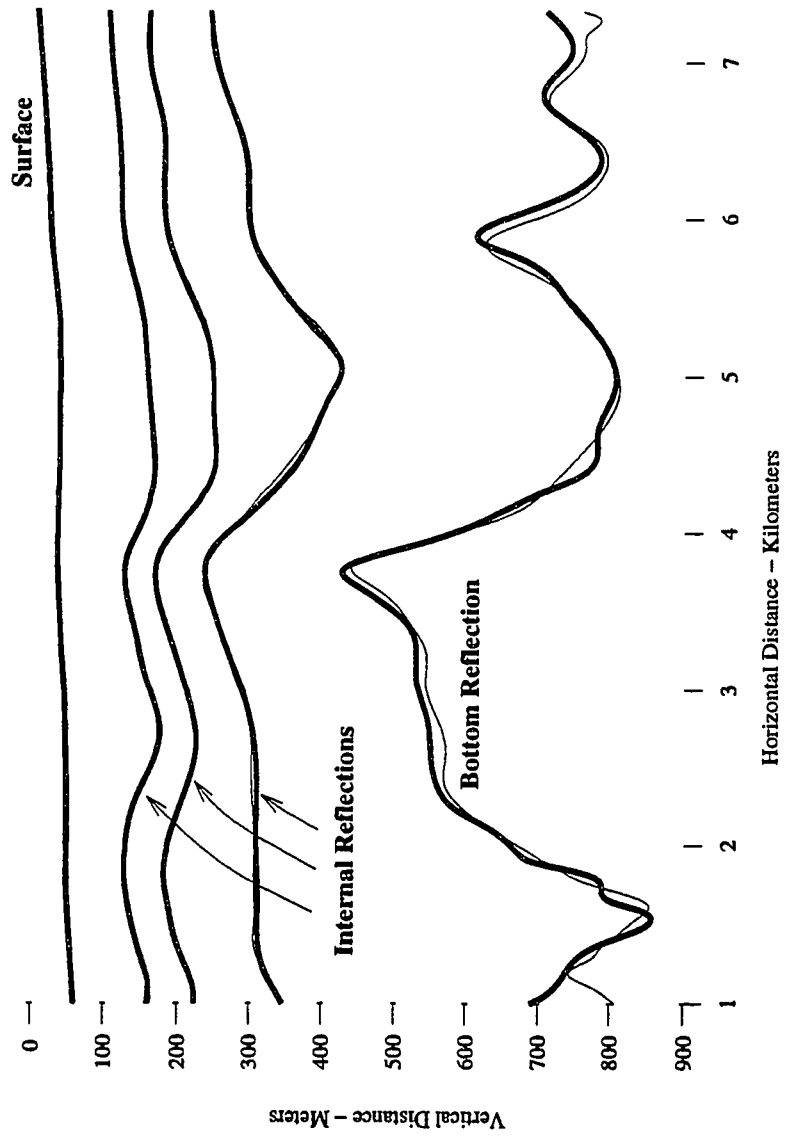

Figure 4.10: A comparison of the bottom topography and some of the internal layers determined from the un-migrated (thin lines) and migrated (thick lines) sections of radar data shown in figure 4.11. The method that was used for determining the bottom topography from the un-migrated data is discussed in the text.

from the apexes of the bottom reflection hyperbolas as discussed above. As can be seen the reflection depths picked from migrated and un-migrated data are essentially identical. From this I conclude for these circumstances that by using a judicious selection of bottom

echoes, bottom location can be estimated essentially as accurately as by migration and internal layers are so near to horizontal that the nadir approximation is adequate.

4.5 - Digitization of RES Internal and Bed Reflections

At this point in the data analysis a tool was needed for digitizing the reflections from internal layers and the bottom echo. After some searching I determined that there was no previously written software which would allow me to do this in the manner that I desired. To solve the problem I wrote my own program name *PICK* for picking layers seen by the RES traverses. A flow chart showing the flow of data into and out of *PICK* is shown in figure 4.11. *PICK* accepts binary raster files generated by the program *TRAP* and uses

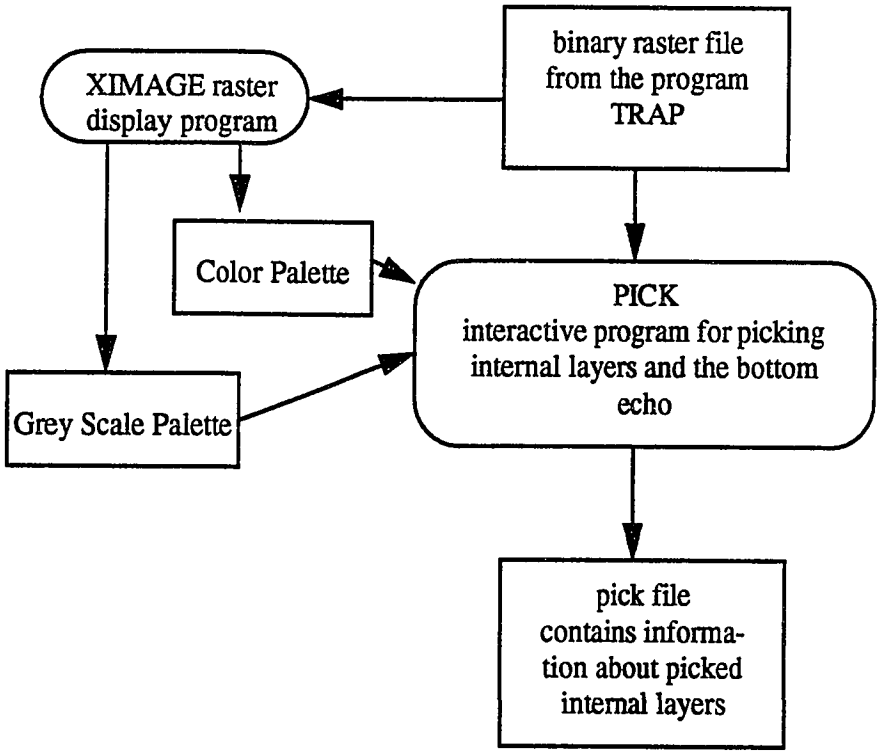

Figure 4.11: A depiction of the flow of data into and out of the program PICK. PICK is used for picking (digitizing) reflection horizons.

palettes created by the program *Ximage* to determine how colors are assigned to data values. With the mouse and keyboard the user traces out layers seen in the RES data. The pro-

gram uses cubic splines to represent the traced layers. By using splines it is unnecessary to pick layer depths for each trace. The program allows the splines to be easily modified once they are drawn, it allows additional splines to be drawn between existing splines if needed and it allows splines to be removed as necessary.

The results from *PICK* are used directly by several other data analysis programs which I have written. By using the digitized data from *PICK* instead of the raster files directly it has been possible to condense the amount of data need for access by a factor of 400.

4.6 - Time to Depth Conversion

For all interpretation of RES data which I have done it has been necessary to convert reflector depths which are originally measured in terms of two-way travel times to reflector depths measured in terms of distance. In this section I briefly explain the method that I have used for doing this.

If the transmitter and receiver were exactly coincidental and the velocity of propagation was depth invariant and equal to that of pure ice this would be a trivial problem and the depth would simply be given by

$$z = V_{\text{ice}} t/2 \tag{4.1}$$

where V_{ice} is the velocity of propagation in ice and t is the two way travel time. However, the situation which I have worked with is more complicated for two reasons: (1) the transmitter and receiver are not coincident and (2) the velocity decreases with depth due to the densification of firn to ice with depth. Although I am not the first person using ice radar to tackle this type of problem, I have had to take a different approach than the earlier researchers (Rasmussen, 1986; Rees and Donovan, 1992) because their work has involved time to depth calculations in which the transmitter and receiver are taken to be coincident.

The assumptions which I work with are as follows:

1. The ice density varies vertically but not spatially and can be adequately described as a piecewise linear function of depth.

2. The dependence of the index of refraction, n, on density, ρ, is adequately described by

$$n = 1 + \frac{n_{ice} - 1}{\rho_{ice}}\rho, \tag{4.2}$$

3. where the index of refraction of pure ice, n_{ice}, is taken to be 1.77 (Rees and Donovan, 1992) and the density of pure ice, ρ_{ice},is taken to be 920 kg m^{-3} (Rees and Donovan).
4. Observed reflections originate from reflectors that are situated exactly half-way between the transmitter and receiver.
5. The airwave on which the receiver triggers travels at the speed of light in vacuum, C.
6. The RES radio waves can, for travel time calculation purposes, be adequately described using ray paths which originate and end at antenna feed points.

The combination of the first two assumptions leads to an implicit assumption of the index of refraction being a piecewise linear function of depth. The fourth assumption has been tested and is discussed in § 4.6.1.

I have taken a two step approach to determining depths from travel times. In the first step I calculate and tabulate two-way travel times for depths ranging from the deepest depth in consideration up to the shallowest detectable layer at evenly spaced depth increments. In the second step, the tabulated depth-time pairs are used to make a piecewise linear function for finding depths given two-way travel times. Breaking the problem into two steps simplifies computer programming and increases overall execution times when many identical computations of depth from travel time are needed.

4.6.1 - Airwave Velocity and Trigger Timing

I have experimentally verified the fifth assumption by measuring relative differences in travel times between (1) a light pulse run between the transmitter and receiver through a fiber optic and (2) the transmitter airwave. I varied the distance between the transmitter

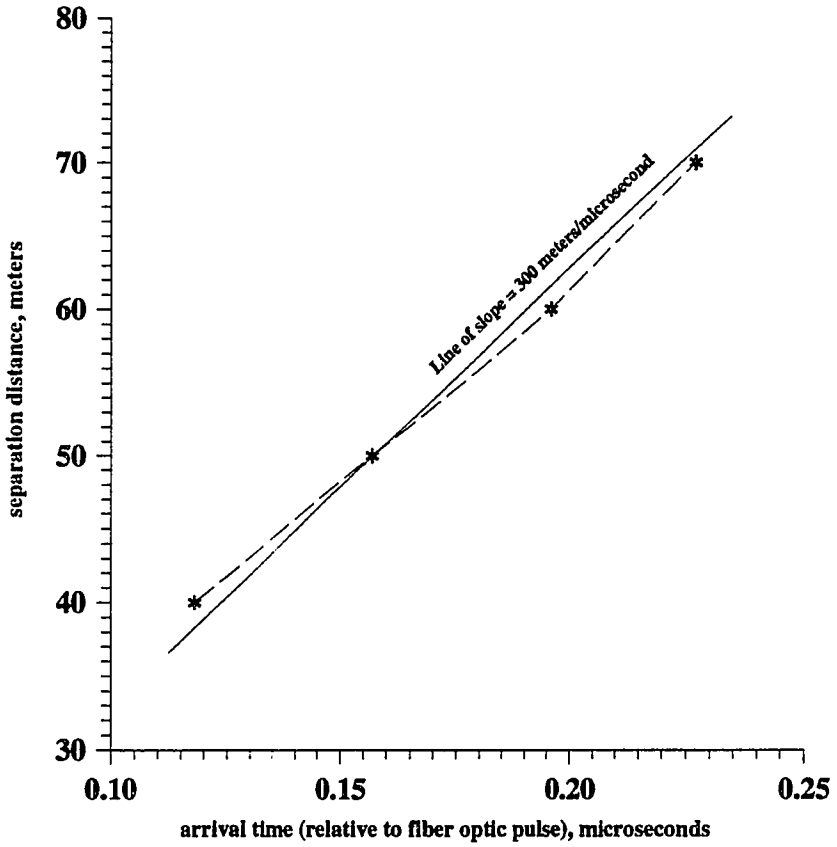

Figure 4.12: Transmitter-receiver separation distance plotted as a function of the airwave arrival time. The solid line runs close to the data points and has a slope equal to the speed of light (300 m/μsec). The airwave arrival time was measured relative to a light pulse run through a fiber optic cable going from the transmitter to the receiver.

and receiver from 40 to 70 meters and observed arrival time differences change at a rate consistent with the speed of light (figure 4.12).

A fiber optic cable was used to send a timing pulse rather than a wire because a wire would alter the coupling characteristics of the transmitter and receiver antennas. A fiber optic cable was not used to set the timing in normal profiling because the optic fiber is delicate and awkward to use in the towing arrangement.

Because the airwave takes a finite time to propagate, times measured between the airwave arrival, which triggers the oscilloscope, and reflection arrivals will be slightly less

than two-way travel times as measured from the transmitter firing to the receiver detecting a reflected pulse. To find actual two-way travel times one needs to add the air-wave travel time to the time measured between airwave and reflection arrivals. This time is equal to the transmitter-receiver separation distance divided by the speed of light.

4.6.2 - Ray Paths and Two-way Travel Times

Figure 4.13 illustrates the appearance of a radio wave ray path running from a trans-

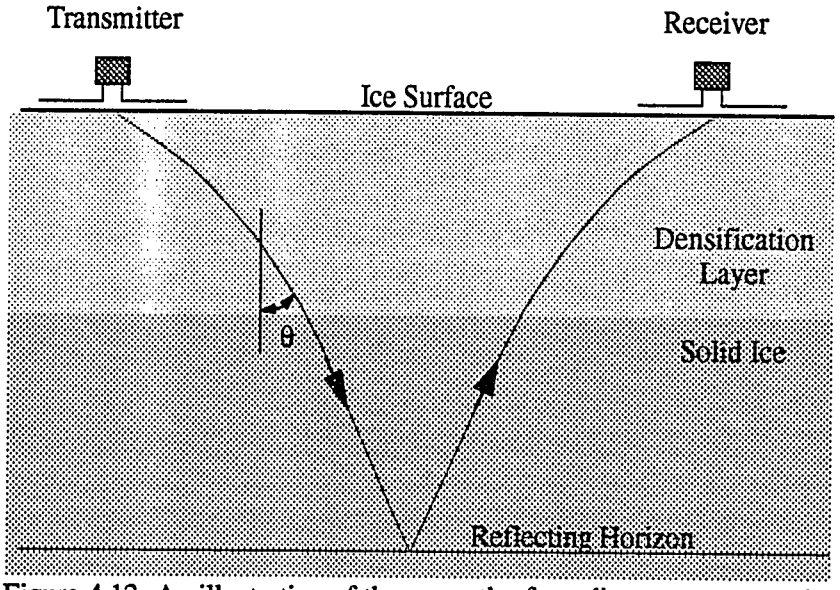

Figure 4.13: An illustration of the ray path of a radio wave propagating from the transmitter to the receiver. In the densification layer the ray path bends with depth and in the solid ice below it follows a straight line. θ represents the angle of the ray with respect to the vertical.

mitter to a horizontal reflector and then to a receiver. As a radio wave travels through the densification layer, the change in the index of refraction with depth will cause its ray path to bend. However, as the ray travels its ray parameter, S, which is defined as

$$S = n\sin\theta$$

will remain constant because of Snell's law[5] (θ is the vertical angle of the ray as indicated

5. Snell's law is expressed as $n_1/n_2 = \sin\theta_2/\sin\theta_1$ where the subscripts indicate sides of a dielectric interface and angles are measured with respect to the normal of the interface.

in the figure). Because the ray parameter does not vary it is relatively simple to calculate ray paths.

If the index of refraction varies linearly with depth as $n(z) = az + b$, where z is the depth, then relation between the depth and horizontal coordinate, x, of a ray is found to be

$$x - x_0 = \frac{S}{a} ln\left(\frac{az + b + \sqrt{(az+b)^2 - S^2}}{az_0 + b + \sqrt{(az_0+b)^2 - S^2}}\right) \tag{4.3}$$

where x_0 is the starting horizontal coordinate and z_0 is the starting depth.

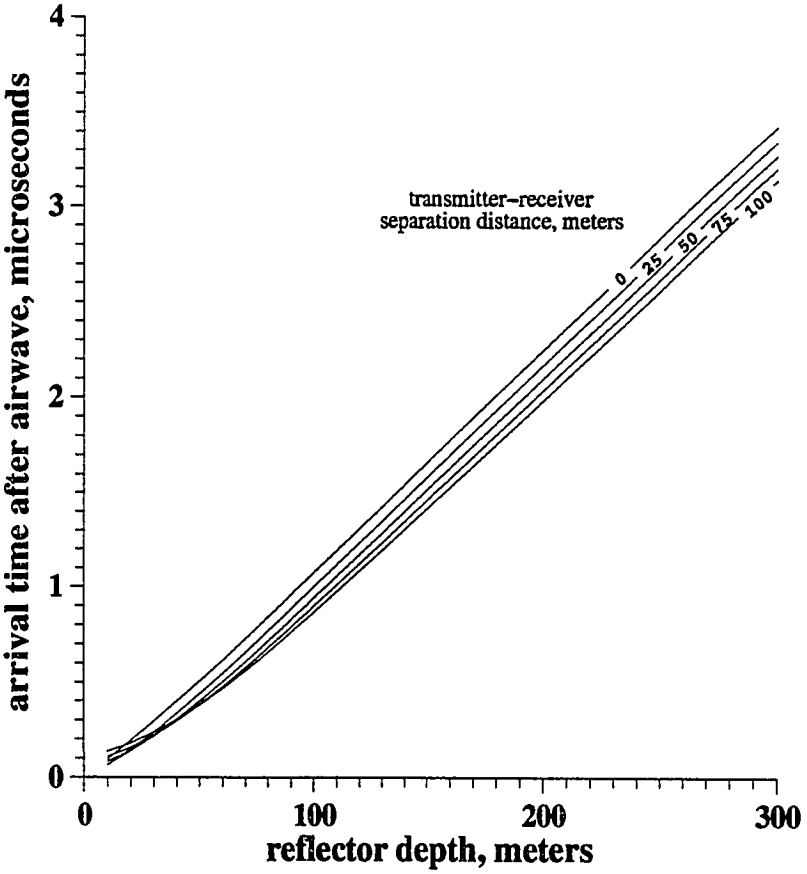

Figure 4.14: Plots of the time differences between airwave and reflection arrivals as a function of reflector depth for five antenna spacings. The curves are based on a density depth profile that was measured at the Dyer Plateau ice summit.

In making my calculations of ray paths I have applied equation 4.3 to each piecewise linear depth section from the surface down to a depth of interest and have then summed $x - x_0$ for each section. I have then adjusted S to make this sum equal to half of the transmitter receiver separation distance.

The travel times through each layer are then found by integration of the inverse of the velocity, $V^{-1} = n/C$, along ray paths. When this is done for the ray paths found from equation 4.3, the travel time through each layer is found to be

$$t = \frac{1}{2Ca}\left(n\sqrt{n^2 - S^2} - n_0\sqrt{n_0^2 - S^2} + S^2 \ln\left(\frac{n^2 + \sqrt{n^2 - S^2}}{n_0^2 + \sqrt{n_0^2 - S^2}}\right)\right), \tag{4.4}$$

where $n = az + b$ and $n_0 = az_0 + b$. To find the complete two-way travel time equation 4.4 is applied to each layer down to the depth of interest with the previously determined ray parameter. The times found for each layer are then summed and then doubled (to account for both the downward and upward legs) to yield the two-way travel time.

Figure 4.14 is a plot of calculated times of arrival (as measured after the arrival of the airwave) for horizontal reflectors of depths ranging from 10 to 300 meters. The plot shows time-depth curves for five transmitter-receiver antenna separation distances which are based on a density profile measured at the primary Dyer Plateau drill site. The travel times vary linearly with depth for depths deeper than approximately 100 meters and show an increase in non-linearity with increased transmitter-receiver separation as one would expect. In the linear region the two-way travel times are found to vary with depth at a rate equal to the inverse of $83.3 m/\mu sec$.

Chapter 5

Radar Detection of the Spatial Pattern of Accumulation Rate

If a typical glaciologist were to have one question about an ice body magically answered it would probably be: "is it growing or shrinking?" The chief difficulties to answering such a question usually stem from the long times required for ice masses to change and the large number of observations needed for adequate coverage. The time required for "something to happen" and the number of necessary observations both increase with ice body size. On many large ice sheets these difficulties are compounded by low accumulation rate. Recent advances in satellite remote sensing (e.g. Zwally et al. 1989; Bindschadler, Vornberger, 1990; Bindschadler, Scambos, 1991; Doake and Vaughan 1991; Mantripp, Ridley and Rapley 1992) have revolutionized some aspects of how data are gathered. For instance, velocities of fast moving ice streams in West Antarctica can now be measured from satellite images and changes in surface topography of Greenland and Antarctic ice sheets are being measured with satellite radar altimetry. To date however little has been done in terms of remotely determining one of the most fundamental glaciological measurements, accumulation rate.

In this chapter I present a method to deduce the spatial pattern of accumulation rate based on the depths of a near surface radio-echo sounding reflection horizons of known ages. The method can be rapidly applied to large surface areas and it produces accumulation rates which are inherently smooth and have been averaged over relatively long periods of time. The method is applied to data from the Dyer Plateau and its results are compared with recent stake measurements.

5.1 - Theory of Method

In this section I will show how the depth and age of a shallow isochrone layer can be used to infer the spatial pattern of accumulation rate. In principle this is a simple problem, but it is somewhat complicated by thinning caused by horizontal stretching. If the layer used is shallow, then accumulation rate can be found accurately from its ice or water

equivalent depth divided by its age. For example, in regions of low accumulation rate such as near the South Pole it is practical to drill shallow ice cores to identify nuclear bomb fall-out horizons (Picciotto and Wilgain, 1963). These horizons date back to 1952 and are identified by their β-activity. Because the accumulation rate at the South Pole is extremely low these horizons are still less than 10 meters beneath the surface.

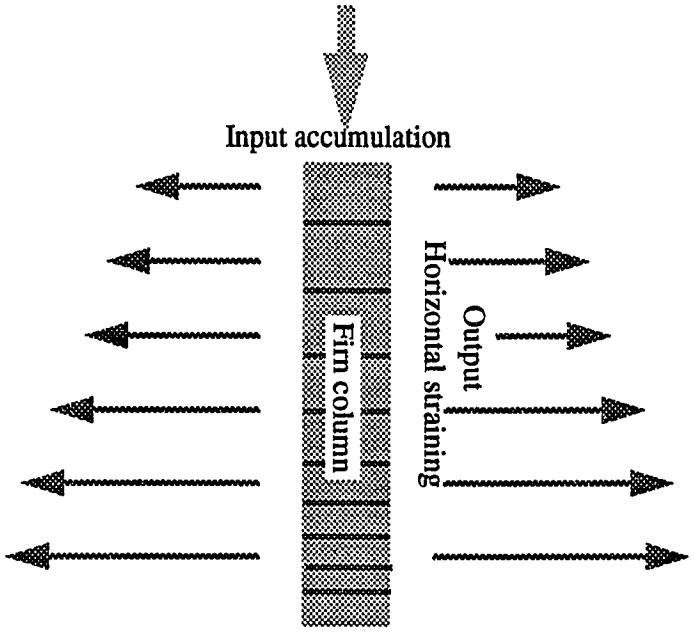

Figure 5.1: An illustration showing how a shallow column of ice behaves as a 'leaky' precipitation gauge. The 'leakyness' of the gauge is caused by horizontal straining. Were it not for the horizontal straining, accumulation rate could be found from the column's mass divided by the age of the ice at its bottom and its horizontal area.

To deduce accumulation rates from layers that are not shallow, the effects of horizontal stretching must be taken into account. A shallow column of ice can be thought of as a leaky precipitation gauge (figure 5.1). The amount that the precipitation gauge leaks is determined by the horizontal strain-rate. For older and deeper layers more will have leaked out of the column. If the leaking is not taken into account, accumulation rates will be underestimated. In order to correctly estimate accumulation rate based on a dated layer's depth the horizontal strain-rate must be known from the surface to the depth of the

layer.

I will now determine the accumulation rate required to place a layer at an observed depth given the layer's age, density-depth profile, horizontal strain-rate and the following three assumptions:

1. the horizontal strain-rate does not vary with depth,
2. the horizontal paths of individual particles do not cross significant inhomogeneities in horizontal strain-rate or accumulation rate,
3. the density-depth profile does not vary with time (Sorge's law) or horizontal position.

A natural starting point is conservation of mass which can be expressed as

$$\frac{\partial \rho}{\partial t} + \rho\left(\frac{\partial u}{\partial x} + \frac{\partial v}{\partial y} + \frac{\partial w}{\partial z}\right) + u\frac{\partial \rho}{\partial x} + v\frac{\partial \rho}{\partial y} + w\frac{\partial \rho}{\partial z} = 0, \tag{5.1}$$

where ρ is density, t is time , (x, y, z) is a three-dimenstional spatial coordinate and (u, v, w) is its corresponding velocity vector. If z is vertical, for typical ice sheets the terms $u\partial\rho/\partial x$ and $v\partial\rho/\partial y$ will be roughly two orders of magnitude smaller than the other terms and can be omitted. If the density at a particular location and depth does not vary with time then the first term can be omitted. With these two omissions equation 5.1 reduces to

$$\rho\left(\dot{\varepsilon}_0 + \frac{\partial w}{\partial z}\right) + w\frac{\partial \rho}{\partial z} = 0, \tag{5.2}$$

where $\dot{\varepsilon}_0 \equiv \partial u/\partial x + \partial v/\partial y$ represents the surface horizontal strain-rate which is assumed to be depth invariant for the depths in consideration. For a given density profile, $\dot{\varepsilon}_0$ and input accumulation rate, equation 5.2 could be solved for the vertical velocity w. The inverse of the vertical velocity could then be integrated with respect to depth to yield the age at depth. The accumulation rate could then be chosen so that the age at the layer's depth matches the layer's age. However, there is a more direct approach to finding the age at depth (and hence the required accumulation rate) which I will now derive.

Consider a slab of material which is buried into an ice sheet that does not flow in the y direction (figure 5.2). If the slab has an initial length of Δx_0 then after a period of time t it will have a length of

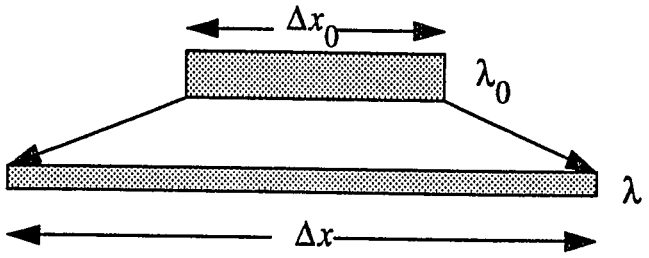

Figure 5.2: An illustration of a slab of material which is advected into a planar ice sheet. The mass of the slab must remain constant, but its density will vary.

$$\Delta x = \Delta x_0 exp\,(t\dot{\varepsilon}_0)\,. \tag{5.3}$$

This comes from the horizontal strain-rate being horizontally and vertically invariant. If the slab has an initial thickness of λ_0 and density ρ_0 then its starting mass per width in the y direction will be given by

$$\frac{\text{mass}}{\text{width}} = \Delta x_0 \lambda_0 \rho_0.$$

Mass conservation requires that the buried layer have the same mass per width, so that

$$\Delta x \lambda \rho = \Delta x_0 \lambda_0 \rho_0.$$

When combined with equation 5.3 this implies a density of

$$\rho = \frac{\rho_0 \lambda_0}{\lambda} exp(-t\dot{\varepsilon}_0). \tag{5.4}$$

For infinitesimal layer thicknesses the surface vertical velocity is $w_0 = \lambda_0/dt$ and internal vertical velocity is $w = \lambda/dt$. Combining these two equations gives

$$dz = \frac{\lambda w_0}{\lambda_0} dt. \tag{5.5}$$

If both sides of equation 5.4 are integrated with respect to depth and 5.5 is substituted for dz on the right side of the equation then one finds that

$$\int_0^z \rho dz' = \frac{\rho_0 w_0}{\dot{\varepsilon}_0}(1 - exp(-T\dot{\varepsilon}_0)),$$

where T represents age. After rearrangement this yields the useful relation

$$T = -\frac{1}{\dot{\varepsilon}_0} ln(1 - \frac{\dot{\varepsilon}_0}{\rho_0 w_0}\int_0^z \rho dz'). \tag{5.6}$$

As one might expect, the age at any particular depth is a function of only the overlying ice mass and not a function of the details of the density distribution. This is approximated to first order in $\dot{\varepsilon}_0$ by

$$T = \frac{1}{\rho_0 w_0}\int_0^z \rho dz' + \frac{\dot{\varepsilon}_0}{2}\left[\frac{1}{\rho_0 w_0}\int_0^z \rho dz'\right]^2. \tag{5.7}$$

This approximation is accurate when

$$\left|\frac{\dot{\varepsilon}_0}{\rho_0 w_0}\int_0^z \rho dz'\right| \ll 1.$$

The first term in equation 5.7 is the age as a function of depth with no correction for horizontal straining and the second term is a first order correction that accounts for horizontal straining. Equation 5.7 can be used to estimate the relative influence of horizontal straining on the age depth relation. The relative influence is found to be

$$\frac{\Delta T}{T} \approx \frac{1}{T}\left(\dot{\varepsilon}_0 \frac{\partial T}{\partial \dot{\varepsilon}_0}\right) \approx \frac{\dot{\varepsilon}_0}{2}\frac{1}{\rho_0 w_0}\int_0^z \rho dz'. \tag{5.8}$$

We are interested in deriving the input accumulation rate, w_0. This can be found by rearranging equation 5.6 to yield

$$w_0 = \frac{\dot{\varepsilon}_0}{\rho_0 (1 - exp(-T\dot{\varepsilon}_0))}\int_0^z \rho dz'. \tag{5.9}$$

This is approximated to first order in $\dot{\varepsilon}_0$ by

$$w_0 = \left[\frac{1}{T} + \frac{\dot{\varepsilon}_0}{2}\right] \frac{1}{\rho_0} \int_0^z \rho \, dz'.$$

From this the relative influence of horizontal straining on the estimated accumulation rate is found to be

$$\frac{\Delta w_0}{w_0} \approx \frac{1}{w_0} \left(\dot{\varepsilon}_0 \frac{\partial w_0}{\partial \dot{\varepsilon}_0} \right) \approx T \frac{\dot{\varepsilon}_0}{2}. \tag{5.10}$$

If the dated layer is at a depth where the density no longer varies vertically it is convenient to substitute the integrated density by

$$\int_0^z \rho \, dz' = (z - z_c) \rho_i, \tag{5.11}$$

where z_c is the amount that the upper part of the ice sheet could be compacted to reach the final density ρ_i, the density of pure ice. If z_t is the depth at which the density becomes approximately constant then the *compaction thickness*, z_c, is given by

$$z_c = z_t - \frac{1}{\rho_i} \int_0^{z_t} \rho \, dz. \tag{5.12}$$

It is possible to estimate the relative importance of horizontal straining on the accumulation rate estimates based solely on the ice equivalent depth of the layer relative to ice sheet thickness. This can be done by approximating the ice sheet as a two-dimensional slab of constant thickness in which the horizontal velocity does not vary with depth and the accumulation rate does not vary with horizontal position. In order to have a steady-state mass balance the horizontal strain-rate must be related to the accumulation rate, total ice thickness H and surface density ρ_0 by

$$\dot{\varepsilon}_0 = \frac{\rho_0}{\rho_i} \frac{w_0}{H}. \tag{5.13}$$

If the influence of horizontal straining is neglected, the age at an ice equivalent depth z is

$$T \approx \frac{\rho_i}{\rho_0} \frac{z}{w_0}. \tag{5.14}$$

If equations 5.13 and 5.14 are substituted into 5.10 the relative effect of horizontal straining on the estimated accumulation rate is found to be approximately

$$\frac{\Delta w_0}{w_0} \approx \frac{z}{2H}. \tag{5.15}$$

To illustrate the significance of horizontal straining consider using a layer which is at an ice equivalent depth of 50 meters. At the south pole where the ice is 3000 meters deep, based on equation 5.10, horizontal straining should have less then a 1% effect on the estimated accumulation rate whereas on the summit of the Dyer Plateau where the ice is 365 meters deep it should have close to a 7% effect.

In general equation 5.13 will underestimate the surface horizontal strain-rate because horizontal straining usually tends to be concentrated towards the surface. If the bed is assumed to be non-sliding, a reasonable approach to finding a more accurate estimate of the surface horizontal strain-rate is to assume that the upper two-thirds of an ice sheet flows as a column and the lower third flows with a linearly decreasing horizontal velocity that reaches zero at the bed (Dansgaard and Johnsen, 1969). The horizontal strain-rate required to achieve steady-state mass balance is then found to be equation 5.13 multiplied by 1.2.

In areas where there is no horizontal strain-rate information available, equation 5.13 multiplied by a suitable constant could be used as proxy for the horizontal strain-rate in equation 5.9.

5.2 - Analysis of Data From The Dyer Plateau

Figure 5.3 is a section of RES data which crosses the ice divide of the Dyer Plateau in the vicinity of the ice core drilling site. Its path is shown in figures 5.4, 5.5 and 5.6 which are contour maps of the surface topography, the depth of a shallow reflection horizon and the ice sheet thickness. The depth of near surface reflection horizons vary spa-

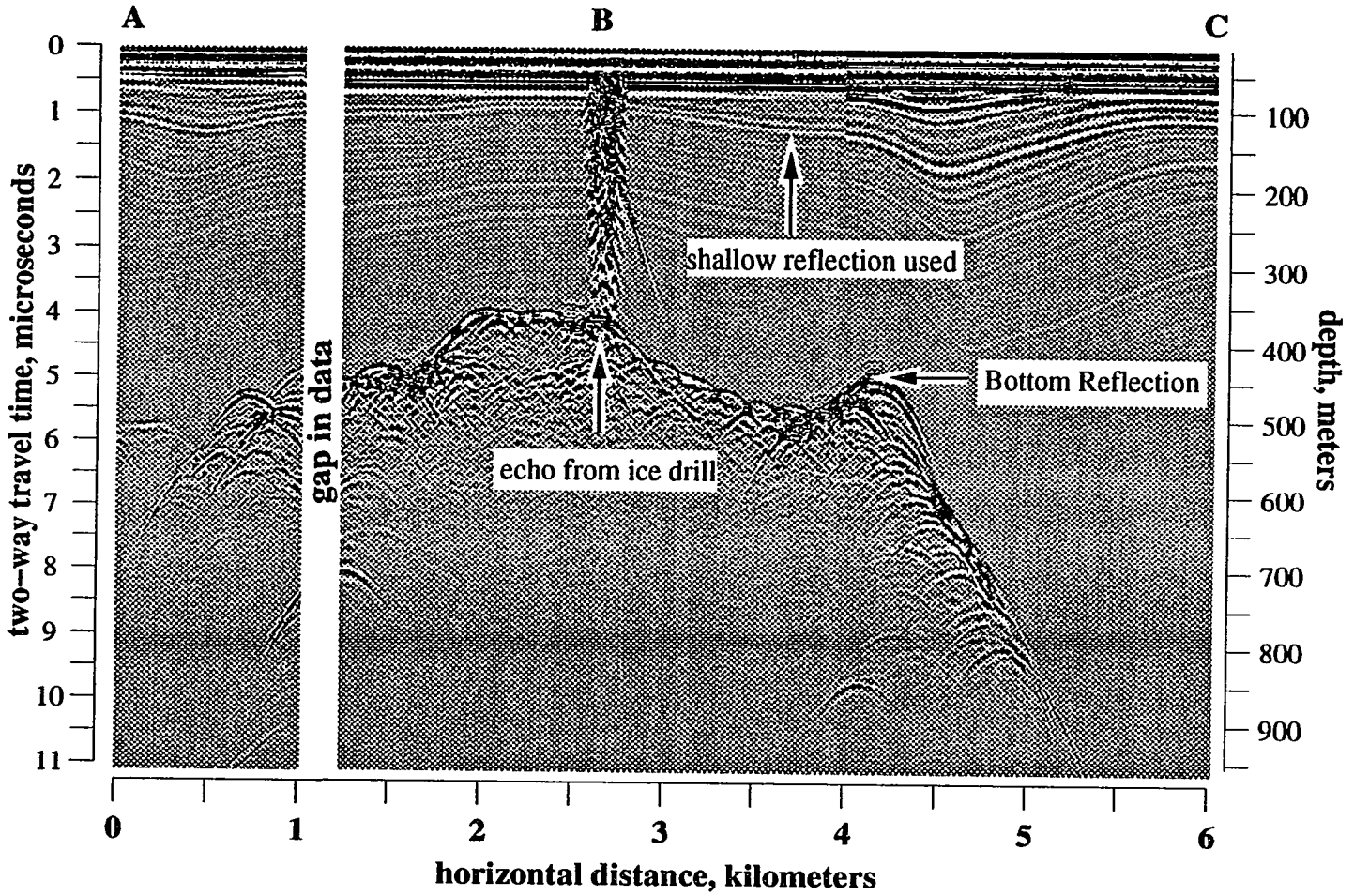

Figure 5.3: A section of RES data illustrating the marked variation of the depth of near surface as well as deep reflection horizons. The path of this profile is shown in figure 5.4. The break at ~4 km is a result of a misalignment of two RES profiles.

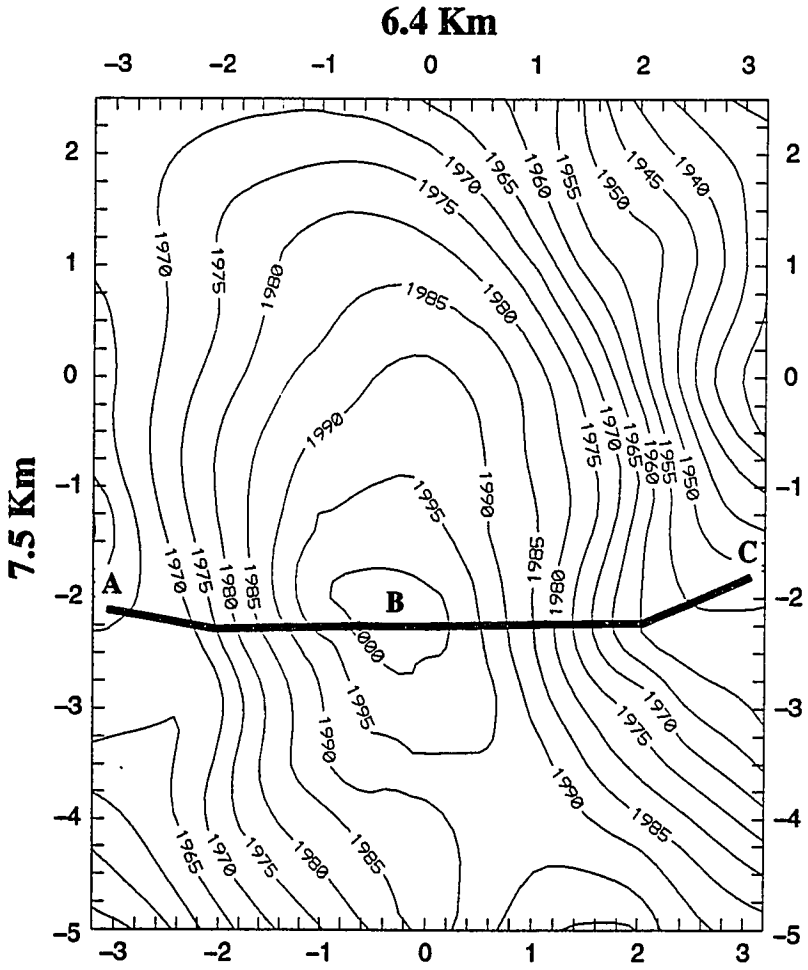

Figure 5.4: Map of the surface altitude in the vicinity of a local ice summit of the Dyer Plateau. The contour interval is 5 meters. The heavy line indicates the RES profile shown in figure 5.3. 200 meter ice cores were taken from close to the ice summit at the location marked 'B'.

tially by approximately 50%. Even though the near divide surface topography appears to be relatively flat, stake measurements have shown that snowfall amounts can very greatly within a few kilometers of the divide apparently in response to subtle features of the surface topography (compare figures 5.4 and 5.7).

Although the spatial sampling density of measured accumulation rates is much less than that of the radar measurements, the map of accumulation rate (figure 5.7) shows a

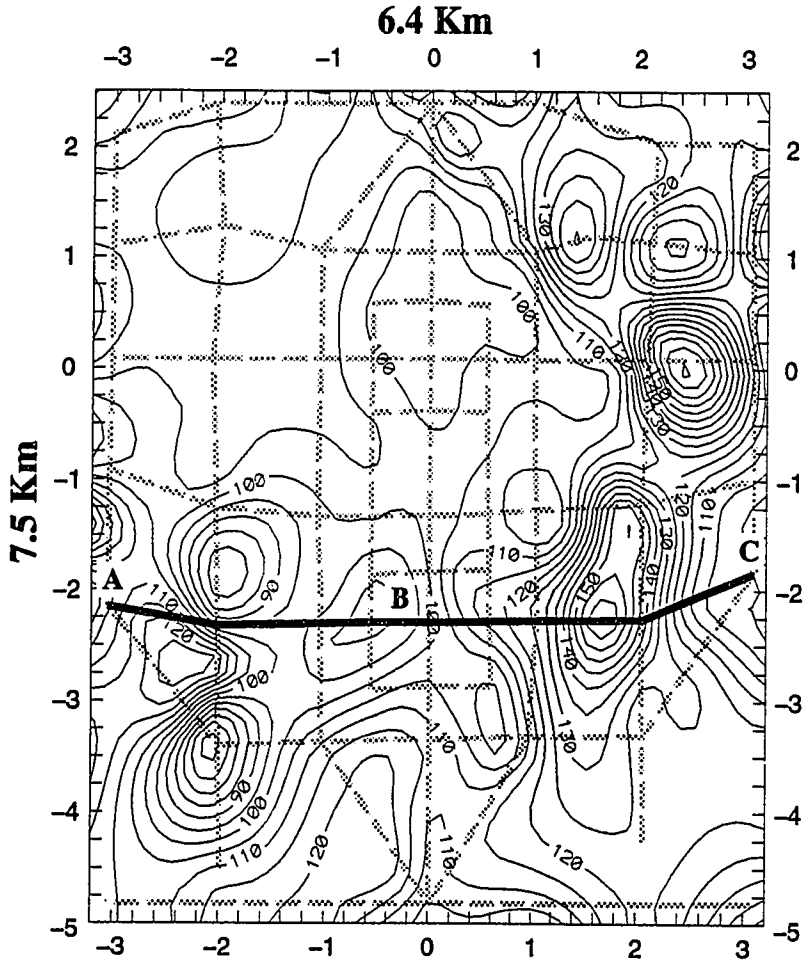

Figure 5.5: Depth of the horizon that dates to A.D. 1815. The contour interval is 5 meters. Dashed lines indicate paths of radar profiles used to establish layer's depth. The heavy line indicates the RES profile shown in figure 5.3.

high degree of visual correlation with the map of the depth of a near-surface reflector (figure 5.5). This observation led me to investigate how well the depth of the shallow reflection horizon could be used to infer the spatial pattern of accumulation rate. The main purpose of this exercise is to demonstrate the feasibility of using radar reflection horizons to infer the pattern of accumulation rate and to determine what influence horizontal straining has on this estimate.

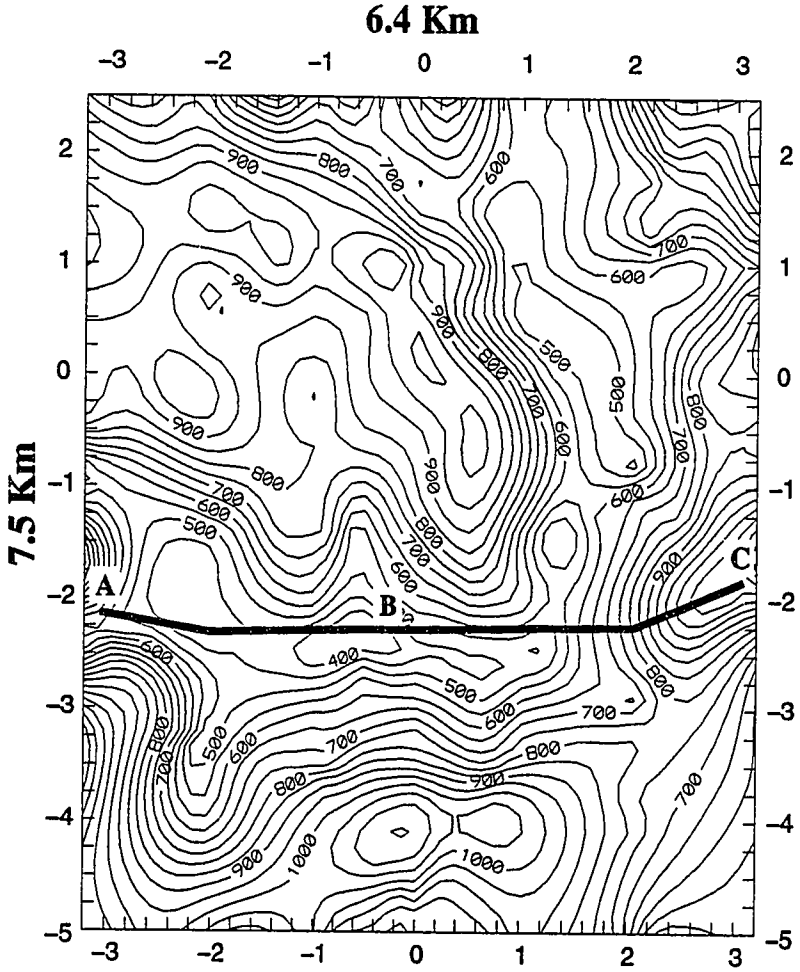

Figure 5.6: Ice thickness in vicinity of drill site. The contour interval is 50 meters. The heavy line indicates the RES profile shown in figure 5.3.

5.2.1 - Choice of Radar Reflection

Because of the large RES air-wave signal[1], it was not possible to detect internal layering shallower than 80 meters. Fortunately there was a bright reflection horizon just below the 80 meter air-wave cut-off at the drill site. This horizon was below the air-wave cut-off except for two short profile intervals where it was too shallow. This horizon

1. This is a general property of RES transmitters. Higher frequency impulse systems tend to have shorter air-wave signals.

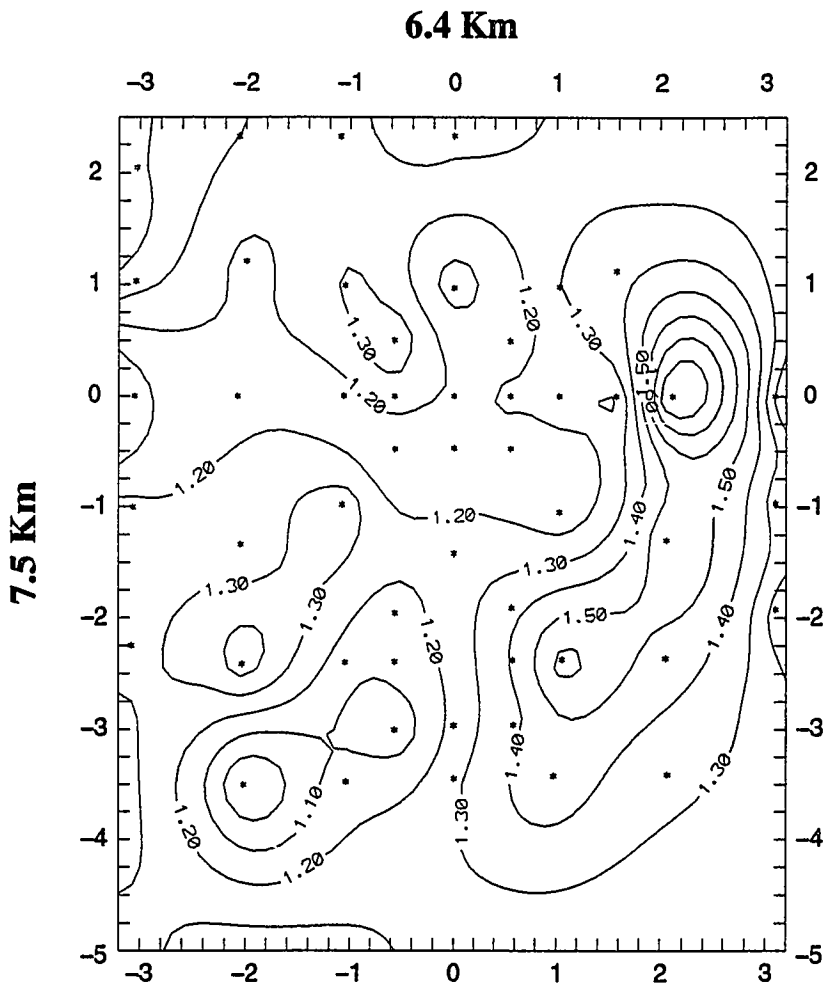

Figure 5.7: Accumulation rates derived from the measured burial rates of survey poles (asterisks). The contour units are meters per year at a density of $0.4 gm/cm^3$.

reached a maximum depth of 170 meters (figure 5.5).

Measurements of complex dielectric permittivity performed on an ice core from the summit show a large spike near this depth (John Moore; personal communication). This spike has been dated to the year 1815 by counting annual variations of non-sea salt sulfate (Lonnie Thompson; personal communication). In 1815 the volcano Tambora erupted and it therefore seems likely that the radar horizon is caused by the fallout from this eruption.

The influence of horizontal straining on an accurate estimate of accumulation rate

based on the 1815 layer's depth can be found from equation 5.13. The total ice thickness in the vicinity of the of the ice divide varies from 365 meters to over one kilometer and the layer's average depth is approximately 90 meters. Based on these values the relative influence should vary from 4 to 12 percent. This indicates that if an accuracy of better than 12 percent is desired, horizontal straining must be taken into account. This estimate is crude not only because it assumes that the ice flows in a simple way but also because it does not account for the variation of the layer's depth with position.

5.2.2 - Horizontal Strain-Rate Measurements

During the 1988-89 field season a grid of survey poles was deployed across the Dyer Plateau ice divide. The position of the poles was determined with theodolite and EDM measurements. During the 1989-90 field season the grid was resurveyed and expanded and during the 1991-92 field season the grid was remeasured. The poles were spaced on a $1\text{km} \times 1\text{km}$ grid except close to the divide crest, where they were spaced on a $½\text{km} \times ½\text{km}$ grid. No absolute reference point such as a nunatak was available to determine the absolute motion of the strain survey grid. To make up for this deficiency a survey pole located near the ice summit was assumed to have zero velocity. An additional pole situated on the divide crest was assumed to move along the divide away from the fixed summit pole in order to fix the rotation the entire pole array. Pole velocities in two perpendicular horizontal directions were then estimated and a *minimum-curvature* surface was fitted to each of them by use of a commercially available gridding program. The spatial derivatives of these surfaces were then estimated in the corresponding direction of velocity components and the total horizontal strain-rate, $\dot{\varepsilon}_0$, was found from their sum. Figure 5.8 is a map of pole motion vectors and the estimated horizontal strain-rates. The horizontal strain-rate is higher near the ice summit where the ice is thin (see figure 5.6). The estimated strain-rate varies wildly near the edges in some places. This is caused by the interpolation algorithm and is not a necessary feature of the data.

The estimated horizontal strain-rate varies from 0 to $2\times10^{-3} yr^{-1}$ (figure 5.8). Based on this range, equation 5.10 predicts that the influence of the horizontal strain-rate on accurate estimates of accumulation rate should vary from 0 to 17.5 percent if the layer is

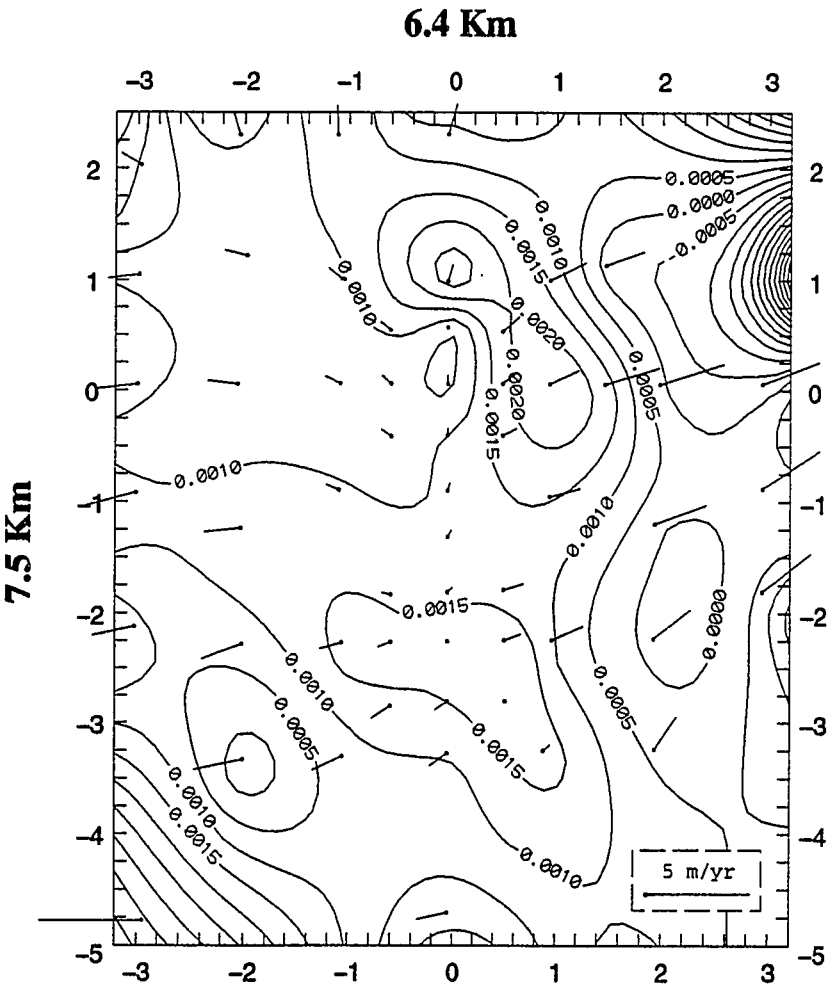

Figure 5.8: Measured horizontal strain-rates. Units are year^{-1}. The short lines indicate survey pole motions; the dots represent pole locations and the lines indicate magnitude and direction of motions

175 years old. This range is similar to the deductions in § 5.2.1.

5.2.3 - Estimated and Measured Accumulation Rates

Figure 5.9 (data points) shows the measured density of an ice core taken from near

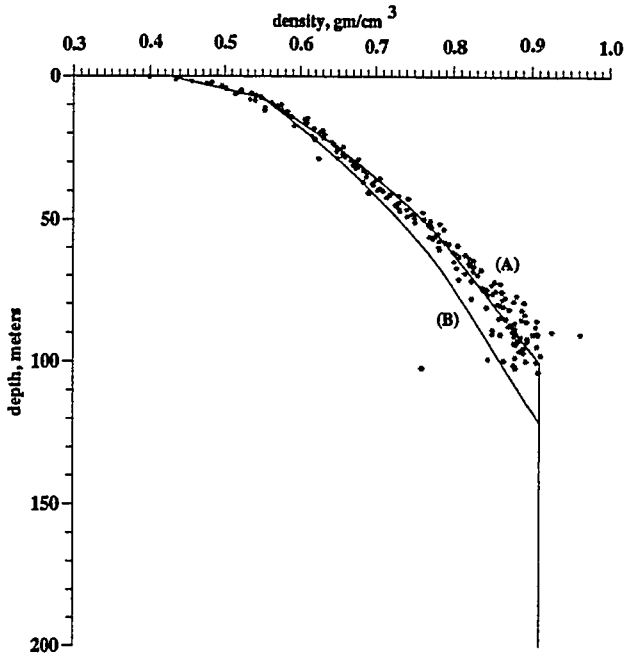

Figure 5.9: Observed and modelled density depth curves. The asterisks are density measurements from an ice core. Curve (A) is the best fit density of a modified Herron & Langway firn density model. Curve (B) is the same density model except accumulation rate is increased by 50%.

the ice summit. The density approaches a value of 0.91 gm/cm^3 at a depth of 85 meters. The 1815 layer is everywhere beneath this depth making it convenient to use equation 5.11 for the integrated density. This equation requires a compaction depth, z_c, which was found to be 17.5 meters from equation 5.12.

The layer depth and measured strain-rate information can now be combined to yield the spatial pattern of accumulation rate. This was accomplished using equations 5.9 and 5.11. The results are displayed in figure 5.10. Comparison of this figure with figure 5.7

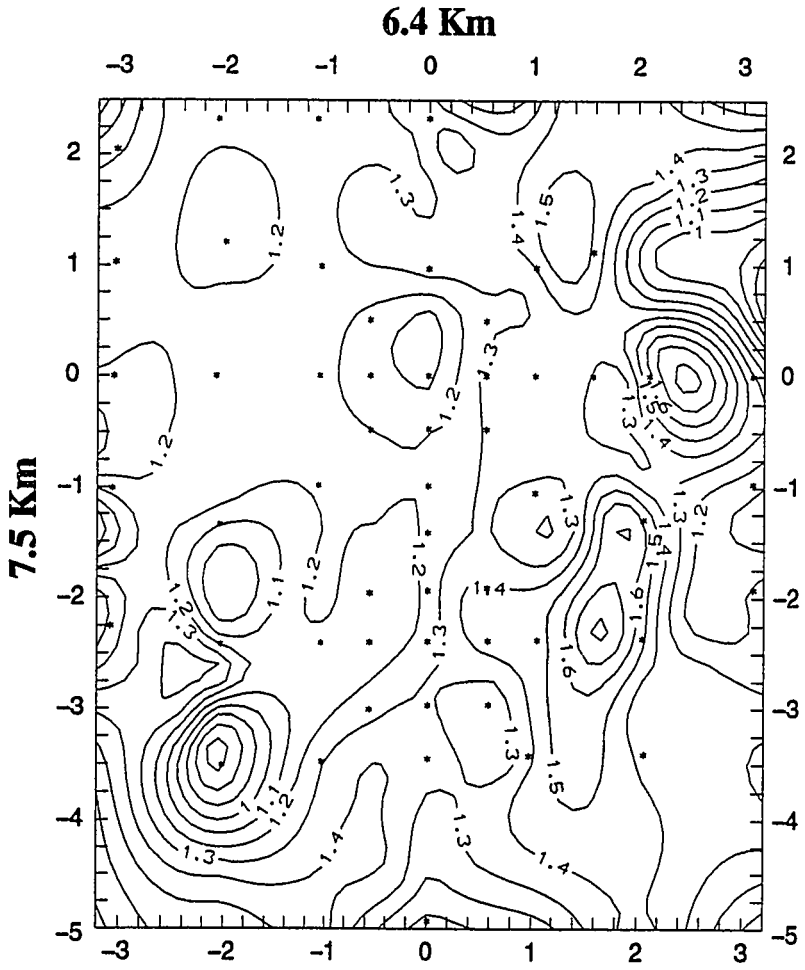

Figure 5.10: Accumulation rates estimated from the depth of 1815 horizon and horizontal strain-rates. Asterisks indicate positions of survey poles where accumulations were measured. Units are meters per year at a density of $0.4 gm/cm^3$.

shows relatively good agreement. The degree of agreement is shown in figure 5.11. If the estimated and measured accumulation rates were in perfect agreement the points would all appear on a straight line of slope unity which they in fact approximately do to within an average absolute deviation of 0.24 meters per year. Yearly accumulation rates based on pole height measurements that are spaced by one year will have uncertainties which are at least as large as the surface roughness. Surface roughness varies both spatially and tempo-

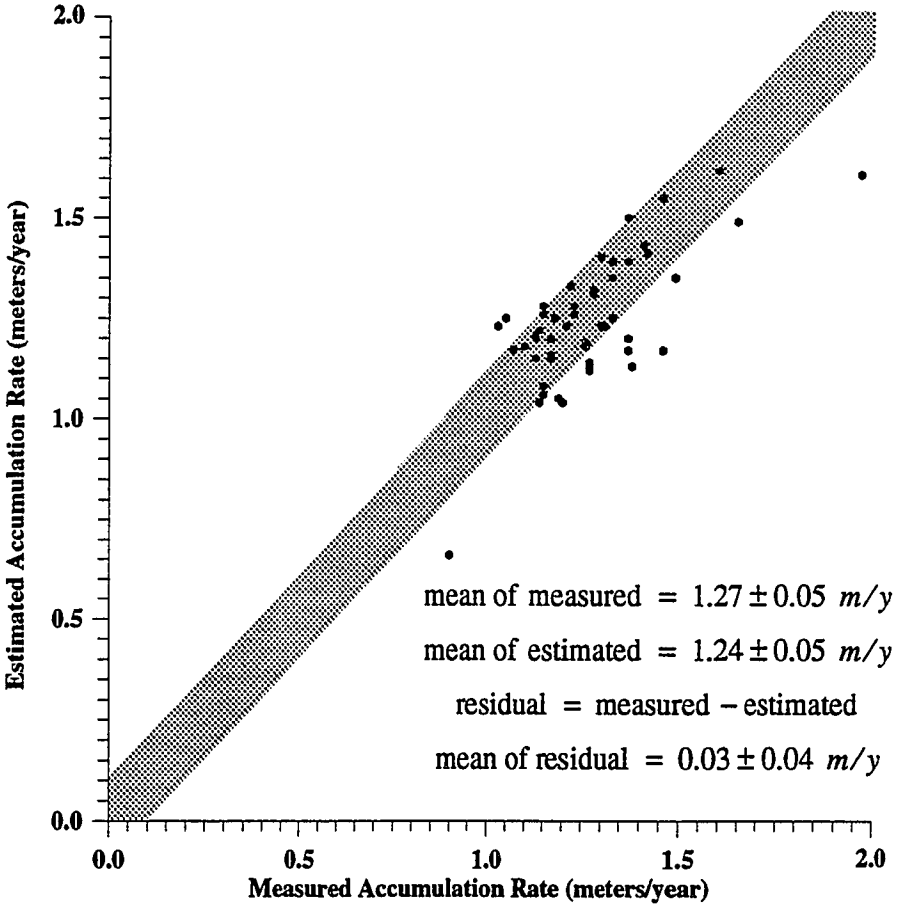

Figure 5.11: A comparison of accumulation rates derived from surface burial measurements (horizontal axis), and RES measurements (vertical axis). The grey swath indicates the uncertainty associated with burial rate measurements. There are 50 data points.

rally but is commonly ~0.2 meters. This could explain some of the discrepancy between measured and inferred accumulation rates.

If the prevailing winds shifted over time it is likely that the accumulation rate pattern would have also shifted. Because the pole measurements represent the present accumulation rate pattern and the accumulation rate estimates based on the 1815 horizon represent

an average over the past ~175 year, it may be possible to detect changes in the atmospheric circulation by comparing differences in accumulation rates deduced from pole measurements and the 1815 horizon. Since the ice divide is mainly a north-south structure, accumulation rate changes would probably appear as east-west gradients. To determine if there is an east-west dependence in the difference between the present accumulation rate pattern (measured from survey poles) and the 175 year average accumulation rate pattern (estimated from the 1815 horizon) I have plotted in figure 5.12 the difference between the two accumulation rates versus east-west position relative to the divide crest. The data points do not show any conspicuous east-west dependence and therefore no such shift seems to have taken place in the recent past. This result is discussed further in chapter 6, page 124.

Figure 5.13 is a contour diagram showing the relationship between the depth of a 175 year old layer, the horizontal strain-rate and the input accumulation rate based on a compaction thickness of 17.5 meters for the approximate range of accumulation and horizontal strain-rates observed. The figure shows that the variability of accumulation rate is capable of generating approximately four to five times greater range of layer depth than is the variability of horizontal strain-rate. This supports the argument that the reason that the layer appears relatively deep in some regions is primarily a result of high accumulation rate and is not a result of a low or compressive horizontal strain-rate.

5.2.4 - Sensitivity of Accumulation Rate Estimate to the Density Profile

I now investigate the sensitivity of the accumulation rate estimate to the density profile. If the density profile is not spatially invariant as I have assumed it to be, estimated accumulation rates will be in error. It is likely that in regions of higher accumulation rate the firn layer will be relatively thicker and relatively less dense since the ice column will be younger. If two different density profiles are available then the relative difference in inferred accumulation rate which they would produce can be found from

$$\frac{\Delta w_0}{w_0} \approx \left(\int_0^z \rho_a dz' - \int_0^z \rho_b dz' \right) \Big/ \left(\int_0^z \rho_a dz' \right), \tag{5.16}$$

where a and b indicate the two profiles; this equation is found from equation 5.9. Density

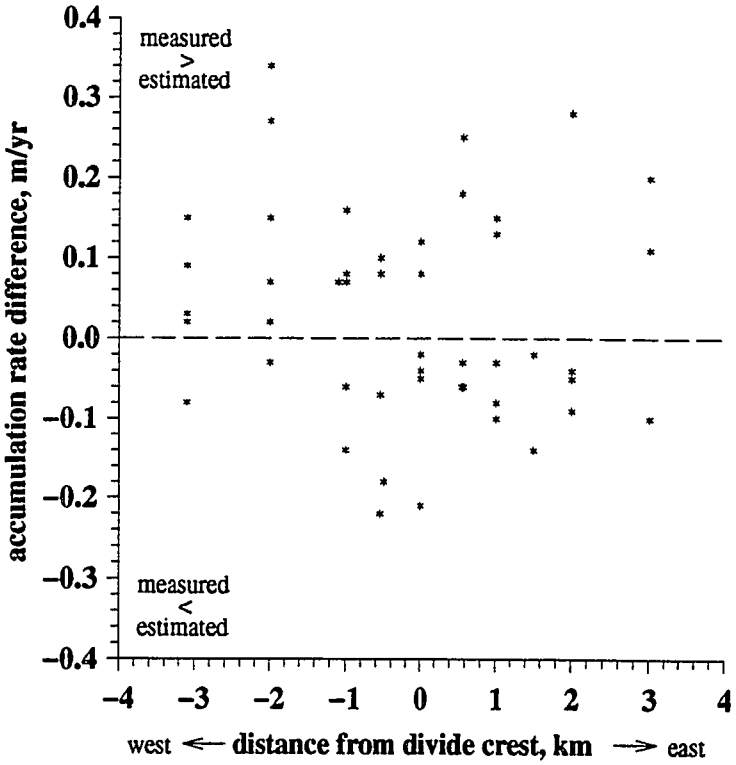

Figure 5.12: The difference between accumulation rates measured from survey pole burial rates and estimated from the 1815 reflection horizon plotted as a function of horizontal distance from the divide crest. The horizontal axis is the same as the horizontal axes in figures 5.4 to 5.8 and 5.10. The accumulation rate difference does not show any significant dependance on east-west position.

profiles have been measured at two locations on the Dyer Plateau. Unfortunately, the profiles happen to be from regions of similar accumulation rate and consequently are not well suited for investigating this sensitivity. To estimate density profiles in regions of high accumulation rate I have made use of an empirical model developed by Herron and Langway (1980). This model parameterizes the density depth profile in terms of temperature, surface density, and accumulation rate. Their model applies only to depths above pore close-off.

The model was fit to the observed density depth profile available from the ice summit using a non-linear least squares algorithm. Based on stake measurements made near

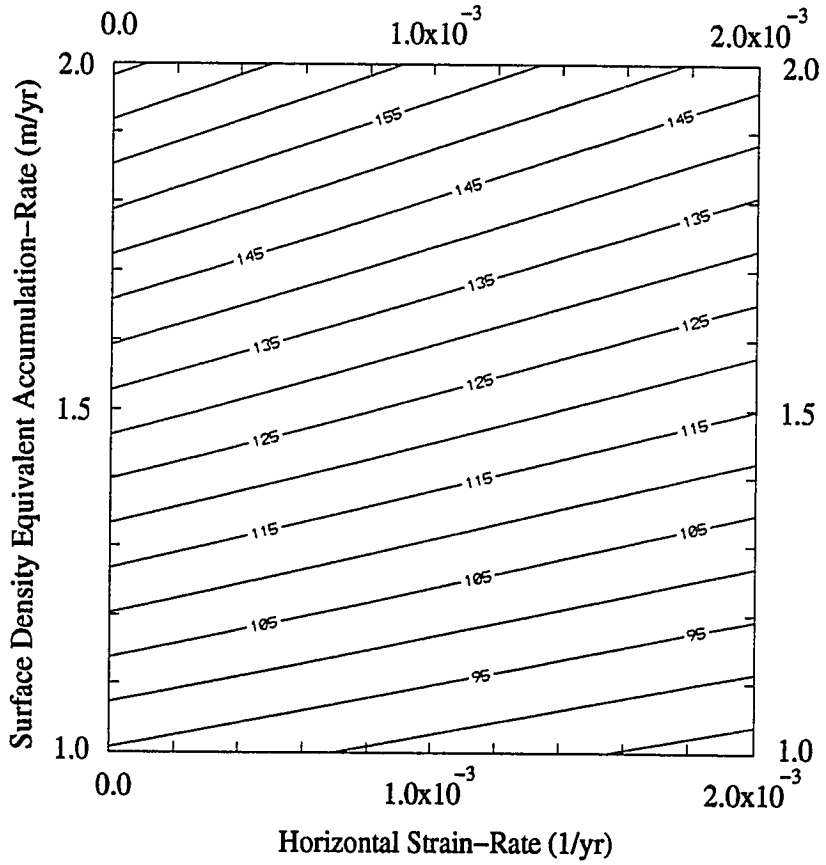

Figure 5.13: Contour diagram showing the theoretical relation between the depth of a 175 year old layer (contours), horizontal strain-rate (horizontal axis) and accumulation-rate (vertical axis) based on the density profile shown in figure 5.9. The ranges of accumulation-rate and strain-rate approximately match observed ranges.

the drill site the input accumulation rate was forced to be $1.20 \mathrm{m\,yr^{-1}}$ and the other two parameters were adjusted to find a best fit[2]. In finding the best fit the model was only applied to density measurements from depths shallower than pore close-off which was assumed to occur at a density of $0.82 \mathrm{Mg\,m^{-3}}$. The best fit required a firn temperature of

2. Allowing the input accumulation rate to be a variable does not significantly increase the goodness of fit and it results in much larger uncertainties in the other two parameters. Additionally the inverted input accumulation rate is found to have extremely large uncertainties (±0.42meters/year).

$-21.5 \pm 0.5°C$ (in good agreement with a measured ten meter temperature of $-21°C$) and a surface density of $0.418 \pm 0.006 Mg\,m^{-3}$. The modelled density curve shows good agreement with the observations and is shown as curve (B) in figure 5.9. I have extended the model from the pore close-off depth to the depth of solid ice by assuming that the rate of change of density with depth is constant and equal to the value found at pore close-off and once the density reaches the value appropriate for solid ice, it is then constant. Although this is a somewhat *ad hoc* extension of the model, it seems to give a good agreement with the measured density (curve (A) in figure 5.9).

To simulate the density profile in a high accumulation rate region, the model surface density and temperature were set at the values as found above, and the input accumulation rate was increased by 50% to $1.80 m\,yr^{-1}$. The resulting simulated density profile is shown as curve (A) in figure 5.9. As expected, the density is lower in the densification region and the densification layer is thicker.

The two modelled density curves were next applied to equation 5.16 and the resulting relative difference in inferred accumulation rates is shown in figure 5.14. The maximum effect is only 3.6% and is seen to occur at a depth of 107 meters. At depths shallower then 8 meters the accumulation rate difference is zero because the Herron-Langway firn model is not sensitive to accumulation rate at depths above the *critical-density* of $0.55 Mg\,m^{-3}$. Beneath 107 meters the densification layer has a diminishing influence on the inferred accumulation rate and as a result the relative difference in inferred accumulation rates decreases.

5.2.5 - Investigation of Time Variation of Accumulation Rate

I now investigate the assumption of steady-state accumulation rate. If the accumulation rate has not been constant in time the current estimates of accumulation rate based on stake measurements may not match those based on radar measurements. At some level of temporal resolution the accumulation rate is guaranteed to be non-steady-state. What we are interested in is how the non-steady-state nature of accumulation rate impacts our estimate of the accumulation rate.

The analysis of non-sea salt sulfate (Lonnie Thompson; personal communication) of

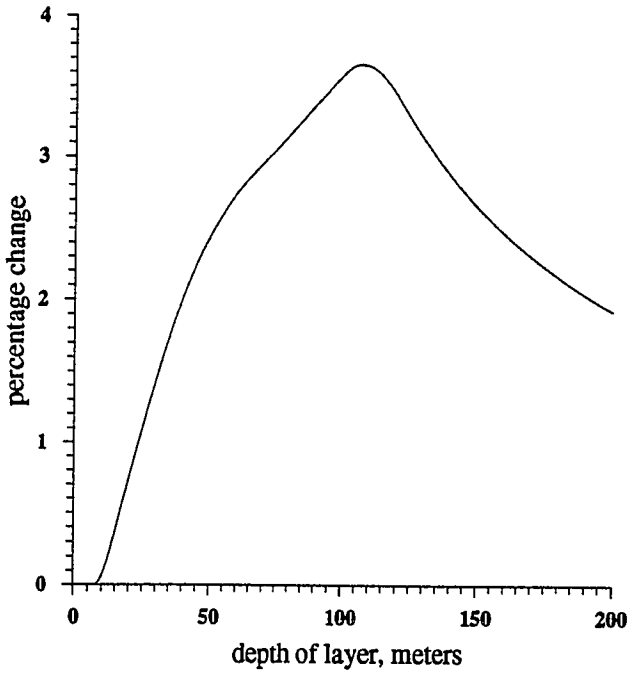

Figure 5.14: The relative percentage change in inferred accumulation-rate from the (A) and (B) modelled density profiles shown in figure 5.9. The horizontal axis represents depth (meters) and the vertical axis represents percentage difference of inferred accumulation-rate.

an ice core extracted from near the ice summit has made it possible to determine the age-depth relation in the upper 180 meters of the ice sheet (figure C.1, page 166). Given the density profile, the horizontal strain-rate and this age-depth relation it is possible to find the time-averaged accumulation rate through equation 5.9. Figure 5.15 shows accumulation rate inferred for four values of horizontal strain-rate. In order to make accumulation rates inferred after 1800 time invariant it is necessary to use a horizontal strain-rate that is larger than the horizontal strain-rate needed to make accumulation rates before 1800 time invariant. This is consistent with a horizontal strain-rate which decreases with depth. Whether the time-dependent variation of inferred accumulation rate is a result of a depth dependency of horizontal strain-rate or a time dependency of accumulation rate, the

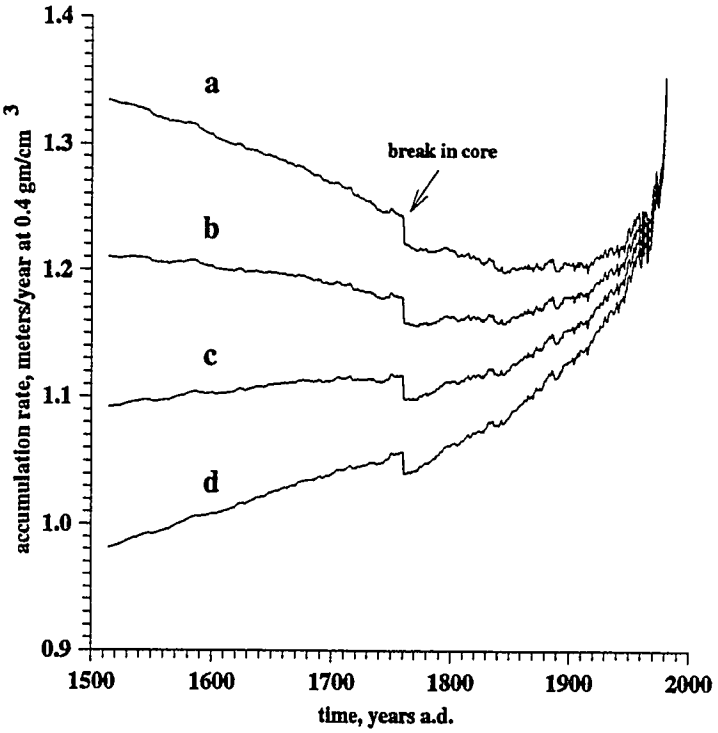

Figure 5.15: Inferred accumulation rates for four different horizontal strain rates as a function of time (years A.D.) based on age-depth and density-depth relations measured from an ice core taken from near the ice summit. If the accumulation-rate did change with time, and the horizontal strain-rate did not change with depth, one of the curves would appear as a horizontal line.

The corresponding horizontal strain-rates are: (a) 2.5×10^{-3}, (b) 2.0×10^{-3}, (c) 1.5×10^{-3}, and (d) 1.0×10^{-3} / year.

inferred accumulation rate taken from layers which date from the time interval 1950 to 1700 does not appear to vary by more than 10%.

The inferred accumulation rate from the very recent past (after 1950) shows a large variance and an increasing trend[3]. The large variance is explained by the short averaging interval over which the accumulation is estimated and the increasing trend may be real or due to an under-sampling of the density depth profile. All four of the inferred accumula-

3. For a more detailed treatment of the past accumulation-rate from annual layer thicknesses, see appendix c.

tion rate curves based on the four different values of horizontal strain-rate converge at the recent past due to the diminishing integrated effect that horizontal straining exerts on shallow young layers.

Chapter 6

Estimation of Internal Velocity Based on Radio-Echo Sounding

In this chapter I present a new method of estimating velocity within an ice sheet. The primary data used by this method are the age distribution (age field) within an ice sheet as determined from the geometries of dated internal layer horizons. It is based on mass conservation (continuity) and assumes that the velocity field has not varied in the past (steady-state flow). A chief advantage is that it does not use momentum or energy conservation and requires no rheological assumptions. If the flow field has varied, the new method can allow inferences to be made about how it has varied. For example, in some circumstances it may be possible to determine accumulation rate histories. Even if one does not apply the new method to actual data, understanding its foundations can aid in understanding geometrical characteristics of internal layers.

At the end of this chapter I apply the new method to a data set collected from the Dyer Plateau and I compare its velocity estimates to those found from a simple method of flow modeling developed by Whillans (1977).

To establish a basis for describing the method I introduce the following terminology:

1. A *flow-line* is defined to be a curve on the surface of an ice sheet which follows the horizontal velocity field as measured on the surface. Flow-lines are often well approximated as following the direction of surface altitude gradients.
2. A *streamline* is defined to be a curve which follows the internal velocity field of an ice sheet. Flow-lines are defined on the surface whereas streamlines are defined internally. If all of the ice inside of an ice sheet originates at the surface and ice flow has been steady-state, then all ice particles on a streamline will have originated at the same point on the surface. If the horizontal direction of flow does not vary with depth, streamlines will lie beneath corresponding flow-lines.
3. A *stream-sheet* is defined as a surface generated by a line defined on an ice sheet surface that is advected into an ice sheet. The line on the surface may be arbitrary,

but is most useful when it follows a flow-line. Stream-sheets are similar to streamlines with the difference being that stream-sheets originate from lines and are surfaces whereas streamlines originate from points and are curves. If the horizontal direction of flow does not vary with depth, stream-sheets which are generated from flow-lines will be vertical surfaces.

4. A *neutral-streamline* is defined to be a streamline which separates the two sides of an ice divide. In a theoretical sense this is the only streamline within a given stream-sheet that reaches bed rock after infinite time (assuming no basal melting) and is the only streamline to cross all isochrones. In three dimensions the collection of neutral-streamlines of an ice divide will form a *neutral-streamline surface.* For simple ice sheet geometries it is convenient to approximate neutral-streamlines as vertical lines and neutral-streamline surfaces as vertical sheets.

6.1 - Relation Between Age and Velocity Fields for Steady-State Ice Sheets

I now investigate the relationship between the age and velocity fields of a steady-state ice sheet. Nothing is assumed about the material behavior of the ice sheet except that it be incompressible. Modifications will be introduced later to account for near-surface densification.

If the velocity field of a steady-state ice sheet is known then its age field can be found from the line integral

$$T(\zeta) = \int_0^{\zeta} V^{-1} d\zeta' \quad , \tag{6.1}$$

where $T(\zeta)$ is the age and $V(\zeta)$ is the velocity at a distance ζ down a streamline. The problem here is the inverse; we wish to determine velocity from age. If the age field is known, it is not clear that the velocity field can be found from it. In this section I will present simple arguments which will show under what circumstances the velocity field can be found from the age field and a simple method for finding it.

6.1.1 - Basic Differential Relations

As a first step I derive two basic differential relations for steady-state flow of an incompressible fluid. The first equation gives the relationship between age, velocity and time and the second equation expresses continuity with incompressibility.

Consider a particle initially at a point (x, y, z) with a velocity $\vec{U} = (u, v, w)$. After a short time interval Δt, its new position will be given by $(x + u\Delta t, y + v\Delta t, z + w\Delta t)$, to first order in Δt. The particle's age at its new position will be given by its original age plus Δt. This can be expressed by

$$T(x + u\Delta t, y + v\Delta t, z + w\Delta t, t + \Delta t) = T(x, y, z, t) + \Delta t,$$

where T is the age field of the ice. This equation can be re-written as

$$\frac{T(x + u\Delta t, y + v\Delta t, z + w\Delta t, t + \Delta t) - T(x, y, z, t)}{\Delta t} = 1. \tag{6.2}$$

To first order

$$T(x + u\Delta t, y + v\Delta t, z + w\Delta t, t + \Delta t) = \left(T + \frac{\partial T}{\partial x}u\Delta t + \frac{\partial T}{\partial y}v\Delta t + \frac{\partial T}{\partial z}w\Delta t + \frac{\partial T}{\partial t}\Delta t\right)\Bigg|_{x, y, z, t}.$$

When combined with equation 6.2 this gives

$$\frac{\partial T}{\partial x}u + \frac{\partial T}{\partial y}v + \frac{\partial T}{\partial z}w + \frac{\partial T}{\partial t} = 1.$$

or

$$\nabla T \bullet \vec{U} + \frac{\partial T}{\partial t} = 1 \tag{6.3}$$

in vector notation. If the flow is steady-state the age will be time independent and this equation reduces to

$$\nabla T \bullet \vec{U} = 1. \tag{6.4}$$

This is the first basic differential equation of steady-state flow.

The second basic differential equation is found from the equation of continuity

$$\nabla \bullet (\rho \vec{U}) + \frac{\partial \rho}{\partial t} = 0. \tag{6.5}$$

In the next section I shall consider the special case where density is constant.

6.1.2 - Implications of Basic Differential Relations

In one dimensional steady-state flow, velocity can be directly determined from age by using equation 6.4. If this velocity does not also satisfy equation 6.5 ($\partial\rho/\partial t = 0$), then the flow must not be steady-state or mass must not be conserved.

In two dimensional steady-state flow, it is reasonable to hope that, given the age field, a unique solution to the velocity field can be determined from equations 6.4 and 6.5 since the number of equations equals the number of unknowns (i.e. the two velocity components). However, questions about the existence and uniqueness do not have obvious answers. I now present an argument showing that in two-dimensions the flow field can be found from the age field if one streamline is specified as a boundary condition.

From equation 6.4 it can be seen that at any particular location the component of velocity in the direction of the age gradient, U_α, will be equal to

$$U_\alpha = |\nabla T|^{-1}. \tag{6.6}$$

If density does not vary with time or position, at any particular location equation 6.5 in two dimensions gives

$$\frac{\partial U_\alpha}{\partial x_\alpha} = -\frac{\partial U_\beta}{\partial x_\beta}, \tag{6.7}$$

where α and β denote the age gradient and normal to age gradient directions respectively. When equations 6.6 and 6.7 are combined they yield

$$\frac{\partial U_\beta}{\partial x_\beta} = -\frac{\partial}{\partial x_\alpha}|\nabla T|^{-1} = (\hat{\alpha} \bullet \nabla)|\nabla T|^{-1}, \tag{6.8}$$

where $\hat{\alpha}$ is the unit vector in the direction of the age gradient.

Equations 6.6 and 6.8 show that the component of velocity normal to isochrones, U_α, and the derivative of the component of velocity tangential to isochrones, $\partial U_\beta/\partial x_\beta$, can be found directly at any particular location. By taking the line integral of the function represented by equation 6.8 along an isochrone the component of velocity tangential to the isochrone can be found to within an additive constant. The additive constant can be found

by evaluating the tangential component of velocity where a known streamline crosses the isochrone. Hence the necessary boundary condition for solving the velocity field in two dimensions is one streamline which crosses all isochrones. In work dealing with ice divides it is natural to choose the neutral-streamline as that boundary condition streamline.

In three dimensions a similar argument can be made. As in two dimensions, the component of the velocity normal to the isochrone surface will be given by equation 6.6. However, now equation 6.8 will have to be replaced by

$$\frac{\partial U_\beta}{\partial x_\beta} + \frac{\partial U_\Gamma}{\partial x_\Gamma} = (\hat{\alpha} \bullet \nabla) |\nabla T|^{-1}, \tag{6.9}$$

where β and Γ denote two directions perpendicular to the age gradient and to each other. The left side of this equation can be represented by

$$\nabla \bullet \vec{V} = f(x_\beta, x_\Gamma), \tag{6.10}$$

where $\vec{V}$ is the velocity and x_β and x_Γ are the curvilinear coordinates in the isochrone surface. If a velocity field in the isochrone surface is found that satisfies equation 6.9, then another velocity field that also satisfies it can be found by the addition of a divergence-free field. Because it is always possible to find a divergence-free field[1], the velocity field in three dimensions is under-determined.

6.1.3 - Streamline Parameterization in Two Dimensions

Consider a particle imbedded in a layer of finite thickness, Δz, in an ice sheet with two dimensional geometry and flow (figure 6.1). As the particle moves, the mass per unit width (width measured perpendicular to the cross section) of the portion of the layer between the particle and the neutral streamline must remain constant if mass is conserved. The mass per unit width of the layer segment can be normalized by dividing it by its age thickness, ΔT (age difference between the top and bottom of the layer). In the limit of the layer approaching infinitesimal thickness, the normalized mass per unit width of the layer segment, $S(x)$, will be given by

1. For example, a simple rotation field has no divergence.

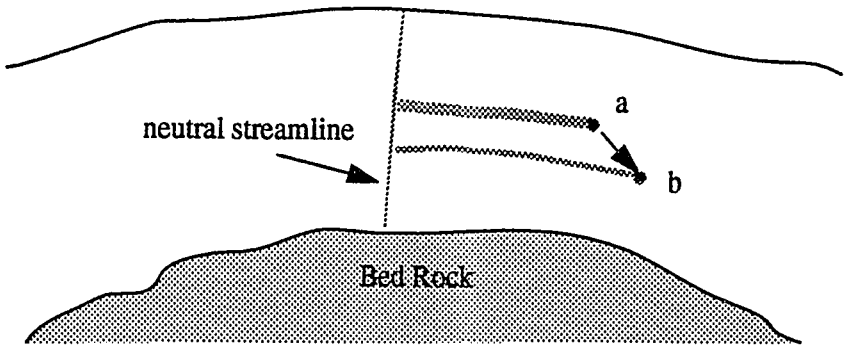

Figure 6.1: A cross sectional view of an ice divide depicting the motion of a particle imbedded in an isochrone layer. As the particle moves from (a) to (b) the mass per unit width of the layer segment will remain constant if mass is conserved within the ice sheet. If the flow is steady-state, over equal time intervals layer segments in position (a) will exactly replace layer segments in position (b).

$$S(x) = \lim_{\Delta z \to 0} \int_{x_0}^{x} \rho \frac{\Delta z}{\Delta T} dx' = \int_{x_0}^{x} \rho \hat{w} dx', \tag{6.11}$$

where x is the horizontal coordinate of the particle, x_0 is the horizontal coordinate of the neutral streamline where it intercepts the layer, ρ is the density, Δz is the vertical physical thickness of the layer thickness and $\hat{w}$ is the inverse of the vertical component of the age gradient which is expressed by

$$\hat{w} = \left[\frac{\partial T}{\partial z}\right]^{-1}.$$

Equation 6.3 shows that $\hat{w}$ will equal the vertical velocity, w, if the age gradient is vertical and the flow is steady-state. If mass is conserved within the ice sheet, S will remain constant as the particle moves. Thus, S will parameterize the particle's streamline.

If the flow of an ice sheet is steady-state, segments of different layers that have the (1) same age thickness and (2) terminate on the same streamlines will have the same masses. Since the streamline parameter defined in equation 6.11 is the mass of a layer segment as a function of horizontal position normalized with respect to the layer segment's

age thickness, it follows that equation 6.11 can be used to determine streamlines in a steady-state ice sheet. The horizontal coordinate where a streamline intercepts an isochrone layer will be the horizontal coordinate at which equation 6.11 evaluates to the streamline's streamline parameter value.

To determine streamlines from observed radio echo horizons one needs to: (1) date the observed horizons, (2) determine a neutral streamline that crosses the horizons and (3) approximate equation 6.11 along each of the observed horizons. Any given streamline should then cross the observed horizons at locations that have the same value of estimated streamline parameter S. If $S(x)$ is evaluated along all isochrones, streamlines will occur on contours of constant parameter value.

Although I have parameterized streamlines in reference to a neutral-streamline, there is in principal no reason why the parameterization could not be ascribed to any other reference streamline available. Such a streamline might be available from flow modeling alone or flow modelling coupled with surface movement measurements or bore hole measurements.

If the flow is steady-state, $S(x)$ gives the mass flux per unit width crossing a layer of constant age measured between the neutral-streamline, x_0, and a horizontal position, x. Thus, an alternative name for the function represented by this equation might be 'mass flux function'. If an ice sheet is steady-state, the mass flux crossing horizon segments that are bounded by the same two streamlines must be equal. Because of this, it is clearly seen that equation 6.11 will have the same value for different layers when evaluated at the same streamline and thus, it will parameterize streamlines.

6.1.4 - Streamline Parameterization in Three Dimensions

In the previous section I showed how streamlines can be parameterized for two dimensional flow. This is useful in the vicinity of a horizontal divide ridge where the flow and slopes of layering are known to be perpendicular to the ridge. Ice divides are seldom truly horizontal ridges and ice flow is usually not strictly two dimensional. However, if the flow at depth follows surface altitude gradients, then flow will not be fully three dimensional in the sense that a horizontal coordinate alone will specify the horizontal direction

of flow. In this situation it may still be possible to infer an internal velocity field from an age field.

Parameterizing streamlines in three dimensions is more complicated than in two-dimensions because in three dimensions the variability of the width of layer segments must be taken into account; in two dimensions the width of a layer segment is not dependent on the horizontal coordinate but in three dimensions it can be. In general, as a layer segment moves its width will be described by the distance between two stream-sheets. Figure 6.2 depicts the appearance of a narrow layer segment and its accompanying

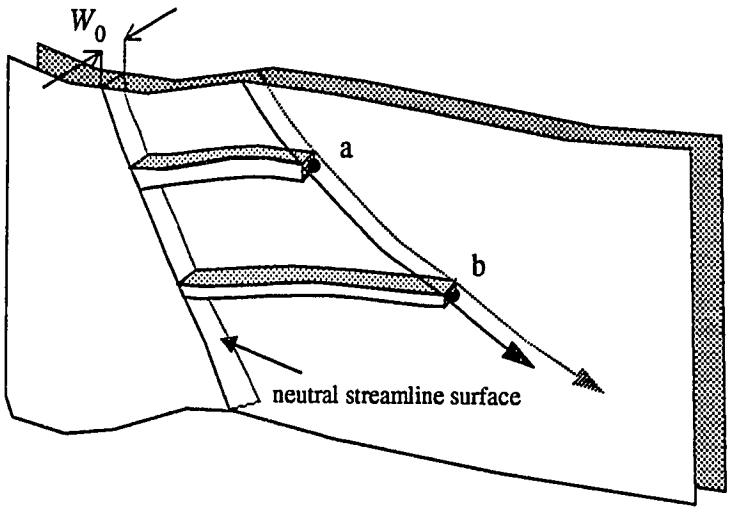

Figure 6.2: An illustration of the movement of a particle at the end of a layer segment. As the particle moves from (a) to (b) the mass of the layer segment will remain constant if mass is conserved within the ice sheet. If the flow is steady-state, over equal time intervals layer segments in position (a) will exactly replace layer segments in position (b).

stream-sheets.

As was shown in § 6.1.3, the mass of a layer segment can be normalized with respect to its age thickness by dividing it by its age thickness. In three dimensions an additional normalization is required to take into account a segment's width which is assumed to vary

along its length. This can be done by dividing a segment's mass by a reference width which is in some way directly related to the width everywhere on the layer segment. A convenient choice for a reference width is the width that the layer segment had when it was at the surface as measured at the ice divide.[2] The width and age thickness normalized mass of a layer segment will be given by

$$S(\xi) = \int_{\xi_0}^{\xi} \rho \hat{w} \frac{W}{W_0} d\xi' , \tag{6.12}$$

where ξ_0 is the horizontal distance along the layer segment at the neutral streamline surface, ξ is the horizontal distance along the layer segment at its end, W is the width of the layer segment, W_0 is a reference width and $\hat{w}$ is as before. To emphasize that the layer segment can be horizontally curved, ξ is used as the integration variable rather than x.

$S(\xi)$ will remain constant as the layer segment moves, if mass is conserved. Thus, equation 6.12 will parameterize the streamline of a particle existing at the end of such a layer segment.

If the flow of an ice sheet is steady-state, individual layer segments that have the same (1) age thickness, (2) terminate on the same streamlines and (3) exist within the same stream-sheets of infinitesimal width, will have the same masses. Since the streamline parameter defined in equation 6.12 is the mass of a layer segment as a function of horizontal distance normalized with respect to the segment's age thickness and starting width, it follows that equation 6.12 can be used to determine streamlines within stream-sheets in a steady-state ice sheet. The horizontal distance, ξ, where a streamline in a stream-sheet intercepts an isochrone will be the horizontal distance at which equation 6.12 evaluates to the streamline's streamline parameter value.

If the flow is two dimensional, and the stream-sheet chosen parallels flow-lines and has constant width, equation 6.12 reduces to equation 6.11 because W/W_0 will be unity.

If the flow at depth follows the direction of flow at the surface a convenient choice for the stream-sheet defining surface lines are flow-lines because their corresponding

2. The ice divide is the curve formed by the intersection of the neutral-streamline surface and the ice surface.

stream-sheets will be vertical surfaces. Because of this the width between two close stream-sheets that are generated from flow-lines will not vary with depth. If the flow follows surface elevation gradients W/W_0 can be easily calculated from a surface map. This is done by noting that the horizontal rate of change in the width between two close curves which follow surface gradients is given by

$$\frac{dW}{d\xi} = \frac{W}{R},$$

where R is the radius of curvature of surface contours along the curves. Rearranging this gives

$$\frac{dW}{W} = \frac{d\xi}{R}$$

which can be integrated to yield

$$ln\left(\frac{W}{W_0}\right) = \int_{\xi_0}^{\xi} \frac{d\xi'}{R(\xi')}.$$

From this it can be seen that

$$\frac{W}{W_0} = exp\left(\int_{\xi_0}^{\xi} R^{-1}(\xi')d\xi'\right). \tag{6.13}$$

This result is also derived by Reeh (1989). When equation 6.13 is substituted into equation 6.12 one finds

$$S(\xi) = \int_{\xi_0}^{\xi} \rho\hat{w} exp\left(\int_{\xi_0}^{\xi'} R^{-1}(\xi'')d\xi''\right)d\xi'. \tag{6.14}$$

Although the application of equation 6.14 to actual radar data is in principal simple, in practice it does involve some complications (appendix D). In order to estimate streamlines the flow at depth must approximately follow surface gradients, the radius of curvature of surface contours must be measured, the neutral-streamline surface must be estimated, dated radar horizons must be measured along a flow-line and the density depth relation, $\rho(z)$, must be known.

6.2 - Smoothness of Flow and Implications for the Age Field

In steady-state flow streamlines cannot exhibit discontinuous slope (kinks) because to do so requires either abrupt changes in rheology or abrupt changes in stress-field, neither of which is physically realistic. This condition implies constraints on the age field of a steady-state ice sheet. More specifically, if an ice sheet is steady-state it (1) cannot have discontinuities in its age gradient and (2) cannot have discontinuities of isochrone slopes (creases) which cross horizontal direction of flow. In this section I explain why these two points are true, and I investigate the implications of the presence of age gradient discontinuities and isochrone creases in an observed age field.

6.2.1 - Age Gradient Discontinuities

Under the assumption that an ice sheet is steady-state, any discontinuities in age gradient will in general imply streamlines that are discontinuous (figure 6.3a). This can be seen by examination of the streamline parameter equation. If layering is flat, the neutral streamline is vertical and flow is two-dimensional, equation 6.11 gives streamline parameters

$$S(x) = \rho \hat{w} x,$$

where x is the distance from the neutral streamline. Each streamline will have associated with it a streamline parameter value. The horizontal coordinate of a streamline with a streamline parameter value equal to S will be given by

$$x = \frac{S}{\rho \hat{w}} = \frac{S \partial T}{\rho \partial z}. \tag{6.15}$$

If the vertical age gradient, $\partial T/\partial z$, is discontinuous then so will be the horizontal coordinate. This implies that streamlines are also discontinuous.

If the derivative of the vertical age gradient is discontinuous, streamlines will exhibit kinks (figure 6.3b). More generally, from equation 6.15 it can be seen that discontinuities in the nth depth derivative of the age field will imply discontinuities in the nth $- 1$ derivative of streamlines.

Another generalization can be made from this equation; if the vertical age gradient

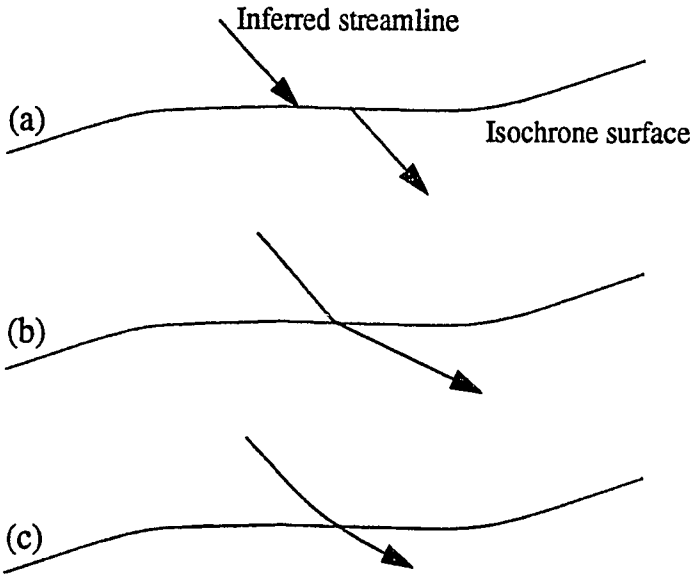

Figure 6.3: The appearance of an inferred streamline crossing an isochrone surface. (a) If there is a discontinuity of the first derivative of the age field across an isochrone, inferred streamlines will have a broken appearance as they cross that isochrone. (b) If there is a discontinuity of the second derivative of the age field across an isochrone inferred streamlines will have a bent appearance. (c) If the age field is continuous to at least the second derivative across isochrones, inferred streamlines will appear smooth.

does not monotonically increase with depth, deduced streamlines will exhibit 'zigzags'. This is illustrated in figure 6.4. The implications of this will be discussed in greater detail in § 6.3 where I will show how in some circumstances it may be possible to distinguish variations of accumulation rate from variations of flow.

The argument I have presented here is simplistic, because I have assumed the simplest flow and layering geometry possible. However, the layering and flow geometries of realistic steady-state ice sheets should be simple and the basic conclusion of how discontinuities of age field relate to discontinuities of flow field should not be fundamentally different from that discussed above.

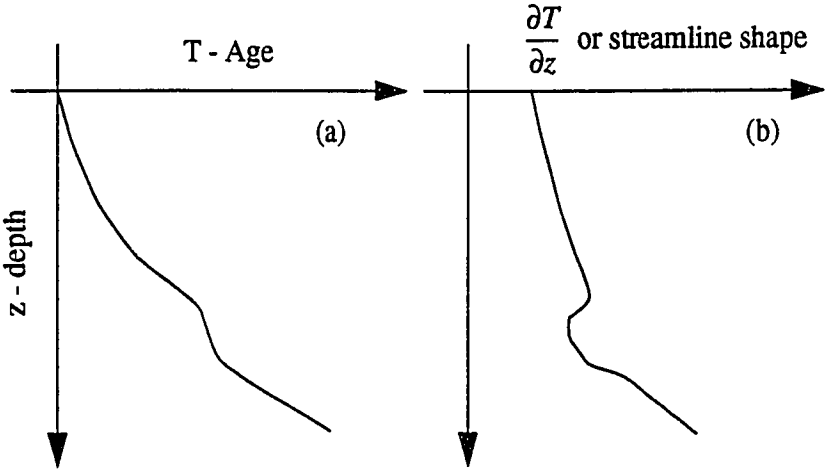

Figure 6.4: The relation between the age-depth curve and inferred streamline shapes for the situation in which internal layering does not significantly change depth with respect to horizontal position (planar assumption). Panel (a) shows a hypothetical age-depth relation and panel (b) shows its corresponding vertical age gradient and inferred streamline shapes.

6.2.2 - Isochrone Creases

Just as discontinuities of age gradient in a steady-state ice sheet generally imply streamlines which are not smooth, so do sharp creases in isochrones. Figure 6.5 illustrates the appearance of streamlines crossing an isochrone crease. As illustrated in the figure, because the angles which streamlines make when crossing isochrones are approximately the same on either side of a crease, streamlines will be bent by approximately the same amount as the angle made by the crease. This can be understood in terms of equation 6.4; on opposite sides of a crease the direction of the age gradient will be different by the angle of the change in slope of the crease. If the magnitude of the age gradient is the same on both sides of the crease, then, by this equation, the direction of flow must change by the angle of the change in slope of the crease.

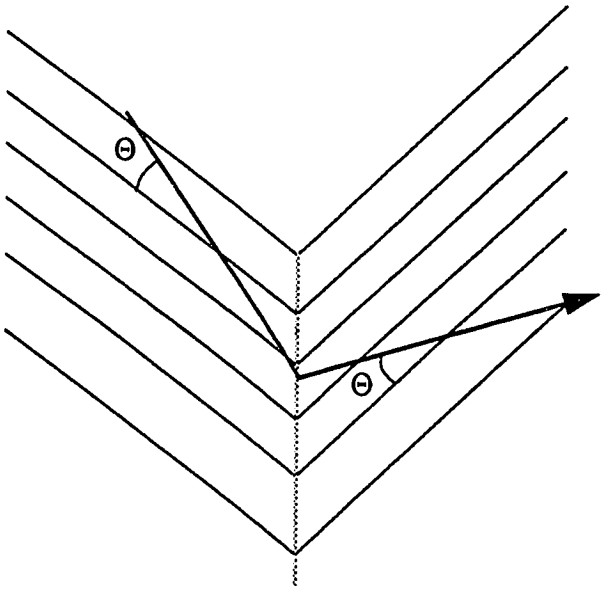

Figure 6.5: Flow passing through a crease. In general a crease in isochrones indicates a sudden change of velocity.

6.2.3 - Implications of Age Gradient Discontinuities and Isochrone Creases

Kinks in calculated streamlines which result from isochrone creases are potentially distinguishable from kinks which result from age gradient derivative discontinuities since kinks in the latter generally run along horizontal surfaces whereas kinks in the former generally run along vertical surfaces. If non-steady-state flow is assumed to be the cause of these features then this observation indicates isochrone creases are formed by a markedly different mechanism than age gradient derivative discontinuities. Age gradient discontinuities are easily explained by accumulation rate variations; a layer that experienced a different accumulation rate than its surrounding layers will have a different age gradient. A bit more imagination is necessary to conceive of a mechanism to generate an isochrone crease. One plausible generic mechanism for generating isochrone creases is a sudden change in ice sheet boundary conditions, either basal or otherwise. Such a boundary condition change could take place when the bed of an ice sheet goes from frozen to non-fro-

zen or when the pore pressure of a till bed reaches the overburden pressure and the till becomes activated. It might also take place when an ice shelf which exerts significant back-pressure on an ice sheet suddenly disintegrates due to a rise of sea water temperature.

The way in which a boundary condition change takes place, and changes the flow of ice, will effect how it influences isochrones; in some circumstances a change in a boundary condition might not cause layering to be conspicuously altered.

The corresponding ages at which deduced streamlines exhibit non-physically plausible patterns should, in most circumstances, indicate the ages at which an ice sheet experiences significant transients. Transients can be pulse or step in character. A pulse transient would include one time events such as a period of low accumulation rate, whereas a step transient would include permanent events such as the sudden disintegration of a bounding ice shelf or a long term increase of accumulation rate.

Figure 6.6 demonstrates the appearance of an idealized streamline for an ice sheet which has been in steady state except for two periods of low accumulation rate and one period of high accumulation rate. This inferred streamline curve can be easily understood in terms of the streamline parameter equation. In periods of low/high accumulation rate, the age gradient will increase/decrease which will cause the inverse of the age gradient to decrease/increase. This will then cause the streamline parameter equation to have lower/higher values and one will have to go out a further/shorter distance on an isochrone from the neutral streamline to find the same streamline parameter value. Inferred streamlines will appear to jump outwards during periods of low accumulation rate and inwards during periods of high accumulation rate. If accumulation rate variations change sufficiently slowly, they may not cause inferred streamlines to have noticeably anomalous shapes and if they change very quickly, they may not be detected due to under-sampling.

Non-steady-state conditions which leave isochrone creases may be recorded in an ice sheet in a fundamentally different fashion than accumulation rate variations if they are the result of sudden boundary condition changes. It is likely that transients of boundary conditions will result in disturbed conditions throughout the thickness of an ice sheet. Thus, inferred streamlines at all depths in the vicinity of a crease are likely to show kinks.

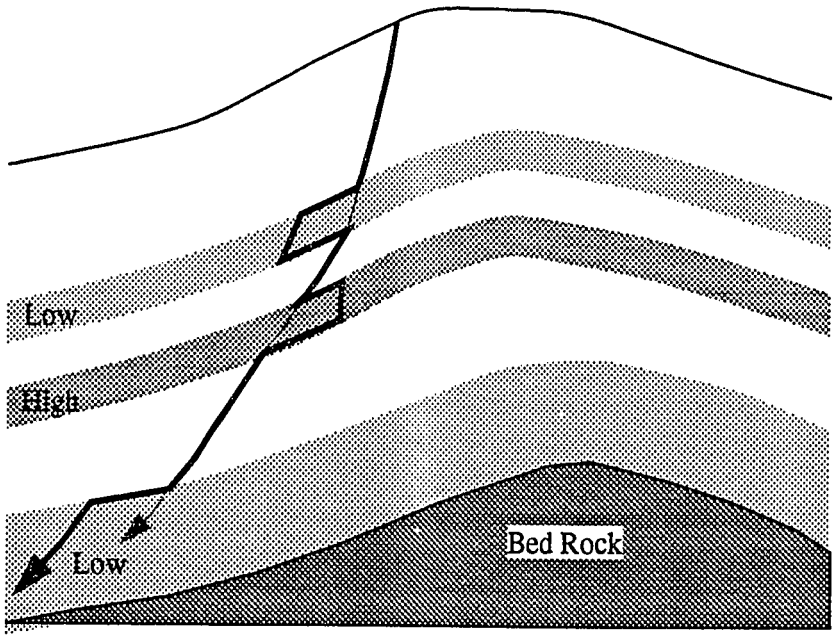

Figure 6.6: This drawing illustrates the general appearance of an inferred streamline based on an assumption of steady-state flow from an ice sheet that has experienced two periods of low accumulation rate and one period of high accumulation rate. The non-shaded bands correspond to periods of time with average accumulation rate. The dashed line indicates what the inferred streamline would look like if there were no accumulation rate variations.

For a period of time after a transient has taken place, any creases produced by it are likely to buried by increasingly smooth layers of ice. Figure 6.7 illustrates how this type of geometry and its corresponding inferred streamlines might appear. Inferred streamlines passing above the crease will not have a kink while inferred streamlines which pass through it will. Inspection of inferred streamlines may be useful in determining the significance of a crease. Unlike age gradient discontinuities isochrone creases should be directly visible. Thus dating crease formation might be most easily found from the dates of the top most creased isochrones and not from the dates at which streamlines first exhibit kinks.

One interpretation of isochrone geometries which seem to imply discontinuous or kinked streamlines is that they are the result of non-steady-state flow. Another potential interpretation is that they are the result of a steady-state flow field which is sufficiently

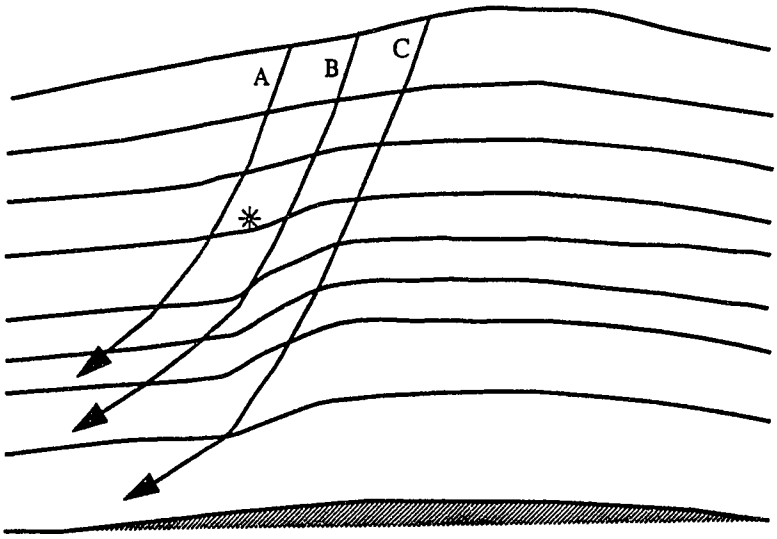

Figure 6.7: This drawing illustrates the appearance of inferred streamlines which pass by a crease in isochrone shapes. The asterisk indicates the first depth at which the crease is strongly present. Inferred streamline 'A' crosses above the asterisk and does not experience a strong bend associated with the crease whereas inferred streamlines 'B' and 'C' do.

three-dimensional to overly complicate the correct estimation of streamlines. In regions of rugged subglacial topography, discerning which of these two interpretations is correct may not be a tractable problem.

Even if the horizontal direction of flow does not vary with depth, the direction of flow relative to a radar profile must be carefully taken into account when interpreting RES profiles. Figure 6.8 shows a section of radar data that appears to show a crease in internal layer geometry. From this one might be tempted to infer that either streamlines are bent in this region or the flow is not steady-state. However, it is likely that neither inference is true because this radar profile mainly runs perpendicular to flow-lines; it is possible for such a feature to exist parallel to the general flow without requiring bent streamlines.

6.3 - Distinguishing Accumulation Rate and Flow Variations

If inferred streamlines indicate that non-steady-state behavior has taken place, one

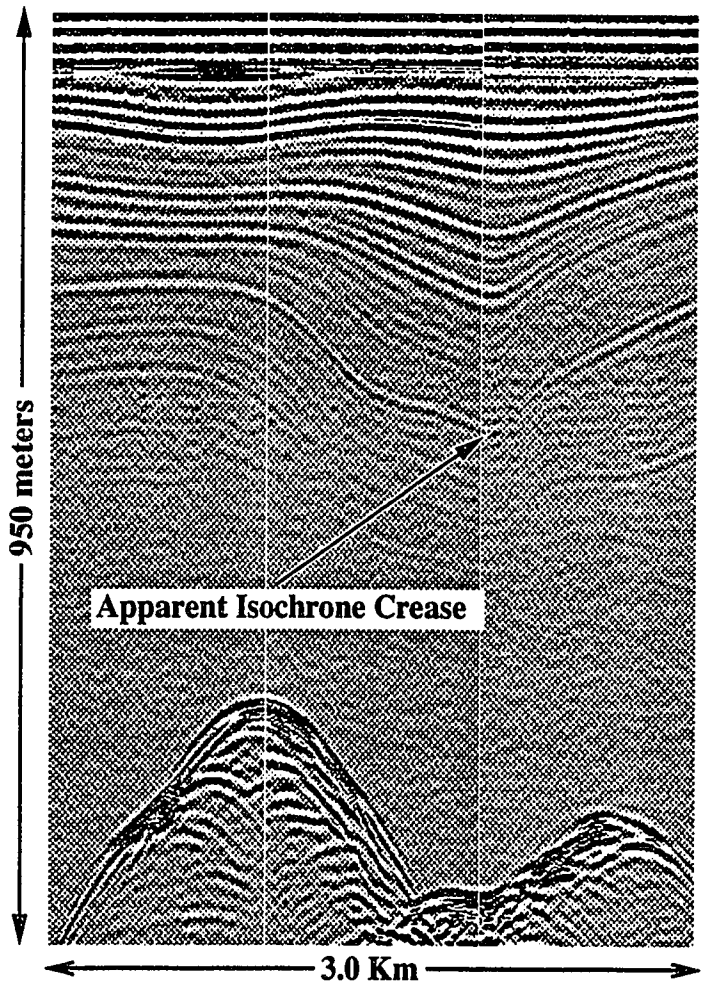

Figure 6.8: A RES profile which shows what appears to be a crease in internal layering (faint horizontal lines are related to the oscilloscope). If the flow were along this profile, streamlines would have to bend as they cross the crease. However, the general direction of flow is across the profile.

may wish to determine if the apparent non-steady-state behavior is the result of (1) accumulation rate variations that have occurred on time scales that are short relative to the ice sheet's dynamical response time, or (2) a result of significant changes in the ice sheet's geometry and flow. Accumulation rate variations that occur on time scales that are short relative to the dynamical response time should not significantly affect the flow field of an ice sheet or its geometry. Because of this, it may be possible to distinguish which of the

two causes is responsible for causing an apparent non-steady-state flow. Being able to do this will be especially important for the interpretation of ice core records; if an ice sheet's geometry has undergone significant changes the interpretation of ice core records from it can be difficult.

As pointed out in § 6.2.1, non-monotonically increasing values of vertical age-gradient will result in inferred streamlines which exhibit zigzags. This interpretation hinges on how horizons are dated. For example, if radar horizons are dated directly from measured ice core dates, it may be possible to eliminate zigzag features by applying a smoothing function to the measured dates. Such smoothing of the age profile has the effect of eliminating high frequency variations of accumulation rate.

If application of smoothed ages to observed radar horizons results in physically plausible inferred streamlines one may conclude that the flow-field has been steady-state. If, after smoothing the ages, the inferred streamlines are still nonsensical then one may conclude that the reason they are nonsensical is at least in part due to a non-steady-state flow-field. It is likely that the second conclusion would be stronger than the first. This is because if nonsensical inferred flow can be eliminated it is not necessarily true that the flow has been steady-state, it may have been non-steady-state but left no conspicuous evidence, but if nonsensical flow cannot be eliminated by smoothing ages then it is very likely that it truly is a result of non-steady-state flow.

If a steady-state flow-field and geometry did exist in the past, but the accumulation rate varied on short time scales, it should be possible to infer what the past accumulation rate history has been based on the measured age field. Reconsider figure 6.6. The heavy line depicts the path of an inferred streamline which has not been corrected for the past accumulation rate history, while the light dashed line depicts the path of an actual streamline. In order to make the inferred streamline match the actual streamline, the calculated streamline parameter values must be scaled to account for accumulation rate variations. For any given layer, the scaling will be given by the average accumulation rate divided by the accumulation rate experienced by that layer. This is expressed by

$$S(x) \rightarrow \frac{A_0}{A} S(x)$$

where A_0 is the average accumulation rate and A is the accumulation rate experienced by the layer.

A steady-state streamline could be estimated by applying a smoothing function to an inferred streamline. For an individual layer, an estimate of the ratio of the accumulation rate experienced by the layer to the average accumulation rate will be

$$\frac{A}{A_0} = \frac{S_i}{S_s} \tag{6.16}$$

where S_i is the streamline parameter value of the inferred streamline and S_s is streamline parameter value where the smoothed streamline crosses the layer. The consistency of the layering with a steady-state flow hypothesis can then be further validated by observing other inferred streamlines which have had their streamline parameter values scaled by the ratio given by equation 6.16 on a layer by layer basis. If the assumption that variations of accumulation rate have not affected the flow field is correct, all accumulation rate corrected inferred streamlines should appear plausible.

6.4 - Analysis of Data From the Dyer Plateau

In this section the method of streamline parameterization is applied to data from the Dyer Plateau. The method is first applied to the stratigraphic age versus depth measured in ice core data to deduce the shape of streamlines locally in the immediate neighborhood of an ice summit (§ 6.4.2). The method is then applied to ice core data combined with radar data to deduce the shape of streamlines located within a stream-sheet that crosses the same ice summit (§ 6.4.3). In both applications the deduced streamlines are compared with streamlines deduced from strain-rate measurements.

6.4.1 - Overview of Ice Flow

Surface and bed topographies of the region investigated are shown in a perspective view in figure 1.2 (page 4). In this region the bed topography is extremely rugged (slopes of 1:3 are common) and appears to have a strong influence on the ice sheet's surface

topography. For example, the ice sheet surface topography is relatively level in regions of deep bed topography and relatively steep in regions of shallow bed topography except in the immediate neighborhood of a divide crest where it is relatively level for a range of ice thicknesses. Additionally, the high points of the surface and bed topographies are approximately coincident, indicating that the present location of the divide is controlled by bed topography and not by side boundary conditions.

The measured motions of surface survey pole markers are well correlated with surface altitude gradients in most regions (Figure 6.9). This indicates that, at least for shallow depths, the horizontal direction of flow follows surface altitude gradients as was assumed in deriving equation 6.13.

6.4.2 - Streamline Analysis of Ice Core Data

In the immediate neighborhood of the drill site and ice summit ice radar measurements indicate that internal layering is relatively level (figure 6.12). Because of this ρ and $\hat{w}$ should be locally independent of horizontal position and as a result it should be possible to deduce streamline shapes close to the ice summit based on ice core information regardless of whether or not the drill site was exactly coincidental with the ice summit.

Before streamline parameterization can be performed the width normalization term, W/W_0, of equation 6.12 which accounts for the lateral spreading of layers must be known. Although precise knowledge of it is not available, it can be adequately approximated by assuming that all ice summit surface contours are similar ellipses in the neighborhood of the ice summit and that the flow follows surface gradients. When this is done, one finds from equation D.3 that

$$\frac{W}{W_0} = kx^{\mathfrak{R}}$$

if the horizontal x axis is aligned with the appropriate axis of symmetry. In this equation $\mathfrak{R}$ represents the aspect ratio of the elliptical surface contours.

If the neutral streamline is vertical and the layering is level, the streamline parameterization of equation 6.12 will be

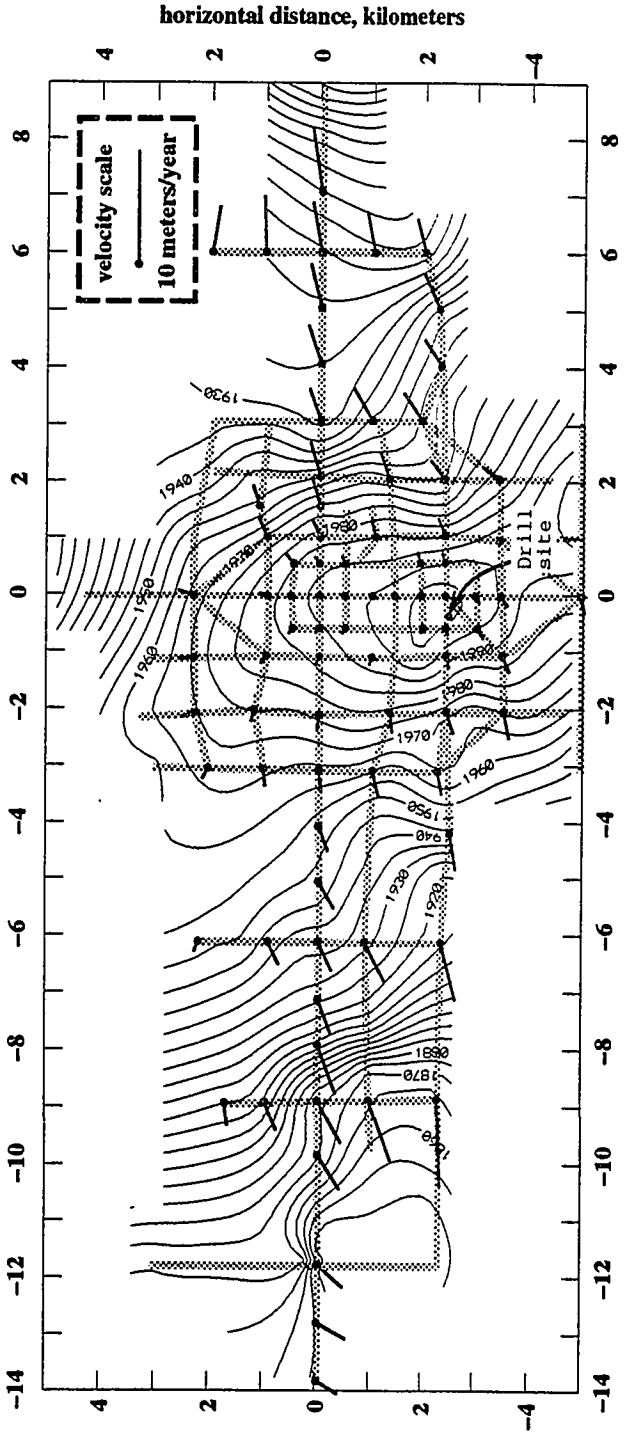

Figure 6.9: A topographic map of the surface altitudes measured on the Dyer Plateau Ice Sheet. Grey lines indicate radar profiles and short lines indicate pole motions. Left (-14 km) is west and right (9 km) is east (approximate).

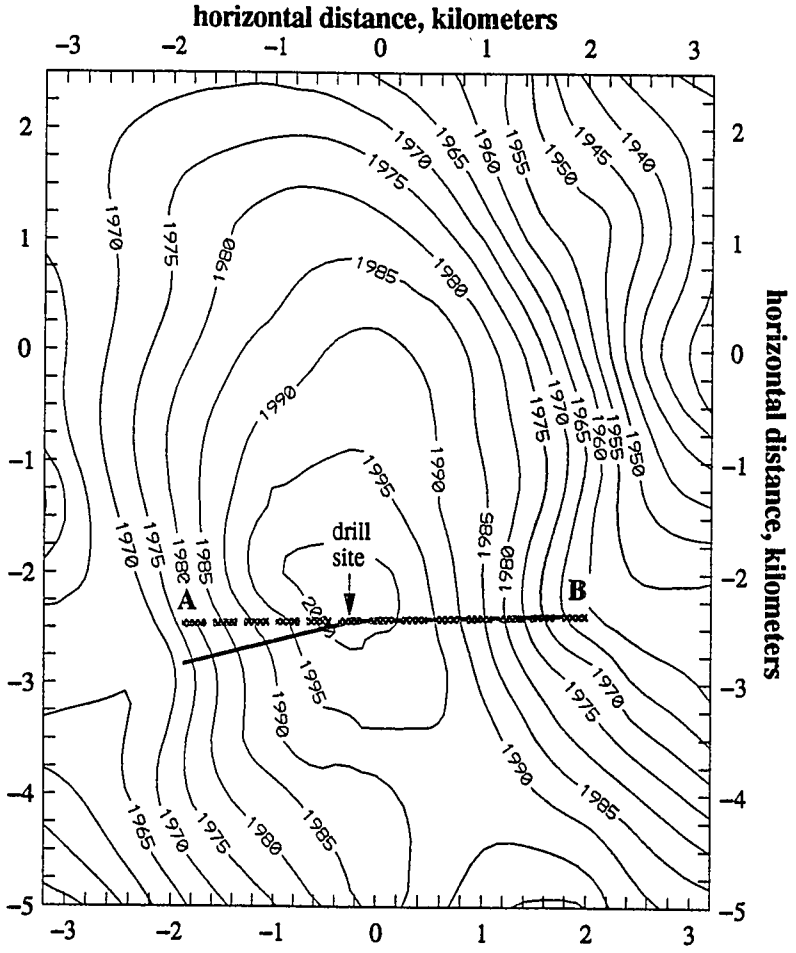

Figure 6.10: Surface topography in the neighborhood of the drill site and ice summit. The grey dashed line indicates the path of the RES profile used for streamline parameterization. The solid dark line indicates the line onto which layer information was projected in order to correct for the moderate deviation of the RES profile from the direction of altitude gradients.

$$S(x) = k\int_0^x \rho \hat{w} x'^{\Re} dx' = \frac{\rho}{\Re + 1} k \hat{w} x^{\Re + 1}. \tag{6.17}$$

A streamline that intercepts the surface a distance x_0 from the divide will have a streamline parameter of

$$S = \frac{1}{\Re + 1} k \rho_0 w_0 x_0^{\Re + 1}, \tag{6.18}$$

where w_0 is the accumulation rate and ρ_0 is the surface density. When equations 6.18 and 6.17 are combined the horizontal distance of a streamline from the divide is found to be

$$x = x_0 \left[\frac{\rho_0 w_0}{\rho \hat{w}} \right]^{\frac{1}{\Re + 1}}. \tag{6.19}$$

An age-depth relation has been determined from ice core chemical analysis to a depth of 180 meters (figure C.1, page 166) and the density-depth relation has been measured to a depth of 100 meters (figure C.2, page 167). Ice core analysis was carried out by Lonnie Thompson of the Byrd Polar Research Center, Ohio State University and David Peel and Rob Mulvaney of the British Antarctic Survey. In the analysis presented here, 10 year time increments have been used when estimating $\hat{w}$ from the measured age-depth relation and a hand fit piecewise linear approximation to the density-depth relation has been used to estimate the density.

For comparison, it is useful to estimate the shapes of streamlines located close to the drill site/ice summit from strain-rate information measured from borehole analysis (Appendix C). If the horizontal strain-rate is directly related to regional surface slope, and all surface contours are similar ellipses, it is reasonable to suppose that the minor-axis to major-axis strain-rate ratio, $\partial u/\partial x : \partial v/\partial y$, will be approximately equal to the aspect ratio, $\Re$ (figure D.2, page 172). Because $\dot{\varepsilon}_0 = \partial u/\partial x + \partial v/\partial y$, the horizontal strain-rate in the x direction will be approximately

$$\frac{\partial u}{\partial x} = \frac{\dot{\varepsilon}_0}{\Re + 1}. \tag{6.20}$$

If a particle enters the ice at the horizontal coordinate $x = x_0, y = 0$ with an age of zero, its x horizontal coordinate at an age T will be

$$x = x_0 exp(\dot{\varepsilon}_0 T / (\Re + 1)), \tag{6.21}$$

if $\dot{\varepsilon}_0$ does not vary with depth (equation 5.3). The age of a particle that has reached a depth

z is

$$T = -\frac{1}{\dot{\varepsilon}_0} ln(1 - \frac{\dot{\varepsilon}_0}{\rho_0 w_0} \int_0^z \rho dz') \tag{6.22}$$

(equation 5.6). When this is substituted into equation 6.21, the horizontal coordinate x of the streamline at a depth z is

$$x = x_0 \left[\frac{\rho_0 w_0}{\rho_0 w_0 - \dot{\varepsilon}_0 \int_0^z \rho dx'} \right]^{\frac{1}{\Re + 1}} . \tag{6.23}$$

Because both equations 6.19 and 6.23 involve an x_0 multiplied by depth dependent quantities raised to the $1/(\Re + 1)$ power, streamlines deduced by streamline parameterization, S-streamlines (equation 6.19), and streamlines deduced from density, horizontal strain-rate and average accumulation rate, $\dot{\varepsilon}_0$-streamlines (equation 6.23), will be directly comparable regardless of the $\Re$ used as long as the same value is used in evaluating both equations.

The measured horizontal strain-rate ratio at the drill site ($\partial v/\partial y : \partial u/\partial x$, where y is along the divide and x is perpendicular to it) is very close to 1:1.5. An ellipse with this aspect ratio fits the highest surface contour shown in figure 6.10 relatively well; this aspect ratio has been used in the analysis presented here.

Figure 6.11 is a comparison of streamlines found by application of equations 6.19 and 6.23. When evaluating both equations $x_0 = 1$ (arbitrary units). The middle smooth curve is the $\dot{\varepsilon}_0$-streamline described by equation 6.23 with best-fit estimates of $\dot{\varepsilon}_0$ and w_0 found from vertical strain analysis. The other two smooth curves represent the 95% confidence intervals indicated by the uncertainties in $\dot{\varepsilon}_0$ and w_0 found from the vertical strain analysis. The jagged curve represents the S-streamline found by application of equation 6.19 with the best-fit estimate of w_0 from the vertical strain analysis. This streamline was not evaluated at the surface. If it did, its horizontal position would equal unity only if the surface value of $\hat{w}$ equaled the w_0 used. The best-fit center $\dot{\varepsilon}_0$-streamline is in approximate agreement with the S-streamline and the bounding 95% confidence streamlines

envelop the S-streamline except close to the surface where the S-streamline is closer to the ice summit. Because the S-streamline is relatively close to the ice summit at shallow depth, this indicates that over the last ~50 years (age at ~40 m) there has been a significant increase in the accumulation rate (§ 6.3).

Equation 6.16 can be applied to the S-streamline and the smooth $\dot{\varepsilon}_0$-streamline

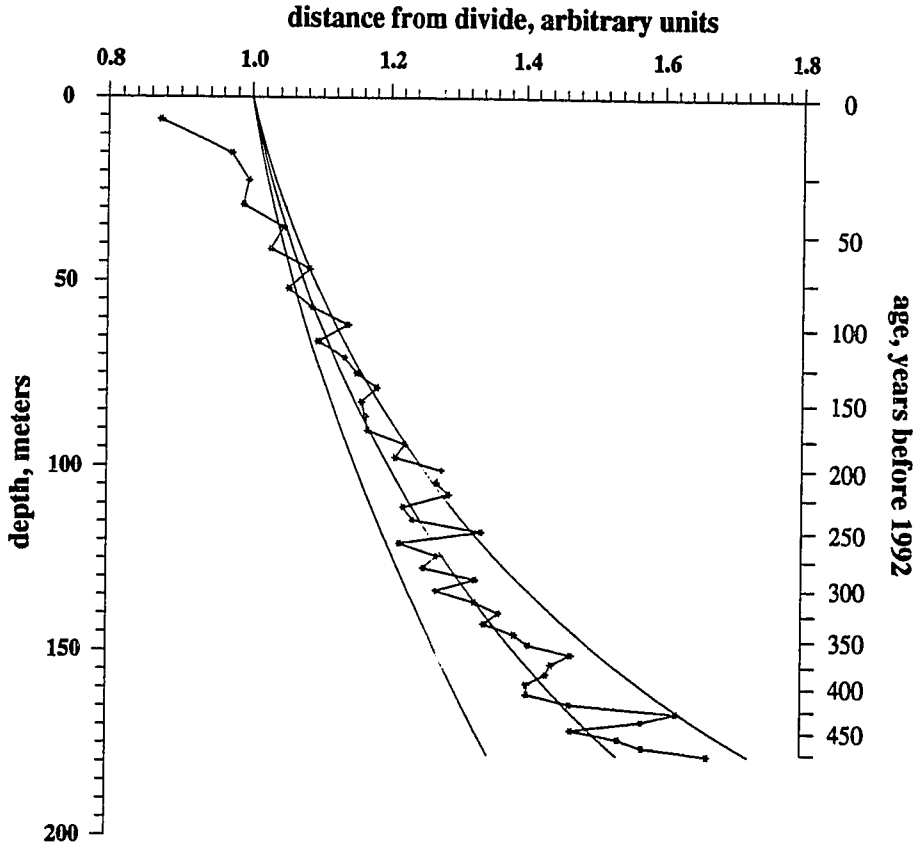

Figure 6.11: A comparison of streamlines determined from streamline parameterization (jagged curve) and vertical velocity information gained from borehole measurements.

defined by equation 6.23 to estimate the past accumulation rate. S_i will be given by equation 6.18 and S_s will be given by equation 6.17 with equation 6.23 substituted for x. When these values are substituted into equation 6.16 the past accumulation rate is found to be

$$A = \rho\hat{w} / \left(\rho_0 - \frac{\dot{\varepsilon}_0}{A_0} \int_0^z \rho dz \right).$$

This is equivalent to equation C.4 ($A \rightarrow \tilde{w}$ and $A_0 \rightarrow w_0$) as one would expect because both equations are based on the assumption that accumulation rate variations occur only on time scales much shorter than an ice sheet's dynamic response time.

In this application of streamline parameterization there is no advantage to estimating the past accumulation rates by the streamline parameterization method over the more conventional treatment discussed in appendix C because within the depths sampled by the shallow ice core, strain effects can be easily modelled. However, in situations where it is more difficult to model ice flow, the streamline parameterization method may be the only method available for estimating past accumulation rates.

6.4.3 - Streamline Analysis of Ice Core Data Coupled With Radar Data

Although over 200 km of radar profiles were collected from the Dyer Plateau Ice Sheet (figure 6.9), only a single 4 km section closely follows a flow-line that crosses an ice summit (figure 6.10). Because the streamline parameterization method requires that horizon depths be known along flow-lines that cross a neutral streamline, only this short 4 km section of radar profile (figure 6.12) appears to be appropriate for streamline parameterization.

The right side of this radar profile (drill site $\leftrightarrow B$) closely follows the direction of altitude gradients (figure 6.10). However, the left side of the radar profile ($A \leftrightarrow$ drill site) moderately deviates from them. This deficiency has been corrected by projecting layer altitudes (surface, internal and bottom) measured along this interval onto a line that more closely follows a flow-line (figure 6.10) by equation D.1. This projection has the effect of stretching horizontal distances along the radar profile to account for the fact that the radar profile does not exactly follow the direction of altitude gradients.

The radius of curvature of surface contours was digitized along the solid dark line shown in figure 6.10 and W/W_0 was calculated as described in appendix D. The digitized radii of curvature and calculated W/W_0 are shown in figure 6.13.

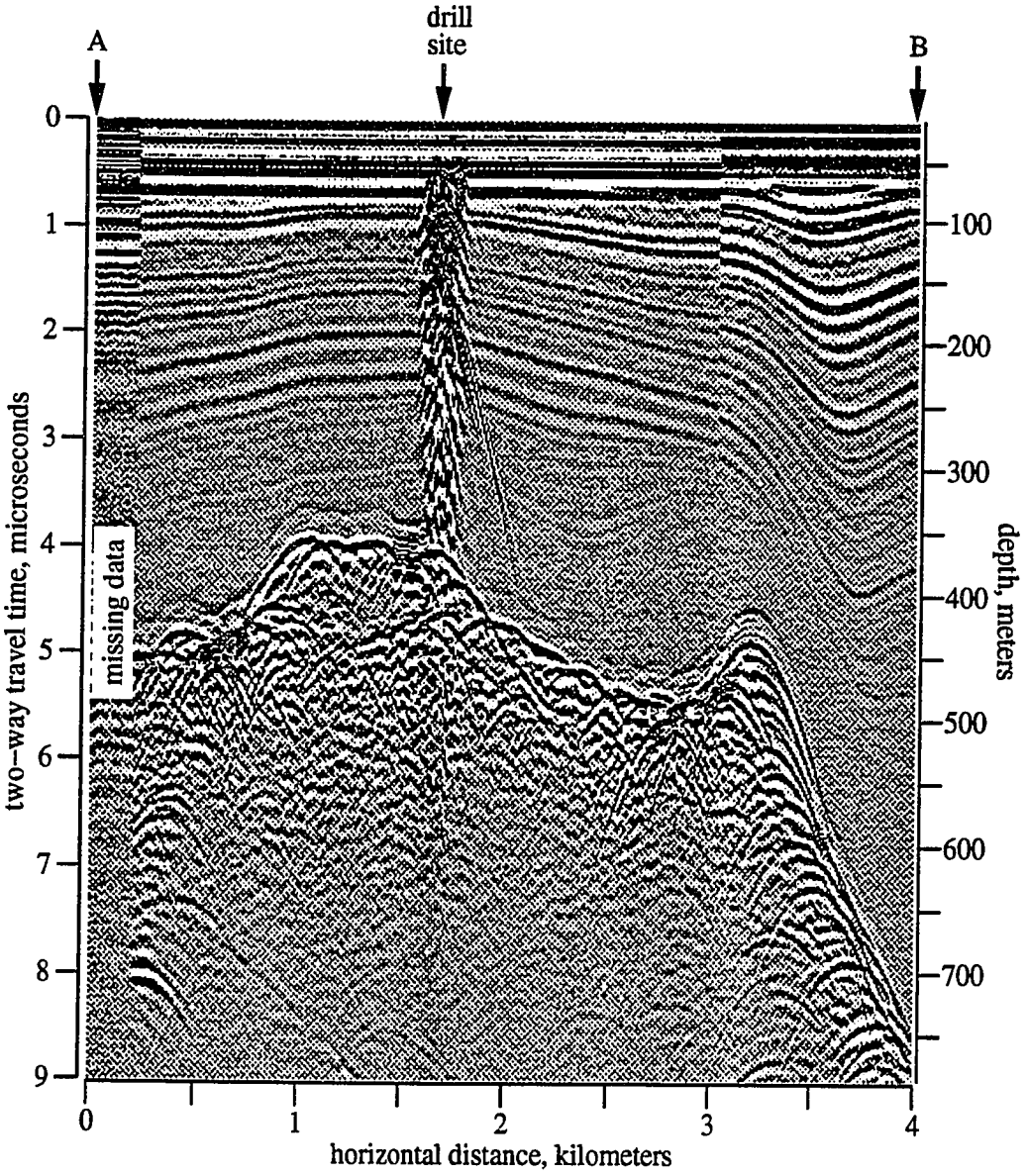

Figure 6.12: RES profile used for streamline parameterization. A, B and 'drill site' are indicated in figure 6.10. The echo from the ice drill is clearly visible. The ice is 365 meters deep beneath the drill site.

The 'picking' program described in § 4.5 was used to digitize six prominent internal reflecting layers. Ice core information was used to establish the ages of the three upper most layers; it was not possible with available data to date the bottom three layers which

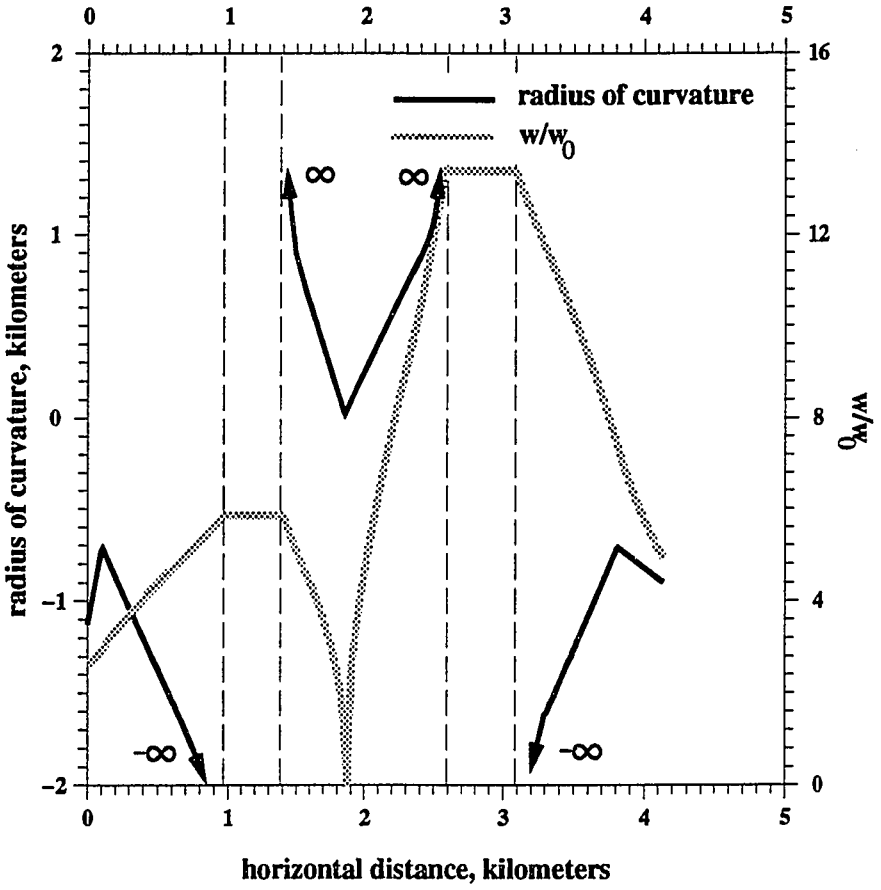

Figure 6.13: Digitized radius of curvature of surface contours (black lines) and lateral spreading factor, W/W_0 (grey lines) used on the radar profile.

were below the deepest ice cores.

The stratigraphically digitized layers are shown in figure 6.14. The first digitized layer is approximately 100 meters deep. Below this depth layers are digitized approximately every 50 meters. Because of the radar transmitter's 0.8 μsecond long air-wave it was not possible to establish radar reflections shallower that about 100 meters.

The inverse vertical age gradient, $\hat{w}$, was established at depths halfway between adjacent measured horizons by

$$\hat{w} = \frac{z_{n+1} - z_n}{T_{n+1} - T_n};$$

z_{n+1} and z_n represent depths of two horizons and T_{n+1} and T_n represent their ages found from the ice cores. Along the surface the vertical age gradients were set equal to the accumulation rates established from surface marker burial rates (§ 5.2.3; figure 5.7).

Densities at the depths halfway between the measured horizons were determined from a piecewise linear approximated density relation discussed above and shown in figure C.2 (page 167).

In order to evaluate the streamline parameterization equation it was necessary to specify a neutral streamline. Due to a lack of knowledge of the ice sheet's absolute motion, the divide crest was selected for the surface location of the neutral streamline and, due to a lack of knowledge of the ice sheets internal motion, the neutral streamline was approximated as a vertical line; these are both standard assumptions.

With the necessary information for the evaluation of streamline parameterization specified, streamlines were calculated; the resulting streamlines are shown in figure 6.14. These streamlines extend to less than half of the total ice thickness because of the shallowness of the ice core information. They do not show any obvious characteristics such as zigzags indicative of non-steady-state flow.

For comparison, streamlines were also calculated from surface motion measurements. This was done by assuming that the horizontal strain-rate is depth independent. With this approximation the horizontal velocity at depth is simply equal to the surface velocity and the vertical velocity at depth is given by equation C.3,

$$w = \frac{\rho_0 w_0}{\rho} - \frac{\dot{\varepsilon}_0}{\rho}\int_0^z \rho dz.$$

The shapes of streamlines were established by numerically tracing particles passing through the specified velocity field. These streamlines are shown in figure 6.14 along with the streamlines found from streamline parameterization.

The streamlines determined from observed surface motions, $\dot{\varepsilon}_0$-streamlines, have

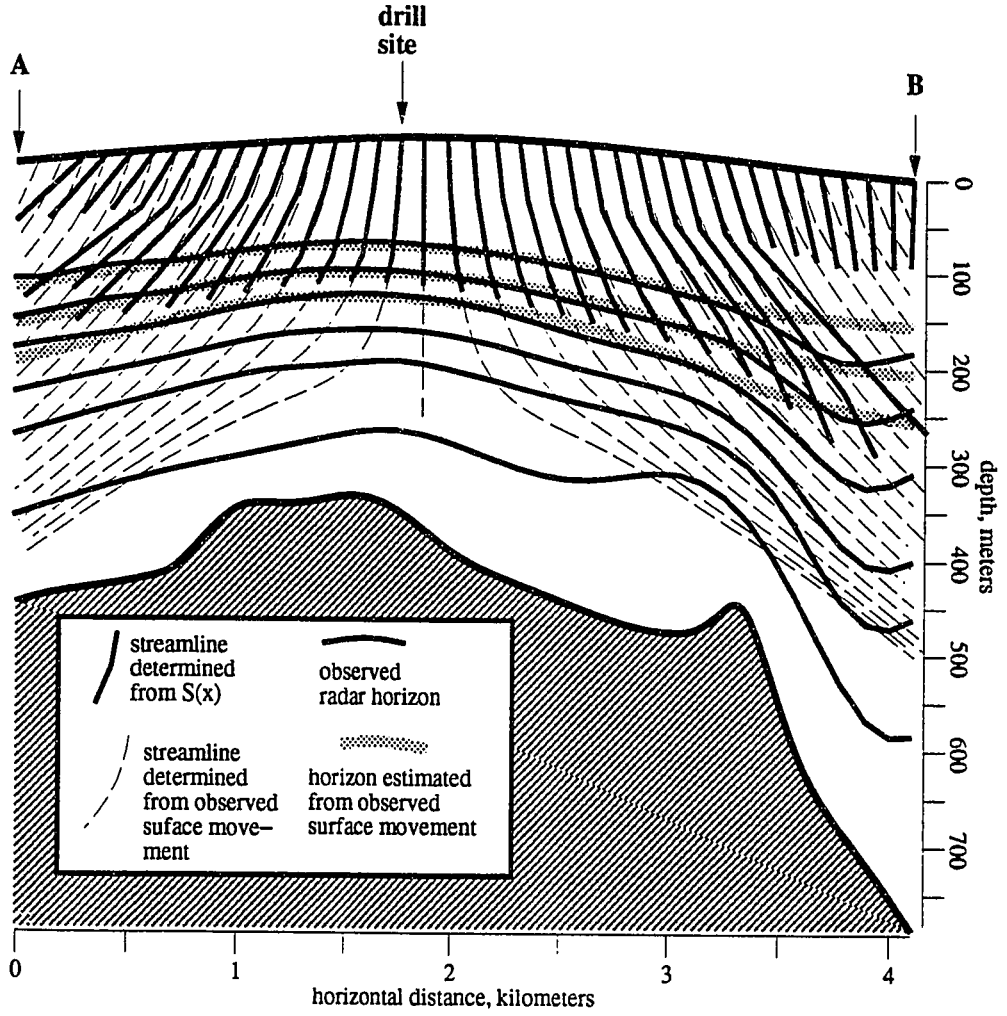

Figure 6.14: Digitized radar profile and deduced streamline and horizons. The dark horizons are digitized reflection horizons and the grey horizons were deduced from surface motions. The dark solid streamlines were deduced from streamline parameterization and the light broken streamlines were deduced from surface motion measurements.

been traced until they stop (center streamline) or they pass out of the stream-sheet. The $\dot{\varepsilon}_0$-streamlines have the physically realistic property of not passing into the ice sheet's bed within the section; if they did, this might indicate basal melting. However, at the left side

of the profile the streamlines almost reach the bed. Additionally, they have the physically unrealistic property of passing through the deepest three horizons more than once on the right side of the section.

By following the ages of particles as they move down the strain-rate streamlines it is possible to generate *synthetic* isochrone horizons that can be compared with observed horizons[3]. This was done for three horizons for ages matching the dated radar horizons (figure 6.14). The synthetic horizons closely follow the radar horizons near the drill site but are significantly shallower than the observed horizons on the right side of the section and significantly deeper than the observed horizons on the left side of the section. This would appear to indicate that on the right side of the profile (east side of the divide) the recent measured accumulation rates were lower than long term past values and on the left side of the profile (west side of the divide) the recent measured accumulation rates were higher than past values. Since the shallowest horizon is 175 years old (this is the same horizon discussed in § 5.2.1), the present measured accumulation rate pattern would then appear to be significantly different from the average accumulation rate pattern over the past 175 years.

The pattern of accumulation rate mismatch can also be seen in a comparison of the streamline parameter streamlines and the strain-rate streamlines close to the surface. As illustrated in figure 6.15, an increase or decrease of the value of accumulation rate, w_0, used at the surface will affect the slopes of the streamline parameterization and strain-rate streamlines close to the surface in opposite senses; parameterization streamline slopes will decrease with an increasing value of accumulation rate, while strain-rate streamline slopes will increase. This is exactly the behavior of the two sets of streamlines shown in figure 6.15. On the left side of the divide parameterization streamlines have lower slopes than the strain-rate streamlines and on the right side of the divide the parameterization streamlines have higher slopes than the strain-rate streamlines.

---

3. This technique was used by Whillans (1976) to analyze the steady-state nature of the West Antarctic Ice Sheet. Whillans determined that internal reflection horizons in central West Antarctica were essentially consistent with horizons deduced from surface velocity and strain-rate measurements.

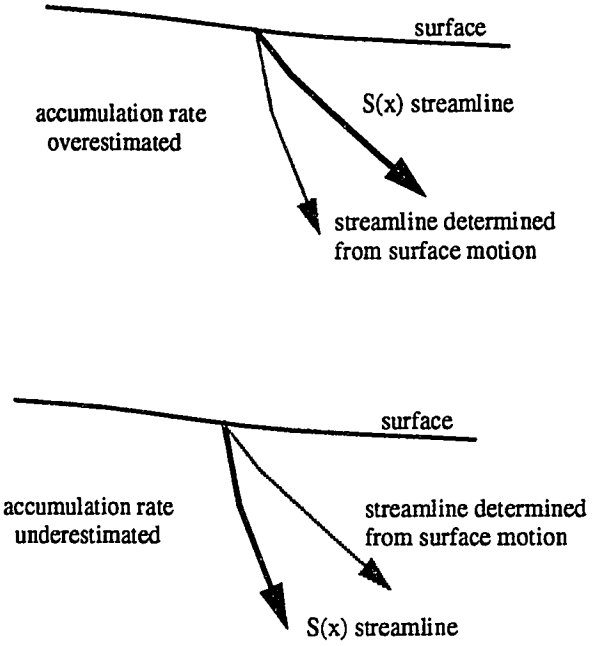

Figure 6.15: A comparison of the effect of over and underestimating the accumulation rate on streamlines deduced from surface motions and streamline parameterization ($S(x)$).

This relationship between streamline slope and accumulation rate is easily understood for the strain-rate streamlines since their slopes near the surface will be equal to the ratio of accumulation rate to horizontal velocity. To see that this is true of the parameterization streamlines one must consider what increasing the accumulation rate does to a streamline's parameter value, S.

For any given horizontal position, X, at the surface the streamline parameter will be

$$S_X = \int_0^X \rho_0 w_0 \frac{W}{W_0} dx'. \tag{6.24}$$

Increasing w_0 will cause S_X to increase. Within a layer in an ice sheet the horizontal coordinate, x, of a streamline is defined by the location at which equation 6.12,

$$\int_0^x \rho \hat{w} \frac{W}{W_0} dx' ,$$

evaluates to the streamline's parameter value. If S_X increases as a result of an increase in w_0, the horizontal position where a streamline originating at X passes through a layer must also increase. As a result, the slope of a streamline passing from the surface (where equation 6.24 is evaluated) to the first internal layer where equation 6.12 is evaluated will increase if w_0 is increased.

The pattern of accumulation rate mismatch also explains why the strain-rate streamlines almost pass into the bed on the left side of the section and why they are so shallow as to pass through horizons twice on the right side of the section. When the accumulation rate is overestimated it causes streamline slopes to be too steep resulting in streamlines running too deep. When the accumulation rate is underestimated it results in streamline slopes that are too shallow and streamlines that are not deep enough.

As mentioned in section 2.1.1 (page 7), past east-west shifts of atmospheric circulation should be detectable in the ice of the Dyer Plateau. One may be tempted to conclude from the streamline analysis that such a shift has taken place; however, the strength of this conclusion seems to be weak. A comparison of figures 6.10 (page 113) and 5.7 (page 78) shows that only six pole burial measurements were used to infer the pattern of accumulation rate along the RES profile used. A comparison of these figures with figure 6.14 (page 121) shows that the streamline mismatch in figure 6.14 is associated with burial measurements from only two poles (the two extreme west-east, left-right, poles) along the RES profile used; the significance of a conclusion based on only two accumulation rate measurements is not clear.

In chapter 5 I have compared 50 accumulation rates from survey pole burial measurements with estimates inferred from a shallow reflection horizon that dates to 1815. Figure 5.12 (page 85) shows the difference between the measured and the estimated accumulation rates plotted against east-west position. If the recent accumulation rate pattern was systematically different from the average over the past ~175 years (1990-1815), one would expect to find structure in this plot. For example, if the recent winds were more easterly than normal, there might be greater accumulation on the sheltered west slopes and more scouring on the exposed east slopes; data points on the left (west) side of the plot

would be generally positive and data points on the right (east) side would be generally negative. No such trend is apparent and therefore the short term (1988-1990) and long term (1815-1990) accumulation rate patterns do not appear to be systematically different.

Because w_0 only determines what streamline parameter values will be on the surface, beneath the surface layer streamlines determined from equation 6.12 will not be influenced by the surface accumulation rate pattern. Because of this, the streamline parameterization method should allow stronger statements to be made about flow than flow modeling methods that are sensitive to the accumulation rate pattern at all depths such as the method used here which is based on observed surface motions.

The analysis of the RES data presented here indicates that internal stratigraphy in the upper half of the Dyer Plateau's ice column is consistent with steady-state flow. Thus, if the flow has changed over the past ~500 years (age at the middle of the ice column), it has not done so in a manner that has left the stratigraphy conspicuously altered. Because ice cores were only collected to a depth of 235 meters, it has not been possible to use the methods developed here to the lower half of the ice column.

The method presented for determining if stratigraphy is consistent with steady-state flow requires a qualitative judgement on whether or not flow deduced from stratigraphy is physically realistic. In the future, this judgement could be made more quantitative by applying a rheological model to the deduced flow in order to determine if it satisfies momentum conservation. An apparent violation of momentum conservation within an ice sheet could then be interpreted as evidence for non-steady-state flow.

The analysis of ice core stratigraphy presented in this chapter and in Appendix C indicates that from 1940 to 1990 the water equivalent accumulation rate has increased from approximately 0.44 to 0.56 meters/year (see figure C.3, page 168). Because of data uncertainty, the long term accumulation rate history before 1940 is more difficult to determine. However, from 1514 to 1940 short term accumulation rate variations comparable to the 1940 to 1990 increase are observed.

Chapter 7

Conclusions

The body of work presented in this thesis is divided in two parts: (1) methods for defining ice sheet stratigraphy (chapters 3-4) and (2) the interpretation of internal layer stratigraphy (chapters 5-6). In this chapter I summarize some of the highlights of these two parts and briefly discuss some future extensions and applications.

7.1 - Methods for Defining Ice Sheet Stratigraphy

A unique, powerful, impulse transmitter was designed and constructed for RES. The transmitter was combined with antennas, an amplifier, a digital oscilloscope and a computer. The RES system has yielded scientifically useful data. On the Dyer Plateau continuous bed echoes have been recorded to depths of over 1000 meters and continuous internal reflection horizons have been recorded to depths over 500 meters. The instrumentation has already benefited other research projects. It has been successfully operated in other parts of Antarctica (Beethoven Peninsula, Taylor Dome), Alaska (Blackrapids Glacier) and the Canadian Arctic (Agassiz Icefield). On Taylor Dome continuous internal layering was detected near bed rock at depths of over 1000 meters.

I have performed a migration analysis on the Dyer Plateau RES data in order to convert observed two-way radio wave travel times into ice depths. From this analysis I have found two useful simplifications: (1) By using only the apexes of reflection hyperbolas when estimating depth, ice depth can be estimated essentially as accurately as by formal migration and (2) internal reflection horizons are so nearly level that they do not require migration. These simplifications will apply to most ice sheets, although not necessarily everywhere. When analyzing data from other ice sheets, future analysts would benefit from determining if they apply before turning to formal migration.

7.2 - Interpretation of Internal Layer Stratigraphy

In this thesis I have assumed that internal RES reflection horizons originate from past ice surfaces and consequently they reveal the geometry of an ice sheet's age structure.

Using this assumption and measured RES horizons that have had their ages determined by comparison to ice core measurements, I have attempted to understand ice flow in the region studied. I have broken this problem into two parts. In the first part I have used a shallow reflector to deduce the spatial pattern of snow accumulation and in the second part I have used deeper horizons to determine ice flow at depth.

Accumulation Patterns and Shallow Reflection Horizons

I have found that in the vicinity of an ice divide on the Dyer Plateau, the depth of a bright near surface reflection horizon correlates well with the present spatial pattern of snow accumulation measured from the burial of survey poles. The reflection horizon was dated from ice core stratigraphy and appears to be associated with the eruption of Tambora (1815 AD). It is likely that this horizon is observable over much of Antarctica and may allow the spatial pattern of accumulation to be rapidly measured over large areas. Previously, the spatial pattern of accumulation had to be determined from shallow snow stratigraphy measurements or from the burial rates of surface markers. The first method is labor intensive because it requires digging snow-pits or drilling ice cores. The second method is time consuming because field sites must be revisited and is potentially inaccurate because of inter-annual accumulation rate variability and snow surface roughness.

In order to directly correlate the depth of shallow marker horizons with the measured accumulation rate I have developed a simple theory that takes into account densification and horizontal divergence. The theory requires knowledge of the density depth profile and the horizontal rate of divergence. If the horizontal rate of divergence is not known, the ratio of the layer's depth to total ice thickness can be substituted.

On the Dyer Plateau, the accumulation rate varies spatially by more than 50%. In general, accumulation rates are highest in areas of concave surface slope. During snow fall and drifting sheltered lee slope areas, defined by the wind direction, should receive higher accumulations. Consequently, the accumulation rate pattern should have changed if the prevailing winds have changed and a record of this would have then been left in the stratigraphy. In the area studied, internal layering shows no conspicuous features indicating that this has occurred. Additionally, the recently measured pattern of accumulation rate

is not systematically different from the accumulation rate pattern deduced from the depth of the 1815 horizon. This indicates that the recent pattern of prevailing winds is not significantly different from the average pattern over the past ~175 years (1815-1990). The history of the accumulation rate pattern could be investigated in greater detail by comparing the stratigraphy of ice cores taken from several locations around the ice divide.

Internal Ice Flow and Reflection Horizons

Towards understanding ice stratigraphy I have developed a mathematical framework for describing the relationship between age and velocity in a steady-state flow. I have shown that under the following conditions velocity can be deduced from a steady-state age field:

> **One-dimensional flow:** Velocity can be deduced from an age field but the deduced velocity may not be consistent with mass conservation (continuity).
>
> **Two-dimensional flow:** Velocity can be uniquely deduced from an age field if one streamline that crosses all isochrones is specified.
>
> **Three-dimensional flow:** Velocity cannot be uniquely deduced from an age field. However, if the horizontal direction of flow does not vary with depth, a unique velocity field can be deduced within any *stream-sheet* generated from a *flow-line* if one streamline that crosses all isochrones is specified within that stream-sheet (see page 91 for terminology).

I have found a simple equation that parameterizes streamlines. The parameterization is based on continuity and an assumption of steady-state flow and it involves an integral that is evaluated along isochrones. The integral can be easily applied to RES internal reflection horizons that have been dated. If the ice sheet has been in steady-state, contours of constant parameterization value will coincide with streamlines.

Features in the shapes of streamlines deduced from the parameterization that show physically implausible characteristics may indicate that flow has not been steady-state. I have outlined a procedure to determine if such implausible streamlines require non-steady-state flow or if they can be more easily explained by high frequency accumulation

rate variations that have not significantly effected ice flow. This should be especially useful in the interpretation of ice core records because if an ice sheet's flow and geometry have undergone significant changes, the interpretation of ice core records taken from it will be more difficult. It should also be useful in the interpretation of RES profiles from regions such as the West Antarctic ice sheet where there is interest in flow history (Alley and Whillans, 1991).

The streamline parameterization method does not require force balance calculations. This is advantageous when ice rheology or boundary conditions are not well known. Another advantage of the method is that it does not require an input accumulation rate pattern. If accumulation rate variations are taken into account, in principal the method can be used to determine the strain-rate at depth.

The streamline parameterization requires that RES profiles follow the horizontal direction of flow. RES was not performed with this particular goal. Consequently, of the 200 km of profiles recorded, only one 4 km section was easily usable for streamline parameterization. Other profiles require difficult and uncertain interpolation between grid lines. Ice core stratigraphy measurements were used to date some of the horizons from this section and with this information streamlines were calculated. The deduced streamlines show no conspicuous features indicative of non-steady-state ice flow. However, the ice cores used to date the reflection horizons penetrated to only half of the ice sheet's thickness. Therefore, the ice sheet may still harbor unobserved evidence of a non-steady-state past on longer time scales.

In the region investigated, surface motion measurements show that horizontal direction of flow is well correlated with the direction of surface slope. Therefore, even though surface motion measurements were not available at the time, it would have been possible to have recorded RES profiles that followed the direction of flow by following surface slopes. This should be kept in mind in the future; square grid profile strategies may not always be the best approach.

The method that I have used for determining if measured stratigraphy is consistent with steady-state flow requires a qualitative judgement on whether or not deduced flow is

physically realistic. This step could, in the future, be made more quantitative by applying a rheological model to the deduced flow in order to determine if the deduced flow satisfies momentum conservation within an ice sheet.

The streamline parameterization has also been directly applied to stratigraphic age versus depth measured in an ice core to deduce the shape of streamlines locally in the immediate neighborhood of an ice summit. With an assumption that the flow field of the ice sheet has been steady-state, the shape of these deduced streamlines indicate that over the past 50 years (1940 to 1992) accumulation rate has increased. A separate analysis derived from ice core stratigraphy that directly takes into account horizontal divergence and densification arrives at the same conclusion (Appendix C). The streamline analysis, and the analysis presented in Appendix C, indicates that there were significant accumulation rate variations before 1940. The history prior to 1940 is more difficult to interpret due to data uncertainty but it is consistent with a trend of increasing accumulation rate over the past 200 years. As discussed above, recent accumulation rate measurements made from survey poles are consistent with rates inferred from a RES horizon of 175 years age. This indicates that if the measurements made from the survey poles follow the 50 year increasing trend, the average accumulation rate from 1815 to 1940 must have been greater than the value at 1940. The trend of increasing accumulation rate over the past 50 years agrees with snow fall observations and inferred accumulation rates from other locations around the Antarctic Peninsula (pages 9-10). This trend may be related to a general warming trend that has resulted in increased humidity and a subsequent increased precipitation.

Perhaps the most significant aspect of this thesis is that I have shown that ice stratigraphy can be analyzed directly to infer ice motion. In doing this I have bypassed the oft travelled path of ice flow modelling. Although this new approach does not necessarily make ice flow modelling obsolete, it does, at very least, offer a new way to think about ice flow.

Bibliography

Ackley, S. F. and T. E. Keliher, 1979. Ice sheet internal radio-echo reflections and associated physical property changes with depth. *J. Geophys. Res.*, **84**(B10), 5675-5680.

Alley, R. B. and I. M. Whillans, 1991. Changes in the West Antarctic Ice Sheet. *Science*, **254**, 959-963.

Annan, A. P., 1973. Radio interferometry depth sounding: part I - theoretical discussion. *J. Geophys. Res.*, **38**(3), 557-580.

Annan, A. P., 1973. Radio interferometry depth sounding: part II - experimental results. *J. Geophys. Res.*, **38**(3), 581-599.

Bogorodsky, V. V., Bentely, C. R., Gudmandsen, P. E., 1985. *Radioglaciology*, D. Reidel Publishing Co., Dordrecht, etc.

Berry, M. V., 1975. Theory of radio echoes from glacier beds. *J. Glaciol.*, **15**(73), 65-74.

Bindschadler, R. A. and P. L. Vornberger, 1990. A VHRR imagery reveals antarctic ice dynamic. *Eos Trans. Amer. Geophys. Union*, **71**(23), 741-742.

Bindschadler, R. A. and T. A. Scambos, 1991. Satellite-image-derived velocity field of an antarctic ice stream. *Science*, **252**, 242-246.

Björnsson, H, 1986. Surface and bedrock topography of ice caps in Iceland, mapped by radio echo-sounding, *Ann. Glaciol.*, **8**, 11-18.

Bond, G., W. Broecker, S. Johnsen, J. McManus, L. Labeyrie, J. Jouzel, G. Bonani, 1993. Correlations between climate records from North Atlantic sediments and Greenland ice. *Nature*, **365**(6442), 143-147.

Brown, C. S., L. A. Rasmussen, M. F. Meier, 1986. *Bed topography inferred from airborne radio-echo sounding of Columbia Glacier, Alaska* (U.S. Geological Survey Professional Paper 1258-G), U. S. Gov. Printing Office, Washington.

Comlinear Corporation, 1991. *1991 Databook, Amplifiers and Data Conversion.* Comlinear Corporation, Fort Collins, CO.

Dansgaard, W., S. J. Johnsen, 1969b. A flow model and a time scale for the ice core from Camp Century, Greenland. *J. Glaciol.*, **8**, 215-223.

Doake, C. S. M., 1975. Glacier sliding measured by a radio-echo technique. *J. Glaciol.*, **15**(73), 89-91.

Doake, C. S. M., 1982. State of balance of the ice sheet in the Antarctic Peninsula. *Ann. Glaciol.*, **3**, 77-82.

Doake, C. S. M., D. G. Vaughan, 1991. Rapid disintegration of the Wordie Ice Shelf in response to atmospheric warming. *Nature,* **350**(6316), 328-330.

Drewry D. J., E. M. Morris, 1992. The response of large ice sheets to climatic change. *Phil. Trans. R. Soc. Lond. B,* **338**, 235-242.

Evans, S., 1965. Dielectric properties of ice and snow - A review. *J. Glaciol.*, **5**(42), 773-92

Fitzgerald, W. J. J. G. Paren, 1975. The dielectric properties of Antarctic Ice. *J. Glaciol.*, **15**(73), 39-48

Fletcher, N. H., 1970. *The Chemical Physics of Ice.* Cambridge University Press, London.

French, W. S., 1974. Two-dimension and three dimensional migration of model-experiment reflection profiles. *Geophysics,* **39**(3), 265-277.

French, W. S., 1975. Computer migration of oblique reflection profiles. *Geophysics,* **40**(6), 961-980.

Glen J. W., J. G. Paren, 1975. The electrical properties of snow and ice. *J. Glaciol.*, **15**(73), 15-37.

Grant, F. A., 1958. Use of complex conductivity in the representation of dielectric phenomena. *J. Appl. Phys.*, **29**(1), 76-80.

Gudmandsen, P., 1975. Layer echoes in polar ice sheets. *J. Glaciol.*, **15**(73), 95-101.

Gudmandsen, P., S. Overgaard, 1978. Establishment of time horizons in polar ice sheets by means of radio echo sounding. Electromagnetics Inst., Technical University of Denmark, Lyngby, Report P312

Hagedoorn, J. G., 1954, A process of seismic reflection interpretation, *Geophys. Prospecting.* **2**(2), 85-127.

Hagen, J. O., A. Sætrang, 1991. Radio-echo sounding of sub-polar glaciers with low-frequency radar. *Polar Res.*, **9**(1), 99-107.

Hammer, C. U., 1980, Acidity of polar ice cores in relation to absolute dating, past volcanism, and radio-echoes. *J. Glaciol.*, **25**(93), 359-372.

Hammer, C. U., H. B. Clausen, W. Dansgaard, 1980. Greenland ice sheet evidence of post-glacial volcanism and its climatic impact. *Nature.* **288**(5788), 230-235.

Hammond, W. R., K. F. Sprenke, 1990. A PC-based portable ice-radar receiver. *J. Glaciol.*, **36**(123), 255-277.

Harrison, C. H., 1973. Radio echo sounding of horizontal layers in ice. *J. Glaciol.*, **12**(66), 383-397.

Hayt, W. H. jr., G. H. Neudeck, 1976. *Electronic circuit analysis and design.* Houghton Mifflin Company, Boston, etc.

Hayt, W. H. jr., 1974. *Engineering Electromagnetics. Third edition.* McGraw-Hill Book Company, London, etc.

Herron, M. M., C. C. jr. Langway, 1980. Firn densification: an empirical model. *J. Glaciol.*, **25**(93), 373-385.

Hodge, S. M., D. L. Wright, J. A. Bradley, R. W. Jacobel, N. Skou, B. Vaughn, 1990. Determination of the surface and bed topography in central Greenland. *J. Glaciol.*, **36**(122), 17-30.

Hobbs, P. V., 1974. *Ice Physics.* Clarendon Press, Oxford.

Hughes, T. J., 1973, Is the West Antarctic Ice Sheet disintegrating? *J. Geophys. Res.*, **78**(33), 7884-7910.

Imbrie, J., K. P. Imbrie, 1979. *Ice Ages, Solving The Mystery.* Harvard University Press, Cambridge, etc.

Jacobel. R. W., S. M. Hodge, D. L. Wright, 1991. Studies of internal layering and bedrock topography on ice stream C, West Antarctica. *Ant. J. U. S.*, **25**(5), 82-85.

Jezek, K. C., 1983. Measurements of radar wave speeds in polar glaciers using a down-hole radar target technique. *Cold Regions Sci. Tech.*, **8**, 199-208.

Jóhannesson, T., C. F. Raymond, E.D. Waddington, 1989. A simple method for determining the response time of glaciers. *Glacier Fluctuations and Climate Change. Symposium Proceedings.* Amsterdam, Institute for Meteorology and Oceanography, 343-352.

Jóhannesson, T., C. F. Raymond, E.D. Waddington, 1989. Time-scale for adjustment of glaciers to changes in mass balance. *J. Glaciol.*, **35**(121), 355-369.

LaMarche, V. C. jr., Hirschboeck, K. K., 1984. Frost rings in trees as records of major volcanic eruptions. *Nature,* **307**, 121-126.

Legrand, M., R. J. Delmas, 1987. A 220-year continuous record of volcanic H_2SO_4 in the Antarctic ice sheet. *Nature,* **327**(25), 671-676.

Lehman, S., 1993. Ice sheets, wayward winds and sea change. *Nature,* **365**(6442), 108-109.

MacAyeal, D. R., 1992. Irregular oscillations of the West Antarctic ice sheet. *Nature,* **359**, 29-32.

Mantripp, D. R., J. K. Ridley, C. G. Rapley, 1992. Antarctic map from the Geosat geodetic mission. *Eos Trans. Amer. Geophys. Union,* **73**(51), 545 & 549.

Millar, D. H. M., 1981. Radio-echo layering in polar ice sheets and past volcanic activity. *Nature,* **292**, 441-443

Millar, D. H. M., 1981. *Radio-echo layering in polar ice sheets.* Unpublished Ph. D. thesis, University of Cambridge.

Moore, J. C., 1988. Dielectric variability of a 130 m antarctic ice core: implications for radar sounding. *Ann. Glaciol.,* **11**, 95-99.

Moore, J. C., 1991. A continuous 770-year record of volcanic activity from East Antarctica. *J. Geophys. Res.,* **96**(D9), 17,353-17,359.

Moore, J. C., J. G. Paren, 1987. A new technique for dielectric logging of Antarctic ice cores. *J. de Physique.,* **48**, C1/155-C1/160.

Moore, J. C., J. G. Paren, R. Mulvaney, 1990. Chemical evidence in polar ice cores from dielectric profiling. *Ann. Glaciol.,* **14**, 195-198.

Moore, J. C., J. G. Paren, H. Oerter, 1992. Sea salt dependent electrical conduction in polar ice. *J. Geophys. Res.,* **97**(B13), 19,803-19,812.

Moore, J. C., R. Mulvaney, J. G. Paren, 1989. Dielectric stratigraphy of ice: a new technique for determining total ionic concentrations in polar ice cores. *Geophys. Res. Lett.,* **16**(10), 1177-1180.

Moore, J. C., E. W. Wolff, H. B. Clausen, C. U. Hammer, 1992. The chemical basis for the electrical stratigraphy of ice. *J. Geophys. Res.,* **97**(B2), 1887-96.

Morris, E. M., 1991. Antarctic ice studies in global climatic change: a comment. In Harris, C. and Stonehouse, B. eds. *Antarctic and Global Climatic Change.* Belhaven Press, 51-62.

Mulvaney, R., E. W. Wolff, K. Oates, 1988. Sulfuric acid at grain boundaries in Antarctic ice. *Nature,* **331**(6153), 247-249.

Nishio, F., H. Ohmae, 1985. Internal radio-echo reflections of polar snow covers in relation to acidic layers and density fluctuations. *Ann. Glaciol.,* **6**, 289-290.

Nye, J. F., 1963. Correction factor for accumulation measured by the thickness of the annual layers in an ice sheet, *J. Glaciol.*, **4**(36), 785.

Oswald, G. K. A., 1975. Investigation of sub-ice bedrock characteristics by radio-echo sounding, *J. Glaciol.*, **15**(73), 75.

Paren, J. G., G. de Q. Robin, 1975. Internal reflections in polar ice sheets. *J. Glaciol.*, **14**(71), 251-259.

Paterson, W. S. B., 1981. *The Physics of Glaciers, second edition.* Pergamon Press, Oxford, etc.

Picciotto, E. E., S. Wilgain, 1963. Fission products in Antarctic snow, a reference level for measuring accumulation. *J. Geophys. Res.*, **68**, 5965-5972.

Raju, G., W. Xin, R. K. Moore, 1990. Design, development, field observations, and preliminary results of the coherent Antarctic radar depth sounder (CARDS) of the University of Kansas, U. S. A. *J. Glaciol.*, **36**(123), 247-254.

Ramo, S., J. R. Whinnery, T. V. Duzer, 1965. *Fields and Waves in Communication Electronics.* John Wiley & Sons, Inc., New York, etc.

Rasmussen, L. A., 1986. Refraction correction for radio echo-sounding of ice overlain by firn. *J. Glaciol.*, **32**(111), 192-194.

Raymond, C. F., 1983. Deformation in the vicinity of ice divides. *J. Glaciol.*, **29**(103), 357-373.

Raymond. C. F., B. R. Weertman, 1991. Glaciological studies of Dyer Plateau, Antarctic Peninsula. *Ant. J. U. S.*, **25**(5), 90-92.

Raymond. C. F., B. R. Weertman, R. Mulvaney, D. A. Peel, 1992. Glaciological observations on Antarctic Peninsula. *Ant. J. U. S.*, **27**(5), 38-40.

Reeh, N., 1989. The age depth profile in the upper part of a steady-state ice sheet. *J. Glaciol.*, **35**(121), 406-417.

Rees, W. G., R. E. Donovan 1992. Refraction correction for radio-echo sounding of large ice masses. *J. Glaciol.*, **38**(129), 302-308.

Reynolds, J. M., J. G. Paren 1984. Electrical resistivity of ice from the Antarctic Peninsula, Antarctica. *J. Glaciol.*, **30**(106), 289-295.

Reynolds, J. M., 1985. Dielectric behavior of firn and ice from the Antarctic Peninsula, Antarctica. *J. Glaciol.*, **31**(109), 253-262.

Robin, G. de Q., S. Evans, J. T. Bailey, 1969. Interpretation of radio echo sounding in polar ice sheets. *Philosophical Transactions of the Royal Society of London.* Ser A **265**(1166), 437-505.

Robin, G. de Q., 1975. Velocity of radio waves in ice by means of a bore-hole interferometric technique. *J. Glaciol.,* **15**(73), 151-157.

Robin, G. de Q., D. H. M. Millar, 1982.Flow of ice sheets in the vicinity of subglacial peaks. *Ann. Glaciol.,* **3**, 290-294.

Robinson, E. A., S. Treitel, 1980. *Geophysical signal analysis.*Prentice-Hall, Inc., Englewood Cliffs, N. J.

Sætrang A. C., W. Bjørn, Results from the radio echo-sounding on parts of the Jostedalsbreen ice cap, Normay. *Ann. Glaciol.,* **8**, 1986.

Sanson, J., 1989. Antarctic surface temperature time series. *J. Climate 2,* 1164-71.

Smith B. M. E., S. Evans, 1972. Radio echo sounding: absorption and scattering by water inclusion and ice lenses. *J. Glaciol.,* **11**(61), 133-146.

Waddington. E. D., D. L. Morse, M. J. Balise, J. Firestone, 1991. Glacier geophysical studies for an ice core site at "Taylor Dome". *Ant. J. U. S.,* **26**(5).

Waddington. E. D., D. A. Fisher, R. M. Koerner, W. S. B. Paterson, Flow near an ice divide: analysis problems and data requirements. *Ann. Glaciol.,* **8**, 1986.

Watts, R. D., A. W. England., R. S. Vickers, M. F. Meier, 1975. Radio-echo sounding on South Cascade Glacier, Washington, using a long wave-length mono-pulse source. *J. Glaciol.* **15**(73), 459-461.

Watts, R. D., A. W. England., 1976. Radio-echo sounding of temperate glaciers: ice properties and sounder design criteria. *J. Glaciol.* **17**(75), 39-48.

Watts, R. D., D. L. Wright., 1981. Systems for measuring thickness of temperate and polar ice from the ground or from the air. *J. Glaciol.* **27**(97), 459-469.

Weertman, J., 1961. Stability of ice-age ice sheets. *J. Geophys. Res.,* **66**(11), 3783-3792.

Weertman, J., 1964a. Rate of growth or shrinkage of nonequilibrium ice sheets. *J. Glaciol.,* **5**, 145-158.

Weertman, J., 1974. Stability of the junction of an ice sheet and an ice shelf. *J. Glaciol.,* **13**, 3-11.

West, J. C., Demarest, K. R. 1987. The radiation characteristic of an arbitrary antenna positioned on a polar ice sheet. *Geophysics,* **52**(12), 1689-1696.

Whillans, I. M., 1976. Radio-echo layers and the recent stability of the West Antarctic ice sheet. *Nature,* **264**(5582), 152-55.

Whillans, I. M., 1977. The equation of continuity and its application to the ice sheet near "Byrd" Station, Antarctica. *J. Glaciol.,* **18**(80), 359-71.

Whillans, I. M., 1979. Ice flow along the Byrd Station strain network, Antarctica. *J. Glaciol.,* **24**(90), 15-26.

Whillans, I. M., S. J. Johnsen, 1983. Longitudinal variations in glacial flow: theory and test using data from the Byrd Station strain network, Antarctica. *J. Glaciol.,* **29**(101), 78-97.

Whillans, I. M., K. C. Jezek, 1987. Folding in the Greenland Ice Sheet. *J. Geophys. Res.,* **92**(B1), 485-493.

Whillans, I. M., R. B. Alley, 1991. Changes in the West Antarctic Ice Sheet. *Science,* **254**, 959-963.

Wu, T. T., W. P. King, 1965. The cylindrical antenna with nonreflecting resistive loading. *IEEE Trans. Antennas Propagat.,* **AP-13**, 369-373.

Wright, D. L., J. F. Prewitt, 1975. Radiating dipole antenna with tapered impedance loading. *IEEE Trans. Antennas Propagat.,* **AP-23**(6), 811-814.

Wright, D. L., S. M. Hodge, J. A. Bradley, T. P. Grover, R. W. Jacobel, 1990. A digital low-frequency, surface profiling ice-radar system. *J. Glaciol.,* **36**(122), 112-121.

Wolff. E. W., J. G. Paren, 1984. A two-phase model of electrical conduction in polar ice sheets. *J. Geophys. Res.,* **89**(B11), 9433-9438.

Zwally, H. J., A. C. Brenner, J. A. Major, R. A. Bindschadler, J. G. Marsh, 1989. Growth of Greenland Ice Sheet: measurement. *Science,* **246**, 1587-89.

Zwally, H. J., 1989. Growth of Greenland Ice Sheet: interpretation. *Science,* **246**, 1589-91.

Zwally, H. J., J. C. Comiso, C. L. Parkinson, W. J. Campbell, F. D. Carsey, P. Gloersen, 1983. *Antarctic sea ice, 1973-1976: satellite passive*-microwave observations (Report SP-459). Washington, NASA, Scientific and Technical Information Branch.

Appendix A

Calculation of Reflection Coefficients

Many types of dielectric interfaces can exist within an ice sheet and for each type there are likely to be several factors which will determine the observed strength of a radio wave reflection from it. In this appendix I explore what I believe to be some common dielectric interfaces within many glaciers and ice sheets. A fairly accessible treatment of much of the material presented here is given by Hyatt (1958) and Ramo (1965).

A.1 - Wave Equation

It is appropriate to begin by examining the electromagnetic wave equation for a dielectric material. I start by deriving the wave equation for a perfect dielectric from three of Maxwell's equations:

$$\nabla \times \vec{E} = -i\omega\mu\vec{H} \tag{A.1}$$

$$\nabla \times \vec{H} = i\omega\varepsilon\vec{E} \tag{A.2}$$

$$\nabla \bullet \varepsilon\vec{E} = \rho_c. \tag{A.3}$$

When the curl of equation A.1 is taken and equation A.2 is substituted for the curl of $\vec{H}$ it results in

$$\nabla \times \nabla \times \vec{E} = -i\omega\mu\,(i\omega\varepsilon\vec{E}) \tag{A.4}$$

which simplifies to

$$\nabla \times \nabla \times \vec{E} = \omega^2\mu\varepsilon\vec{E}. \tag{A.5}$$

The left side of A.5 expands to

$$\nabla \times \nabla \times \vec{E} = \nabla\,(\nabla \bullet \vec{E}) - \nabla^2\vec{E}.$$

In the absence of a net space charge the charge density, ρ_c, will be zero allowing equation A.5 to be simplified to

$$\nabla^2 \vec{E} = -\omega^2 \mu\varepsilon \vec{E}. \tag{A.6}$$

Equation A.6 is the wave equation for a perfect dielectric and it has the solution

$$\vec{E} = \vec{E}_0 e^{ix\omega\sqrt{\mu\varepsilon}}.$$

The quantity $\gamma \equiv \omega\sqrt{\mu\varepsilon}$, known as the propagation constant, describes how a wave's phase changes with position. The quantity $v \equiv (\mu\varepsilon)^{-1/2}$ is the velocity of wave propagation.For an imperfect dielectric equation A.2 becomes

$$\begin{aligned} \nabla \times \vec{H} &= i\omega\vec{E} + \sigma\vec{E} \\ &= i\omega\left(\varepsilon + \frac{\sigma}{i\omega}\right)\vec{E}. \end{aligned} \tag{A.7}$$

The quantity inside of the brackets, $\varepsilon^* \equiv \varepsilon + \sigma/i\omega$, is defined as the complex permittivity of the dielectric. In general $\sigma/i\omega$ can take into account any process which is attenuating and does not have to correspond to an actual physical current. It is useful to define the loss tangent, $\tan\delta \equiv \sigma/\omega\varepsilon$, which is the ratio of the effective conduction current to the effective displacement current. In the frequency band used in RES the loss tangent of ice is off the order of 10^{-3}. For small values of loss tangent the propagation constant is

$$\gamma \equiv i\frac{\sigma}{2}\sqrt{\frac{\mu}{\varepsilon}} + \omega\sqrt{\mu\varepsilon}\left(1 + \frac{1}{8}\tan^2\delta\right).$$

$1/(Im\gamma)$ is the characteristic distance of attenuation. For polar ice at RES frequencies $\varepsilon \equiv 3.2\varepsilon_0$ and $\sigma \sim 10\mu S/m$. This yields a characteristic distance of approximately one kilometer. The thickest ice sheets are of this same scale which means that it is possible to sound their depths. When the propagation constant is complex the wave velocity is given by $\omega/(Re\gamma)$. Since $\tan^2\delta/8 \ll 1$ the wave velocity depends primarily on the real part of the permittivity.

A.2 - Reflection from of a Dielectric Boundary at any Angle of Incidence

Figure A.1 illustrates an electromagnetic wave being reflected and transmitted from a dielectric interface. The interface is defined as the boundary between two half spaces of different intrinsic impedances η_1 and η_2. Intrinsic impedance is defined as the electric to

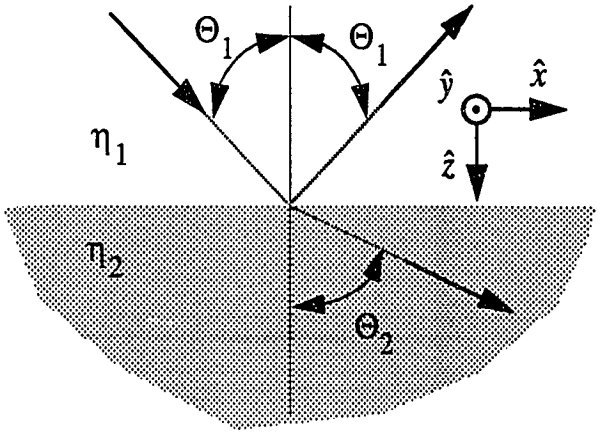

Figure A.1: The nomenclature used in describing a wave reflecting off of a dielectric interface.

magnetic field ratio ($\eta \equiv E/H$) of an electromagnetic wave. It is easily shown that $\eta = \sqrt{\mu/\varepsilon}$. In SI units the intrinsic impedance has units of ohms and that of free space is approximately 377Ω.

Polarization 1: $\vec{E}$ in plane of incidence

The electromagnetic continuity conditions of the interface are

$$E_{x+} + E_{x-} = E_{x2} \tag{A.8}$$

and

$$H_{y+} + H_{y-} = H_{y2}. \tag{A.9}$$

where the + and - symbols indicate down and up going waves in region 1 and the 2 indicates fields in region 2. The wave impedance in terms of the tangential field components is

$$Z_{t1} = \frac{E_{x+}}{H_{y+}} = -\frac{E_{x-}}{H_{y-}} \tag{A.10}$$

in region 1 and

$$Z_{t2} = \frac{E_{x2}}{H_{y2}} \tag{A.11}$$

in region 2. Combining equations A.9, A.10 and A.11 gives

$$\frac{E_{x+}}{Z_{t1}} - \frac{E_{x-}}{Z_{t1}} = \frac{E_{x2}}{Z_{t2}}. \tag{A.12}$$

Combining equation A.8 and A.12 gives the reflection coefficient

$$r = \frac{E_{x-}}{E_{x+}} = \frac{Z_{t2} - Z_{t1}}{Z_{t2} + Z_{t1}}. \tag{A.13}$$

However the tangential wave impedances are also given by

$$Z_{t2} = \eta_2 \cos\Theta_2 \tag{A.14}$$

and

$$Z_{t1} = \eta_1 \cos\Theta_1. \tag{A.15}$$

From Snell's law it can be shown that

$$\cos\Theta_2 = \sqrt{1 - (v_2/v_1)^2 \sin^2\Theta_1} \tag{A.16}$$

where v_1 and v_2 are the respective wave velocities. If the magnetic permeability, μ, is the same in the two regions then

$$(v_2/v_1)^2 = \varepsilon_1/\varepsilon_2 \tag{A.17}$$

and

$$\eta_1/\eta_2 = \sqrt{\varepsilon_2/\varepsilon_1} \tag{A.18}$$

When equations A.14 through A.18 are substituted into equation A.13 the reflection coefficient, r, is found to be

$$r = \frac{\sqrt{1 - \frac{\varepsilon_1}{\varepsilon_2}\sin^2\Theta_1} - \sqrt{\frac{\varepsilon_2}{\varepsilon_1}}\cos\Theta_1}{\sqrt{1 - \frac{\varepsilon_1}{\varepsilon_2}\sin^2\Theta_1} + \sqrt{\frac{\varepsilon_2}{\varepsilon_1}}\cos\Theta_1}. \tag{A.19}$$

Figure A.2 (dashed lines) shows the power reflection coefficient ($R \equiv |r|^2$) for a 2% range of dielectric contrasts for the range of angles 0° to 45°. Close to 45° the reflection coefficient drops to zero. This angle is named for its discoverer, Sir David Brewster, and is

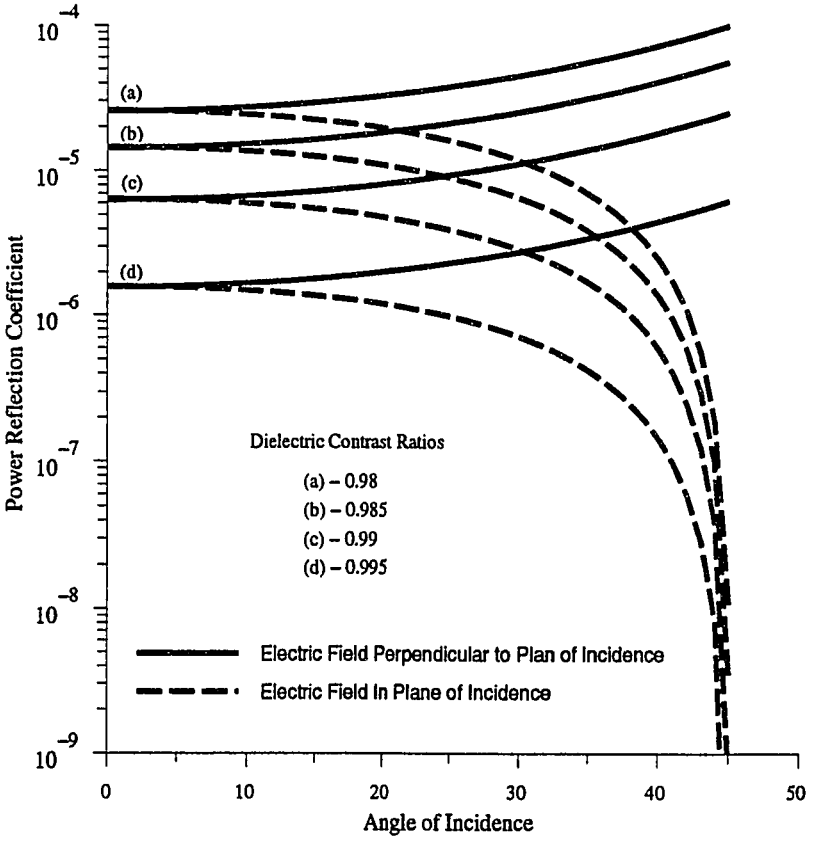

Figure A.2: Power reflection coefficients for a 2% range of dielectric contrast and a 0 to 45 degree range of angle of incidence for the two principal polarizations. For the polarization of the electric field in the plane of incidence there is an angle at which the reflection coefficient is zero (Brewster angle).

given by

$$\Theta_B = \tan^{-1}\sqrt{\varepsilon_2/\varepsilon_1}.$$

As a practical example consider a reflection from a quartz rich bed rock. The relative permittivity of quartz is approximately 5.0 and that of ice is approximately 3.0. This gives a Brewster angle of 52°. Typical ice-ice interfaces will have a dielectric contrast ratios which are close to unity and will thus have Brewster angles which are close to 45°.

Polarization 2: $\vec{E}$ normal to plane of incidence

The arguments leading to the derivation of the reflection coefficient for the case of $\vec{E}$ normal to the plane of incidence are identical to those of $\vec{E}$ in plane of incidence up until the point at which the tangential wave impedances are specified as a function of angle and intrinsic impedance. At this point equations A.14 and A.15 must be replaced by

$$Z_{t2} = \eta_2 / \sqrt{1 - (v_2/v_1)^2 \sin^2\Theta_1} \tag{A.20}$$

and

$$Z_{t1} = \eta_1 \sec\Theta_1. \tag{A.21}$$

The reflection coefficient is then found to be

$$r = \frac{(1 - (\varepsilon_1/\varepsilon_2)^2 \sin^2\Theta_1)^{-1/2} - \sqrt{\varepsilon_2/\varepsilon_1}\sec\Theta_1}{(1 - (\varepsilon_1/\varepsilon_2)^2 \sin^2\Theta_1)^{-1/2} + \sqrt{\varepsilon_2/\varepsilon_1}\sec\Theta_1}. \tag{A.22}$$

Figure A.2 (solid lines) shows how this appears for a 2% range in dielectric contrast. The power reflection coefficient slowly increases with angle.

A.3 - Reflection Coefficient of a Thin Layer

I will now derive the reflection coefficient of a thin dielectric slab imbedded in a host medium of different dielectric constant. Such a slab might exist in an ice sheet if, for example, one season's thickness of ice at depth has different dielectric constant than normal.

First consider a sinusoidal wave impinging on a dielectric interface as shown in figure A.3. The magnetic field is taken to run in the $\hat{y}$ direction and the electric field is taken to run in the $\hat{x}$ direction. On the $z < 0$ side of the interface the electric field will be composed of the sum of the forward and backward travelling wave components. Their sum is given by

$$E(z<0) = e^{i\omega t}\left[E_+ e^{-iz/v} + E_- e^{+iz/v}\right] \tag{A.23}$$

where plus and minus signs indicate the direction of motion and t, ω, and v represent time, angular frequency and wave velocity respectively. Omitting the time dependance

part of the solution, $e^{i\omega t}$, the magnetic field is given by

$$H = \frac{1}{\eta_1}\left[E_+ e^{-iz/v} - E_- e^{+iz/v}\right]. \tag{A.24}$$

Requiring continuity in the electric and magnetic fields across the interface and following derivations similar to those found in sections A.2 and A.3 it can be shown that the electric field ratio on the left hand side of the interface is given by

$$\frac{E_-}{E_+} \equiv r = \frac{\eta_2 - \eta_1}{\eta_2 + \eta_1} \tag{A.25}$$

At this point it is possible to find the effective wave impedance at some distance l in front of an interface. This is the ratio of the electric and magnetic fields and includes both incident and reflected components. It is found by dividing equation A.23 by A.24 and then substituting A.25. This gives

$$\eta_i \equiv \eta_1\left[\frac{e^{i\beta l} + re^{-i\beta l}}{e^{i\beta l} - re^{-i\beta l}}\right]. \tag{A.26}$$

The i subscript denotes that this is the effective impedance of the interface and $\beta \equiv \omega/v$, where v is the velocity of propagation. When equation A.25 is substituted into A.26 it gives

$$\eta_i = \eta_1\left[\frac{\eta_2 \cos\beta l + i\eta_1 \sin\beta l}{\eta_1 \cos\beta l + i\eta_2 \sin\beta l}\right]. \tag{A.27}$$

At the point $z = -l$ we now introduce a second dielectric interface:

$$\eta_0 \quad \Big| \quad \eta_1 \quad \Big| \quad \eta_2$$

$$z = -l \qquad z = 0$$

The reflection coefficient of the two interfaces will be given by

$$r = \frac{\eta_i - \eta_0}{\eta_i + \eta_0} \tag{A.28}$$

from equation A.25.

We are interested in a thin slab wedged between two half-spaces of equal dielectric constant. This requires that $\eta_2 = \eta_0$ and $l \ll \lambda$ where λ is the wavelength. The intrinsic impedance just right of (behind) the first interface will now be approximately

$$\eta_i = \eta_1 \left[\frac{\eta_0 + i\eta_1 \beta l}{\eta_1 + i\eta_0 \beta l} \right].$$

When this is substituted into A.28 it gives

$$r = \frac{i\beta l (\eta_1^2 - \eta_0^2)}{2\eta_1\eta_2 + i\beta l (\eta_1^2 + \eta_0^2)}. \tag{A.29}$$

This can be evaluated for the power reflection coefficient which is found to be

$$R = \frac{\theta^2 (\eta_1^2 - \eta_0^2)^2}{4\eta_1\eta_2 + \theta^2 (\eta_1^2 + \eta_0^2)^2} \tag{A.30}$$

where $\theta \equiv \beta l$. For a thin layer

$$4\eta_1\eta_2 \gg \theta^2 (\eta_1^2 + \eta_0^2)^2.$$

This allows A.30 to be simplified to

$$R = \frac{\theta^2}{4} \left(\frac{\Delta\varepsilon}{\varepsilon_0} \right)^2 \tag{A.31}$$

where $\Delta\varepsilon$ is the difference in permittivity between the host material and the layer.

Reflection Due to a Conductivity Change:

If the low frequency conductivity of the thin layer is different than that of the host material then the complex permittivity, $\varepsilon^* \equiv \varepsilon_\infty + \sigma/i\omega$, of the layer will be different by the amount $\Delta\varepsilon = \Delta\sigma/\omega$ (see section 2.3.3 for an explanation of ε_∞). When this is substituted into equation A.31 the power reflection coefficient is found to be

$$R = \left(\frac{l\Delta\sigma}{v\varepsilon_\infty} \right)^2. \tag{A.32}$$

It is some what surprising that this is not a function of the frequency of the radio wave.

As a useful example consider a layer which is 10 centimeters thick and has a conductivity which is $10\mu S/m$ different than the host material. This is a situation which might commonly occur within actual ice bodies. This would result in a power reflection coefficient of

$$R = \left(\frac{l\Delta\sigma}{v\varepsilon_\infty}\right)^2 = \left(\frac{(0.1m)\ (10\mu S/m)}{(167m/\mu s)\ (3.0\times 8.85\times 10^{-12}C^2N^{-1}m^{-2})}\right)^2 = 5\times 10^{-8} = -72dB.$$

Reflection Due to a Density Change:

Ackley and Keliher (1979) show that the permittivity of ice as a function of density, D, is given by

$$\varepsilon = \varepsilon_{ice}\left[1+3\left(\frac{D_{ice}-D}{D_{ice}}\right)\left(\frac{\varepsilon_0-\varepsilon_{ice}}{2\varepsilon_{ice}+\varepsilon_0}\right)\right]$$

where ε_{ice} is the permittivity of solid ice and ε_0 is the permittivity of free space.

If the thin layer in question has a different density than the host material then it will have a corresponding difference of permittivity which is given by

$$\Delta\varepsilon = 3\varepsilon_{ice}\left(\frac{D_1-D_0}{D_{ice}}\right)\left(\frac{\varepsilon_0-\varepsilon_{ice}}{2\varepsilon_{ice}+\varepsilon_0}\right)$$

where D_0 and D_1 are the densities of host and the layer respectively. Substituting this into equation A.31 gives a reflection coefficient of

$$R = \left(\frac{9}{7}\frac{\omega l}{v}\frac{(D_1-D_0)}{D_{ice}}\right)^2 \qquad \text{(A.33)}$$

if the permittivity of ice is taken to be exactly three times that of free space. Notice that unlike the reflection coefficient due to a conductivity variation, equation A.32, the reflection coefficient due to a density variation is frequency dependent and increases as the frequency squared.

For example the power reflection coefficient at 10 MHz for a layer 10 centimeters thick and has a density 1% different than the host material, which is a reasonably large

variation beneath the densification layer, is about 4×10^{-8} $(-74dB)$.

Reflection From a Film of Water:

Because water molecules are more free to rotate the permittivity of water is much higher than that of ice ($\varepsilon_w/\varepsilon_0 \cong 80$, $\varepsilon_{ice}/\varepsilon_0 \cong 3$) at RES frequencies. The velocity of wave propagation in water is approximately $33m/\mu s$. When this velocity and these primitivities are inserted into equation A.31 the power reflection coefficient for a 1 millimeter thick film of water is found to be 6×10^{-4} $(-32dB)$ at a frequency of 10 MHz. This is more than four orders of magnitude larger than the power reflection coefficients found above! and shows that if liquid water is present inside an ice body it should act as a strong scatterer regardless of its electrical conductivity.

Appendix B

Circuit Design of MOSFET Transmitter

In this appendix I present detailed circuit diagrams of the MOSFET transmitter discussed in chapter 3. Component values and part numbers are listed at the end of the this appendix.

In figure B.1 I break the transmitter circuit into five sections. The logic circuit section is further broken down into six subsections as shown in figure B.2. The ±15volt circuit used was commercially produced and its circuit diagram is not shown here.

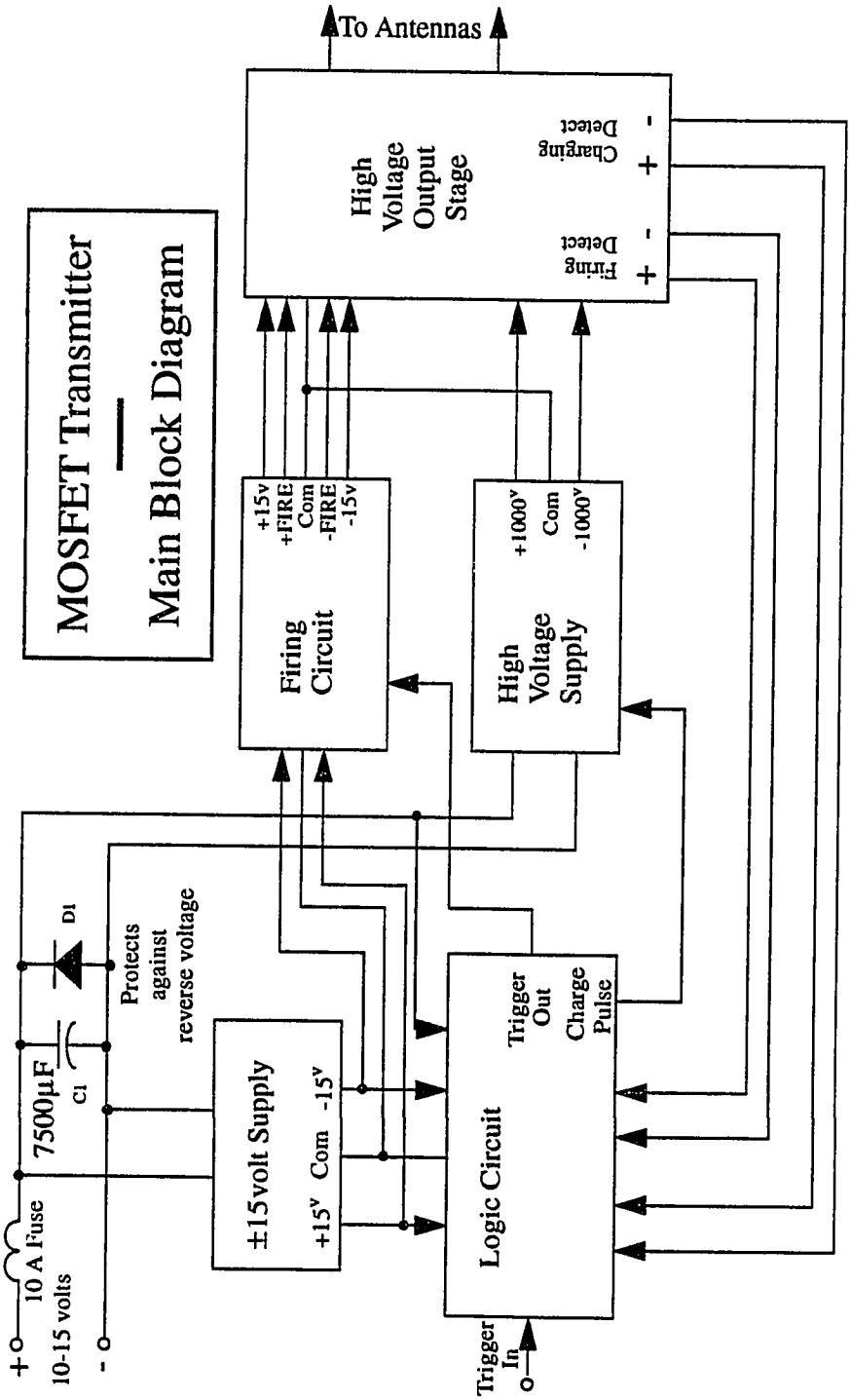

Figure B.1: Block diagram of MOSFET transmitter.

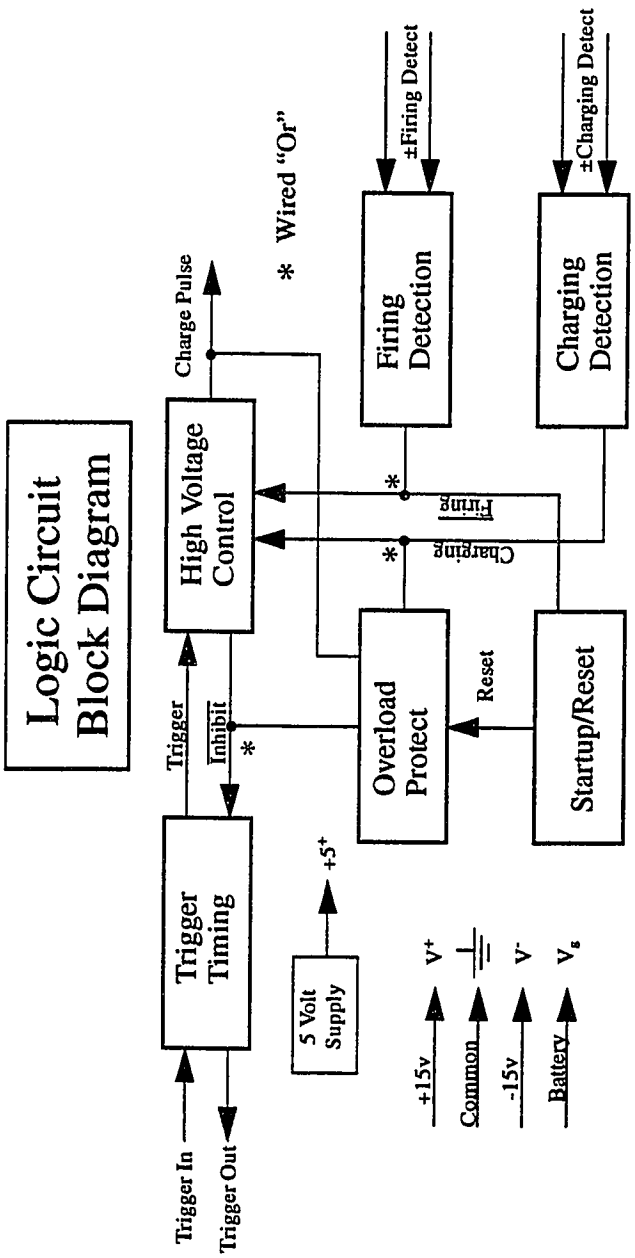

Figure B.2: Block diagram of the transmitter's logic circuit.

Logic Circuit: Trigger Timing

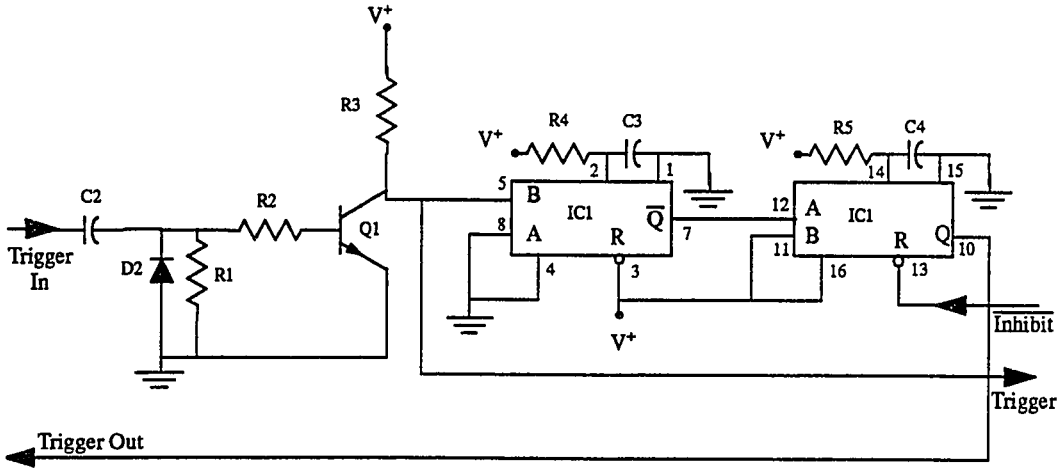

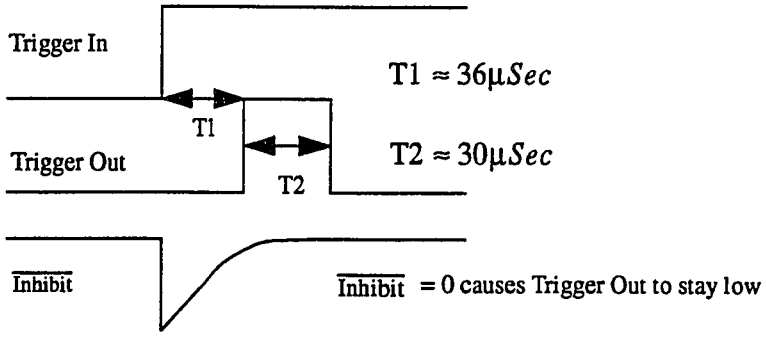

Figure B.3: Trigger timing subsection of logic circuit. The "Trigger Out" line toggles approximately 36μseconds after the "Trigger In" line swings high. During this time interval the output capacitors (C21 and C22) are charged. When the "Trigger Out" line swings high, it causes the firing circuit to switch the output MOSFETs (Q16-Q19).

Logic Circuit: High Voltage Control

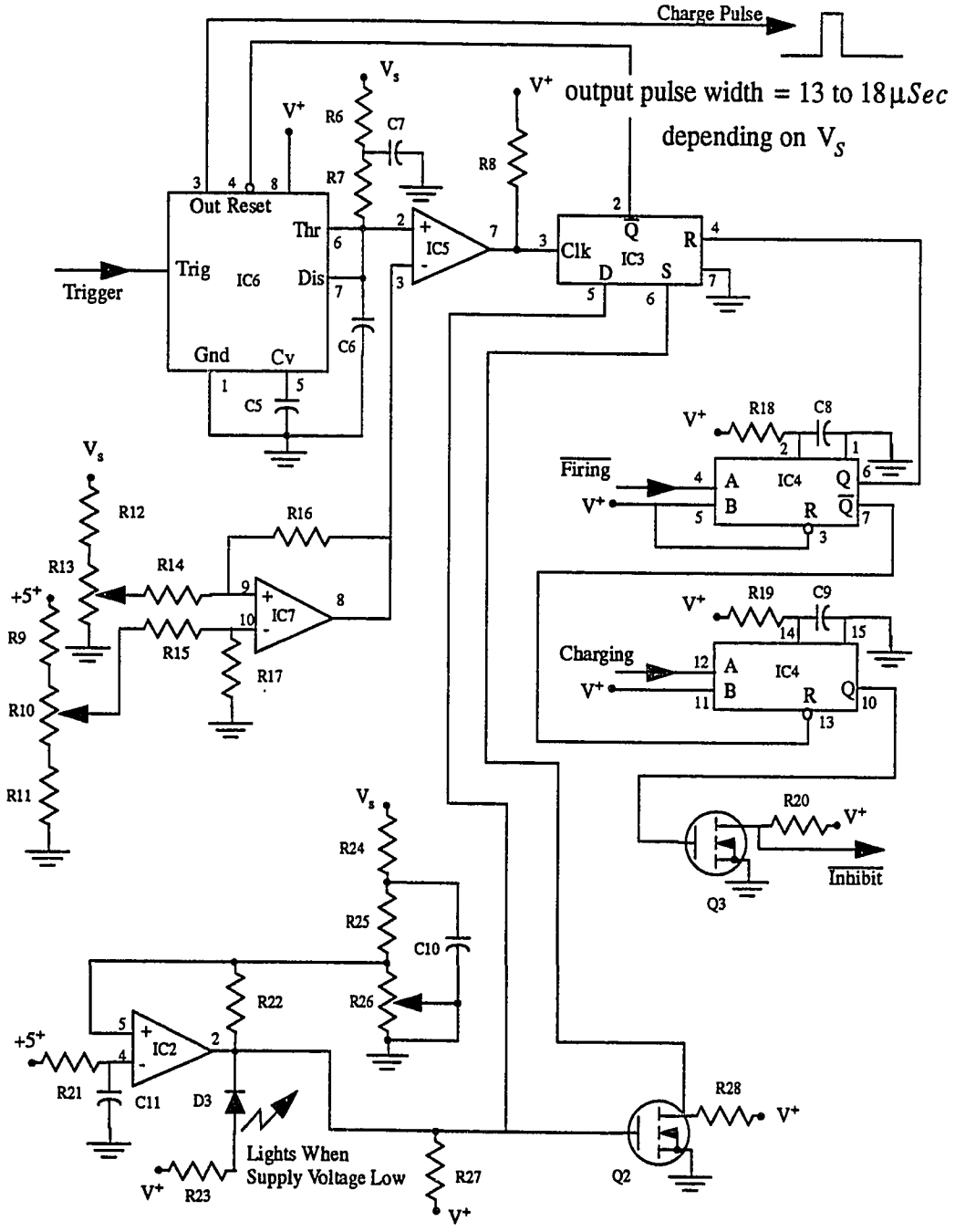

Figure B.4: High voltage control subsection of logic circuit. This circuit

pulses the high voltage transformer (see figure B.11).

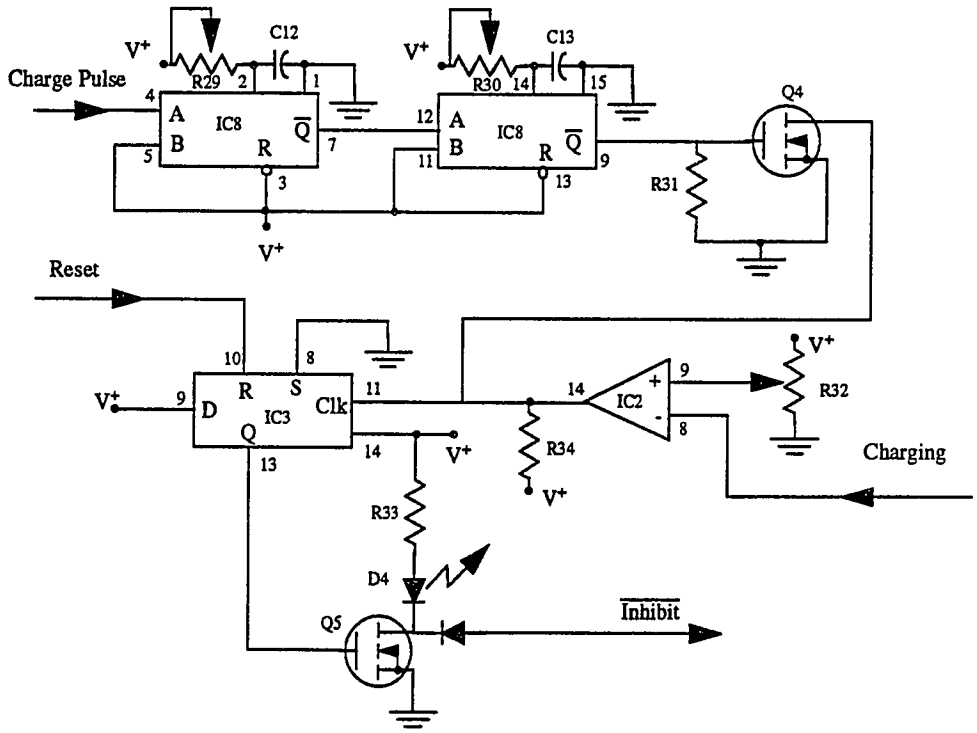

Figure B.5: Overload protect subsection of logic circuit. This circuit prevents the transmitter from firing if a short is place across the transmitter output.

Logic Circuit: Firing Detection

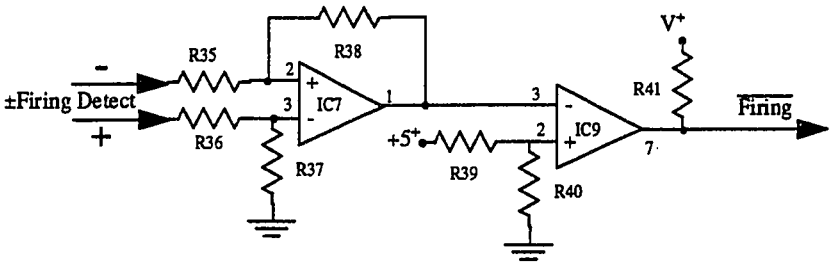

Figure B.6: Firing detection subsection of logic circuit. This circuit directly detects the firing of the transmitter

Logic Circuit: Charging Detection

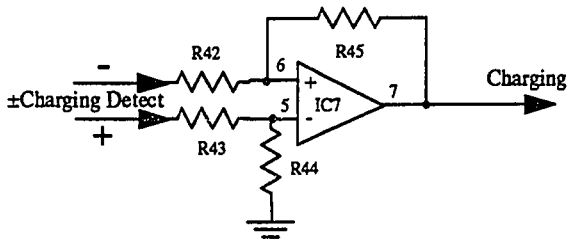

Figure B.7: Charging detection subsection of the logic circuit. This circuit directly detects the charging of the output capacitors

Logic Circuit: Startup/Reset

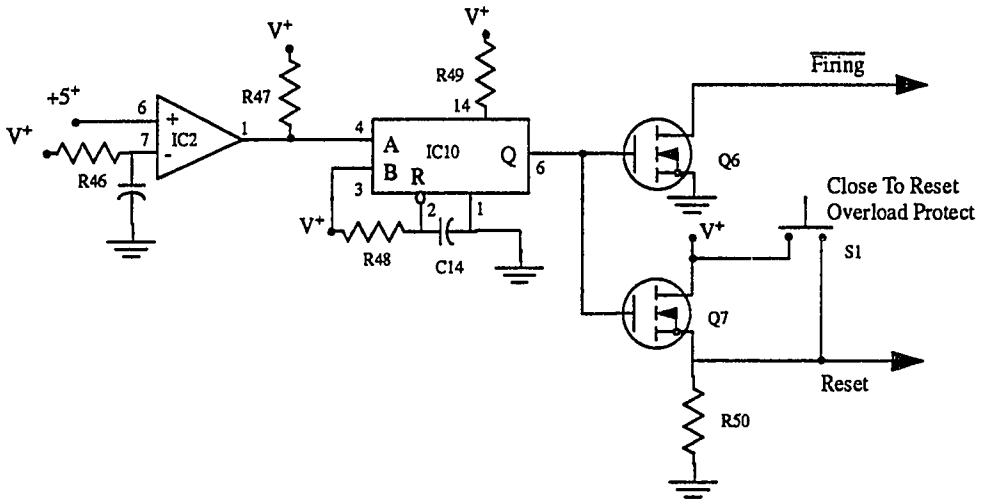

Figure B.8: Startup/reset subsection of logic circuit. This toggles the firing and reset lines approximately one second after the transmitter has been turned on. This sets the logic circuit in a state in which it can be fired. If the overload detect subsection detects that the transmitter has been shorted, closing switch S1 will return the logic circuit to a state in which it can be fired.

Firing Circuit

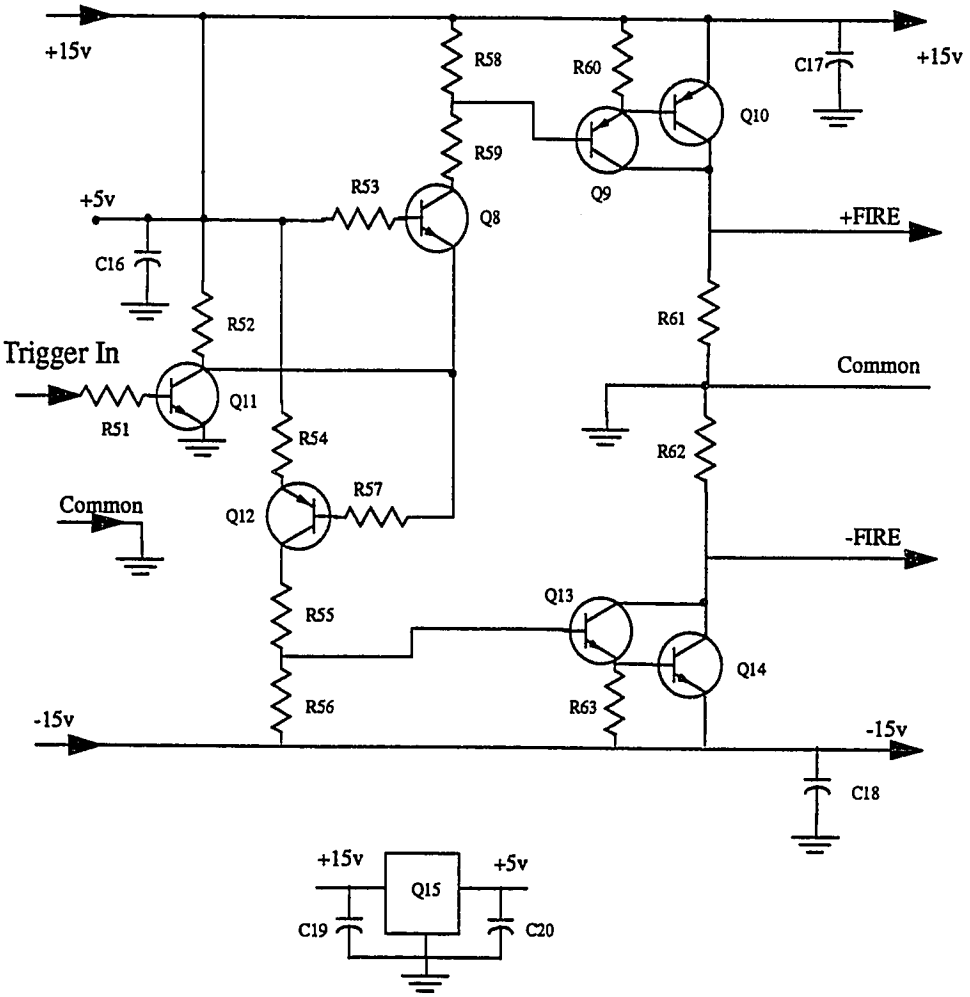

Figure B.9: Transmitter firing circuit. When the voltage on the "Trigger in" line rises the voltage in the "+FIRE" and "-FIRE" lines simultaneously go to +15 volts and -15volts respectively. This causes the output MOSFETs to switch.

High Voltage Output Stage

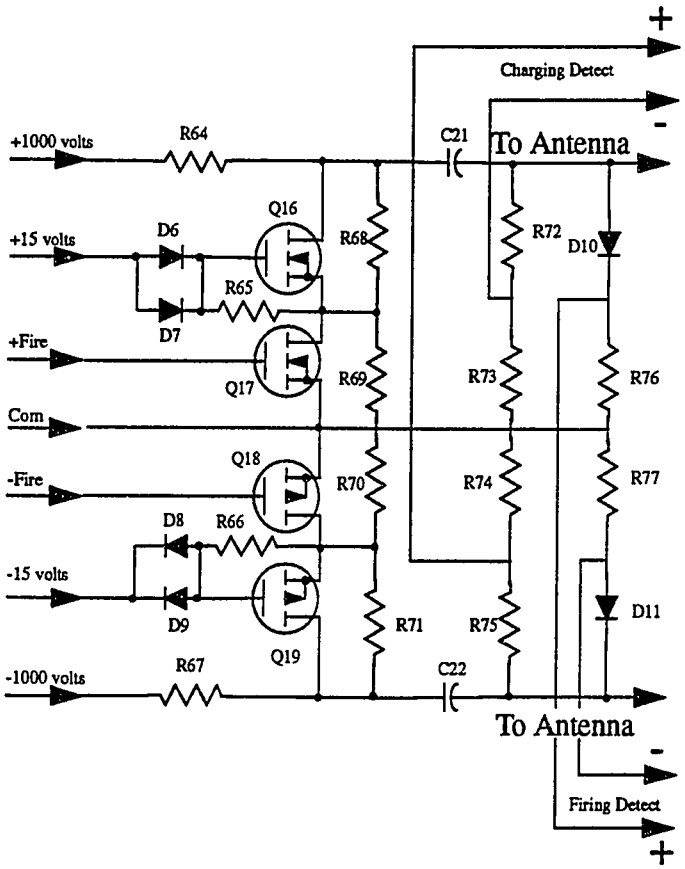

Figure B.10: Transmitter high voltage output stage. When the "+FIRE" and "-FIRE" lines go to +15 and -15 volts MOSFETs Q16-Q19 switch causing an abrupt change in voltage to occur on the lines labeled "To Antenna". See section 3.4.2 for a more detail discussion.

High Voltage Supply

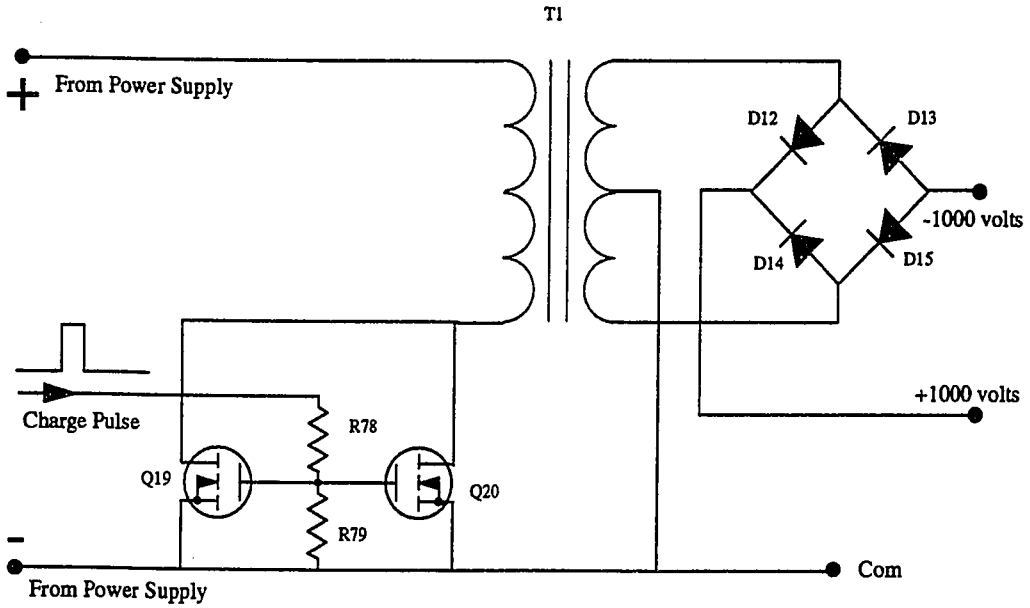

Figure B.11: Transmitter high voltage supply circuit. When the "charge pulse" line is pulsed it causes MOSFETs Q19 and Q20 to momentarily switch. This causes a current pulse to pass through transformer T1 which in turn causes a high voltage pulse to be generated at the transformers output side. This high voltage pulse is then sent to the output capacitors via the rectifier bridge of diodes D12-D15 and the charging resistors R64 and R67.

Table of Resistor Values (all values are in Ohms)

#	Value	#	Value	#	Value	#	Value	#	Value
R1	1k	R2	100	R3	2.2k	R4	56k	R5	47k
R6	105	R7	6.8k	R8	5.6k	R9	1k	R10	2k
R11	1k	R12	1k	R13	5k	R14	12k 1%	R15	12k 1%
R16	12k 1%	R17	12k 1%	R18	12k	R19	39k	R20	1k
R21	1.5M	R22	51k	R23	1k	R24	1k	R25	10k
R26	20k	R27	12k	R28	6.8k	R29	20k	R30	20k
R31	5k	R32	20k	R33	1k	R34	10k	R35	12k 1%
R36	12k 1%	R37	12k 1%	R38	12k 1%	R39	27k	R40	1k
R41	10k	R42	15k 1%	R43	15k 1%	R44	50k 1%	R45	50k 1%
R46	1M	R47	10k	R48	100k	R49	9.1k	R50	1k
R51	1k	R52	1k	R53	15	R54	120	R55	270
R56	270	R57	100	R58	270	R59	270	R60	47
R61	220 ½w	R62	220 ½w	R63	47	R64	1k 25w	R65	2.2k ½w
R66	2.2k ½w	R67	1k25 w	R68	4.7M 2w	R69	4.7M 2w	R70	4.7M 2w
R71	4.7M2 w	R72	1k25 w	R73	2.7 ½w	R74	2.7 ½w	R75	1k 25w
R76	3.3 ½w	R77	3.3 ½w	R78	100 ½w	R79	1k ½w		

Table of Capacitor Values

#	Value	#	Value	#	Value	#	Value	#	Value
C1	7500uf	C2	100pf	C3	1nf	C4	1nf	C5	0.1uf
C6	10nf	C7	330uf	C8	470pf	C9	1nf	C10	82uf
C11	0.2uf	C12	470pf	C13	470pf	C14	1uf	C15	1uf
C16	15uf	C17	15uf	C18	15uf	C19	0.33uf	C20	0.01uf
C21	5nf-2kv	C22	5nf-2kv						

Table of Integrated Circuits, Transistors, Diodes etc.

#	Value	#	Value	#	Value	#	Value	#	Value
IC1	MC-14528	IC2	LM339	IC3	4013	IC4	MC-14528	IC5	LM211
IC6	LM555	IC7	TL084	IC8	MC-14528	IC9	4013	IC10	MC-14528
Q1	2N7000	Q2	2N7000	Q3	2N7000	Q4	2N7000	Q5	2N7000
Q6	2N7000	Q7	2N7000	Q8	2N3904	Q9	2N3906	Q10	MJE172
Q11	2N3904	Q12	2N3906	Q13	2N3904	Q14	MJE182	Q15	MC7805
Q16	VN035-0N1	Q17	VN035-0N1	Q18	VP035-0N1	Q19	VP035-0N1	Q20	IRFZ40
Q21	INF740	D1	SD41	D2	IN914	D3	LED	D4	LED
D5	MR856	D6	MR856	D7	MR856	D8	MR856	D9	ECG525
D10	ECG525	D11	HI6013	D12	HI6013	D13	HI6013	D14	HI6013

Table of Integrated Circuits, Transistors, Diodes etc.

#	Value	#	Value	#	Value	#	Value	#	Value
S1	momentary	T1	custom						

Appendix C

Past Accumulation Rates From Ice Core and Borehole Data

In this appendix I present an analysis of Dyer Plateau's past accumulation rate. The analysis is made from dated layer depths and ice densities determined from an ice core, surface horizontal strain-rates determined from survey pole relative motions and vertical strain-rates determined from borehole marker relative motions. In this analysis it is assumed that the information originates from a location where the ice layering is flat and the ice flows vertically. The results of this analysis are discussed further in chapter 6.

C.1 - Theory of Analysis

If accumulation rates have varied only on time scales which are significantly shorter than an ice sheet's dynamic response time it is reasonable to assume that the vertical velocity at any given depth is approximately time invariant. In this situation it should be possible to accurately estimate the past accumulation rate, $\tilde{w}$, by the equation

$$\tilde{w}(T) = \underline{w}_0 \frac{\hat{w}(z(T))}{w(z)}, \tag{C.1}$$

where $\underline{w}_0$ is the time average accumulation rate, $\hat{w}$ is inverse of the vertical age gradient as measured from an ice core at the depth z which corresponds to a given age T and w is the vertical velocity at the depth where $\hat{w}$ is measured. If the assumption of steady-state velocity is correct, $\underline{w}_0$ will equal w_0, the vertical velocity at the surface; from here on I will refer to w_0 rather than $\underline{w}_0$.

If equation C.1 is to be used to estimate accumulation rate it will be necessary to have an estimate of the vertical velocity profile. In principle this could be achieved by measuring vertical motions within a borehole that reaches bedrock. If the borehole does not reach bedrock, it will typically be difficult to determine the absolute vertical motion of the ice column[1].

---

1. In some situations it maybe possible to over come this hurdle with GPS geodetic positioning equipment.

If borehole vertical motion measurements are unavailable then mass conservation can be used to estimate the absolute vertical velocity. For ice layers that are significantly shallower than the total ice thickness it is reasonable to assume that the horizontal strain-rate is depth invariant. If (1) the vertical density profile does not vary in the horizontal direction (or the ice flows only vertically), (2) the horizontal strain-rate does not vary with depth and (3) the flow is steady-state, conservation of mass can be expressed by

$$\rho\left(\dot{\varepsilon}_0+\frac{\partial w}{\partial z}\right)+w\frac{\partial \rho}{\partial z} = 0, \tag{C.2}$$

where z is depth, ρ is density and $\dot{\varepsilon}_0$ is the horizontal component of strain-rate. Section 5.1 gives a more detailed discussion of this equation. Equation C.2 has the solution

$$w = \frac{\rho_0 w_0}{\rho} - \frac{\dot{\varepsilon}_0}{\rho}\int_0^z \rho dz, \tag{C.3}$$

where ρ_0 is the surface ice density. This solution can be derived from equation 5.6 and can be verified by substitution into equation C.2. When equation C.3 is substituted into equation C.1 one finds

$$\tilde{w}(T) = \rho(z(T))\cdot\hat{w}(z(T))/\left(\rho_0-\frac{\dot{\varepsilon}_0}{w_0}\int_0^{z(T)}\rho(z')dz'\right). \tag{C.4}$$

From this it can be seen that estimates of accumulation rate are dependent on the ratio of the horizontal strain-rate to the average accumulation rate. Typically, $\dot{\varepsilon}_0$ can be accurately measured from the differential motions of survey poles. Because past accumulation rate estimates are dependent on the ratio of horizontal strain-rate to vertical surface velocity, they will be equally sensitive to proportional inaccuracies in either parameter.

The $\dot{\varepsilon}_0/w_0$ ratio will have a greater influence on estimates of accumulation rate of the more distant than estimates of the more recent past. This is because the integral of the density appearing in equation C.4 increases with increasing depth (age).

The problem of not knowing w_0 when using equation C.4 to estimate accumulation rates can be overcome by enforcing consistency between the average of the estimated accumulation rates for all times analyzed and the value used for w_0

$$w_0 = \frac{1}{N}\sum_{i=1}^{N} \tilde{w}_i(w_0).^2 \qquad \text{(C.5)}$$

However, there is a danger in doing this because it adds a degree of circularity to how accumulation rates are estimated.

If borehole vertical deformation measurements are available, but not to bedrock and there is no way of absolutely determining w_0, equation C.3 can be used to estimate w_0 and $\dot{\varepsilon}_0$. This is done by finding the values of these two parameters that give the best agreement between measured relative vertical motions and those predicted by equation C.4.

The change δ_n in separation distance between two borehole markers at depths z_n and z_{n-1} after a time interval will be

$$\delta_n = (z'_n - z'_{n-1}) - (z_n - z_{n-1}) = (z'_n - z_n) - (z'_{n-1} - z_{n-1}), \qquad \text{(C.6)}$$

where the primes indicate depths after the time interval. If the time interval, Δt, is short this will be equal to

$$\delta_n = [w(z_n) - w(z_{n-1})]\,\Delta t. \qquad \text{(C.7)}$$

If equation C.3 is substituted for $w(z)$ and equation C.7 is evaluated for each pair of vertical markers then the system of equations

$$\begin{aligned}
\frac{\delta_1}{\Delta t} &= w_0\left(\frac{\rho_0}{\rho(z_1)} - \frac{\rho_0}{\rho(z_0)}\right) - \dot{\varepsilon}_0\left(\frac{1}{\rho(z_1)}\int_0^{z_1}\rho\,dz - \frac{1}{\rho(z_0)}\int_0^{z_0}\rho\,dz\right)\\
\frac{\delta_2}{\Delta t} &= w_0\left(\frac{\rho_0}{\rho(z_2)} - \frac{\rho_0}{\rho(z_1)}\right) - \dot{\varepsilon}_0\left(\frac{1}{\rho(z_2)}\int_0^{z_2}\rho\,dz - \frac{1}{\rho(z_1)}\int_0^{z_1}\rho\,dz\right) \qquad \text{(C.8)}\\
&\cdots\\
\frac{\delta_N}{\Delta t} &= w_0\left(\frac{\rho_0}{\rho(z_N)} - \frac{\rho_0}{\rho(z_{N-1})}\right) - \dot{\varepsilon}_0\left(\frac{1}{\rho(z_N)}\int_0^{z_N}\rho\,dz - \frac{1}{\rho(z_{N-1})}\int_0^{z_{N-1}}\rho\,dz\right)
\end{aligned}$$

can be formed. This system of equations can be solved in a least squares sense for the two parameters w_0 and $\dot{\varepsilon}_0$. Beneath the densification layer where the density is constant

2. This equation weights all ages equally.

($\rho = \rho_{ice}$) the terms multiplying w_0 in equation C.8 will be zero. Thus, when performing the least squares inversion, all of the information about w_0 will come from the densification layer. If the accumulation rate has varied on a time scale longer than the time required to pass through the densification layer, the estimate of w_0 will be incorrect.

In general most difficulties associated with estimating past accumulation rate will be related to the non-steady-state nature of an ice sheet. If past accumulation rates have undergone significant long term trends, determining past accumulation rates is not necessarily a tractable problem with these data alone.

If an absolute measure of the vertical surface velocity is available, comparing it to a value of w_0 determined by one of the two methods discussed above may aid in determining whether an ice sheet is thickening or thinning. For example, if the actual surface vertical velocity is greater than the vertical velocity found from the analysis presented above, it would indicate that the ice sheet is thinning.

Differences between w_0 and $w(z = 0)$, the vertical surface velocity, will indicate longer term trends of an ice sheet's mass balance then differences between $\tilde{w}(T = 0)$, the accumulation rate measured at the surface, and $w(z = 0)$. This is because w_0 represents a long term accumulation rate average whereas $\tilde{w}(T = 0)$ represents a short term accumulation rate average.

C.2 - Analysis of Dyer Plateau Data

Two 230 meter deep ice cores[3] were extracted from a local ice summit of the Dyer Plateau. Ice chemistry was analyzed for annual layer variations and an age depth relation was established for every year from 1989 to 1514 A.D. Figure C.1 shows the relation found between age and depth. Because of the large scatter in annual layer thicknesses (figure C.1), layers spaced by ten years were used in all subsequent analysis.

Ice densities were also measured from the ice cores down to a depth of 100 meters. Beyond 100 meters the ice cores were too fractured to allow densities to be accurately measured. Figure C.2 shows a measured density depth relation. Because of the large scat-

3. Ice core analysis was carried out by Lonnie Thompson of the Byrd Polar Research Center, Ohio State University and David Peel and Rob Mulvaney of the British Antarctic Survey.

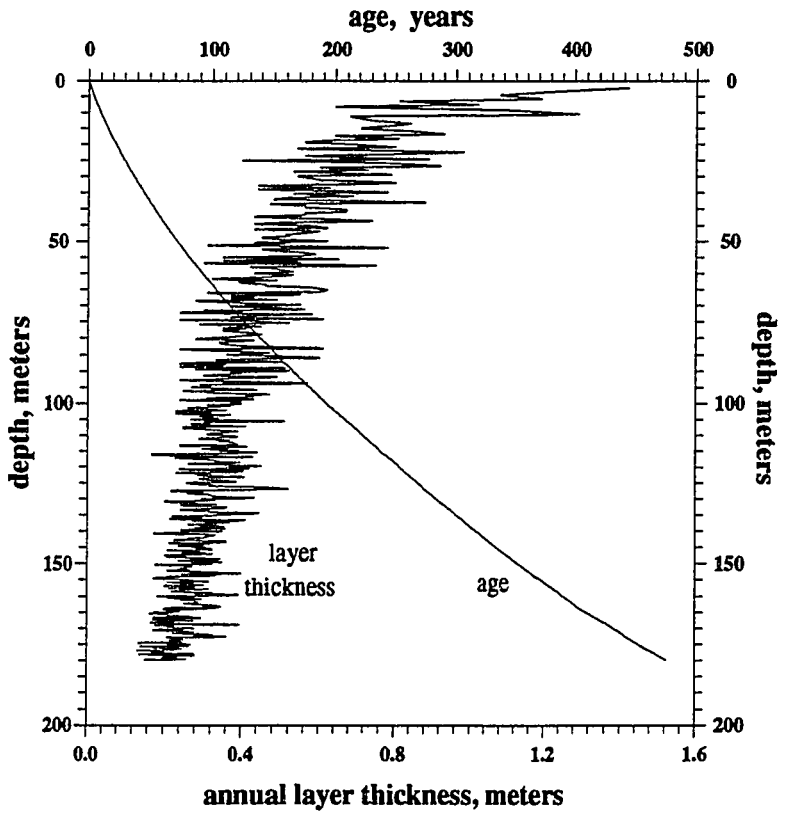

Figure C.1: Age and annual layer thickness measured from ice core stratigraphy.

ter present in the density measurements, the solid hand fit piecewise linear curve was used in all subsequent analysis.

After the cores were extracted, 14 metal bands were placed in one of the boreholes. Their vertical positions were carefully measured by means of a metal detector attached to a measuring tape tied to it. This arrangement allowed the bands to be repeatedly located to an accuracy of ~4 millimeters. After two years the drill site was revisited and the metal band depths were remeasured. It was possible to relocate all of the metal bands except for the very deepest one.

Survey marker poles were positioned on a 1/2km × 1/2km grid in the vicinity of the drill site and were located by means of optical survey equipment to a relative[4] accu-

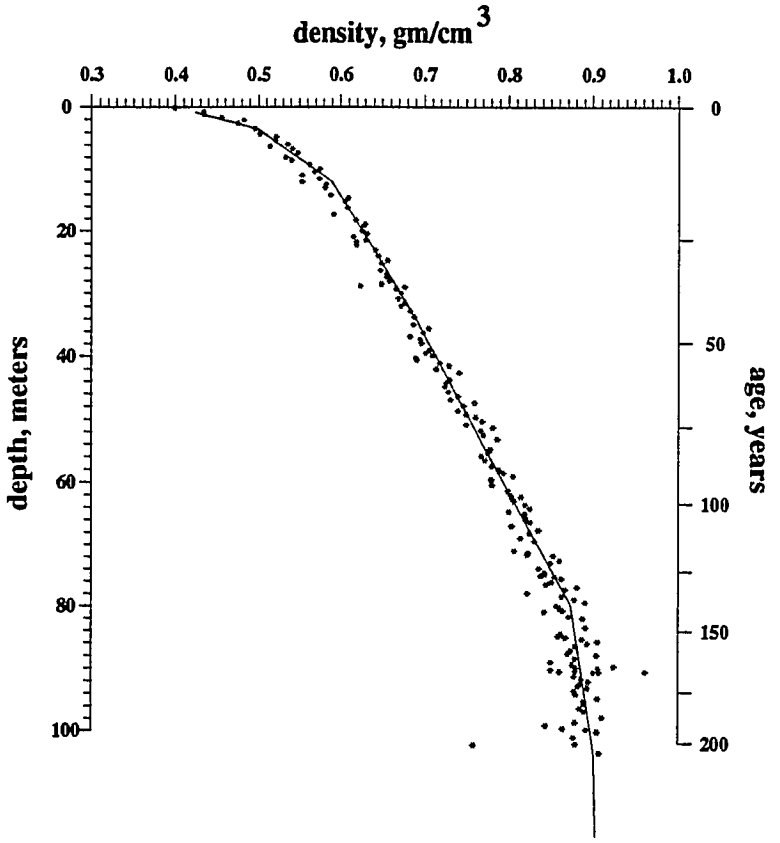

Figure C.2: Measured ice density as a function of both depth (left vertical axis) and age (right vertical axis) as found from ice core measurements.The line represents the densities used in the analysis.

racy of approximately $20cm$. After two years the survey poles were remeasured. From these measurements I found that the horizontal strain-rate at the drill site is $(1.7 \pm 0.1) \times 10^{-3} yr^{-1}$.

Using the value of horizontal strain-rate $\dot{\varepsilon}_0 = 1.7 \times 10^{-3} yr^{-1}$, I found that $w_0 = 1.12 m/yr$ satisfied equation C.5. The past values of accumulation rate found from this 'consistency' analysis are shown as curve (a) in figure C.3.

I next generated the system of equations C.8 and performed a least squares analysis. The least-squares analysis gave a horizontal strain-rate of $\dot{\varepsilon}_0 = (1.54 \pm 0.29) \times 10^{-3} yr^{-1}$ and the surface vertical velocity of $w_0 = 1.09 \pm 0.06$. These values are in good agreement

4. There was no maker such a nunatak available to establish an absolute reference position.

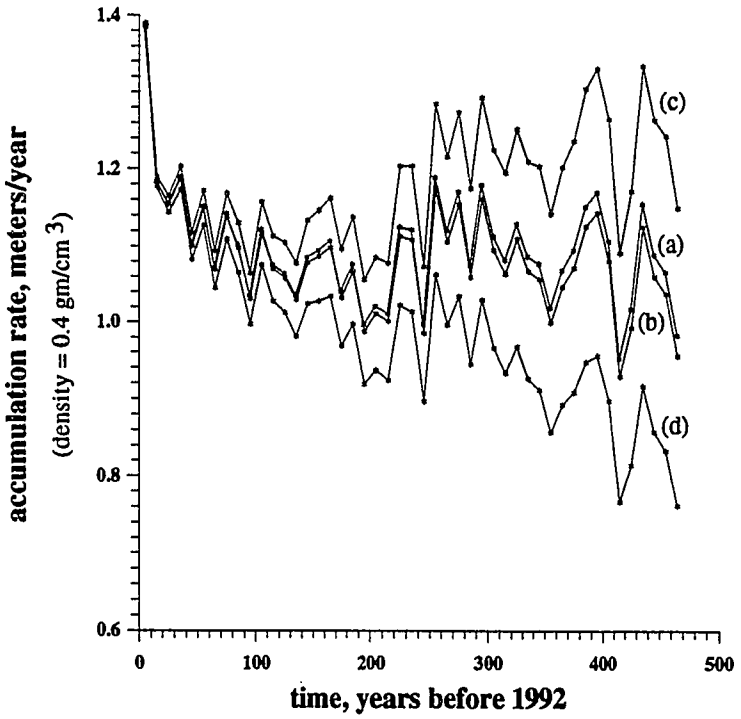

Figure C.3: Deduced past accumulation rate histories. Curve (a) represents accumulation rate history deduced from a *consistency* analysis, (b) represents the *best fit* accumulation rate history and (c) and (d) represents the 95% confidence intervals associated with the best fit.

with the consistency estimate performed above and the measured surface horizontal strain-rate. Curves (b), (c) and (d) in figure C.3 show the past accumulation deduced from these values and equation C.4. Curve (b) is based on the best fit values and curves (c) and (d) are the 95% confidence intervals indicated by this analysis. Because accumulation rate estimates of the more distant past are influenced more by w_0 and $\dot{\varepsilon}_0$ than are estimates for the more recent past, estimates of the more distant past are more poorly constrained than estimates of the more recent past.

Figure C.4 shows the strain-rates measured from the borehole marker motions and those predicted by the least squares analysis. There is good agreement between modelled and measured finite strain-rates. The two measured strain-rates that significantly deviate

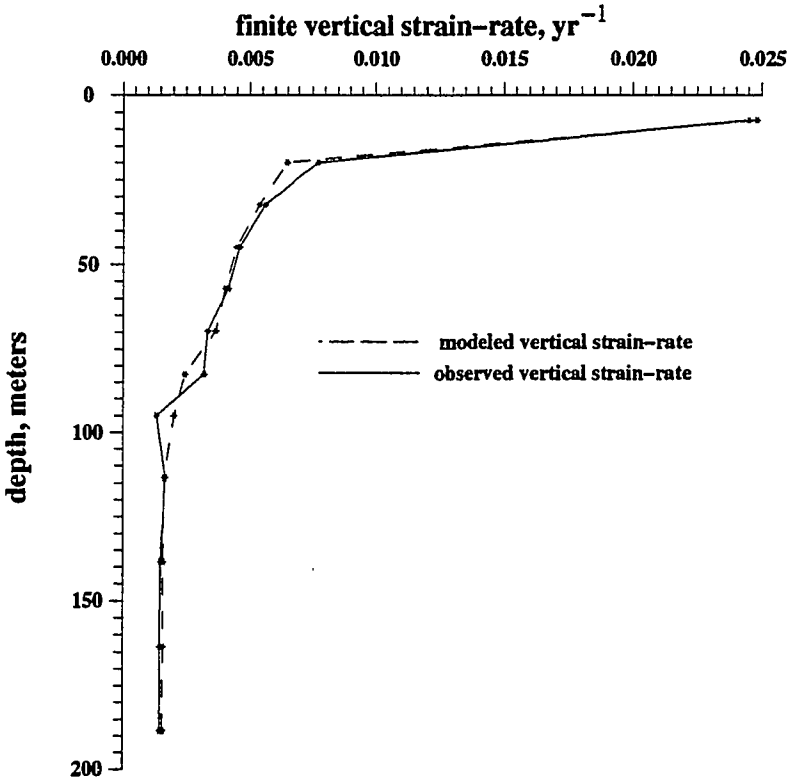

Figure C.4: Measured and predicted vertical strain-rates.

from the modelled finite strain-rates are probably due to a marker which slipped some time during the time interval.

Appendix D

Details of the Evaluation of Streamline Parameterization

In this appendix I explain details of the application of equation 6.14 to actual RES data. It is important that these details be worked out before actual data are analyzed. In section D.1 I discuss how this equation can be applied to RES data when RES profiles do not exactly follow flow-lines and in section D.2 I discuss how the width normalization which appears as the inner integral of equation 6.14 can be numerically evaluated.

D.1 - Estimation of Streamlines Based on RES Profiles that do not Exactly Follow Flow-Lines

Ideally, if layer information from a RES profile is to be used in calculating streamlines, the RES profile should follow flow-lines so that streamline parameters can be calculated by equation 6.14. To do this the surface topography of an ice sheet must be known prior to radio echo sounding. Typically, the surface topography is found at the same time that radio echo sounding is done. Either by chance or by a rough understanding of an ice sheet's geometry the person performing radio echo sounding is likely to record some RES profiles that approximately follow surface gradients. This is illustrated in figure D.1which depicts the appearance of a RES profile that roughly follows a flow-line.

If layer depths vary slowly in the direction normal to a RES profile, then depths along a nearby stream-sheet which parallels a flow-line can be approximated by projecting the RES profile depths onto the stream-sheet. If the RES profile is straight and the stream-sheet is curved and x represents the distance along the RES profile, ξ represents the horizontal distance along the stream-sheet and y represents the separation distance in the direction normal to the RES profile, then a projection perpendicular to the profile, from the RES profile onto the stream-sheet, will be given by

$$\xi = \int_{x_0}^{x} \sqrt{1 + (dy/dx)^2}\, dx' + \xi_0. \qquad \text{(D.1)}$$

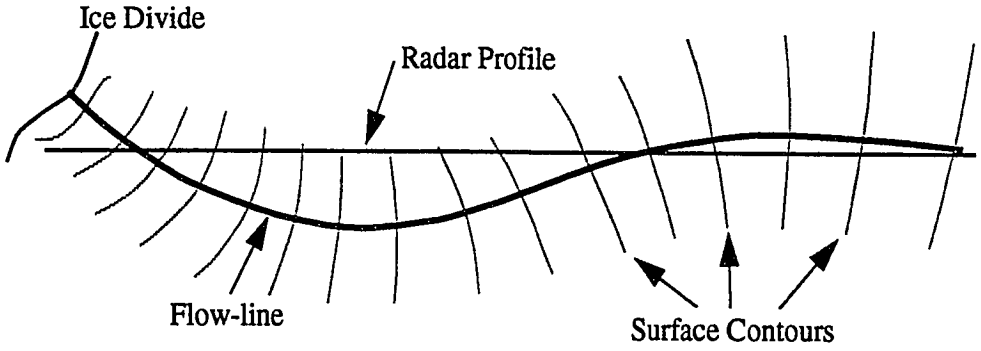

Figure D.1: This map view drawing illustrates the relationship between a radar profile and a nearby flow-line. A flow-line is a curve which follows the horizontal velocity field on the surface of an ice sheet. The flow-line depicted here follows surface altitude gradients.

The accuracy of the projection will be determined by the slope of layers normal to the direction of the profile multiplied by the separation distance y. If there are other RES profiles which cross the primary RES profile used, a projection could be made that accounts for the slopes of layers in the cross direction.

If it is impractical to find an appropriate flow-line because of having limited information away from a RES profile, the dy/dx term could be substituted by the inverse of the inner product of the direction of the horizontal velocity field, as measured along the RES profile, relative to the RES profile,

$$\frac{\left|\vec{V}_h\right|}{\left|\vec{V}_h \bullet \vec{D}\right|} \rightarrow \frac{dy}{dx},$$

or the inverse of the inner product of the direction of the gradient of the surface altitude, and the direction of the RES profile

$$\frac{\left|\nabla Z_s\right|}{\left|\nabla Z_s \bullet \vec{D}\right|} \rightarrow \frac{dy}{dx}$$

where $\vec{V}_h$ and Z_s represent the horizontal velocity of flow and surface altitude along the RES profile and $\vec{D}$ represents the direction of the RES profile.

These substitutions will be useful if all flow-lines which cross a RES profile are approximately parallel. This will be untrue at some level if the radii of curvature along the stream-sheets are not infinite.

D.2 - Calculation of Width Normalization

In section 6.1.4 I derived a streamline parameter width normalization based on the radius of curvature of surface contours for stream-sheets which parallel flow-lines. This normalization is expressed by equation 6.13 and appears in the inner integral of equation 6.14. In this section I will concentrate on the evaluation of this normalization:

$$\frac{W}{W_0} = exp(\int_{\xi_0}^{\xi} R^{-1}(\xi')d\xi').$$

I start by considering the evaluation of this normalization for a stream-sheet that originates on the summit of an elliptical ice dome (figure D.2). If a stream-sheet originates

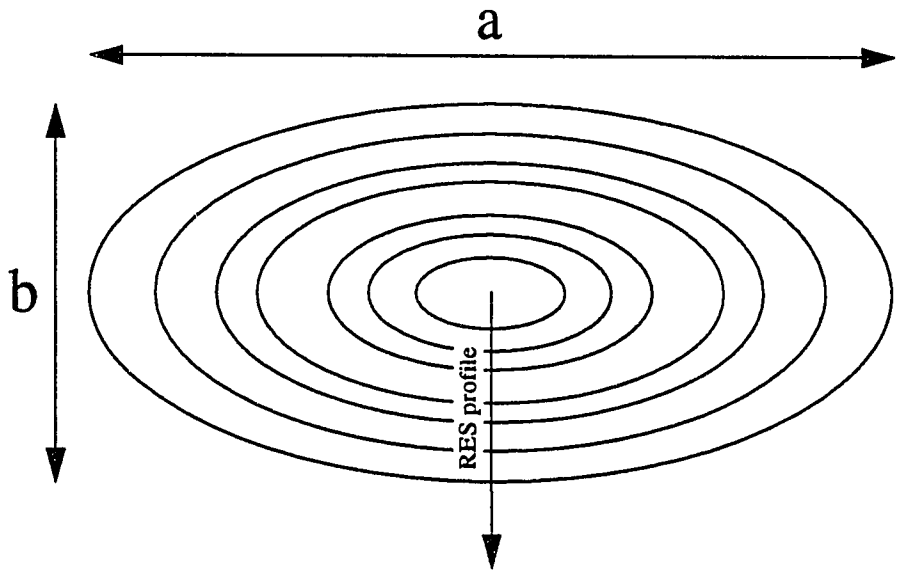

Figure D.2: Map view of an elliptical ice dome with a RES profile running along one of its major axes. On this ice dome the surface contours all have the same major to minor axes ratios $\Re = a/b$.

at the summit of an elliptical ice summit and it parallels a major axis of symmetry, the

radius of curvature of surface contours along the stream-sheet will be given by

$$R = \Re\xi, \tag{D.2}$$

where $\Re$ is the major-minor axis ratio and ξ is the horizontal distance along the stream-sheet. The width normalization will be

$$\frac{W}{W_0} = \left[\frac{\xi}{\xi_0}\right]^{\Re}, \tag{D.3}$$

where ξ_0 is the horizontal distance along the stream-sheet at the ice summit.

I now consider the evaluation of the width normalization when the radius of curvature is specified as a piecewise linear function of horizontal distance along a stream-sheet. Having R specified in this fashion will be convenient for computational purposes. When this is done the radius of curvature will be given by

$$R = m_i\xi + b_i \qquad \xi_i \le \xi \le \xi_{i+1}.$$

In order to have continuity in R the terms should be related by

$$b_{i+1} = (m_i - m_{i+1})\,\xi_i - b_i.$$

However, if the radius of curvature changes sign, as is demonstrated in figure D.3, it will be necessary to place one of the piecewise section joints (i.e. a ξ_i) at the location where R changes sign and at that location R should not be made continuous.

If the horizontal position ξ is in the in the piecewise interval $\xi_n < \xi \le \xi_{n+1}$ then the width normalization be given by

$$\frac{W}{W_0} = exp\left[\frac{1}{m_0}\log\left(\frac{m_0\xi_1 + b_0}{m_0\xi_0 + b_0}\right) + \frac{1}{m_1}\log\left(\frac{m_1\xi_2 + b_1}{m_1\xi_1 + b_1}\right) + \cdots + \frac{1}{m_n}\log\left(\frac{m_n\xi + b_n}{m_n\xi_n + b_n}\right)\right]$$

which reduces to

$$\frac{W}{W_0} = \left(\frac{m_n\xi + b_n}{m_n\xi_n + b_n}\right)^{1/m_n} \prod_{i=0}^{n-1}\left(\frac{m_i\xi_{i+1} + b_i}{m_i\xi_i + b_i}\right)^{1/m_i}. \tag{D.4}$$

In piecewise sections where the horizontal rate of change of the radius of curvature is small, $|m_i| \ll 1$, the linearization

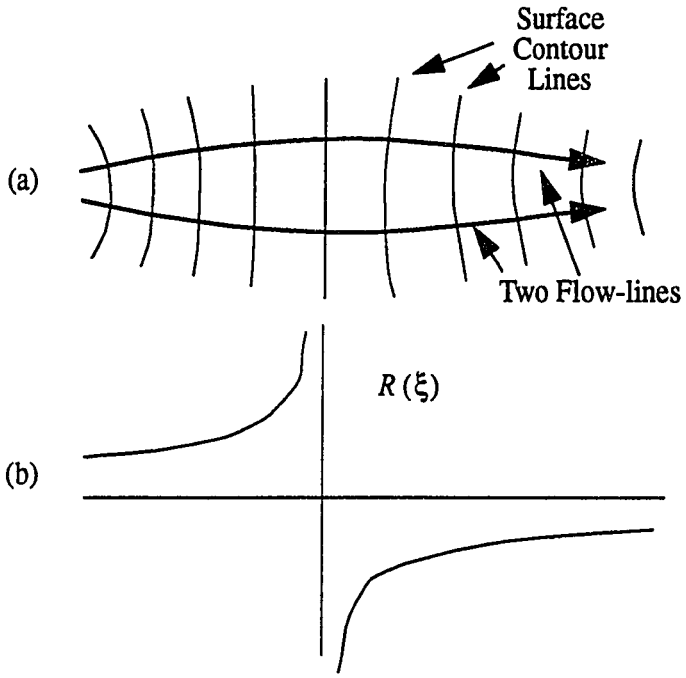

Figure D.3: (a) A map view drawing of a pair of diverging and then converging flow lines and (b) the corresponding radii of curvature of the surface contours which they cross.

$$\left(\frac{m_i x + b_i}{m_i x_i + b_i}\right)^{1/m_i} \cong exp\left(\frac{x - x_i}{b_i}\right) - exp\left(\frac{x - x_i}{b_i}\right)\left(\frac{x^2 - x_i^2}{2b_i^2}\right)m_i \qquad |m_i| \ll 1$$

should be made when evaluating equation D.4 in order to avoid the singularity in the exponent when $m_i = 0$. The derivation of this linearization is tedious and is omitted here.

Appendix E

Atlas of Radio-Echo Sounding Profiles

This appendix displays most of the RES profiles collected from the Dyer Plateau. Figures E.2and E.3 show the paths of the RES profiles in relation to the surface and bed topography. All of the profiles have the same vertical scale. All of the profiles have the same horizontal scale except the longest three (figures E.6, E.7 and E.8). The horizontal and vertical scales are shown below. The vertical exaggeration is 11.4 for the longest three profiles and is 4.7 for the remainder.

5 MHz antennas were used for all of the profiles except the one shonw in figure E.16 which was collected with 2 MHz antennas. This profile can be compared with figure E.15.

When this atlas was produced, polarity correction was accidentally disabled (page 53). Consequently there are occasional polarity changes (e.g. figure E.4.)

I hope these images stir the imagination!

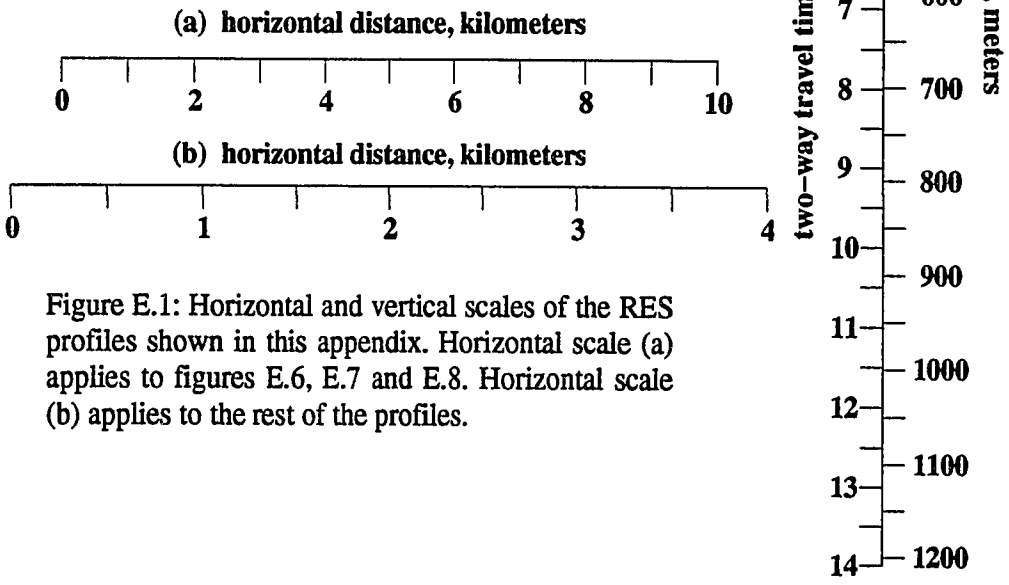

Figure E.1: Horizontal and vertical scales of the RES profiles shown in this appendix. Horizontal scale (a) applies to figures E.6, E.7 and E.8. Horizontal scale (b) applies to the rest of the profiles.

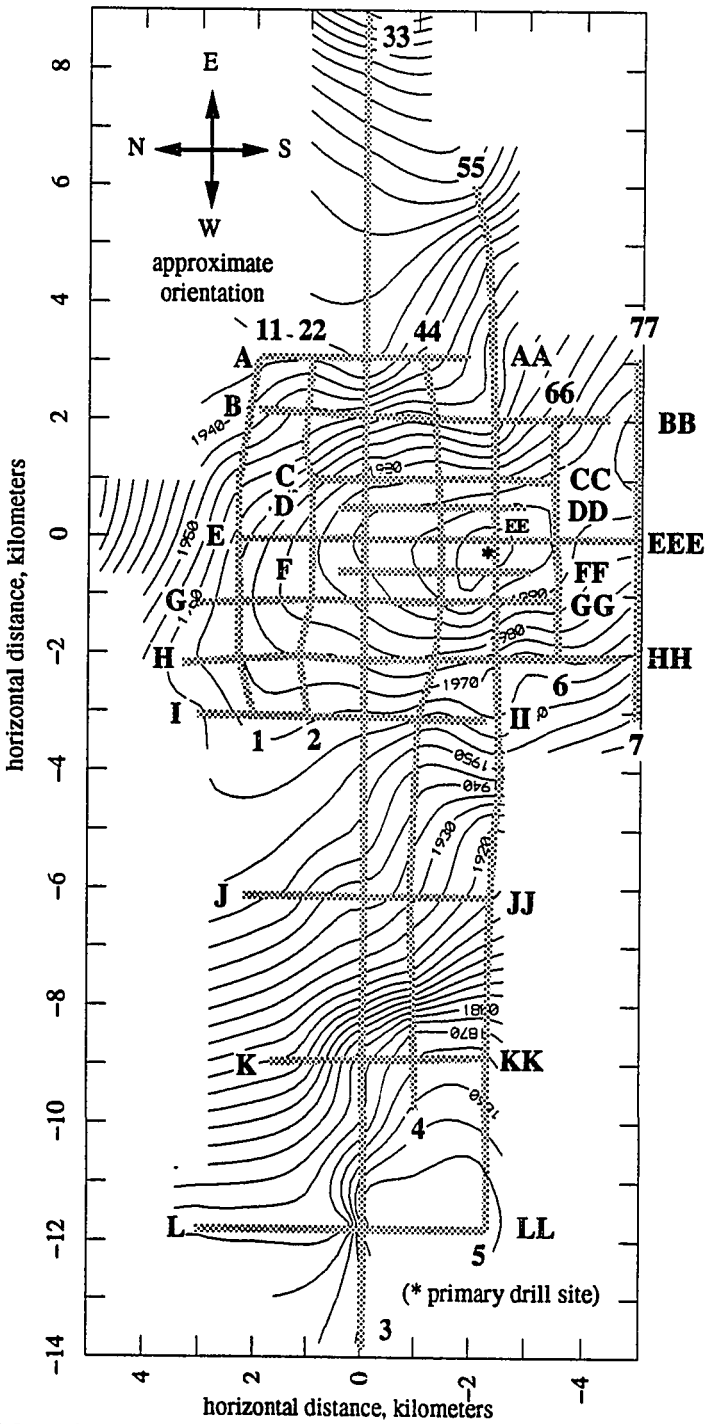

Figure E.2: Map view diagram of surface topography. The gray lines indicate RES profiles shown in this appendix. The contour interval is 5 meters. North as indicated is 8.3 degrees east of true north.

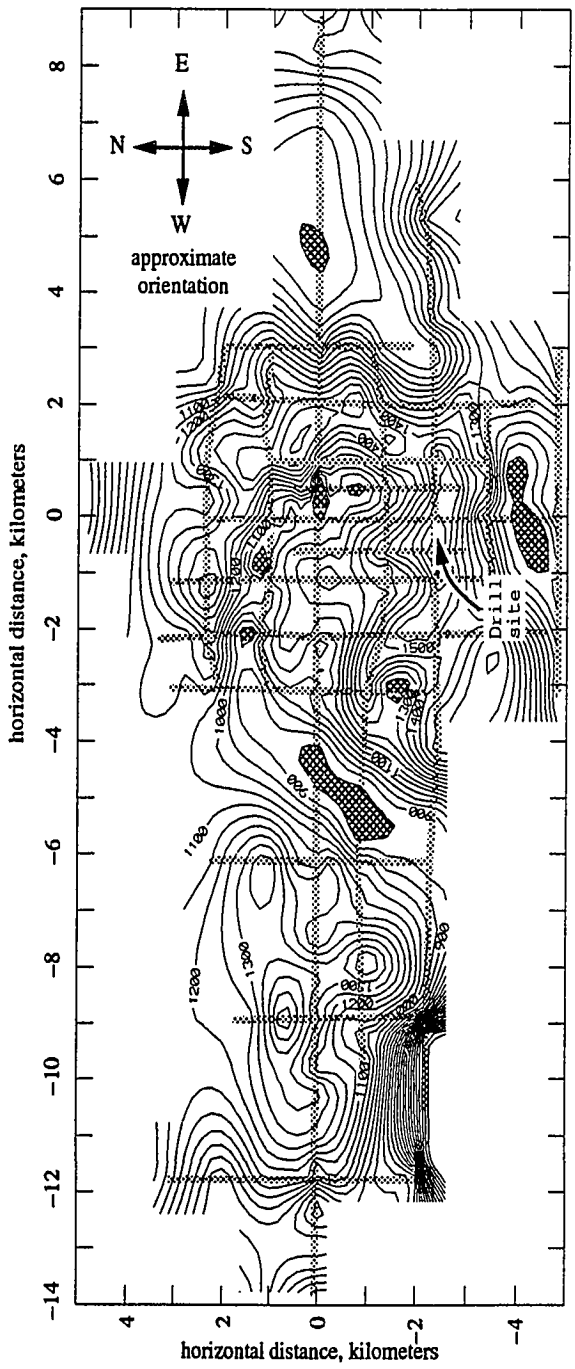

Figure E.3: Map view diagram of bed topography. The gray lines indicate RES profiles shown in this appendix. The contour interval is 50 meters. Shaded regions indicate local depressions.

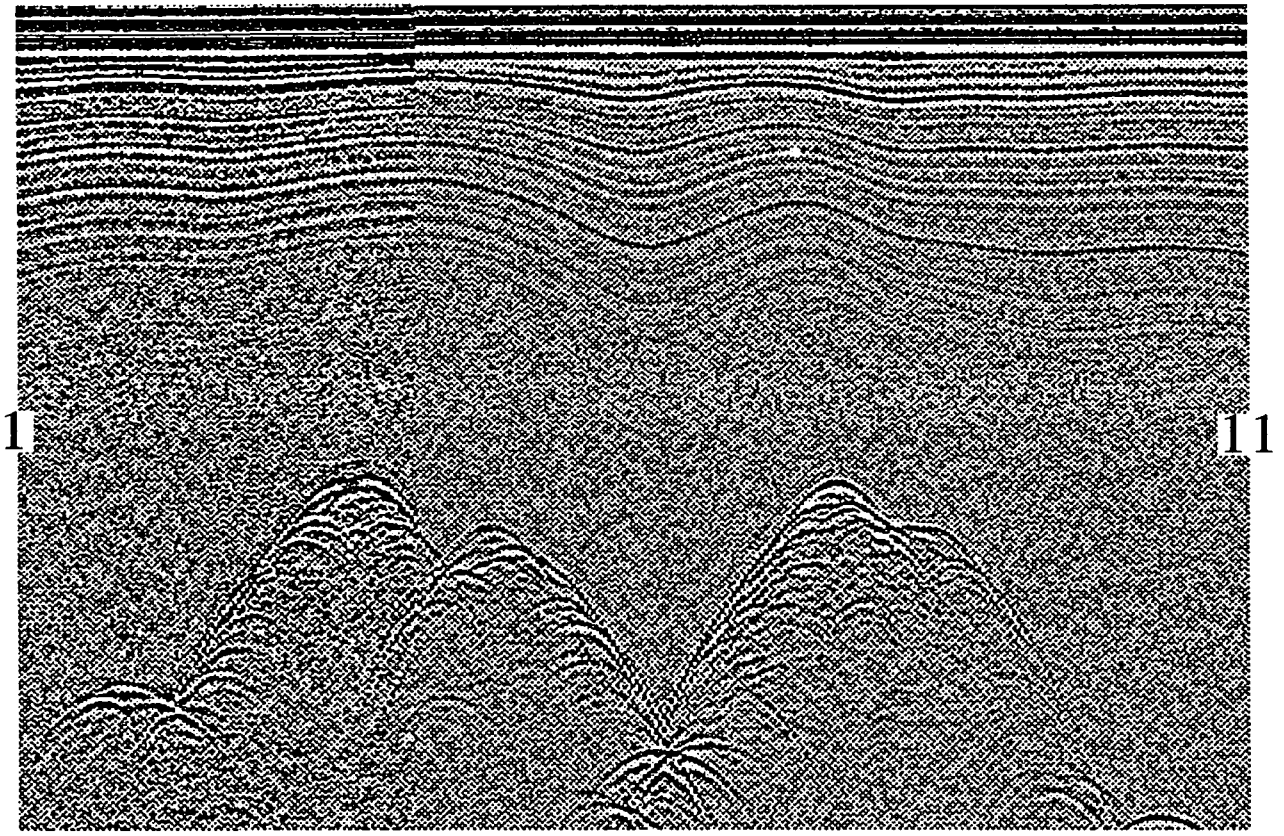

Figure E.4: RES profile running from 1 to 11. The profile is 6.2 km wide and 11 μsec deep.

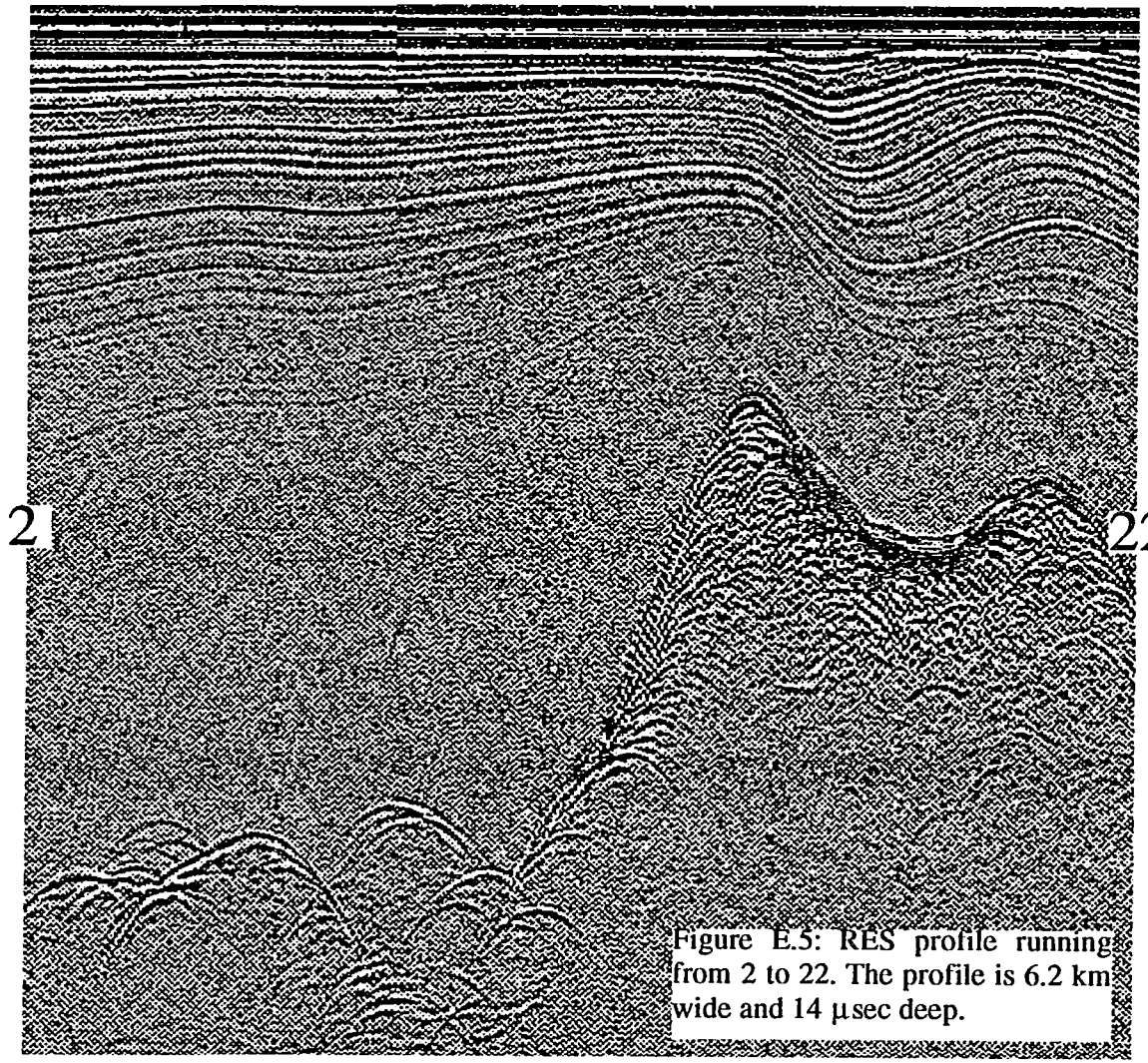

Figure E.5: RES profile running from 2 to 22. The profile is 6.2 km wide and 14 μsec deep.

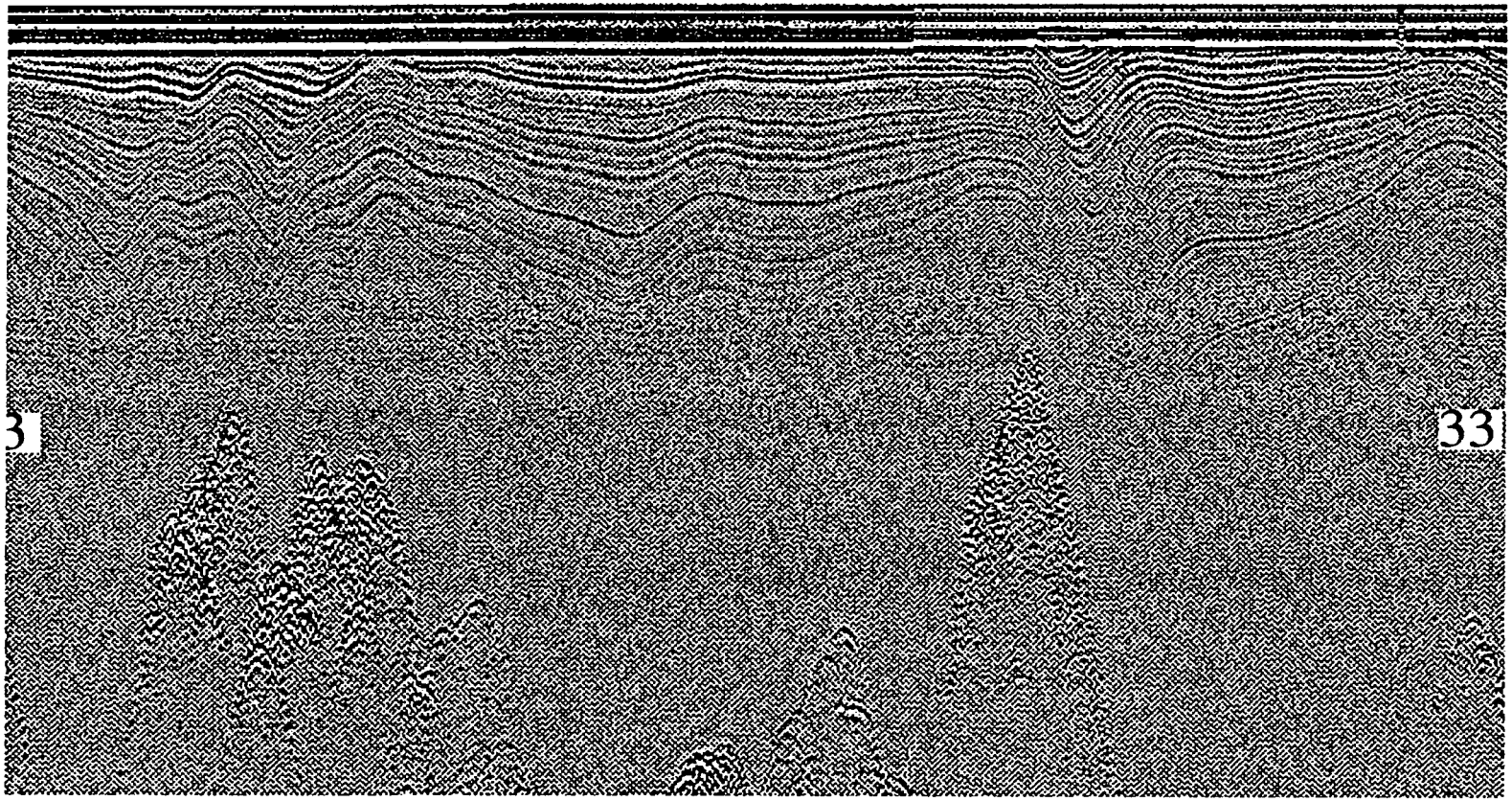

Figure E.6: RES profile running from 3 to 33. The profile is 22.7 km wide and 11 μsec deep.

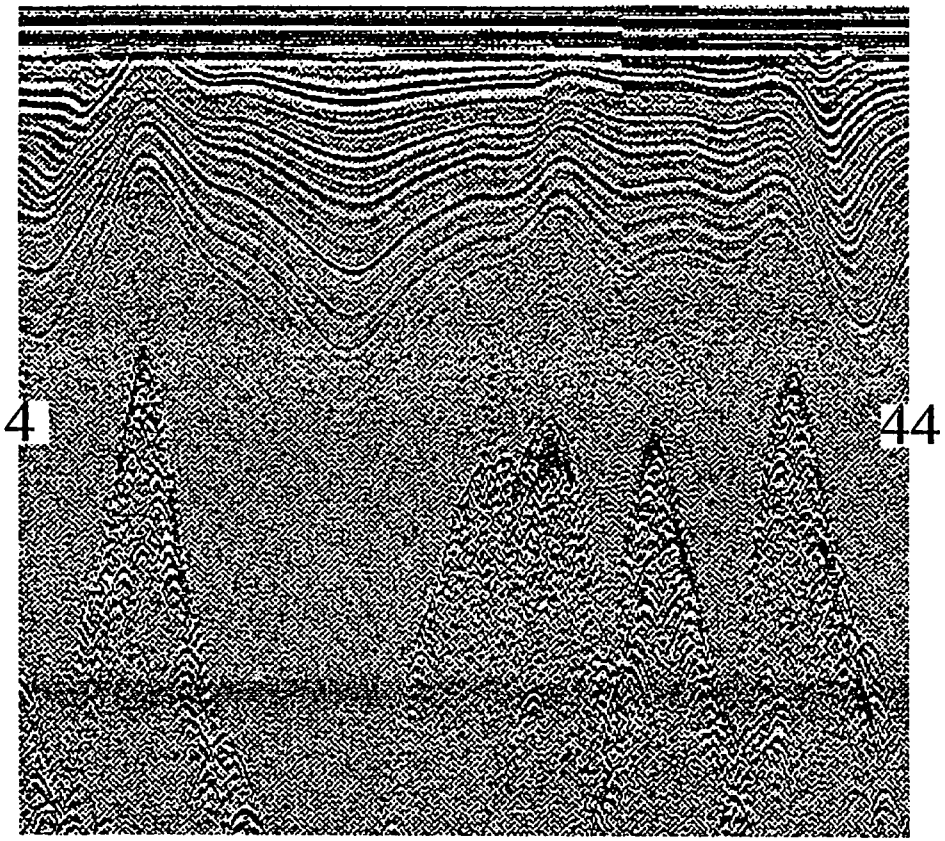

Figure E.7: RES profile running from 4 to 44. The profile is 12.8 km wide and 11 μsec deep.

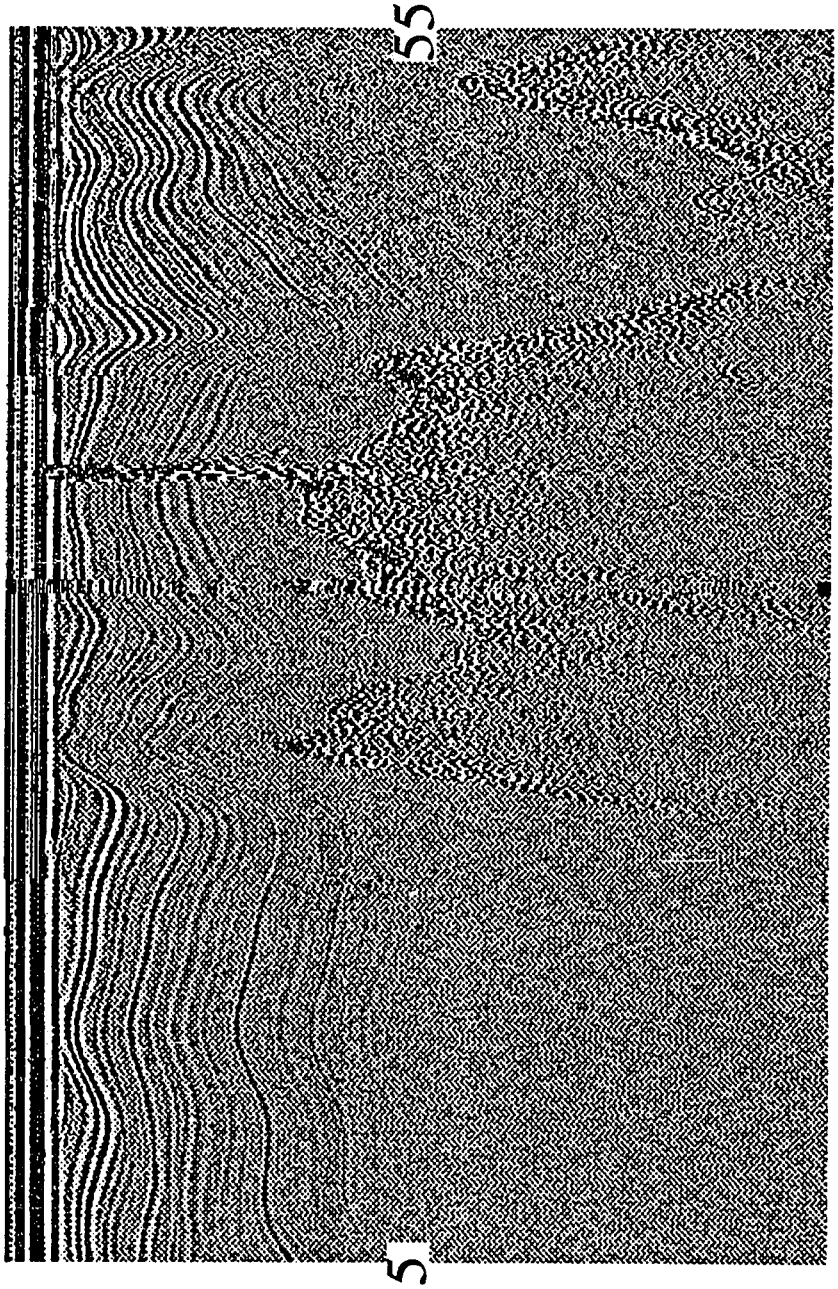

Figure E.8: RES profile running from 5 to 55. The profile is 17.8 km wide and 11 μsec deep.

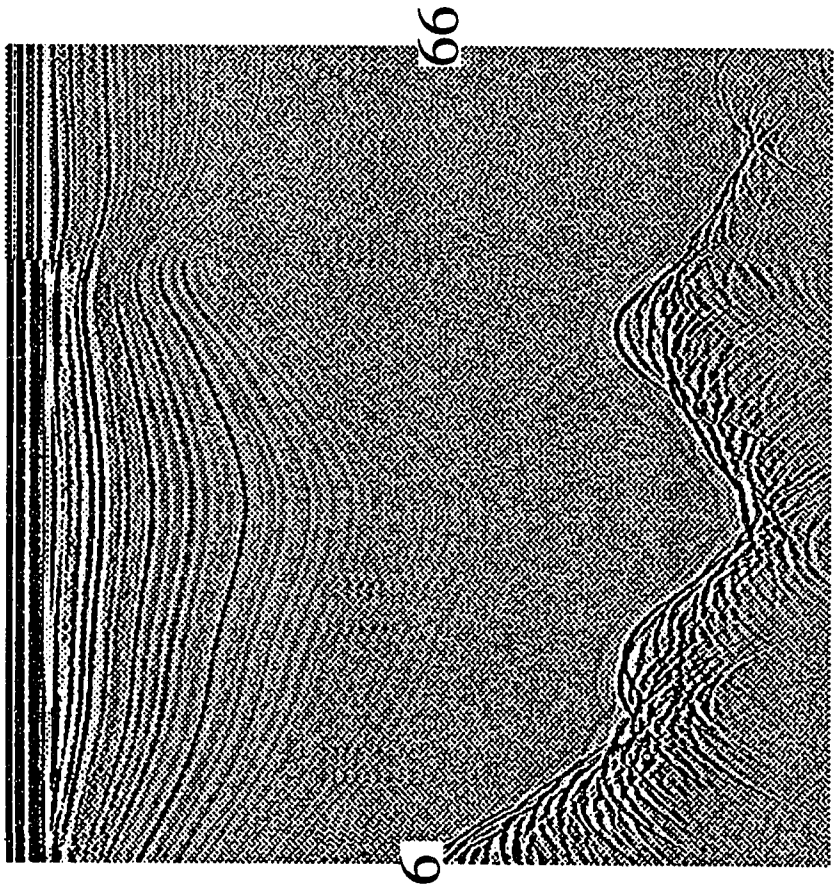

Figure E.9: RES profile running from 6 to 66. The profile is 4.3 km wide and 11 μsec deep.

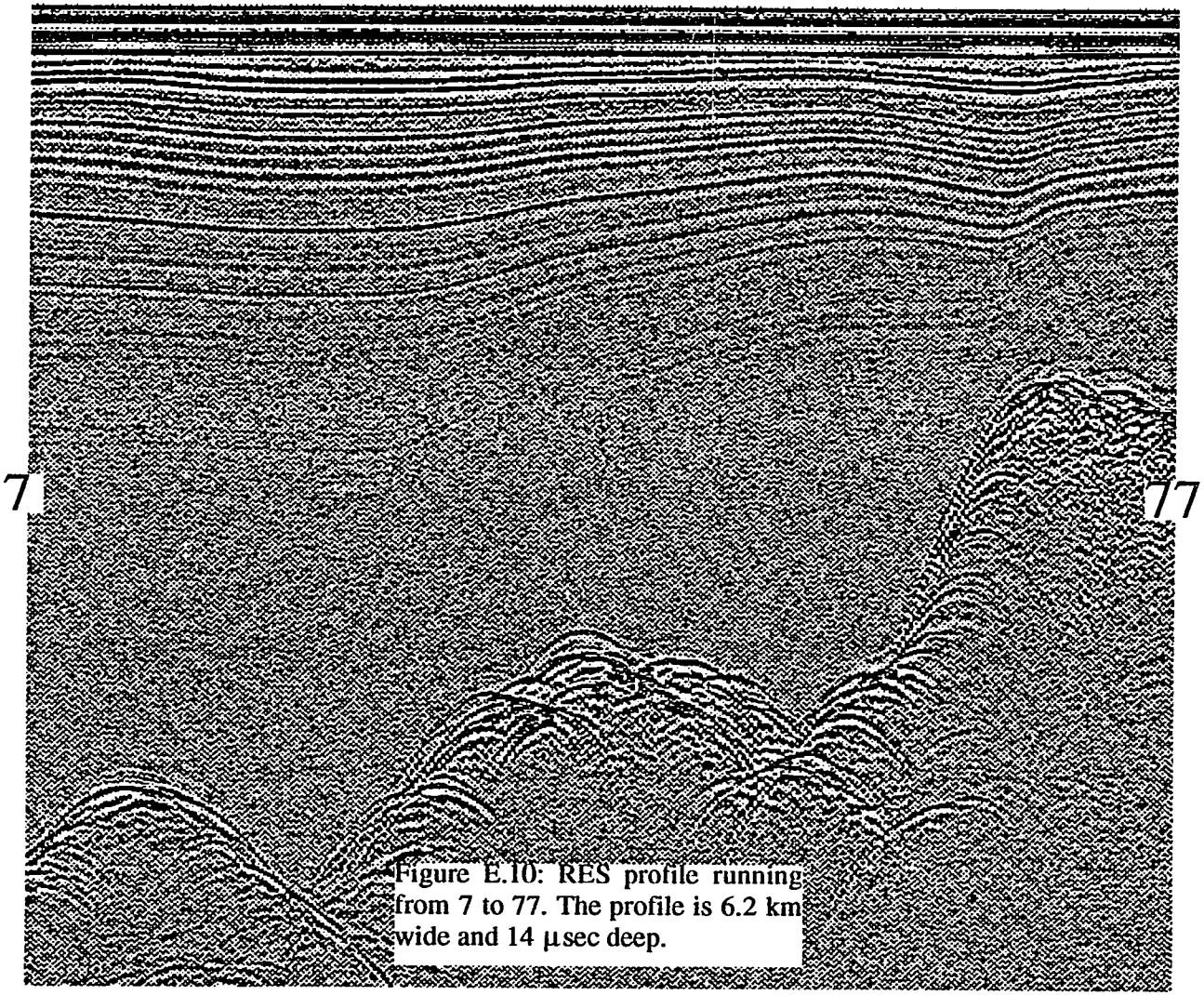

Figure E.10: RES profile running from 7 to 77. The profile is 6.2 km wide and 14 μsec deep.

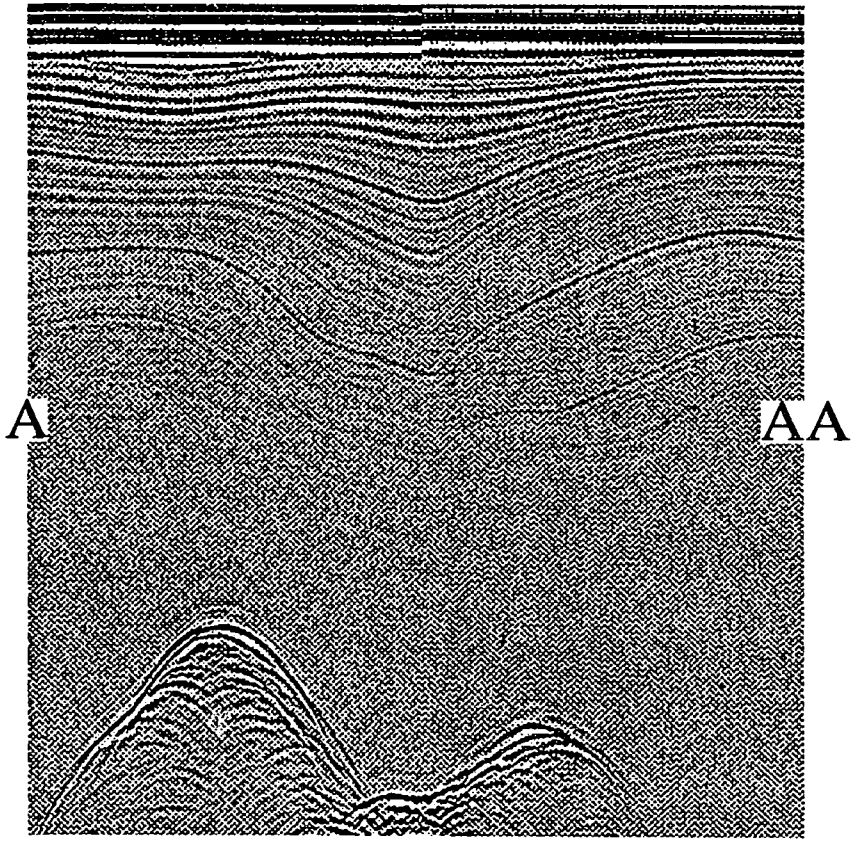

Figure E.11: RES profile running from A to AA. The profile is 3.9 km wide and 11 μsec deep.

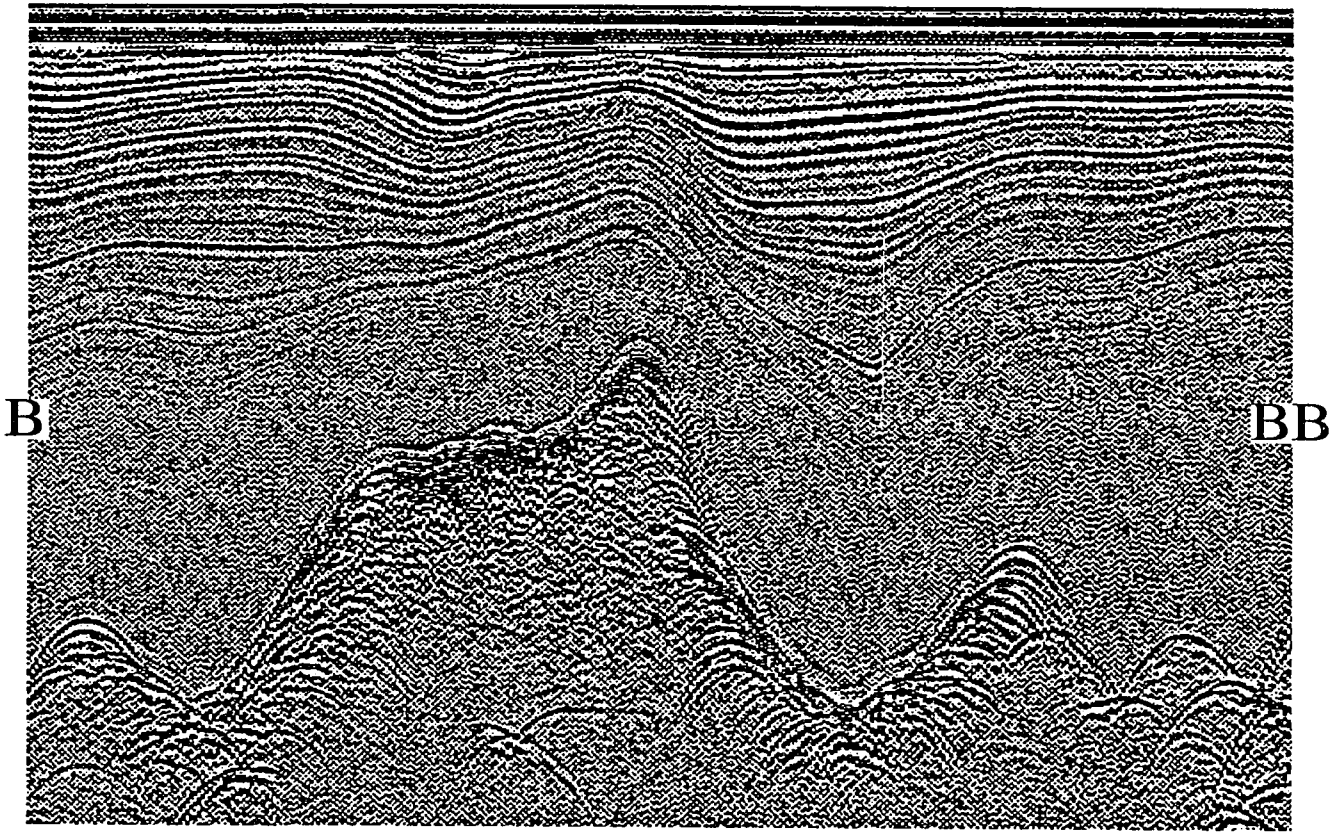

Figure E.12: RES profile running from B to BB. The profile is 6.3 km wide and 11 μsec deep.

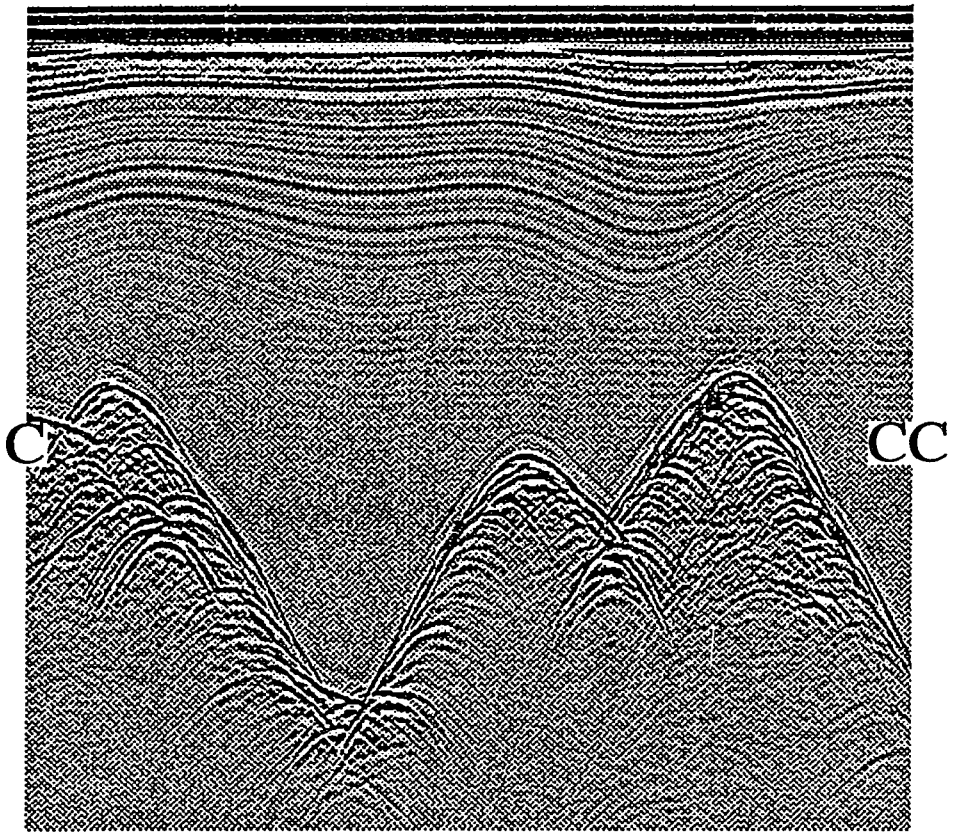

Figure E.13: RES profile running from C to CC. The profile is 4.4 km wide and 11 μsec deep.

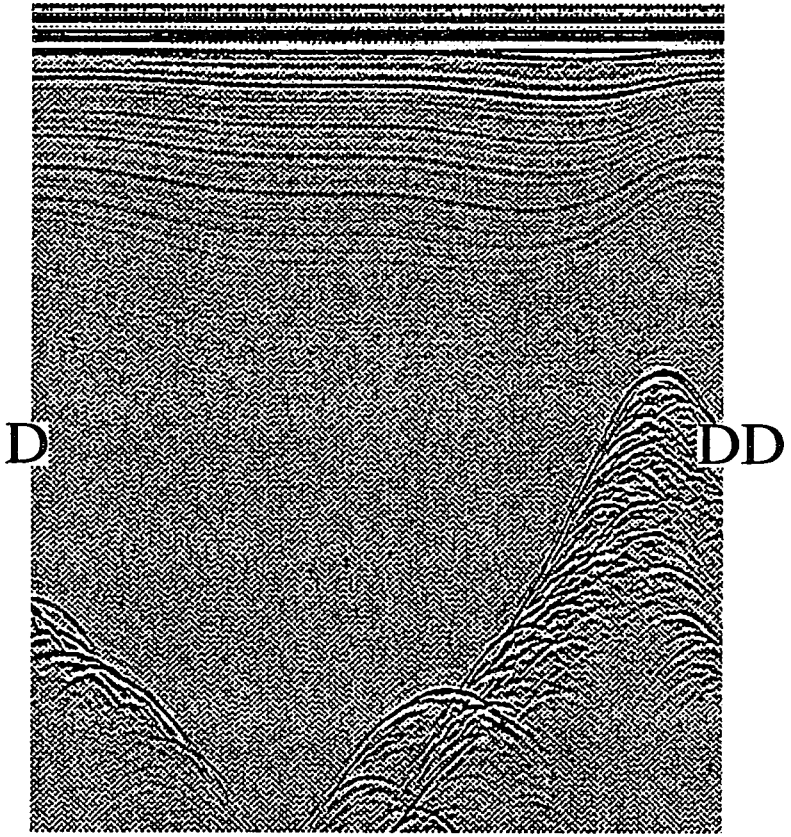

Figure E.14: RES profile running from D to DD. The profile is 3.5km wide and 11 µsec deep.

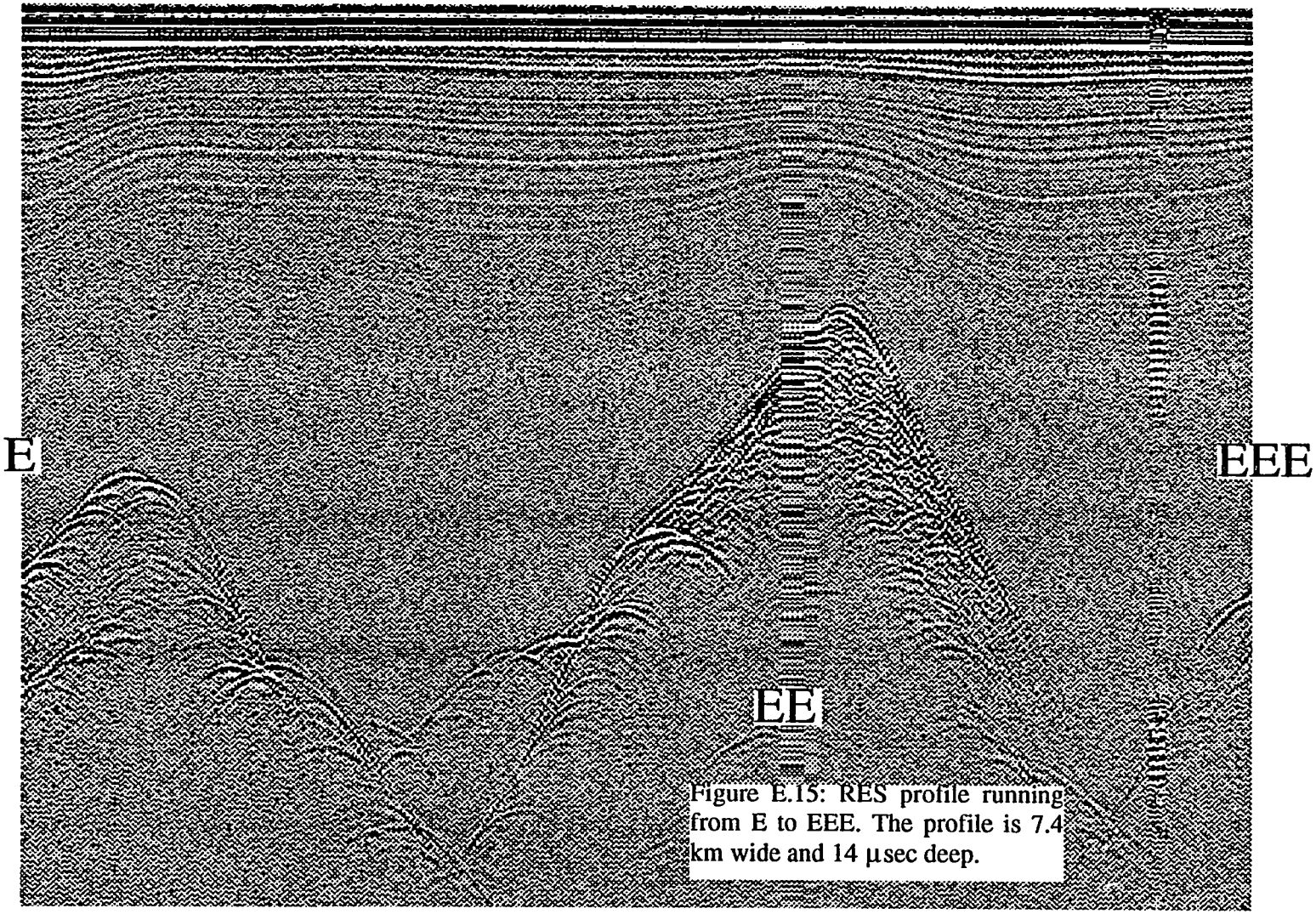

Figure E.15: RES profile running from E to EEE. The profile is 7.4 km wide and 14 μsec deep.

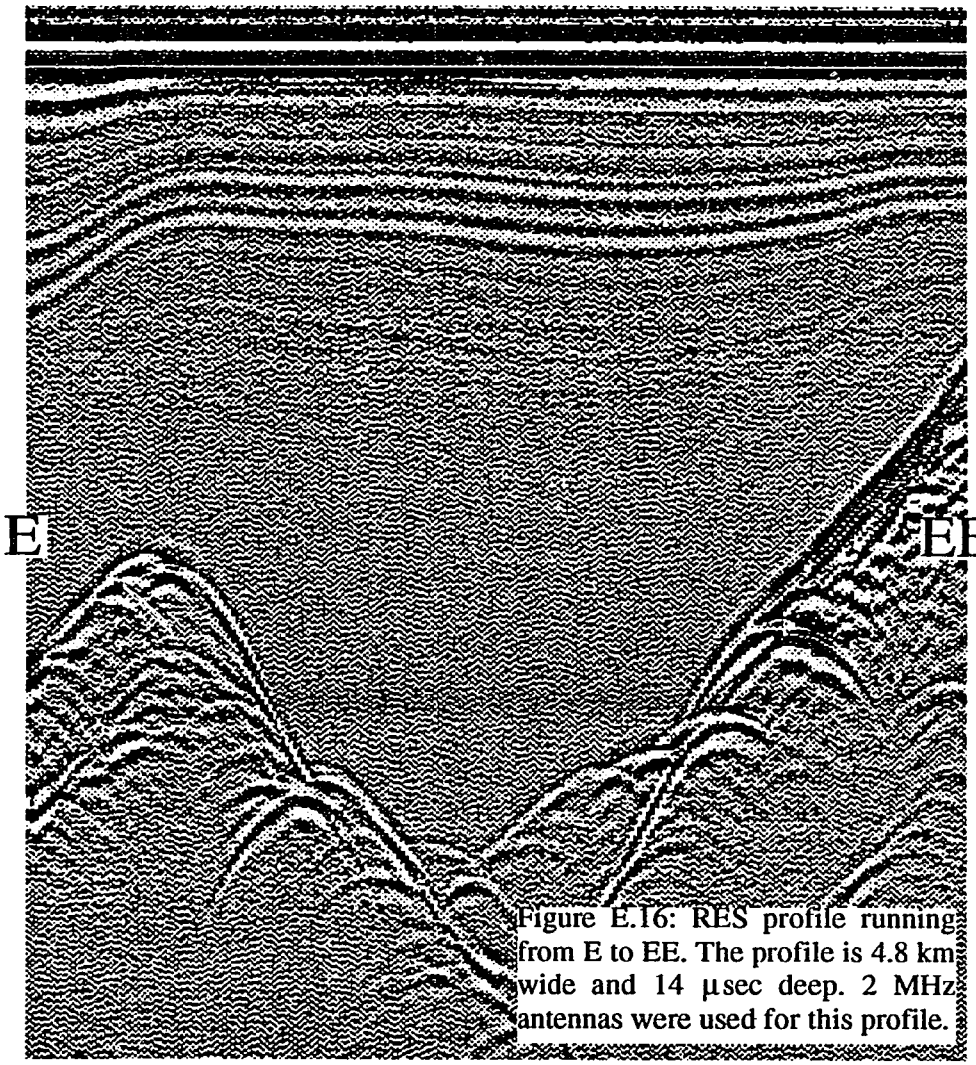

Figure E.16: RES profile running from E to EE. The profile is 4.8 km wide and 14 μsec deep. 2 MHz antennas were used for this profile.

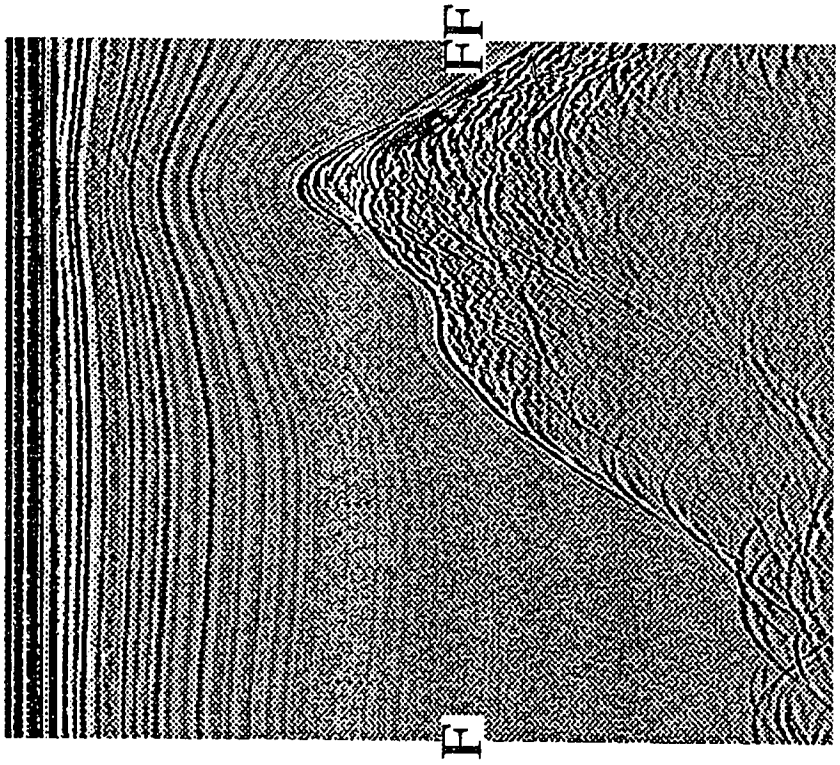

Figure E.17: RES profile running from F to FF. The profile is 3.5 km wide and 11 μsec deep.

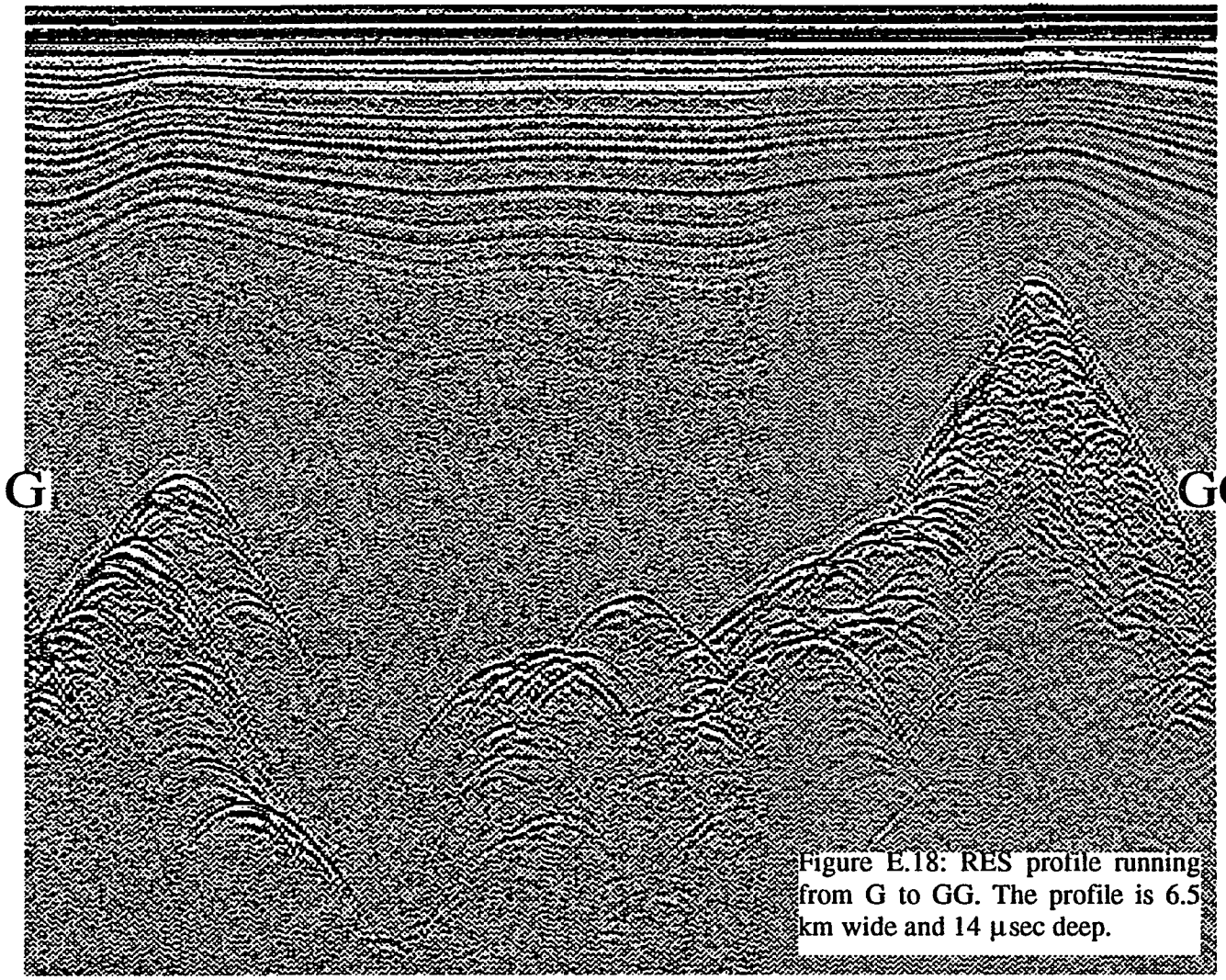

Figure E.18: RES profile running from G to GG. The profile is 6.5 km wide and 14 μsec deep.

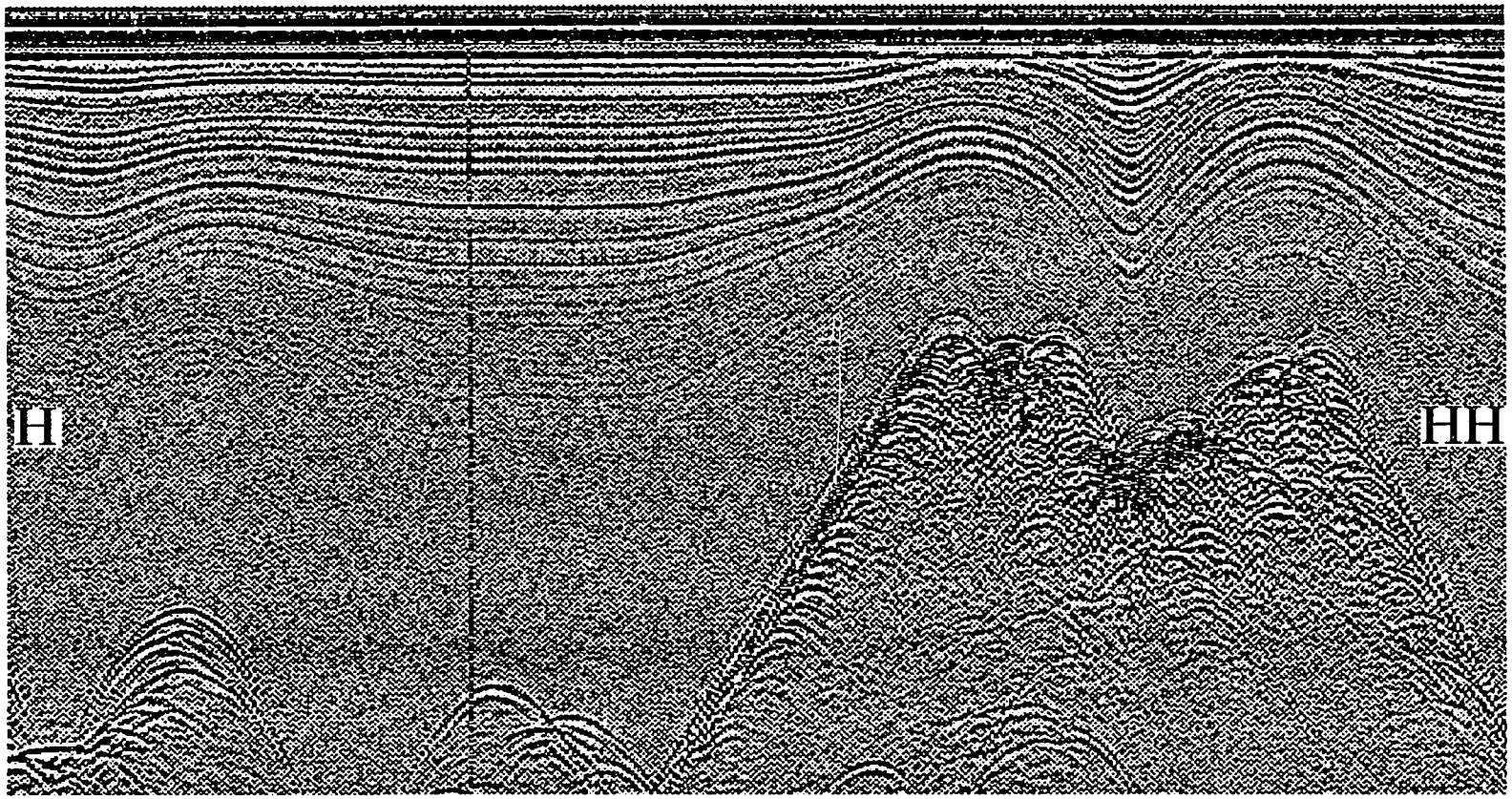

Figure E.19: RES profile running from H to HH. The profile is 7.9 km wide and 11 μsec deep.

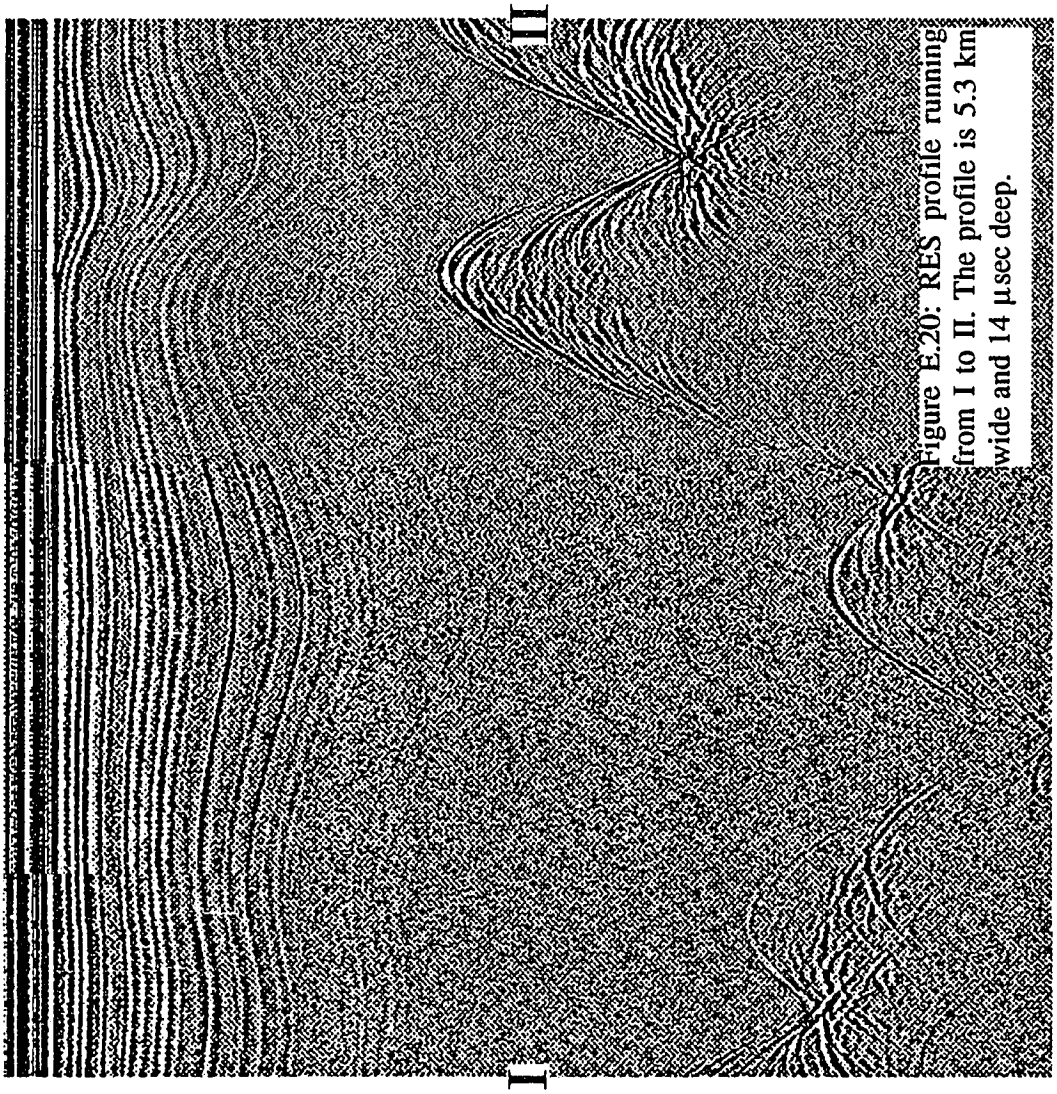

Figure E.20: RES profile running from I to II. The profile is 5.3 km wide and 14 µsec deep.

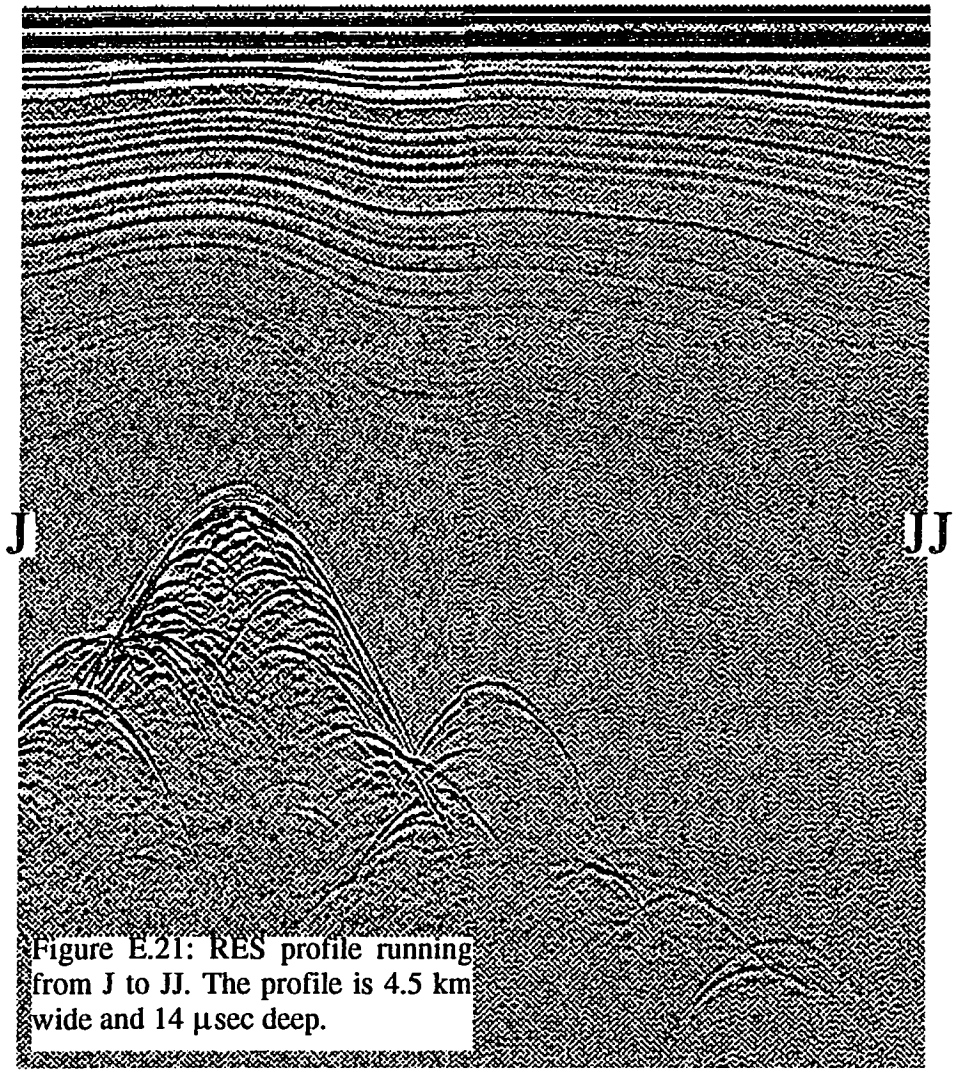

Figure E.21: RES profile running from J to JJ. The profile is 4.5 km wide and 14 μsec deep.

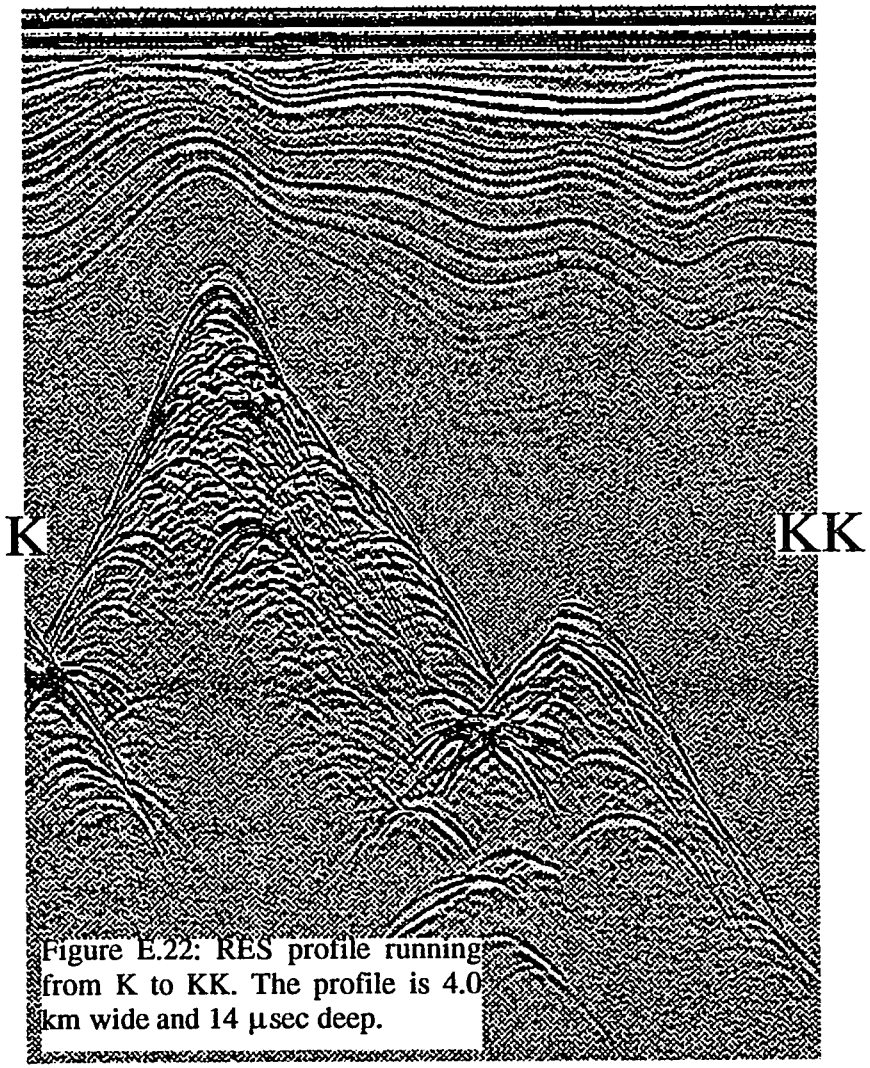

Figure E.22: RES profile running from K to KK. The profile is 4.0 km wide and 14 μsec deep.

L

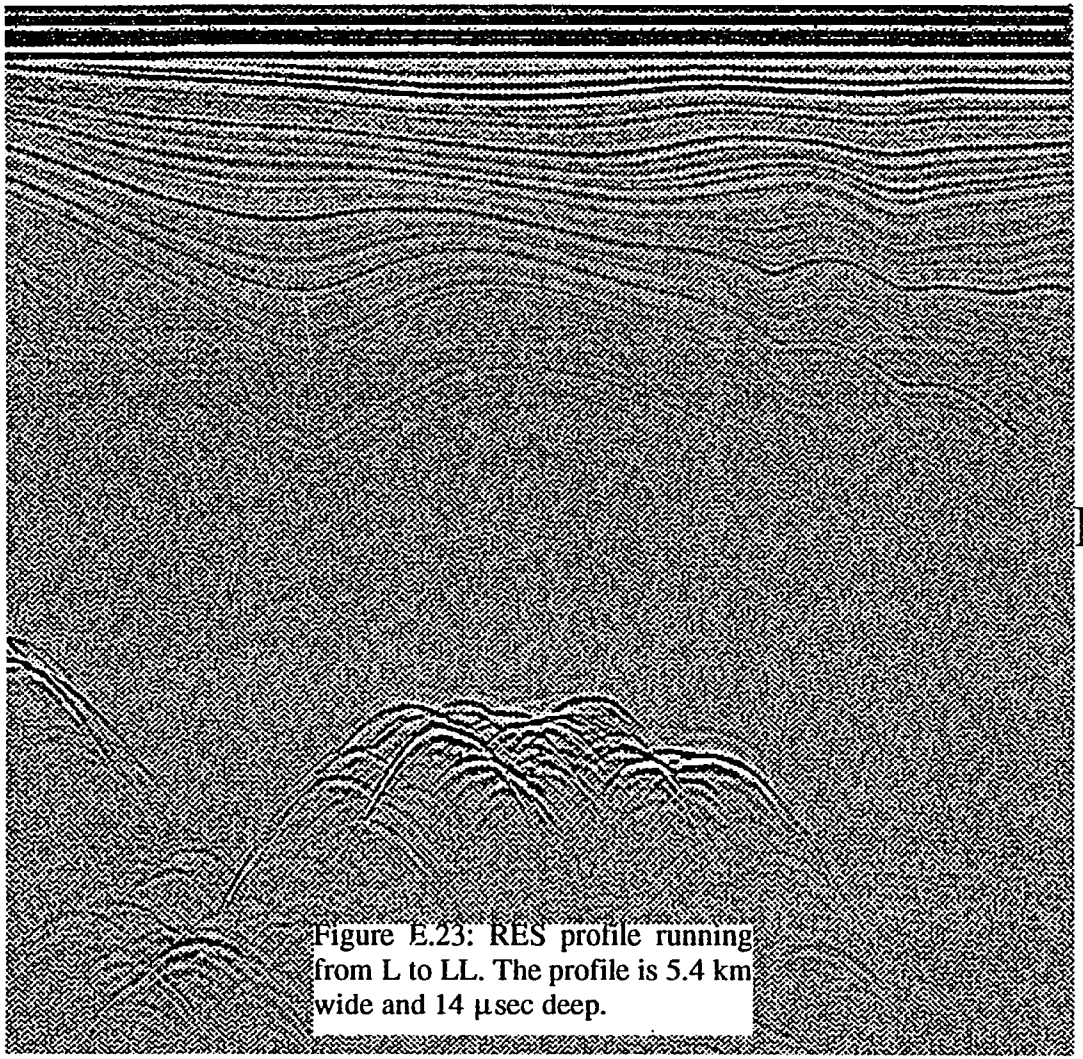

LL

Figure E.23: RES profile running from L to LL. The profile is 5.4 km wide and 14 μsec deep.

Vita

Bruce Randall Weertman was born December 9, 1960 in Evanston, Illinois. His parents are Johannes Weertman and Julia Randall Weertman.

In June, 1984 he received a B.S. in Applied Math, Engineering and Physics (AMPL) from the University of Wisconsin, Madison.